



UNIVERSITY OF IOANNINA
SCHOOL OF SCIENCES
PHYSICS DEPARTMENT



Amorphous or nanostructured composite films with predefined properties

Nikolaos T. Panagiotopoulos

A thesis submitted for the degree of Doctor of Philosophy

Ioannina, 2012

CONSULTANT JURY

- **Prof. G.A. Evangelakis (supervisor)**

Department of Physics, University of Ioannina

- **Assoc. Prof. P. Patsalas**

Department of Materials Science and Engineering, University of Ioannina

- **Prof. C. Kosmidis**

Department of Physics, University of Ioannina

EXAMINATION JURY

- **Prof. G.A. Evangelakis**

Department of Physics, University of Ioannina

- **Assoc. Prof. P. Patsalas**

Department of Materials Science and Engineering, University of Ioannina

- **Prof. C. Kosmidis**

Department of Physics, University of Ioannina

- **Prof. T. Bakas**

Department of Physics, University of Ioannina

- **Assoc. Prof. I. Panagiotopoulos**

Department of Materials Science and Engineering, University of Ioannina

- **Assoc. Prof. M. Kamaratos**

Department of Physics, University of Ioannina

- **Lect. D.C. Koutsogeorgis**

School of Science and Technology, Nottingham Trent University

ΠΡΑΚΤΙΚΟ

Αριθ. Πρωτ. 1231
Παρεροχήν, 22-6-12

ΔΗΜΟΣΙΑΣ ΠΑΡΟΥΣΙΑΣΗΣ ΚΑΙ ΚΡΙΣΗΣ
ΔΙΔΑΚΤΟΡΙΚΗΣ ΔΙΑΤΡΙΒΗΣ

Σήμερα, 21/ 6/ 2012, ημέρα **Πέμπτη** και ώρα **12.00**, στην αίθουσα διαλέξεων του Τμήματος Φυσικής, πραγματοποιήθηκε η διαδικασία δημόσιας παρουσίασης και κρίσης ενώπιον της επταμελούς Εξεταστικής Επιτροπής της διδακτορικής διατριβής που εκπόνησε ο υποψήφιος κ. **Νικόλαος Παναγιωτόπουλος** στα πλαίσια του **Προγράμματος Μεταπτυχιακών Σπουδών στη Φυσικής**.

Την επταμελή Εξεταστική Επιτροπή, που όρισε με σχετική απόφασή της η Γενική Συνέλευση με Ειδική Σύνθεση του Τμήματος Φυσικής σύμφωνα με το άρθρο 8.2 του Κ.Μ.Σ. (συν. αρ. **405 / 19-06-2012**) αποτελούν οι:

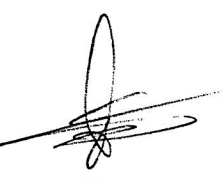
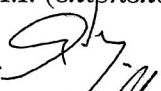


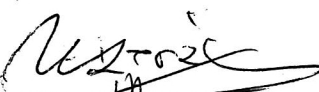

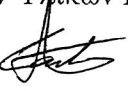
1. Γ. Ευαγγελάκης Καθηγητής Τμήματος Φυσικής Π.Ι. (επιβλέπων)
2. Κ. Κοσμίδης, Καθηγητής Τμήματος Φυσικής Π.Ι.
3. Θ. Μπάκας, Καθηγητής Τμήματος Φυσικής Π.Ι.
4. Μ. Καμαράτος, Αναπλ. Καθηγητής Τμήματος Φυσικής Π.Ι.
5. Π. Πατσαλάς, Αναπλ. Καθηγητής Τμήματος Μηχανικών Υλικών Π.Ι.
6. Ι. Παναγιωτόπουλος, Αναπλ. Καθηγητής Τμήματος Μηχανικών Υλικών Π.Ι.
7. Δ. Κουτσογεώργης, Lecturer, Nottingham Trent University, UK

Ο υποψήφιος παρουσίασε και υποστήριξε δημόσια ενώπιον των μελών της Εξεταστικής Επιτροπής την εκπονηθείσα διδακτορική διατριβή με τίτλο: «*Αμορφα ή Νανοδομημένα σύνθετα υμένια με προκαθορισμένες ιδιότητες*»

Εν συνεχεία, τα μέλη της Επιτροπής δήλωσαν ομόφωνα ότι έμειναν ιδιαίτερα ικανοποιημένοι από την παρουσίαση και από τις απαντήσεις του υποψηφίου στις ερωτήσεις που του υποβλήθηκαν και έκριναν ομόφωνα ότι η εργασία είναι άρτια, άριστου επιπέδου και επιστημονικά ορθή.

Με βάση τα παραπάνω, η Επιτροπή εγκρίνει τη διδακτορική διατριβή, την βαθμολογεί με βαθμό **Άριστα (10 δέκα)** και εισηγείται την έγκρισή της από το Τμήμα Φυσικής καθώς και την απονομή στον κ. **Νικόλαο Παναγιωτόπουλο** του Διδακτορικού Διπλώματος στη Φυσική.

Τα μέλη της Εξεταστικής Επιτροπής

1. Γ. Ευαγγελάκης Καθηγητής Τμήματος Φυσικής Π.Ι. (επιβλέπων) 
2. Κ. Κοσμίδης, Καθηγητής Τμήματος Φυσικής Π.Ι. 
3. Θ. Μπάκας, Καθηγητής Τμήματος Φυσικής Π.Ι. 
4. Μ. Καμαράτος, Αναπλ. Καθηγητής Τμήματος Φυσικής Π.Ι. 
5. Π. Πατσαλάς, Αναπλ. Καθηγητής Τμήματος Μηχανικών Υλικών Π.Ι. 
6. Ι. Παναγιωτόπουλος, Αναπλ. Καθηγητής Τμήματος Μηχανικών Υλικών Π.Ι. 
7. Δ. Κουτσογεώργης, Lecturer, Nottingham Trent University, UK 

Preface

This thesis focuses on the growth of thin films with predefined properties by controlling the deposition conditions and by post growth processing. Briefly, we studied the control of the optical properties of hydrogenated amorphous diamond-like carbon (a-C:H) films, as well as their photosensitivity and optical performances by post growth laser irradiation. In addition, binary, ternary and quaternary metallic Zr-based glassy films were grown and used as templates for the production of selective ZrO_2 phases (material that is widely used due to their catalytic activity) by oxygen plasma treatment. Ti-based polycrystalline films were grown aiming in the stabilization of the Ti in the β -phase, which is widely used as a biocompatible implant. Moreover, we studied metal containing (Nickel and Silver) amorphous diamond-like carbon (DLC:Ni and DLC:Ag) as catalysts for carbon nanotubes (CNTs) growth and as biocompatible coatings, respectively. Additional study, which has been accomplished on the growth of CNTs, was performed for their use as solar energy collector coatings, while the a-C:Ag films were examined for their biocompatibility.

The deposition techniques, which were used for the growth of thin films, were the plasma enhanced chemical vapor deposition (PECVD), the magnetron sputtering and the pulsed laser deposition (PLD). For post growth treatments and the CNTs growth, oxygen plasma and thermal chemical vapor deposition (TCVD) were used, respectively. Laser irradiations were performed by a picosecond laser.

The physical properties of all films were examined by various characterization techniques. Electronic characterization was performed by Auger electron (AES), X-ray photoelectron (XPS) and energy dispersive electron (EDS) spectroscopy. For the structural characterization X-ray diffraction (XRD) were used, while morphology characterization was performed by scanning electron microscopy (SEM), specular and nonspecular X-ray reflectivity (XRR) and atomic force microscopy (AFM). The electronic structure and the optical properties of the films were performed by normal and variable angle specular and nonspecular optical reflectivity (ORS) and electron energy loss spectroscopy (EELS).

Acknowledgements

I would like to acknowledge and honour personally all the people that contributed, eachone in his way, so that this PhD thesis became possible and established.

First of all I would like to thanks my advisor Prof. G.A. Evangelakis for the choise the topic of this thesis, his constant effort of impartment of knowledge of Physics and giving me a way of analyzing and exploiting every research results.

I would like to give my thanks Assoc. Prof. P. Patsala for his catalytic influence as far as the laboratory activities are concerned, from experimental setup up to conveying the knowledge of the operation principles of several deposition and characterization techniques.

Here I have to express my regards both to Prof. Evangelakis and Dr. Patsalas for giving me the completely freedom of taking initiatives and try to execute them in the laboratory.

My special thanks to Prof. C. Kosmidis and the laser facilities of University of Ioannina for providing the nano and picosecond laser beam sources for the needs of the present thesis referring to the pulsed laser deposition techniques and the post growth irradiations of the samples. In this point I would like to thank Dr. Karras and Dr. S. Kaziannis for the operation of the laser sources and the general discussions about various physical phenomena.

I would like also to thank Prof. M. Mozetic and Dr. J. Kovac of the Department of Surface Engineering and Optoelectronics of Jozef Stefan Institute in Slovenia, who introduced me to the cold plasma treatment technique, during my visit to Jozef Stefan Institute that financed by the Slovenian Research Agency (program P2-0082) and Life Long Learning Programme/Erasmus LLP of the International and Public Relations Directorate of the University of Ioannina.

Also I would like to thank Assoc. Prof. E. Lidorikis for the free access and use of the fitting code of the optical reflectivity spectra and his instant, extent and will to explain the

optical properties of solids and the light-matter interactions. I have the luck of the same helpful addressing by Dr. Anagnostopoulou concerning the experimental measurements and characterization analysis by means of X-ray Fluorescence (XRF) of the Ti-based alloys and the DLC:Ag films that co-financed by the European Union (European Regional Development FundERDF) and Greek national funds through the Operational Program “THESSALY- MAINLAND GREECE AND EPIRUS-2007-2013” of the National Strategic Reference Framework (NSRF 2007-2013).

Also, I would like to thank the Nottingham Trent University for the donation of the PECVD reactor.

I would like to express my gratitude to the other members of the jury committee Prof. T. Bakas, Assoc. Prof. M. Kamaratos, Assoc. Prof. I. Panagiotopoulos and Lect. D.C. Koutsogeorgis for their efforts and time they devoted in reading and commenting this thesis

I would like to express my cordial thanks to Dr. Matenoglou with whom I spent many hours in the laboratory, setting up various experimental techniques and analysis of results. It was with his laboratory experience that I was able to learn many technological and physical meanings. I also want to give my regards to Dr. Koutsokeras for our long discussions and his will to explain to me the X-ray experimental techniques. Also, here I want to express my cordial gratitude to my best friend, PhD candidate A.E. Lagogianni, for her continuous and substantial support and help through all these years. Her existence was truly catalytic.

At last but not least, I want to attribute my extent gratitude to my family; Theodoros, Irene and Stamatis Panagiotopoulos for providing me the chance to continue my education and for their endless support to carry out this PhD thesis.

Devoted to my family

List of papers

- 1) N.T. Panagiotopoulos, P. Patsalas, C. Prouskas, G.P. Dimitrakopoulos, P. Komninou, T. Karakostas, A.P. Tighe, and E. Lidorikis, *Bare-Eye View at the Nanoscale: New Visual Interferometric Multi-Indicator (VIMI)*, ACS Applied Materials and Interfaces 2, 3052 (2010)
- 2) N.T. Panagiotopoulos, G. Karras, E. Lidorikis, D.C. Koutsogeorgis, C. Kosmidis, P. Patsalas, *Photosensitivity and optical performance of hydrogenated amorphous carbon films processed by picosecond laser beams*, Surface and Coating Technology 206, 734 (2011)
- 3) N.T. Panagiotopoulos, J. Kovač, M. Mozetič, P. Patsalas, G.A. Evangelakis, *Formation of Tetragonal or Monoclinic ZrO₂ coatings by oxygen plasma treatment of Zr_{74.7}Cu_{19.7}Nb_{5.6} glassy thin films*, Journal of Vacuum Science and Technology A 29(5), 051303 (2011)
- 4) N.T. Panagiotopoulos, J. Kovač, U. Cvelbar, M. Mozetič, P. Patsalas, G.A. Evangelakis, *Zr-based glassy films as templates for selectively tetragonal or monoclinic ZrO₂ thin film growth with predefined surface morphologies*, 2nd round of review, Journal of Vacuum Science and Technology A (2012)
- 5) N.T. Panagiotopoulos, E.K. Diamanti, L.E. Koutsokeras, E. Kordatos, D. Gournis, T.E. Matikas, and P. Patsalas, *Nanostructured catalysts producing firmly attached, durable, super-black carbon nanotube systems: applications in solar thermal harvesting*, 2nd round of review, ACS Nano (2012)
- 6) N.T. Panagiotopoulos, J. J. Gutierrez-Moreno, P. Patsalas, Ch. E. Lekka, G. A. Evangelakis, *“On the growth of Ti-Nb and Ti-Nb-Hf thin films by magnetron sputtering”*, under preparation

Table of contents

PREFACE	7
ACKNOWLEDGEMENTS	9
LIST OF PAPERS	11
TABLES OF CONTENTS	13
1 INTRODUCTION	17
1.1 Aim of the PhD thesis	19
1.2 Elements and structures involved	20
1.2.1 Amorphous carbon	20
1.2.2 Carbon nanotubes (CNTs)	21
1.2.3 Zr-based metallic glassy films and crystalline Zr oxides	23
1.2.4 Ti-based alloys	24
1.2.5 Ni and Ag-carbon nanostructures	25
1.3 References	27
2 THIN FILMS GROWTH	29
2.1 Introduction	31
2.2 Thin film growth mechanism	31
2.3 Film structures, microstructures and surface morphologies.	34
2.4 Plasma	35
2.5 Chemical vapor deposition (CVD)	37
2.5.1 Atmospheric Pressure Chemical Vapor Deposition (APCVD)	39
2.5.2 Low Pressure Chemical Vapor Deposition (LPCVD)	40
2.5.3 Plasma Chemical Vapor Deposition (PECVD)	40
2.5.4 Experimental setup	45
2.6 Magnetron sputtering	48
2.6.1 Experimental setup	51
2.7 Pulsed laser deposition (PLD)	52

2.7.1	PLD Experimental setup.....	55
2.8	Post growth plasma treatment.....	57
2.8.1	Plasma treatment experimental setup.....	59
2.9	References	61
3	CHARACTERIZATION TECHNIQUES.....	63
3.1	Introduction.....	65
3.2	Electronic characterization techniques	65
3.2.1	Auger electron spectroscopy (AES)	65
3.2.2	X-Ray photoelectron spectroscopy (XPS)	70
3.2.3	Energy dispersive X-rays spectroscopy (EDX).....	75
3.3	Structural characterization techniques	76
3.3.1	X-ray diffraction (XRD).....	76
3.3.1.1	Bragg-Brentano geometry XRD	79
3.3.1.2	Grazing incidence XRD (GID)	80
3.3.2	Grain analysis- Grain size.....	82
3.4	Morphological characterization techniques.....	84
3.4.1	Scanning electron microscopy (SEM)	84
3.4.2	Atomic force microscopy (AFM)	86
3.4.3	X-ray reflectivity (XRR).....	88
3.4.3.1	Film thickness	90
3.4.3.2	Film density	91
3.4.3.3	Film roughness	91
3.4.4	Off specular X-ray reflectivity	93
3.5	Optical properties and electronic structure characterization techniques.....	95
3.5.1	Optical Reflectivity Spectroscopy (ORS)	95
3.5.1	Variable angle optical reflectivity	101
3.5.2	Off specular optical reflectivity	102
3.5.3	Electron energy loss spectroscopy (EELS).....	103
3.6	References.....	105
4	SINGLE ELEMENT AMORPHOUS SOLIDS; CARBON	107

4.1	Introduction	109
4.2	Parameterization of the PECVD reactor.....	111
4.2.1	Influence of the working pressure	112
4.2.2	Influence of the applied RF power	114
4.2.3	Influence of the reactants' percentage flow.....	115
4.3	General properties of the as grown a-C:H films by RF PECVD	116
4.4	Hydrogenated amorphous carbon films as antireflection coatings	119
4.4.1	Experimental setup	119
4.4.2	Determination of optical properties of a-C:H films for specific visible light wavelength antireflection.....	120
4.4.3	Results and discussion.....	122
4.5	Photosensitivity and optical performance of hydrogenated amorphous carbon films by picosecond laser.....	126
4.5.1	Characteristics of the as-grown a-C:H films	127
4.5.2	Photosensitivity of a-C:H films	133
4.6	Conclusions	146
4.7	References.....	148
5	Multi elemental metallic glassy films for selective crystalline oxide films growth.....	153
5.1	Introduction	155
5.2	Experimental setup	157
5.3	Oxidation of Zr-based ternary Zr-Cu-Me, (Me= Al ₅ , Ti ₉ , Si ₆) and the quaternary Zr ₆₂ Cu ₂₃ Ti ₉ Si ₆ metallic glassy films.....	159
5.4	Oxidation of Zr-based ternary metallic glassy films with addition of element known as Zirconia stabilizer.....	165
5.5	Conclusions	173
5.6	References.....	175
6	MULTI ELEMENTAL POLYCRYSTALLINE Ti-BASED FILMS	179
6.1	Introduction	181
6.2	Experimental details.....	182
6.3	Results and Discussion	182
		15

6.3.1	Deposition details of Ti-based films	182
6.3.2	Structural characteristics of Ti-based films	184
6.3.3	Macroscopic density of Ti-Hf films	188
6.3.4	Surface electronic characterization of Ti-based films	191
6.3.5	Bulk electronic characterization of Ti-based films.....	194
6.4	Conclusions.....	196
6.5	References	198
7	METAL-CARBON NANOSTRUCTURED SOLIDS	199
7.1	Introduction.....	201
7.2	Experimental setup.....	204
7.3	Nickel contained nanocomposite amorphous diamond-like carbon catalysts (a-C:Ni).....	207
7.3.1	Growth and Characteristics of DLC:Ni catalysts.	214
7.3.2	Structural and morphological features of CNTs.	216
7.3.3	Functional properties of CNT and solar applications.....	222
7.4	Silver contained nanocomposite amorphous diamond-like carbon films (a-C:Ag)	226
7.5	Conclusions.....	231
7.6	References	233
8	CONCLUSIONS.....	237

APPENDIX

Optical spectroscopy	243
The Lorentz model	244
Absorbance and refractive index	246

1 INTRODUCTION

The main characteristic that can be described in the modern world is the rapid evolution of technology. Of course this is generated by the continuous quest for knowledge through research. Science is continuously developing in all research fields; Physics, Mathematics, Chemistry, History, Human and Social Sciences, etc. Solid state physics and physics of materials are among the most rapidly expanded research fields. This is due to the fact of a wide range of applicable materials that can be developed by manipulation of the control of the existing or by modified physical properties of solids. In the last forty years the most radical developments in the specific field have been emerged for low dimensional solids, such as thin films. The main advantages in research of thin films, as far as the science and the industrial fields are concerned, are their potential in constructing and studying metastable phases of solids and the subsequent scale up to industrial standards.

1.1 Aim of the PhD thesis

The aim of this PhD thesis is a detailed study on the growth and characterization of thin films with predefined physical properties so that they could be suitable for various and foregone applications. In order for this objective to actually be achieved, the research was extended to many and different types of thin films solids by physical and chemical vapor depositions. A qualitative categorization, as far as the structure is concerned, of the studied films can be made as follows:

- I. Single-element amorphous films
- II. Multi-element amorphous metal films
- III. Metastable polycrystalline metal films
- IV. Nanocomposite films consisting of embedded metal nanoparticles in amorphous matrix

Besides the detailed characterization of the as grown samples, the single and the multi element amorphous structured films were selected for the further study of light-matter and plasma-matter interactions by post growth laser and plasma treatment processes, respectively.

The functionalization research of the films was based on the production of antireflective coatings, catalytic oxides, biocompatible coatings and catalysts for carbon nanotubes (CNTs) growth.

1.2 Elements and structures involved

1.2.1 Amorphous carbon

Carbon is one of the most studied elements due to its unique properties originated by the ability of sp^2 and sp^3 orbital hybridizations. Graphite and diamond are constituted of 100% sp^2 and sp^3 hybridized Carbon atoms, respectively. Graphite is a soft, opaque, electrical and thermal conductive solid, in comparison to diamond which is a hard, transparent to visible and infrared light and electrical insulating solid. The last decades the capability of the growth of amorphous diamond-like carbon films (DLC) has been developed. These amorphous films are constituted by sp^2 and sp^3 hybridized Carbon atoms, with physical properties determined by the sp^2/sp^3 ratio. In the general category of the DLC the hydrogenated amorphous diamond-like carbon films (DLC:H) are also included. Hydrogen can be incorporated in both sp^2 and sp^3 hybridized Carbon atoms, modifying significantly the physical properties of the DLC film. Figure 1.1 shows the phase diagram of the different types of DLC versus the sp^2 , the sp^3 and the Hydrogen content.

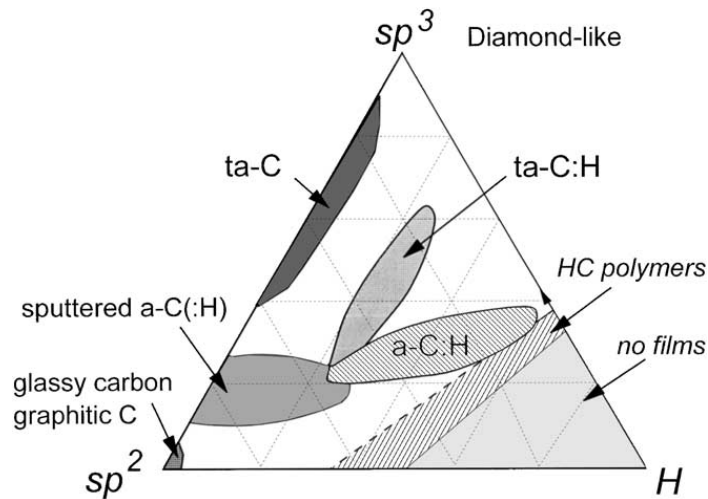


Figure 1.1: Ternary phase diagram of DLC films [1]

1.2.2 Carbon nanotubes (CNTs)

New carbon nanostructures (CNTs) were discovered by S. Iijima at 1991 [2]. The CNTs are large carbon cylinder macromolecules with diameter of some nanometers and length up to some micrometers, or else with aspect ratio up to 1000, figure 1.2. The last years intensive research of CNTs revealed their unique chemical [3], electrical [4], mechanical [5] and thermal properties [6].

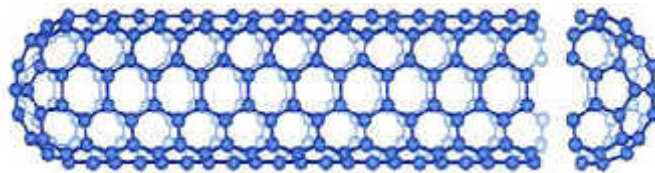


Figure 1.2: Structure of a carbon nanotube

The formation of a CNT can be described as the result of the roll-up of a graphene sheet, figure 1.3.

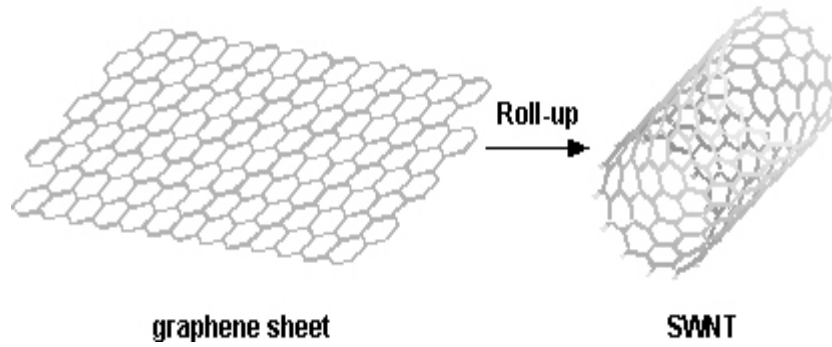


Figure 1.3: graphical presentation of CNT formation

The CNTs can be categorized in two types; 1) the single walled nanotubes (SWNTs) and 2) the multi walled nanotubes (MWNTs). The SWNTs have diameter around 1.2nm. The MWNTs are consisted by several coaxial SWNTs of different diameters with the thicker to include the thinners. The total diameter of MWNTs can be up to 40nm [1].

A SWNT is consisted by two different geometrical parts and so with different physical and chemical properties. The first part is the CNT's cap that has the structure of a fullerene, like the C_{60} . By the Euler's theorem emerges the need of a structure of pentagons surrounded by hexagons so a proper curvature to be formed able to enclose the fullerene's volume. With this structure the minimum topological curvature is achieved leading to the minimum surface stress that stabilizes the fullerene structure. The second part of a SWNT is a cylindrical part that can accrue by rolling up a graphene sheet with specific direction. Since the tube has cylinder symmetry two atoms of the graphene sheet can be chosen to define the direction of the rolling up process. The first atom position is the reference point on which when the second atom position coincide the direction of the roll up can be defined. The vector that joins those two atoms is called chiral vector and has the magnitude of the SWNT perimeter and it is normal to it.

The chiral vector defines the structure of the CNTs and equals to

$$\vec{C} = n\vec{\alpha}_1 + m\vec{\alpha}_2$$

where n and m integer, figure 1.4.

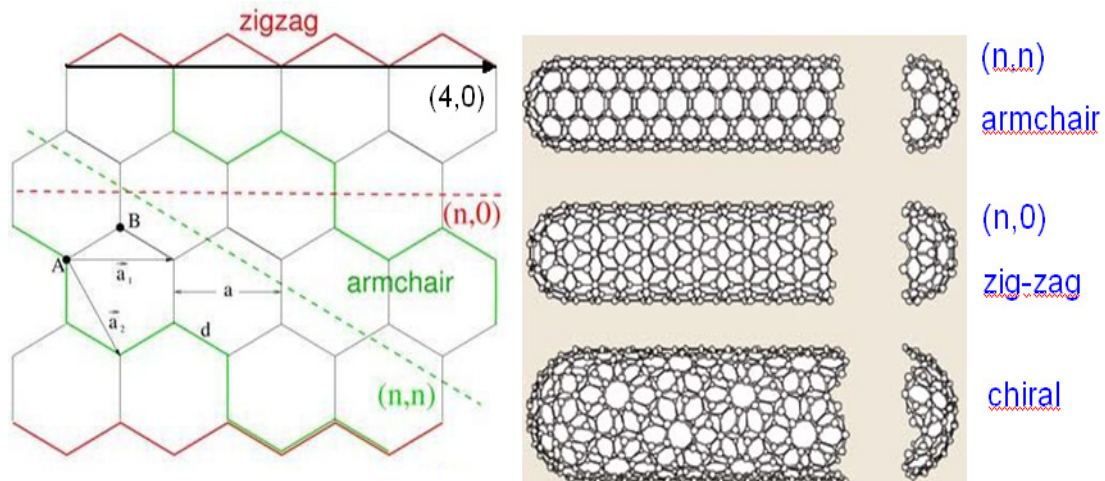


Figure 1.4: SWNTs with different cap chirality and tube structure a) armchair, b) zigzag c) chiral

So if

- $n=m$ the armchair CNT is formed
- $m=0$ the zigzag CNT is formed
- the rolling angle is between 0 and 30 degrees the CNT has chiral symmetry then the CNT is called **chiral**

1.2.3 Zr-based metallic glassy films and crystalline Zr oxides

Although metals are crystalline, the last decades the ability of the transition metals alloys to form glassy structures, i.e. with absence of long range order, has been discovered [7]. Zr-based films are one of the most studied metallic glassy systems. Zr-based metallic glassy films have excellent mechanical properties since they have strength higher than steel and are ductile as polymers, figure 1.5.

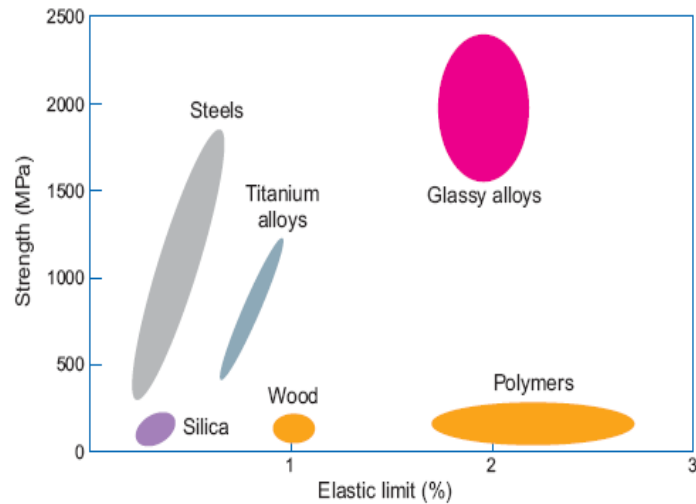


Figure 1.5: Mechanical properties of metallic glasses in comparison with hard brittle metallic alloys and soft elastic polymers

Additionally Zr-based metallic glassy alloys have excellent anticorrosion properties [8] and they are biocompatible [9]. Therefore extended study has been made for the use in microelectromechanical systems (MEMS)[10,11], protective coatings[12,13,14,15] and biomedical applications [16].

Besides the ability of Zr to form metallic glassy alloys, very interesting material with functional properties is the ZrO_2 crystalline oxide. The crystal structures of ZrO_2 are actually three. The stable phase of monoclinic at room temperature, the metastable tetragonal (Zirconia) and the high temperature cubic ZrO_2 . Every ZrO_2 structure has different applications due to its structure which promotes different physical properties. In general ZrO_2 has catalytic activity [17], wide band gap [18] high hardness [19] and it is thermal insulating [20]. So it is widely used as catalyst, as optical and protective coating, in MEMS, etc.

1.2.4 Ti-based alloys

Titanium and its alloys are biocompatible [21] and anticorrosive [22] solids with similar hardness as steel but their weights are almost the half of that of the steel. Therefore they are able to meet applications in aerospace [23], subsea [24], automobile [25], health and

medical industries [26]. Titanium at room temperature, crystallizes in the FCC structure, also known as α -Ti, while at high temperatures it forms BCC structure, known as β -Ti. The main difference of the two phases of Titanium is their hardness with the β -Ti exhibiting almost half hardness than the α -Ti. The last decades extended research has been made on Titanium alloys mechanical properties by controlling their crystal structures. Al [27], Nb [28], Mo[29], etc are the most studied and used elements as β -Ti stabilizers of β -Ti alloys, at room temperature. Control and predefinition of the mechanical properties of Titanium alloys is very important for their usage in industrial scale range, depending on the specific application.

1.2.5 Ni and Ag-carbon nanostructures

The last years extensive research is based on the exploitation of the physical properties of metallic nanoparticles. Growth of nanoparticles embedded in an amorphous matrix of a film has two main advantages; the direct study of the properties of the nanoparticles and the exploitation of the properties that might emerge by the nanoparticles-matrix interaction. Direct growth of such a system presupposes that the chosen element of the nanoparticles and the matrix are immiscible. If that restriction applies the matrix is able to capture and stabilize the desired nanoparticles, figure 1.6. Nickel and Silver fulfill this restriction with Carbon. DLC films can be used as the matrix of Nickel or Silver nanoparticles.

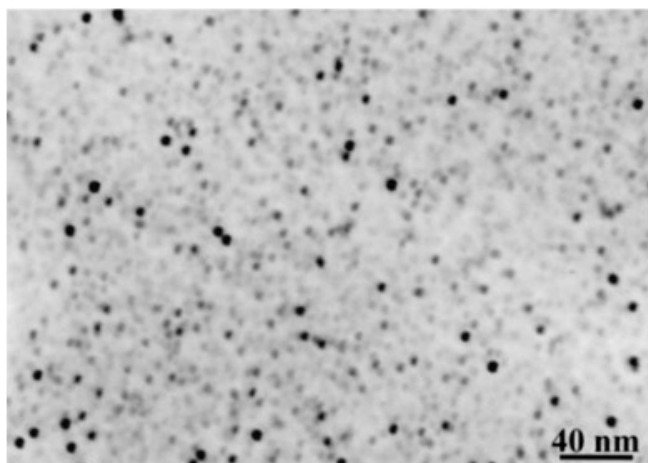


Figure 1.6: TEM image of Ag nanoparticles embedded in a DLC matrix

Nickel is a well known catalyst for the growth of carbon nanotubes (CNTs). DLC:Ni is used here as catalytic templates in film form that evolve the CNTs applications to a large area surfaces.

DLC:Ag films can be used as coatings for any use to medical industry because of the biocompatible properties of DLC and Silver but taking advantage also of the antibacterial properties of Silver.

1.3 References

- [1] J. Robertson, Mater. Sci. Eng. R **37**, 129 (2002)
- [2] S. Iijima, Nature **354**, 6348 (1991)
- [3] D. Tasis, N. Tagmatarchis, A. Bianco, M. Prato, Chem. Rev. **106**, 1105 (2006)
- [4] S. Stankovich, D.A. Dikin, G.H.B. Dommett, K.M. Kohlhaas, E.J. Zimney, E.A. Stach, R.D. Piner, S.T. Nguyen, R.S. Ruoff, Nature **442**, 282 (2006)
- [5] E.T. Thostenson, Z. Ren, T.-W. Chou, Comp. Sci. Tech. **61**, 1899 (2001)
- [6] M. J. Biercuk, M. C. Llaguno, M. Radosavljevic, J. K. Hyun, A. T. Johnson, J. E. Fischer, Appl. Phys. Lett. **80**, 2767 (2002)
- [7] A.L. Greer, Science **267**, 5206 (1995)
- [8] W.H. Peter, R.A. Buchanan, C.T. Liu, P.K. Liaw, M.L. Morrison, J.A. Horton, C.A. Carmichael Jr., J.L. Wright, Intermetallics **10**, 1157 (2002)
- [9] L. Liu, C.L. Qiu, C.Y. Huang, T. Yu, H. Huang, S.M. Zhang, Intermetallics **17**, 235 (2009)
- [10] J. Schroers, Q. Pham, A. Desai, J. Microelectro-mechanical Systems **16**, 240 (2007)
- [11] G.P. Zhang, Y. Liu, B. Zhang, Scripta Mater. **54**, 897 (2006)
- [12] J. Musil, P. Zeman, Vacuum **52**, 269 (1999)
- [13] H.-B. Lu, Y. Li, F.-H. Wang, J. Alloys Comp. **465**, 139 (2008)
- [14] H.S. Chou, J.C. Huang, L.W. Chang, T.G. Nieh, Appl. Phys. Lett. **93**, 191901 (2008)
- [15] O. Jimenez, M. Audronis, M.A. Baker, A. Matthews, A. Leyland, J. Phys. D **41**, 155301 (2008)
- [16] W. He, A. Chuang, Z. Cao, P.K. Liaw, Metall. Mater. Trans. A **41**, 1726 (2010)
- [17] C. Morterra, G. Cerrato, F. Pinna, M. Signoreto, J. Catal. **157**, 109 (1995)
- [18] R.H. French, S.J. Glass, F.S. Ohuchi, Y.-N.. Xu, W.Y. Ching, Phys. Rev. B **49**, 5133 (1993)
- [19] S. Desgreniers, K. Lagarec, Phys. Rev. B **59**, 8467 (1999)
- [20] R. Vassen, X. Cao, F. Tietz, D. basu, D. Stover, J. Amer. Ceram. Soc. **83**, 2023 (2000)
- [21] M. Long, H.J. Rack, Biomaterials **19**, 1621 (1997)
- [22] M.A. Khan, R.L. Williams, D.F. Williams, Biomaterials **17**, 2117 (1996)
- [23] R.R. Boyer, R.D. Briggs, J. Mater. Eng. Perfor. **14**, 681 (2005)

- [24] R.W. Schutz, JOM 46, 24 (1994)
- [25] M.J. Donachie Jr., Titanium a Technical Guide, (ASM international, USA, 2000)
- [26] M. Niinomi, Mater. Sci. Eng. A 243, 231 (1998)
- [27] I. Ohnuma, Y. Fujita, H. Mitsui, K. Ishikawa, R. Kaimuna, K. Ishida, Acta materialia 48, 3113 (2000)
- [28] J. Huang, H. Xing, J. Sun, Scripta Materialia 66, 682 (2012)
- [29] W.F. Ho, C.P. Ju, J.H. Chern Lin, Biomaterials 20, 2115 (1999)

2 THIN FILMS GROWTH

2.1 Introduction

Thin film solids may have different physical properties than their bulk solid counterparts. This is due to their abilities of formation of metastable phases and microstructures originated from the presence of residual stresses and can be achieved by non thermodynamically equilibrium deposition methods.

Thin film growth techniques from gas phase can be divided into the following two major categories.

1. Physical vapor deposition (PVD) and
2. Chemical vapor deposition (CVD)

Basic analyses of the PVD and CVD with emphasis to those that have been used in this thesis are analytically described below.

2.2 Thin film growth mechanism

Vapor deposition of a solid film is a gas to solid phase transition process, figure 2.1.

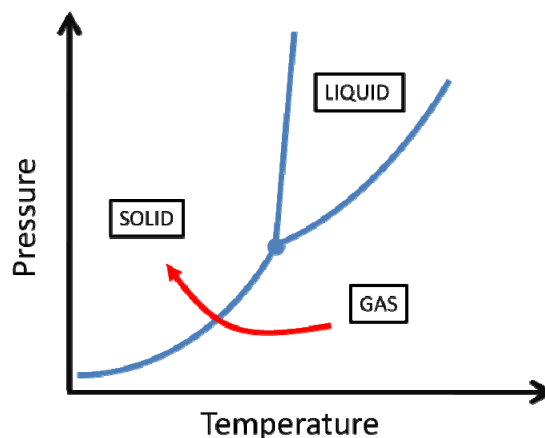


Figure 2.1: Pressure - Temperature phase diagram

The transition's stability can be described by their difference of Gibbs free energies, dG . If the Gibbs free energy is considered to be the state function which describes the stability or the obtainable work of a phase, the lowest it is, the more stable phase formed is, figure 2.2.

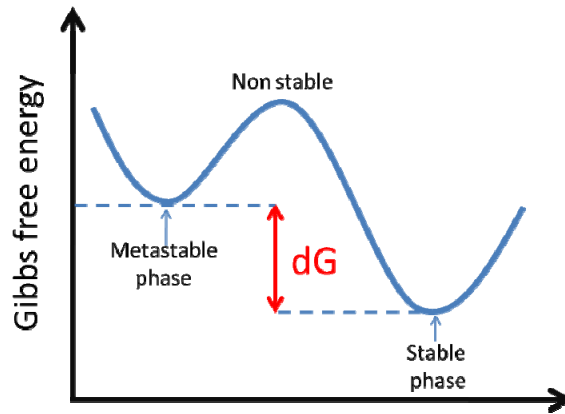


Figure 2.2: Gibbs free energy of stable and metastable phases

The initial states of nucleation of vapors can be studied by the assumption that the nuclei have spherical shape. The change in free energy has as a result the gain of forming a new volume but the loss in creating a new interface. The Gibbs free energy can be written as the sum of the term that corresponds to the volume and the surface free energies as

$$dG \equiv \underbrace{\frac{4}{3}\pi r^3 dG_v}_{\text{Volume Term}} + \underbrace{4\pi r^2 \gamma}_{\text{Surface Term}}$$

where, G_v is the Gibbs free energy per unit volume, γ is the energy per unit area (interfacial energy) and r is the radius of the sphere. Surface energies are called alternatively surface tensions. This is because the initial nuclei have a liquid like behavior allowing for their surface area reconstruction and in consequence their surface energy, since mechanical stretches and strains are absent.

A spherical shaped solid nucleus, on a substrate surface, is under interfacial tensions caused by the surface-vacuum, γ_{sv} , the film-substrate, γ_{fs} , and the film-vacuum, γ_{fv} , interfaces, figure 2.3.

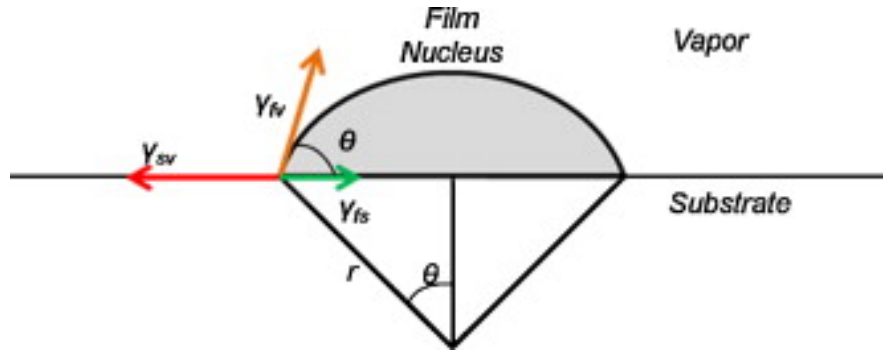


Figure 2.3: Interfacial tensions of droplet on a surface

The mechanical equilibrium of the forming nucleus is determined by the interfacial tensions can be determined by the Young's equations as

$$\gamma_{sv} = \gamma_{fs} + \gamma_{fv} \cos \theta$$

Generally, there are three different types of film growth predetermined by the angle θ between the solid and the substrate.

If the angle $\theta > 0$ then

$$\gamma_{sv} < \gamma_{fs} + \gamma_{fv}$$

island growth (Volmer–Weber) occurs if γ_{fs} is negligible and the surface tension of the film exceeds the one of the substrate. The initial independent islands are formed and as the deposition continuous the film is deposited, 2.4a.

If the angle $\theta = 0$ then

$$\gamma_{sv} \gg \gamma_{fs} + \gamma_{fv}$$

In this case the solid wets homogeneously the substrate and layer by layer deposition occurs (Frank–Van der Merwe). This growth mode is necessary and desirable for epitaxial films deposition, figure 2.4b.

If the angle θ is that so

$$\gamma_{sv} > \gamma_{fs} + \gamma_{fv}$$

the Stranski–Krastanov mode of growth occurs. In that case 5-6 monolayer by monolayer is deposited followed by island growth, figure 2.4c. A possible mechanism for Stranski–Krastanov growth is the energy relief, caused by the substrate and the intermediate deposited film lattice mismatch, which triggers island growth [1].

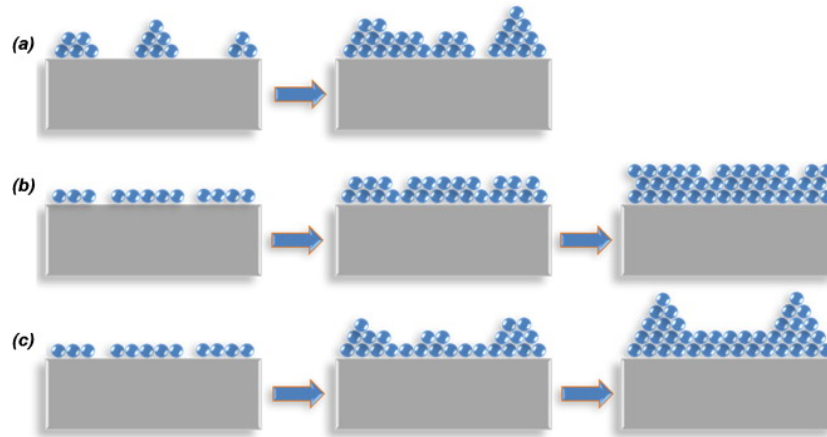


Figure 2.4: Thin films growth modes mechanisms; (a) Volmer–Weber, (b) Frank–Van der Merwe, (c) Stranski–Krastanov [2]

2.3 Film structures, microstructures and surface morphologies.

After the early stages of nucleation of the deposition process, the solid starts to grow by forming its specific structure. The structures can be either crystalline or amorphous or even nanostructured (e.g. carbon nanotubes) in various geometrical microscale morphologies such as films, nanopillars, nanotubes, nanospheres, nanodisk, etc.

Crystalline films can be categorized in two main categories; the single crystals, growing more often by epitaxial deposition and the polycrystalline films. A single crystalline film has a single lattice plane growth direction in respect with the surface plane. In contrast, a polycrystalline film is composed by randomly distributed nano and microcrystals in the film volume. Crystalline solids can be grown in more than one crystal phase depending on the deposition method and parameters.

Amorphous structures exhibit by the lack of long range periodicity, i.e. no unit cell can be defined in such a structure able to fill the crystal volume by axial transformations rendering no translational symmetry. Taking a closer view of the amorphous structures, a sort range periodicity emerges.

In nowadays, nanocomposite films are also widely under research and development due to their interesting properties which are able to make them applicable materials. A nanocomposite film can be a complex solid of an amorphous matrix with embedded crystal nanocrystals or the opposite. Also there is no restriction of the individual physical properties of the matrix and the embedded nanoparticles since the nanocomposite film often has completely different properties.

In the present thesis, crystalline Ti-based films were grown for the study of Ti-based crystal structure phases and selective crystal phases of ZrO_2 films were formed by post growth treatment. Concerning amorphous structures, single and multi element amorphous structured films were deposited. Hydrogenated and pure amorphous diamond like carbon films (DLC and DLC:H) are related with the single element structures, while Zr-based multi element metallic glassy films, deposited by co-deposition, were studied. For the nanocomposite structured films study, Ni and Ag nanoparticles embedded in amorphous DLC matrix were grown.

2.4 Plasma

Plasma is the state of matter in which can coexist ionized molecules, atoms and electron but not combined to each other because of their high kinetic energies. The particles in plasma state are not stable because of the continuous neutralization and ionization that occurs by collisions from other high kinetic particles.

Self-sustaining plasma is needed for the majority of the vapor deposition techniques of thin films. Self-sustaining plasma requires continuous electron-nucleus and nucleus-nucleus collisions. So the rate of ion creation should be equal with the rate of the creation of neutral species. This is obtained only if the mean free path (MFP) of particles is comparable or larger than the electric discharge distances.

When in a neutral gas a high voltage is applied, there is a threshold value above which ionization of the atoms starts. Then the excited electrons are accelerated by the applied electric field acquiring momentum cable enough to ionize other neutral atoms. In this way a snowball effect takes place and the finally the gas is at plasma state, figure 2.5.

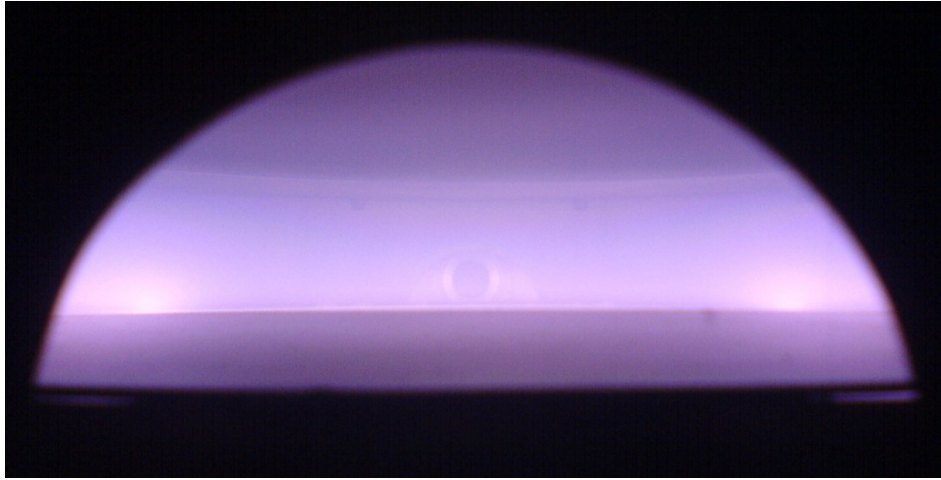


Figure 2.5: Photograph of C_2H_2/Ar plasma

The positive charged ions are accelerated towards the negative electrode-substrate. Secondary electrons emission is caused by the substrate that contributes for a self-sustained plasma. Since the substrate is negatively charged, there is intense repulsion of electrons in that area, resulting in the absence of electrons. In that area the reconnection of electrons and ions is negligible and the so called of dark space area is created. The width of the dark equals to the MFP of the secondary electrons and normally varies from 1 to 4 cm, thus depending on the working pressure.

In the specific reactor, a metallic shield with the open area above the substrate was used for the plasma intensity strengthening by collecting the secondary electrons above the substrate's area.

For the calculation of the lowest working pressure of the specific chamber we can use the equation that correlates the MFP of ions and electrons with the working pressure which is

$$MFP = \frac{5 \times 10^{-3} (mbar \times cm)}{P_w (mbar)}$$

The electrodes distance, of the specific reactor, is 10 cm. For a self-sustained plasma generation and so deposition can be achieved by the higher pressure than

$$P_w = \frac{5 \times 10^{-3} (mbar \times cm)}{10cm} = 5 \times 10^{-4} mbar$$

At lower pressures plasma cannot be created since the atoms and the molecules of the reactants are reconnecting forming a neutral gas [3].

For a-C:H thin films deposition by PECVD both DC and RF voltages were used. When a negative DC voltage is applied, the deposition rate and the film properties are not linear versus thickness due to the minimization of the applied voltage which is caused by the electrical shielding. This is because of the dielectric film that is growing intermediately at the electrodes, screening the voltage to be applied to the plasma. In contrast, use of RF voltage is mostly preferred for dielectric films growth. This is because the polarization of the substrate frequently alternates discharging and electrons and ions are incident at the substrate alternatively. A standard 13.56 MHz generator was used for the growth of a-C:H films by RF-PECVD.

2.5 Chemical vapor deposition (CVD)

Chemical vapor deposition is a widely used, industrial scale deposition technique of films growth based on chemical procedures. A typical procedure of CVD is the exposure of a substrate to chemical active precursor gasses produced by energy absorbance. The energy sources are different for each technique. The activation of the gas precursors can be achieved by thermal or plasma induced procedures, followed by the chemical reaction with the substrate and the film growth. The possible by-products of chemical reactions (e.g. H₂, CO₂, CH₄, etc.) are removed by the pumping system.

Generally, a CVD procedure can be epigrammatically summarized to the following steps

- 1) Injection and diffusion of precursor gasses
- 2) Gas reactions at gas phase
- 3) Adsorption on substrate
- 4) Surface diffusion on substrate
- 5) Surface reactions
- 6) Surface diffusion to the initial growing islands
- 7) Growth of solid state film
- 8) Removal of chemical by-products

or graphical by figure 2.6

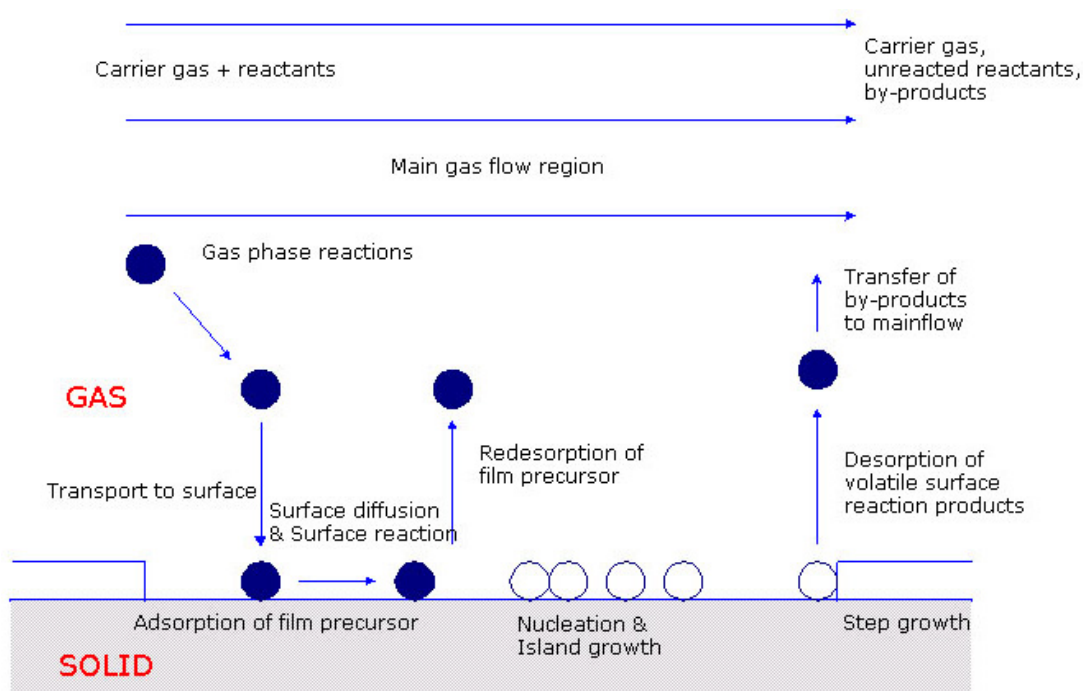


Figure 2.6: Schematically representation of CVD procedure

CVD are multidimensional research and industrial techniques since they are able for deposition of almost every metallic or not elements, carbides, nitrides, borides, oxides as well as bimetallic compounds.

The combination of the CVD advantages makes it one of the foremost industrial scale deposition techniques. By CVD is able to achieve the deposition of high purity films (99.99- 99.999%) in any substrate type in well below melting temperatures of the solid. Also, the deposited films are uniform even at the substrate's edges and it is possible even for deposition on the vertical sides (step coverage). Major advantage of CVD is the low cost of raw precursor gasses and the capability of deposition of large and different types of substrates simultaneously. Finally, CVD's large deposition rate makes it one of the preferred industrial scale thin film deposition technique, especially in microelectronic, optoelectronic and photonics industries.

There are many variations of CVD that can be used, depending on the standards of the specific application.

2.5.1 Atmospheric Pressure Chemical Vapor Deposition (APCVD)

The basic characteristic of the atmospheric pressure chemical vapor deposition (APCVD) is the atmospheric working pressure. This results in very high deposition rates, but non uniform films of low purities due to by-products and contaminant elements such as nitrogen and oxygen. In contrast it is very effective in oxide films growth and in powder production. The deposition temperatures of APCVD vary from 550 to 850 °C.

Various subcategories of APCVD have been developed. The main differentiation which exists is the reactor's wall temperature. In a cold-wall reactor the walls of the reactor are cooled enough with respect to the substrate's temperature. The main advantage of the cold-wall reactors is that the deposition takes place mainly in the substrate's area. In contrast in a hot-wall reactor the temperature of the walls and the substrate is almost the same. This fact results in deposition over the whole volume of the reactor. The substrate can be heated by high frequency RF field, by heating substrate holders or by heating plates close to the substrate. Hot-wall reactors need frequent cleaning in order to avoid the contamination which is caused by the deposition of different elements.

APCVD has been used in this thesis for the growth of CNTs.

2.5.2 Low Pressure Chemical Vapor Deposition (LPCVD)

In a low pressure chemical vapor deposition (LPCVD), the deposition takes place at lower pressures than the atmospheric one. The gas density is up to 1000 times lower. Also LACVD has lower deposition rates than the APCVD, from 10 to 50 nm/min. The main advantage of LPCVD is the homogeneity of the deposited films. In LPCVD the homogeneity and the deposition parameters of the growing films are determined by the temperature and the partial pressure of the precursor gasses. The film's homogeneity is determined by the mean free path (MFP) of molecules and atoms in the reactor. The mean free path is the average distance of an atom between collisions with other atoms or the reactor's walls or the substrate. The larger the MFP the more homogeneous films grow. By decreasing the working pressure two crucial benefits are established. The first is the increment of the MFP and the second one is the decrement of the deposition temperature. Low deposition temperatures are preferred for crystallization efficient increment and also in order to prevent the impurities diffusion.

LACVD is widely used for crystal Silicon growth. The deposition temperatures vary from 550 to 650°C.

2.5.3 Plasma Chemical Vapor Deposition (PECVD)

Plasma enhanced chemical vapor deposition (PECVD) has the most benefits of the LPCVD. The main difference is that in PECVD the precursor gasses become active by plasma generation, while in LPCVD by pyrolysis, so lower deposition temperatures are established. Plasma generation is accomplished by applying high voltages to the substrate. The applied voltage can be direct (DC) or radio frequency (RF). The physical properties of the film are mainly determined by the kinetic energies of the ionized atoms, acquired by the applied voltage. The working pressures of PECVD vary from 10^{-1} to 10^{-4} mbar resulting in high kinetic energies of the deposited atoms. High values of MFP ensure small energy losses of atoms by collisions and so metastable phases of solids can be accomplished.

Summarizing, PECVD is a deposition technique combining high kinetic energy species at low temperatures varying from 25 to 250 °C [4]. This has as a result the capability for deposition of very homogeneous films also in thermal sensitive substrates such as polymers [5].

In LPCVD and PECVD the reactants flow is crucial parameter. CVD reactors can be distinguished in two main types. The first one is the differential reactor in which small percentage of the reactants is used. The second one is the starved reactor where the most percentage of the reactants is used and so big deviations of the outgoing reactants are observed, figure 2.7.

Simplest transport analysis:

$$\frac{\text{reactant out}}{\text{reactant in}} \approx 1 \quad \text{differential reactor}$$

$$\frac{\text{reactant out}}{\text{reactant in}} \ll 1 \quad \text{starved reactor}$$

Figure 2.7: Demarcated conditions of differential and starved reactors

Differential reactors are mostly used in research because of their simplicity and low number of parameters. In contrast, in industries starved reactors are mostly spread since a starved reactor emerges for fast surface reactions. Fast surface reactions are preferred in industries for reactors in order to have a cost-cutting and high production rate.

Defining the following parameters

[pre] = gas concentration (moles/m³)

F = volume flow rate of gasses (m³/sec)

K_s = surface reaction rate constant (m/sec)

ch = concentration inside the reactor

in = concentration of gas inlet

S = surface of substrate (m²)

In figure 2.8 are illustrated the necessary parameters for the CVD type definition.

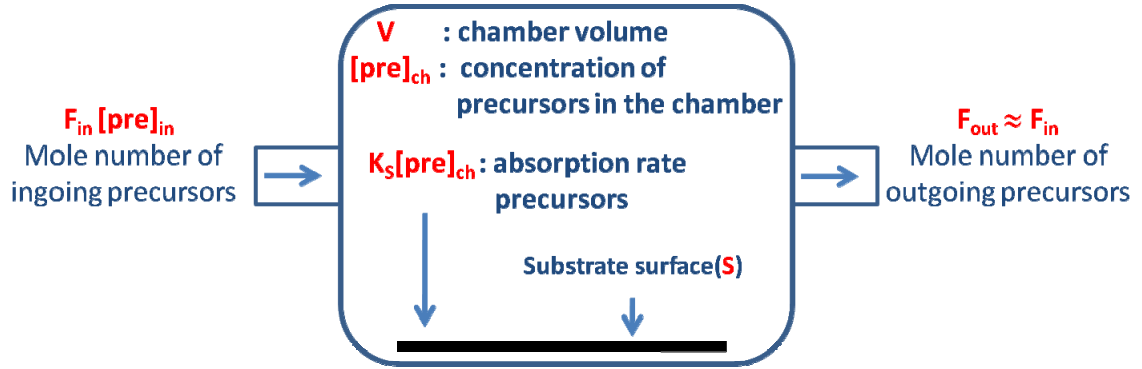


Figure 2.8: deposition details for CVD reactor type determination

Importing the utilization, X , of the reactants as

$$X = \frac{Moles_{(pre)_{in}} - Moles_{(pre)_{out}}}{Moles_{(pre)_{in}}}$$

We have

$X \rightarrow 0$: differential reactor

$X \rightarrow 1$: starved reactor

A more detailed analysis can be performed regarding the reactants concentrations.

Writing the rate of the surface reaction as

$$R = K_s S [pre]_{ch}$$

and the available reactant as

$$Q = V [pre]_{ch}$$

the time consumption needed for the reactant equals to

$$t_{con} = \frac{Q}{R} = \frac{V}{K_s S} \quad (1)$$

and the removal time of the non absorbed reactants away from the reactor is

$$t_{res} = \frac{V}{F_{in}} \quad (2)$$

The number of moles should be equal before and after the reactions, so

$$F_{in}[pre]_{in} = K_s S[pre]_{ch} + F_{in}[pre]_{ch}$$

or

$$[pre]_{ch} = \frac{F_{in}[pre]_{in}}{F_{in} + K_s S}$$

By equating (1) and (2) we have the equation

$$[pre]_{ch} = \frac{[pre]_{in}}{1 + t_{res}/t_{con}} \quad (3)$$

Equation (3) has to two boundary conditions:

$$1. \quad \frac{t_{res}}{t_{con}} \ll 1$$

Equation (3) becomes

$$[pre]_{ch} = [pre]_{in}$$

This means that the concentration of the reactants inside the reactor equals to the inlet reactants concentration when their dwell time inside the reactor is relative small

with the time that is needed for consumption. This is established with high rate of inlet gasses.

This is the case of a differential reactor with the advantage of homogeneous films growth but with low percentage of utilization, X , of the reactants. Because the time of consumption of the reactants depends mainly on the surface reaction rate, the differential conditions are more likely at low temperature reactions. This condition is referred as surface limited.

$$2. \quad \frac{t_{res}}{t_{con}} \gg 1$$

Equation (3) becomes

$$[pre]_{ch} = [pre]_{in} \frac{t_{con}}{t_{res}}$$

and applies when the reactants concentration in the reactor is much less than the inlet concentration and the time of consumption is very low. This happens for slow rate of inlet reactants or for big rates of surface reactions. In this case, starved reactor CVD takes place, and there are big deviations of the reactants concentrations with a result on the inhomogeneity of the deposited films. The reactions take place with high kinetic energies of atoms resulting in high surface reactions rates. This condition is referred as mass transport limited.

Both differential and starved PECVD reactor have been used in this thesis for the growth of DLC films.

2.5.4 Experimental setup

In the present thesis elaboration a PECVD high vacuum reactor was setup for the growth of a-C:H films. The reactor is composed by the main chamber of deposition and a load lock chamber, figure 2.9.



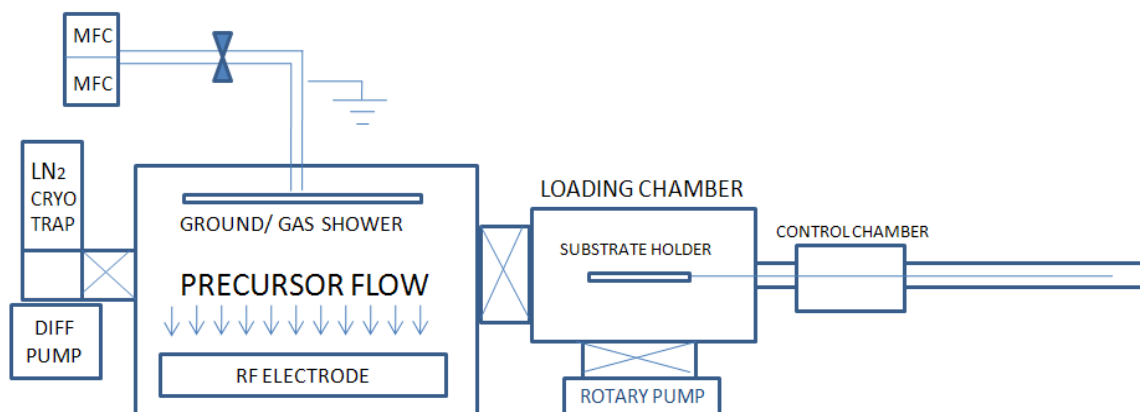


Figure 2.9: Photograph (Upper part) and schematically (lower part) representation of the PECVD reactor

The load lock chamber, of low vacuum (10^{-3} mbar), is used for keeping the main chamber under vacuum in order to prevent contamination from atmosphere molecules (N_2 , O_2 , H_2O , etc.) anytime that a new substrate was needed to be imported.

The main parts of the chamber are two parallel plates used as electrodes. Figure 2.10. High vacuum lines were used for leaking the high purity reactants to the main chamber by a feed through valve attached on the upper electrode. After the upper electrode a gas shower was used for the homogeneous diffusion of the reactants. That electrode was chosen to be grounded. The reactants flow rate was manipulated using electronic mass flow controllers (MFC) in standard cubic centimeter per minute (sccm) units. The achieved base pressure of the main chamber was at low 10^{-6} mbar, using diffusion and a rotary pump in a row.

High vacuum is necessary for the removal of impurities that contaminate the chamber when the vacuum is low. A rough estimation of impurities to the growing film can be done by

$$\#impurities = \frac{P_{basic}(mbar)}{P_w(mbar)}$$

Since the impurities might alter the physical properties of the deposited solid it is desirable the lowest ratio of impurities to the deposition atoms. In our case that ratio was better than 1/10000.

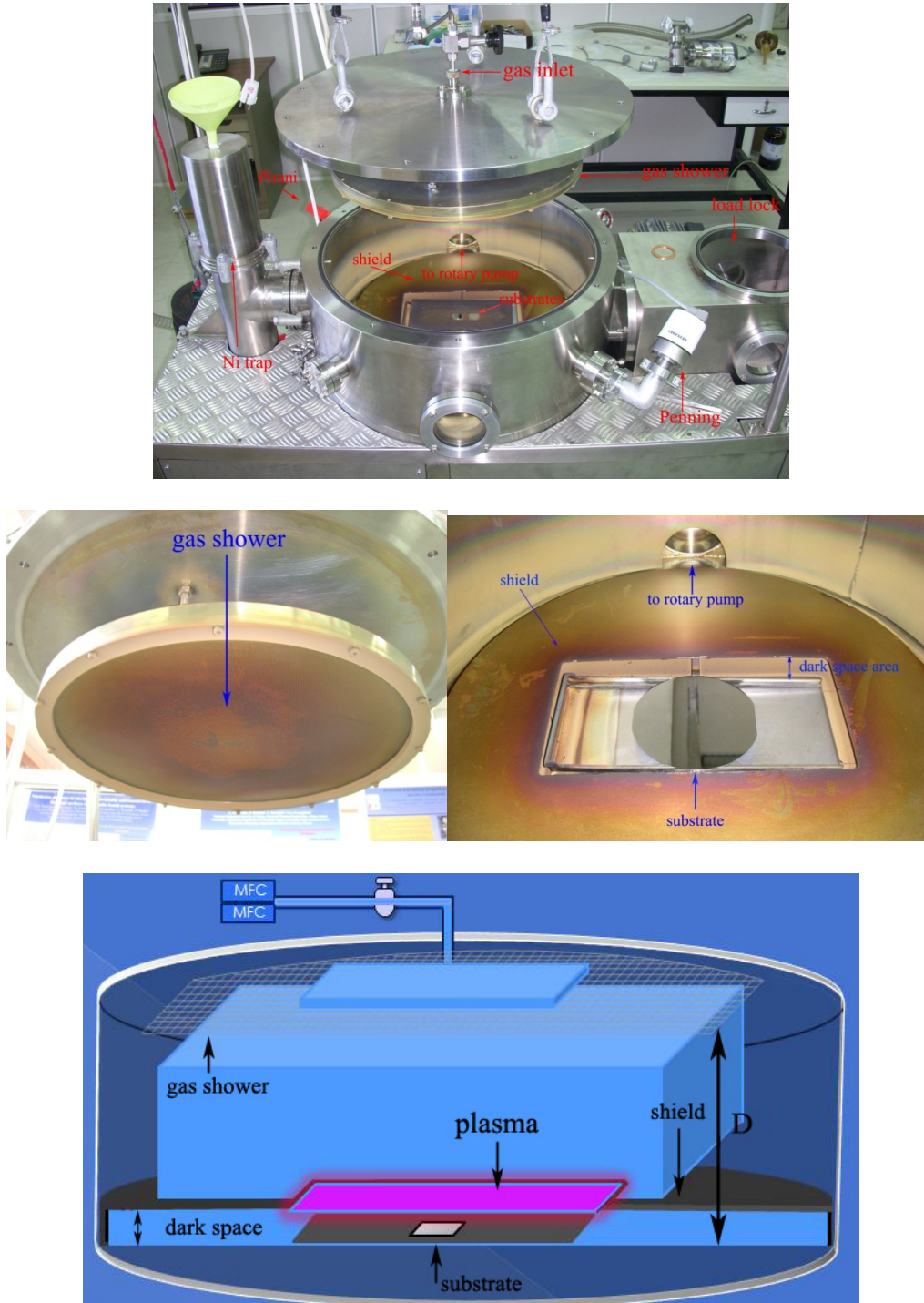


Figure 2.10: Basic parts of the PECVD deposition reactor

The lower plate was a cooling 12'' electrode in which DC or RF voltage was applied. The substrate, which was placed on the lower electrode, could have up to 4'' diameter.

Any moving part of the reactor, such as transfer arms, valves of isolation of the main and load lock chambers and diffusion pumps isolation valves, a complex of electropneumatic valves were used.

The electrodes distance and so the distance of the ionized atoms that travels under acceleration by the applied voltage was 10cm. For maximizing the plasma density on the substrate, the area around the substrate was surrounded by a metal shield letting uncovered the top of the substrate surface.

2.6 Magnetron sputtering

One of the most industrially and research thin films physical vapor deposition techniques is the magnetron sputtering, which is based on a momentum transfer process. The source or target material, is a high purity solid powered by a negative voltage. An inert gas with large atomic number, usually Ar, Kr or Xe, is leaked to the deposition chamber. The gas under the voltage is transformed to plasma and the negative electrode-target is bombarded by the accelerated ions of the sputtering inert ions. For amplifying the plasma dense bellow the target a complex of magnets are placed creating an electron magnetic trap, known as sputtering ring. Enhanced plasma is generated by the trapped electrons above the target's surface making the sputtering process more efficient.

By collisions the ions' momentum is transferred to the target breaking its bonds and thus ionized and neutral atoms or even clusters are knocked out of the target. The ejected matter is directed to the substrate growing the film, figure 2.11.

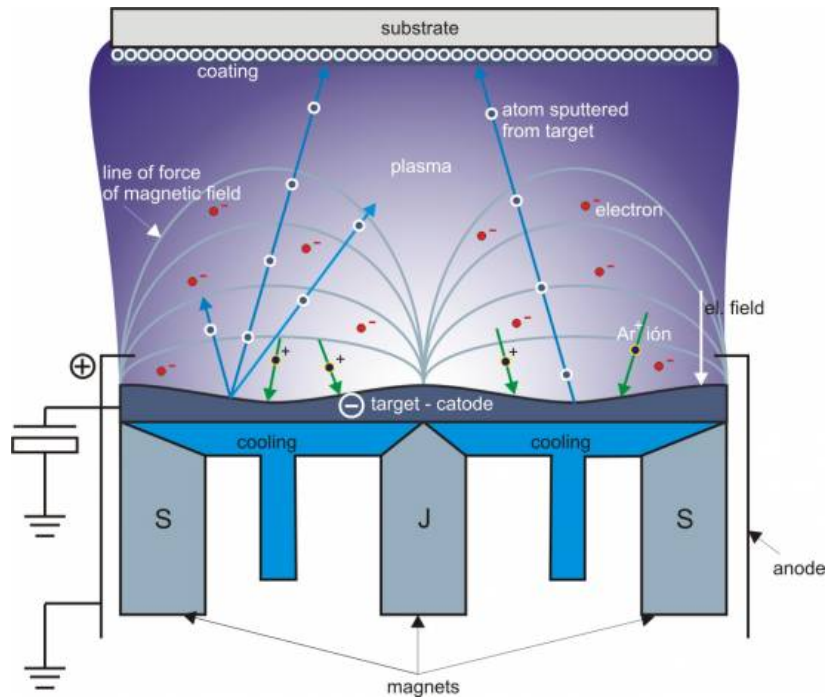


Figure 2.11: Cross section of a magnetron sputtering system.

Other phenomena that take place during bombardment (ion-matter interaction) like secondary electrons emission, creation of vacancies and defects in the target structure, formation of compounds on the target, implantation of the incoming particles and the backscattering by inelastic collisions of some of them are illustrated to figure 2.12. The depth that the above phenomena take place depends mainly on the kinetic energy of the ions and varies from 1 to 2 nm.

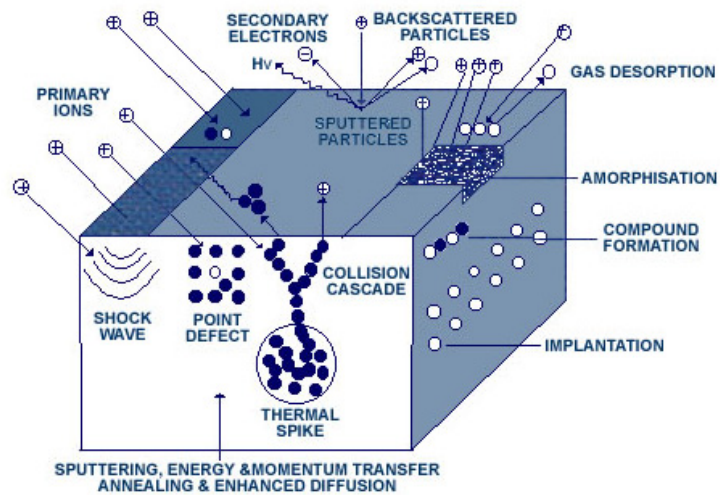


Figure 2.12: Physical phenomena that take place by ion-matter interaction

A characteristic quantity of the sputtering process is the sputtering yield, S , that is defined as the ratio of the ejected atoms or molecules per incident ion

$$S = \frac{\#ejected\ atoms\ or\ molecules}{\#incident\ ion}$$

that depends on the kinetic energy and the angle of incidence of the bombarding ions. Characteristic databases of curves of sputtering yield versus energy and angle of incidence are available online or can be simulated by programs (TRIM), figure 2.13.

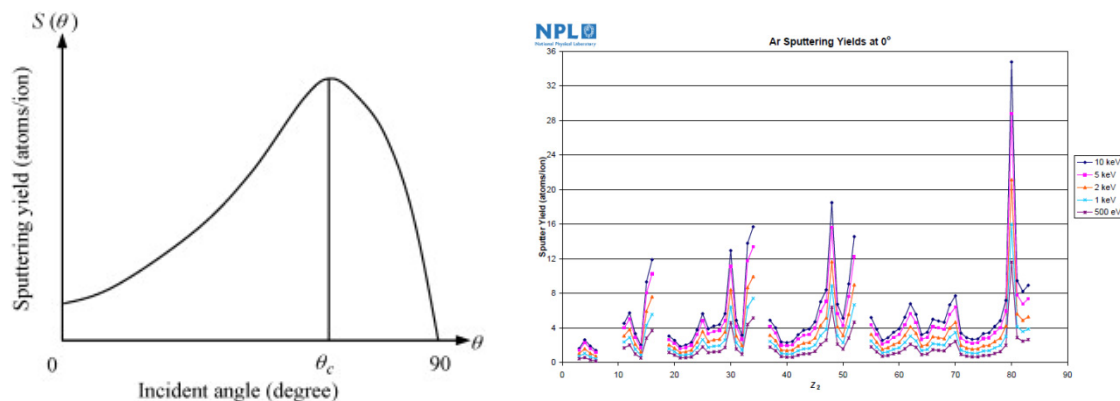


Figure 2.13: Dependence of the sputtering yield of a solid by the angle of ion incidence (left) and by the atomic number of the sputtered element (right) [6]

Except of using inert gas as sputtering gas or ion source, reactive gasses such us nitrogen, oxygen, etc can also be leaked during deposition, thus enabling gas phase reactions of the sputtering element with the reactive gasses in the plasma. This is called reactive magnetron sputtering technique, but it is away from the present thesis topic.

2.6.1 Experimental setup

For the needs of topic of this thesis, a custom made magnetron sputtering deposition chamber was used. The sputtering guns were at 90° each other and the rotated substrate holder was at 45° for both guns, figure 2.14. For the deposition it was applied either DC voltage shared to both guns either RF and DC applied to each gun separately. The base pressure of low 10^{-6} mbar was achieved by a turbo and a rotary in row pump, while the working pressure was at low 10^{-2} mbar. As sputtering gas was used Ar and a presputtering process, with closed the gun shutters, was performed for cleaning the targets surfaces. For ternary films growth, a high purity foil was attached around the sputtering ring of the horizontal sputtering gun.

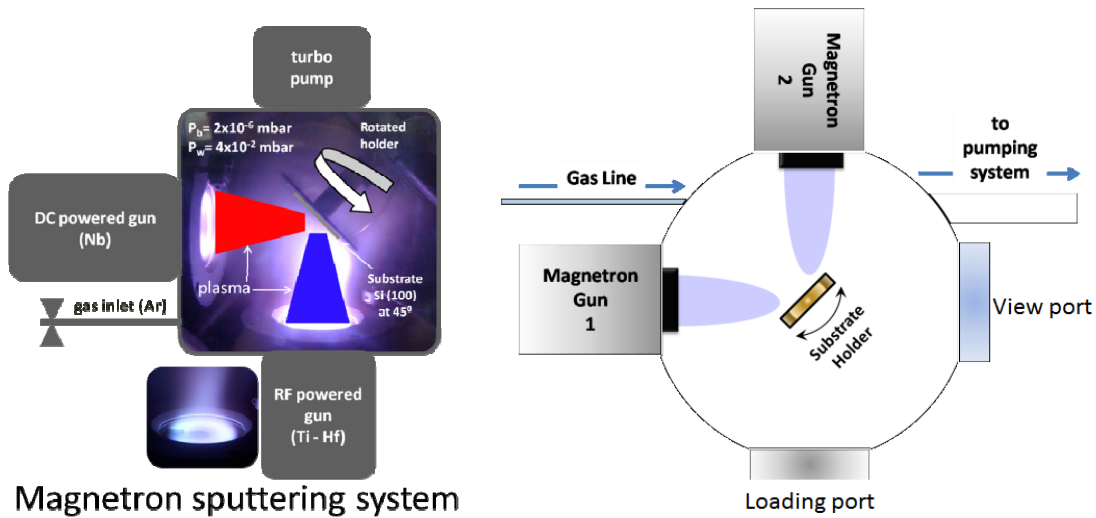


Figure 2.14: Vertical cross section image (left) and top view (right) of the magnetron sputtering deposition chamber

Also optical emission spectroscopy was used of the detection of oxygen impurities control, especially for the Ti-based films growth since Ti is a well oxygen getter, figure 2.15.

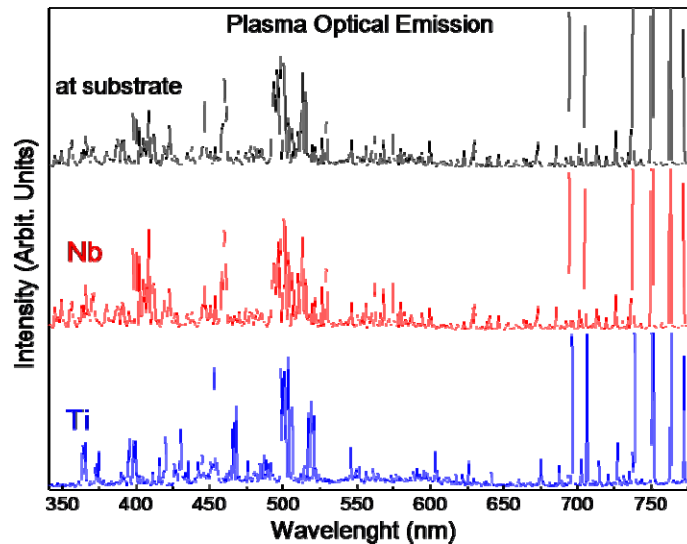


Figure 2.15: Optical emission spectroscopy of the deposition plasma

2.7 Pulsed laser deposition (PLD)

Pulsed laser deposition (PLD) is a very versatile, laboratory-scale PVD technique. It is mainly used as research deposition method because by its capability of metastable state of single elements (DLC), nanocomposited films (DLC:Ni, DLC:Ag), metallic glasses (MG), etc growth. The main disadvantage of the PLD is the non uniformity of the films and the small surface coverage because of the small plume dimensions that prohibits the efficient use of PLD in industrial scale.

The experimental setup of a PLD is simple. The target and the substrate are oppositely housed in a high or ultra high vacuum chamber. A laser beam is guided by a complex of mirrors and a focusing lens on a solid target surface, figure 2.16.

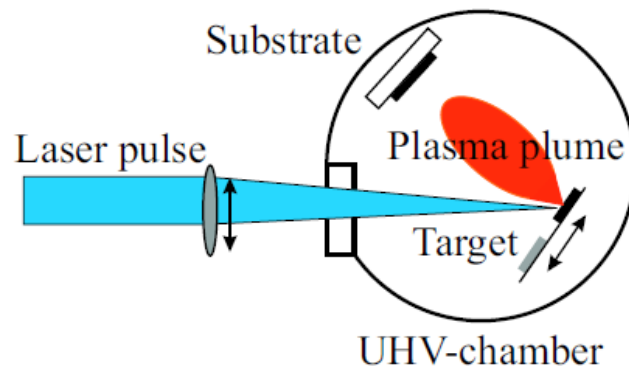


Figure 2.16: Experimental setup of PLD

Generally the pulsed laser systems have a repetition rate of a few Hz and the pulse duration is in the range of nanoseconds. The laser beam wavelength (nm) and fluence (photons energy per unit area per pulse) can be varied depending on the laser source and the preferred PLD experiment process.

High energy photons and high fluence beams penetrate to the target, at depth of around 10nm, depending on the target's electron density and the laser beam wavelength. The target's atoms are ionized, by single or multi process photon absorption. By Coulomb explosion, relaxation of the matter is achieved followed by matter evaporation. The evaporated matter is in plasma state and it is consisted by ionized atoms, molecules, clusters and macroscopic globules of molten material up to $\sim 10\mu\text{m}$ diameter (droplets). The so-called plume has a distribution which can be described by law of $\cos^n(\theta)$, with n to vary from 4 to 30, and a Gaussian shape. In figure 2.17 shows graphically, in process steps, a single pulse deposition.

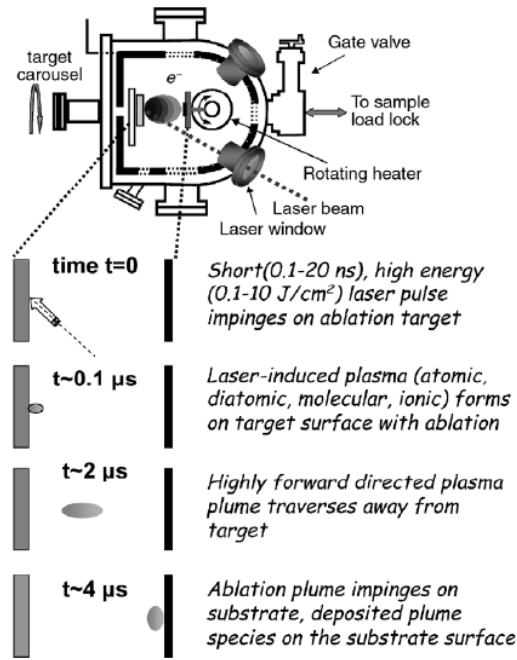


Figure 2.17: Schematically representation of the deposition process by PLD

The plume characteristics can differ by changing mainly three parameters. High pressures and applied voltage, between substrate and target, form a narrower plume, respectively. The third parameter influences more the chemical composition of the plume and refers to the used wavelength and fluence. Using different wavelengths and fluencies of laser beam the ablation process changes followed by different particles evaporation.

One of the basic characteristic of PLD is the stoichiometry transfer from the target to the deposited film. This is because in PLD all the elements composing the target under the intense beam reaches a rate of 10^{12} K/sec up to 5000 K within some nanoseconds [7]. This has as a result as the topological and instant evaporation of the target's elements that are going to be deposited to the substrate.

In table 2.1 are listed the wavelengths and the photon energies of Nd-YAG and Excimer laser sources as well as the strengths and the binding energies of the atomic bonding types of solids.

Table 2.1: General deposition parameters for a PLD deposition

Laser	λ	E_{hv} (eV)
CO ₂	10.6 μ m	0.1
Nd-YAG	1.06 μ m	1.17
2 nd harmonic	532 nm	2.33
3 rd harmonic	355 nm	3.5
4 th harmonic	266 nm	4.66
Excimer		
XeCl	308 nm	4.0
KrF	248 nm	5.0
ArF	193 nm	6.4
F ₂	157 nm	7.9
Bond	Strength (kCal/mol)	E_b (eV)
Ionic	140 - 250	6 - 11
Covalent	30 - 200	1.3 - 9
Metallic	15 - 200	0.65 - 9
Van der Waals	1 - 10	0.043 - 0.43
Hydrogen bond	5 - 12	0.2 - 0.52
C-C	83	3.6
C=C	146	6.34
C \equiv C	200	8.7

2.7.1 PLD Experimental setup

For the scope of this thesis, Ni and Ag nanocomposite amorphous carbon thin films (a-C:Me, Me=Ni, Ag) were grown by PLD. As laser source were used the 2nd and the 3rd harmonics of a Nd-YAG laser. The deposition took place in a high vacuum chamber pumped by a turbo in row with a rotary pump, figure 2.18.

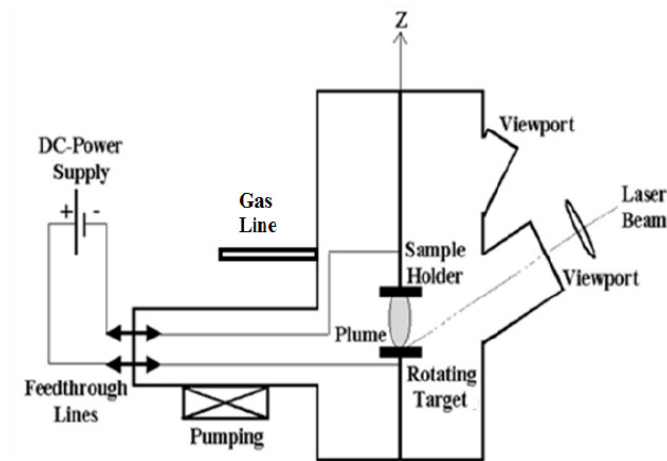


Figure 2.18: schematically presentation of PLD chamber

The base pressure was of the order of low 10^{-7} mbar. As carbon target was used highly ordered pyrolytic graphite (HOPG) on which there was attached high purity Ni or Ag foils in sections. The complex target was rotated and so the laser beam was incident alternatively on graphite and on the metallic sections. Because of the immiscibility of Nickel and Silver with the Carbon, metal nanocomposite in DLC matrix films were grown.

Chemical characterization of the films was performed by in situ transfer to the AES-EELS and to the XPS chamber. In figure 2.13 are shown the load lock and characterization chambers cluster.

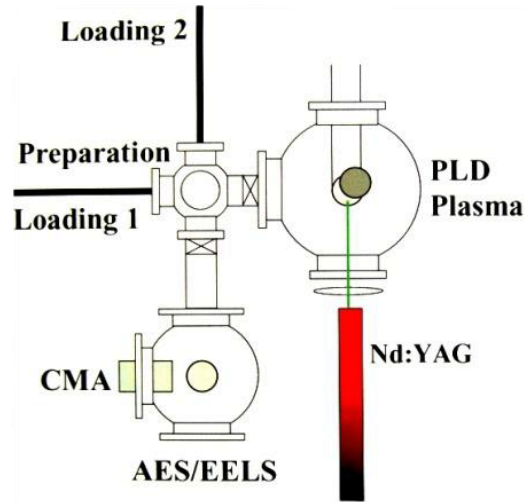


Figure 2.19: Deposition and characterization chambers cluster

2.8 Post growth plasma treatment

Plasma created by electrodeless discharge often exists in two modes known as E and H modes. The differences, as far as the plasma generations are concerned between E and H modes, are the radicals and the intensity of them that are created by plasma generation. The modes, E and H, are created by the different magnetic lines directions inside the coil area. The magnetic lines creating plasma at E mode, are directing from the coil's area towards the edges of the tube which are grounded. In contrast, the magnetic lines creating plasma at H mode are well localized in the coil's area, figure 2.20.

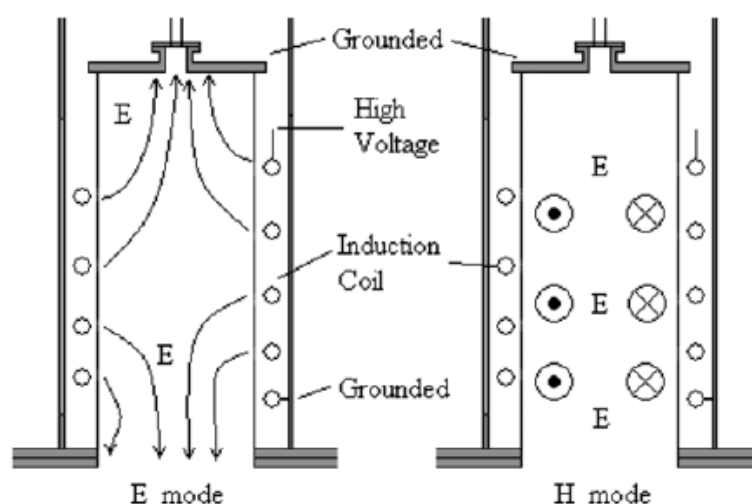


Figure 2.20: The dominating component of the electric field in the discharge region in the E mode and the H mode, respectively[8]

Electrodeless discharge and plasma generation can be achieved using RF power induction. As chamber, a quartz or a borosilicate tube is used with a coil to be adjusted around it. By applying RF power a strong magnetic field is created ionizing and plasma generating of the leaked gas.

For a specific chamber volume, the E-H mode transitions alter depending on the working pressure, the applied power for plasma generation and the gas type. Plasma's radicals are interacting with the sample that can be organic or metallic. In the case of metallic sample heating up to 600 °C occurs by induction.

In figure 2.21 is shown the E and H modes of electrodeless oxygen plasma. In figure 2.21a soft E mode plasma with lots of molecular oxygen radicals as detected by optical emission spectroscopy, figure 2.21b. In figure 2.21c the oxygen plasma in E to H mode transition is shown with clear atomic oxygen radical as detected by optical emission spectroscopy. In figure 2.21e a well formed H mode plasma, limited within the coil, is shown with more atomic oxygen radicals detected, figure 2.21f.

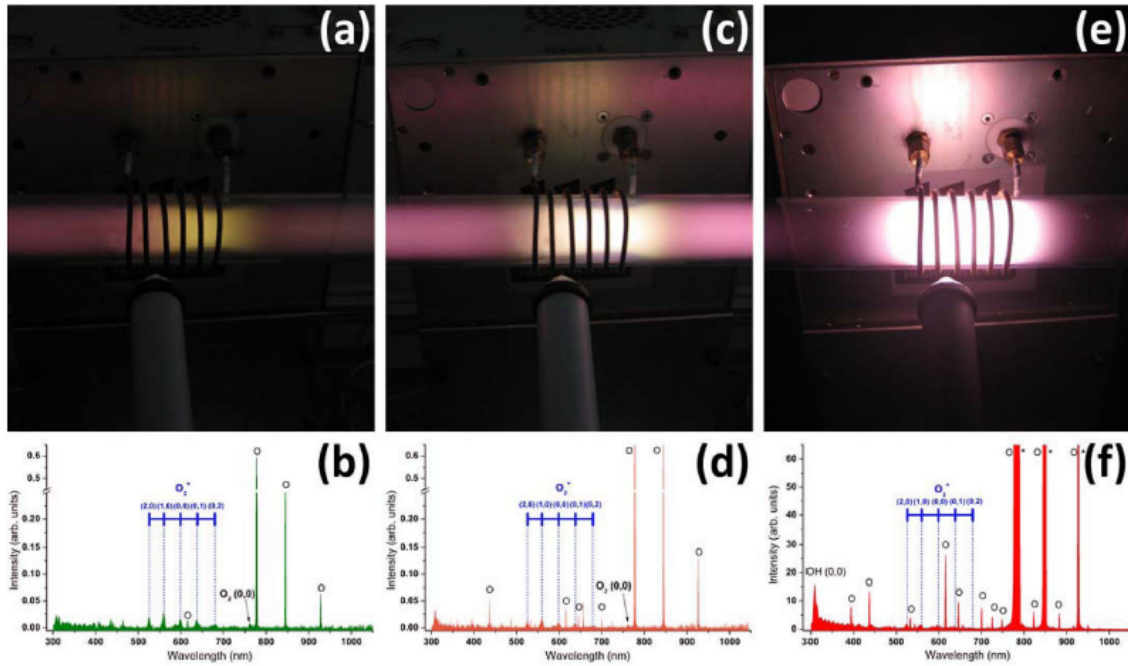


Figure 2.21: Optical emission spectroscopy of the oxygen plasma modes

2.8.1 Plasma treatment experimental setup

For the present thesis, oxygen electrodeless plasma was used in H mode for oxidation of metallic glassy films. The films were inserted in the treatment tube of base pressure of 10^{-3} mbar, achieved by a rotary pump, figure 2.22. Oxygen was leaked to the tube and by applying 500 Watt at working pressure of 5×10^{-1} mbar the plasma generated to H mode. The metallic glassy films were oxidized under oxygen radical and thermal induction, forming oxides of selective structures.

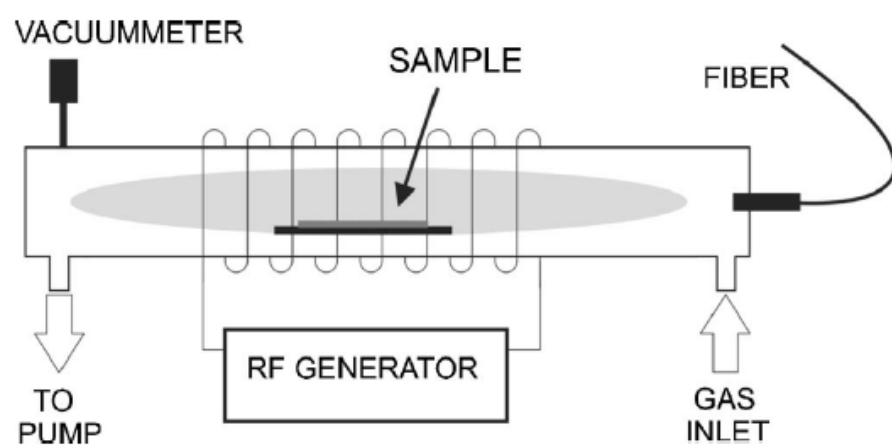


Figure 2.22: Experimental setup of oxygen plasma treatment reactor

2.9 References

- [1] M. Ohring, Materials science of thin films; deposition and structure, (Academic press, San Diego- San Francisco- New York- Boston- Sydney- Tokyo, 2002)
- [2] L.W. Martin, Y.-H. Chu, R. Ramesh, Mater. Sci.. Eng. R **68**, 89 (2010)
- [3] P. Patsalas, Lecture notes, University of Ioannina, (2008)
- [4] H.O. Pierson, handbook of chemicalvapor deposition (CVD), Principles, Technology, and Applications, (Noyes publications, New Jersey, 1999)
- [5] M. J. Davis, M. Tsanos, J. Lewis, D.W. Sheel and M.E. Pemble, Atmospheric-pressure plasma-enhanced chemical vapour
- [6] <http://www.npl.co.uk>
- [7] S. Fahler and H. U. Krebs, Appl. Surf. Sci. **61**, 96 (1996)
- [8] Y. Chen, Z.-G. Guo, X.-M. Zhu, Z.-G. Mao, Y.K. Pu, J. Phys. D **40**, 5112 (2007)

3 CHARACTERIZATION TECHNIQUES

3.1 Introduction

For the needs of this thesis various characterization techniques were used. The basic operation principles of most of the characterization techniques used are categorized according to their measuring physical properties and are analyzed in the following chapter. In the first part the characterization techniques refer to the electronic study of the solids as deduced by electron and X-ray excited Auger electron spectroscopy (AES-XAES), X-ray photoelectron spectroscopy (XPS) and energy dispersive X-rays spectroscopy (EDX). The second part is dedicated to the most commonly used characterization technique, used for the structural characterization of the solids, the X-ray diffraction (XRD). Besides the structural information, macroscopic information, such as the grain sizes and stresses of the films can be extracted also and the analysis procedure is briefly reported. The third part refers to the surface and volume morphological characterization techniques. The study of surface morphologies were performed by scanning electron microscopy (SEM) and atomic force microscopy (AFM), while specular and non specular X-ray reflectivity technique (XRR) was used to deduce properties such as thicknesses, densities and roughness of the films. Last but not least, an interesting part is dedicated to the optical properties and the electronic structure characterization techniques, using normal and variable angle specular and nonspecular optical reflectivity (ORS). The electronic structures of specific samples were deduced by electron energy loss spectroscopy (EELS).

3.2 Electronic characterization techniques

3.2.1 Auger electron spectroscopy (AES)

Auger electron spectroscopy (AES) is a surface sensitive characterization technique that is based on the Auger electrons emission of elements. When a core electron of an atom is ejected it returns to the initial state by filling the electron hole with electrons of higher energies. During relaxation time the extra energy of the electron is emitted as X-ray photons. There is a possibility that the X-ray photon will not be preferably escaped from the atom but to interact with another electron of the same atom and that specific

electron to be ejected. That electron is called Auger electron and its kinetic energy is characteristic for each element. The possibility of relaxation via Auger electron emission is higher for elements of low atomic number Z , while in contrast more possible is the relaxation by X-Ray photons emission, figure 3.1.

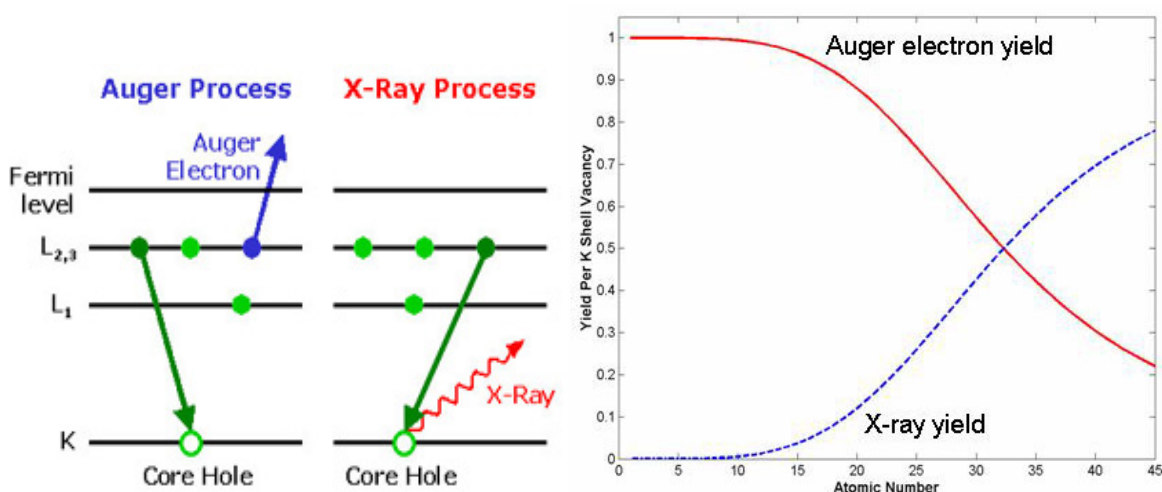


Figure 3.1: Auger and X-ray processes (left) and fluorescence and Auger electron yields as a function of atomic number for K shell (right).

Even if the excitation is performed by X-rays the characterization depth of the sample is up to 2nm because Auger electrons coming from more deep atoms are absorbed by the solid itself. Fluorescence and Auger electron yields as a function of atomic number for K shell vacancies.

By AES the surface stoichiometry of the solid can be determined, taking in account the sensitivity factor of each element, of the relative peak intensities. Also hybridization of bonds can be examined by the AES peak profiles and charge transfer caused by bonding of different elements. The high and surface elemental detection sensitivity, especially for low atomic number elements, makes AES a reliable characterization technique for dopant detection in electronic, pharmacy, etc, industries [M15].

A filament is used for the generation thermal electrons that are accelerated by high voltage field of 100 to 5000V. The penetration depth of the high kinetic energy electrons is illustrated at figure 3.2.

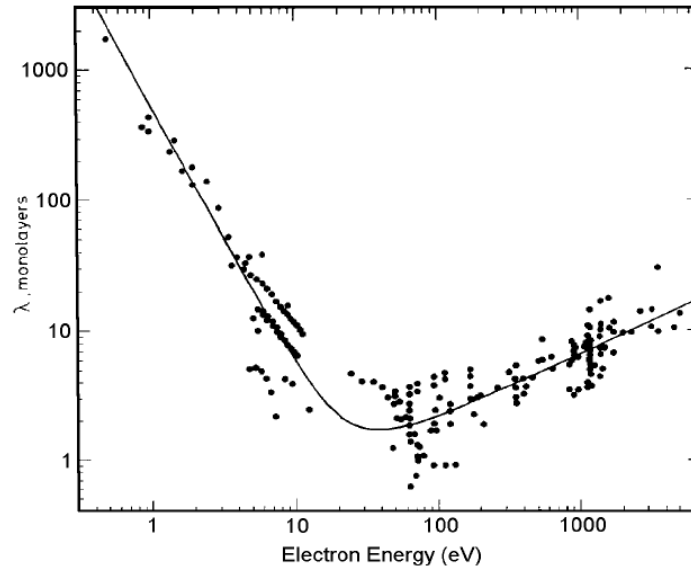


Figure 3.2: Escape depth of electrons versus the kinetic energy of the irradiation electron beam [1]

The emitted Auger and elastic scattered electrons are collected by a kinetic energy electron analyzer and a differential spectrum of counts per electron kinetic energy is formed, figure 3.3. AES measurements are fulfilled under ultra high vacuum (UHV) conditions, at 10^{-10} mbar, so the kinetic energies of the emitted Auger electrons to be unaffected from energy losses by collisions.

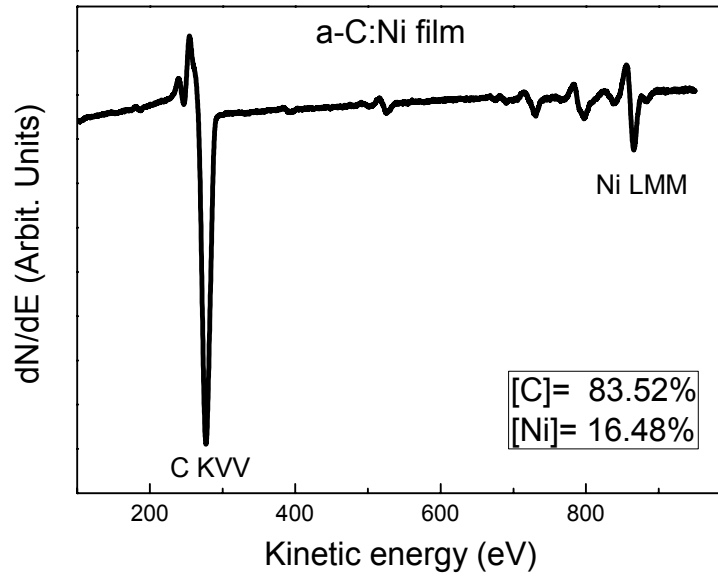


Figure 3.3: Differential AES spectrum of a-C:Ni film

Especially for the element of carbon, which is studied extensively in this thesis, the outer atomic electron states (L1 and L2) create energy bands as the solid is formed.

These energy bands are the valence bands of the solid carbon. The emission path of the characteristic Auger electron of carbon is illustrated in figure 3.4.

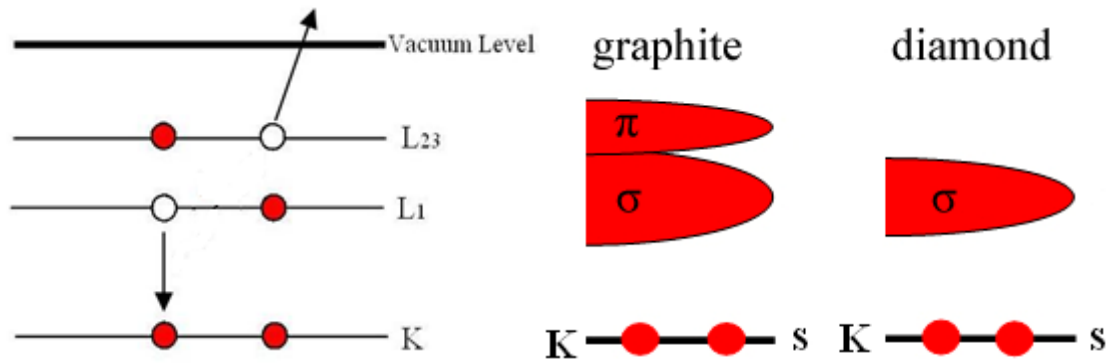


Figure 3.4: Energy states of the atom (left) and the solid Carbon (right)

The kinetic energy of the Auger electron of carbon depends by the two valance bands (K Valence Valence – KVV transition) and equals to

$$KE = (E_K - E_{L1}) - E_{L23} = E_K - (E_{L1} + E_{L23})$$

A typical AES spectrum of carbon can be divided in two regions, A and B, figure 3.5. As electrons are excited from the bonding states π or σ to the antibonding states π^* and σ^* , the majority of them are going to oscillate by the frequency of the external electric field, which is the probe electron beam in our case, creating a plasmon. The region A is formed by Auger electrons with less kinetic energy with the loss energy to be given for the creation of plasmon and to the interactions with the π^* and σ^* energy states. The main peak, region B, is formed by the Auger electrons with the width to be dependent by the percentage of the π and σ states of the solid carbon.

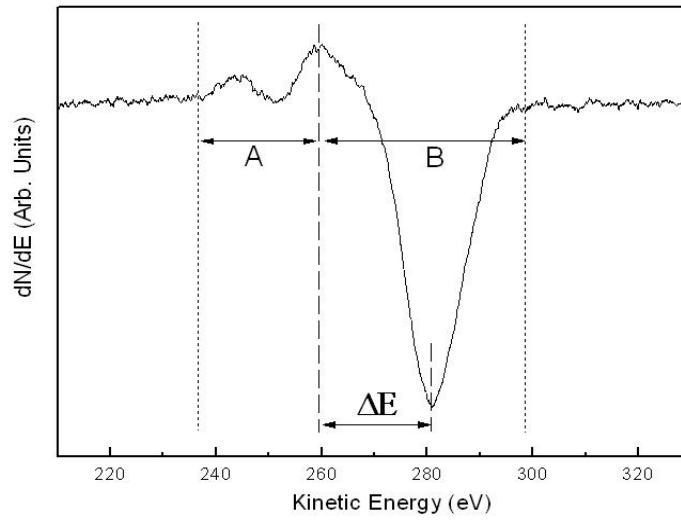


Figure 3.5: Regions of differential AES spectrum of Carbon element

The energy width ΔE of the Auger KVV transitions is proportional with the sp^3/sp^2 ratio of the DLC film. Knowing the ΔE of graphite and diamond the sp^3/sp^2 ratio can be calculated by [2]

$$sp^2 (\%at.) = \frac{\Delta E - \Delta E_{sp^2}}{\Delta E_{sp^3} - \Delta E_{sp^2}}$$

Excitation of Auger electrons can be performed using X-Ray irradiation (XAES). In figure 3.6 is shown a characteristic differential C_{KVV} Auger peak of carbon. The main advantage of XAES is that the sample is not irradiated by electrons damaging the surface and the charging effect is much less intense when dielectric surfaces are measured.

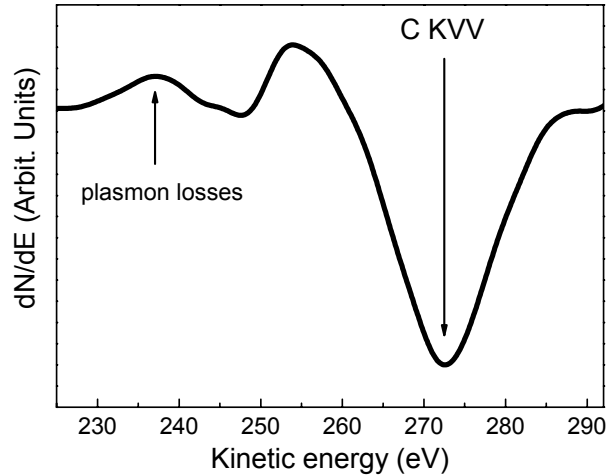


Figure 3.6: Differential XAES measurement of C_{KVV}

The previously elaborated analysis concerning the determination sp^3/sp^2 content of DLC films remains the same.

3.2.2 X-Ray photoelectron spectroscopy (XPS)

X-Ray photoelectron spectroscopy is a high resolution quantitative surface characterization technique of up to 2 nm penetration depth. Except elemental composition, properties such as chemical and electronic states, charge transfers, work function, Auger electrons, relaxation times and valence band structure by direct measurements can be studied. The principal of XPS measurements is based on the photoelectric effect. X-rays, mainly by Mg and Ag sources, are used for the sample's irradiation.

The kinetic energy of the photoelectrons equals to

$$KE = h\nu - (E_B + \varphi)$$

where KE is the kinetic energy of photoelectrons, $h\nu$ is the X-rays photon energy, E_B the binding energy of the electron and φ is the spectrometer work function, figure 3.7.

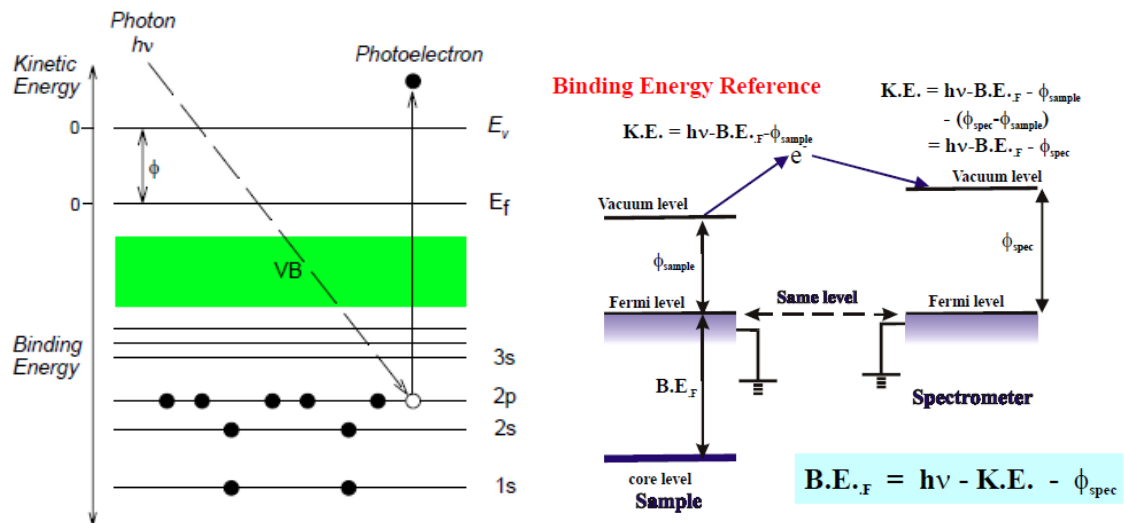


Figure 3.7: Photoelectron emission mechanism on the solid (left) and the total process of the XPS measurement (right)

In XPS measurements the high resolution of the photoelectrons kinetic energies of less than 1eV is achieved by a hemispherical energy analyzer, figure 3.8.

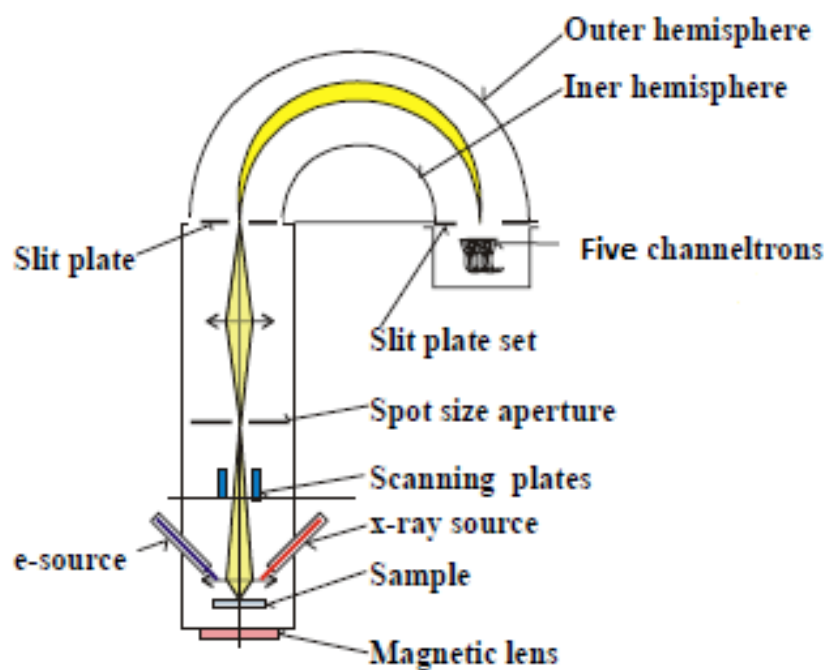


Figure 3.8: X-ray sources and basic part of a hemispherical analyzer used in XPS

The X-ray photon energy is sufficient enough to produce photoelectrons from all the core level of the material. Performing a wide scan (survey scan) all the photoelectrons, from core up to the valence level, are detected. In figure 3.9 it is shown a survey spectrum of a post growth oxidized Zr-Cu-Ti-Si film with all the binding energies positions noted.

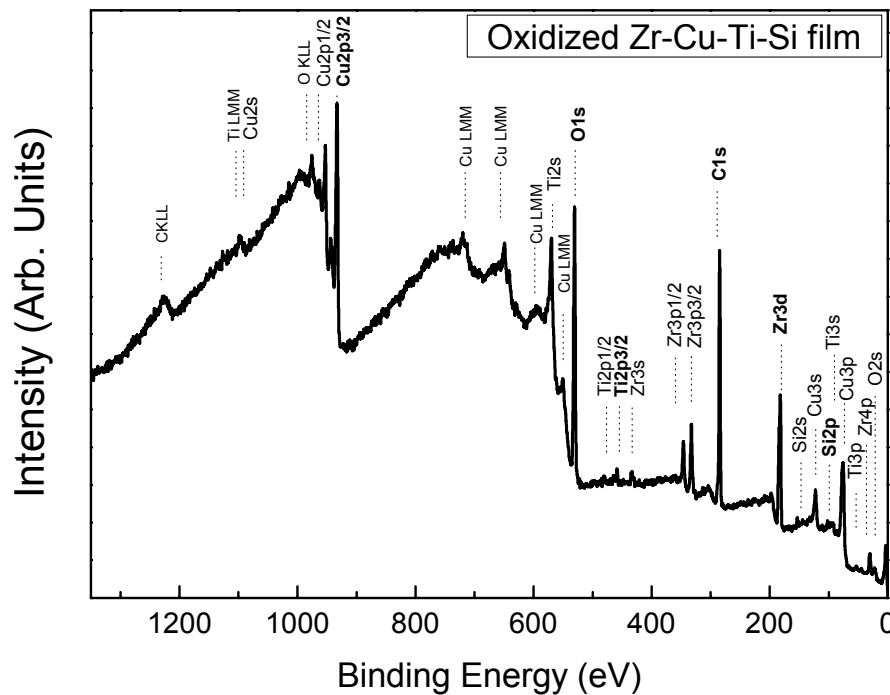


Figure 3.9: XPS survey spectrum of an oxidized Zr-Cu-Ti-Si film

By a XPS survey spectrum the chemical composition of the material can be deduced by numerical integration of the area of the characteristic peak of each element. Further analysis can be executed by high resolution XPS measurements (HRXPS). The peak of interest is selected and a high resolution scan is performed. By HRXPS the exact peak positions can be identified revealing the chemical state of the compounds. For example, in figure 3.10 it is shown XPS measurements of Zr-Cu film before and after cleaning the surface with Ar^+ sputtering. XPS peak shifts reveal the contamination of the metallic Zr and Cu by a surface thin layer of ZrO_2 and CuO , respectively.

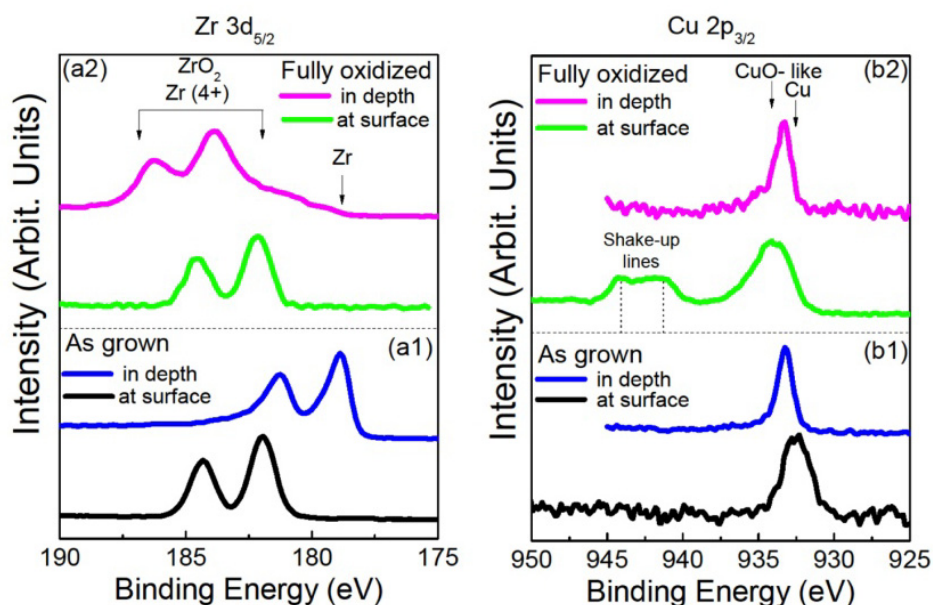


Figure 3.10: High resolution XPS measurements showing different the chemical states of Zr and Cu elements

It is common, even with HRXPS measurements, peaks not be distinguished. In such cases the XPS peaks are fitted by selected peak types (Gaussian, Gaussian-Lorentz, Doniach-Sunjic, etc.) that physically describe the under measurement solid and proper background removal. In figure 3.11 it is shown a fit of the C1s photoelectron peak by three Gauss-Lorentz peaks corresponding to the photoelectrons of the sp^3 and sp^2 hybridization of a DLC film and to the surface contamination of the sample, respectively.

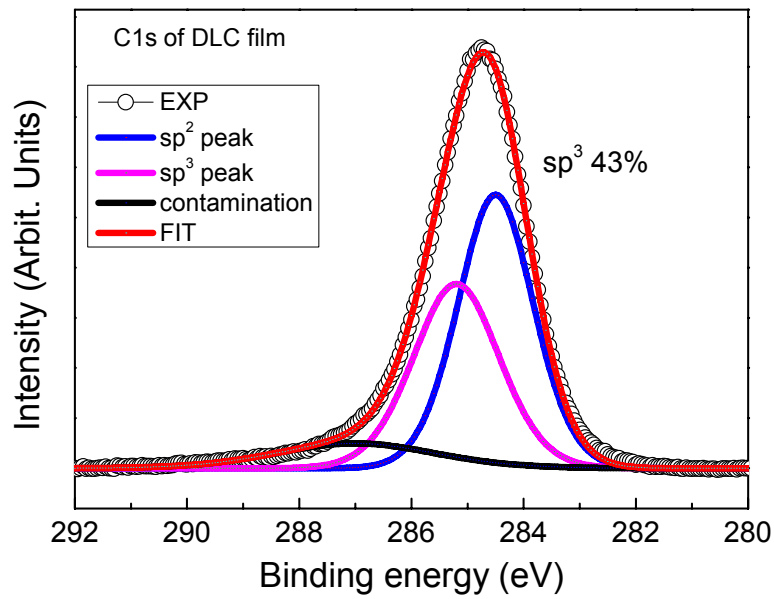


Figure 3.11: Peak fitting of C1s high resolution XPS measurement

3.2.3 Energy dispersive X-rays spectroscopy (EDX)

The Energy dispersive X-rays spectroscopy (EDX), is almost always supplementary technique with the SEM, that is going to be analyzed later. This is because as the high energy electron beam incident to the solid, core electron ionization of the atoms occurs followed by characteristic Auger electrons and X-rays emissions. An energy dispersive X-ray analyzed attached to the SEM chamber can analyze the emitted X-ray photons. Analyzing an EDX spectrum the elemental composition is determined and since the electron beam is well focused to the surface, topological stoichiometry of the sample can be achieved with latter step resolution of almost $1\mu\text{m}$, figure 3.12.

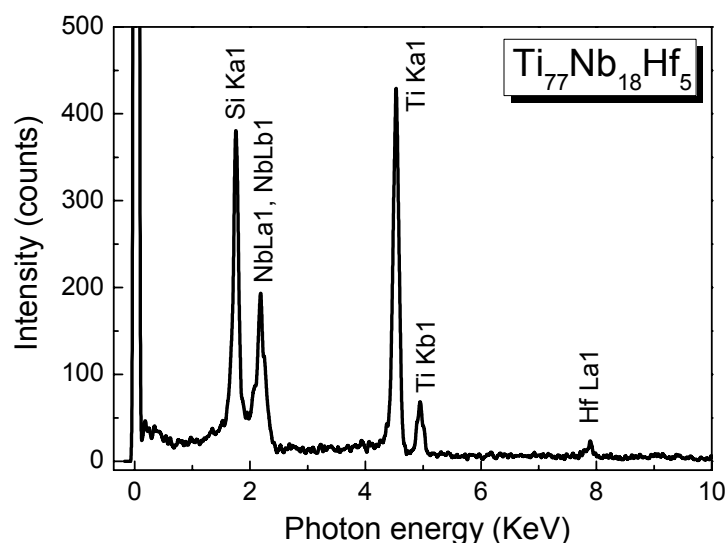


Figure 3.12: EDX spectrum of $Ti_{77}Nb_{18}Hf_5$ film

The penetration depth of the electron beam in the solid's volume mainly depends on the acceleration voltage. At high voltages the penetration length is some μm .

3.3 Structural characterization techniques

3.3.1 X-ray diffraction (XRD)

X-ray Diffraction (XRD) is one of the most basic and important non-destructive characterization methods in solid state physics since the majority of the structural properties of the studied solid can be defined. The most common information that can be provided by a XRD pattern is the crystalline structure, the crystal phases, the lattice constants and the average grain sizes of the solid. XRD measurements can be applied in powder, bulk and in film form of solids. Especially in film solids the existence of preferred crystal orientations (texture) growth can also be detected.

XRD measurements can be performed if a crystal solid is irradiated by a monochromatic beam of wavelength of the same order of magnitude with the interatomic distances (Angstrom 10^{-10} m). If this condition applied then the incident X-rays are interfere by the crystal planes of the solid.

For analysis the Bragg's law can be applied by setting the refractive index equal to unity. That it is because as the wavelength of the irradiation beam tends to Angstrom

order of magnitude the refractive index tends the unit. The principles for constructive interference are illustrated in figure 3.13.

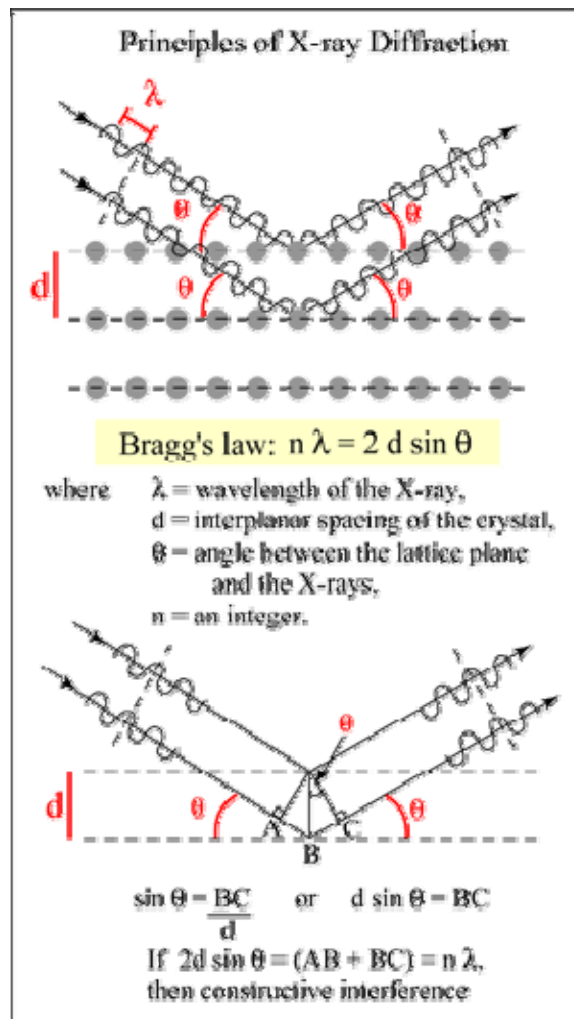


Figure 3.13: Principles of XRD diffraction

At the Bragg angle θ , the reflected rays are in phase and reinforce one another, resulting in constructive interference, while for arbitrary angle of incidence destructive interference occurs.

Since the crystallinity is the basic assumption for X-ray diffraction, amorphous structured solids do not satisfy the Bragg's law and hence no discrete diffraction peaks can be formed. Figure 3.14a shows a typical XRD pattern of an amorphous film. One broad diffraction peak it is formed by the average distances of the film's atoms. In contrast, in figure 3.14b a XRD pattern of a single phase crystal structure is shown with

discrete diffraction peaks in different angles of measurement. In the same solid more than one phases of the solid can coexist that are going to satisfy the Bragg's law. Different crystal structures even of the same solid have different lattice planes distances resulting in the satisfaction of the Bragg's law at different angles of the incidence beam. An XRD pattern of the coexistence of two different crystal structures is shown in figure 3.14.

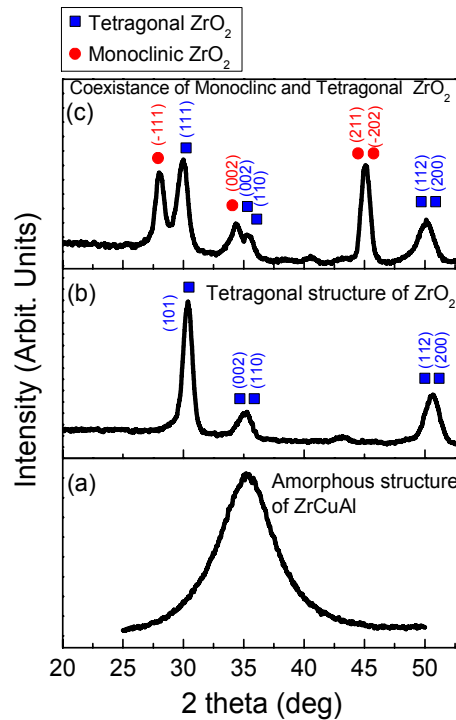


Figure 3.14: XRD diffractograms of a (a) glassy Zr-Cu-Al, (b) single phase and (c) multi phase coexistence of ZrO_2 films

In XRD measurements the detector measures counts/sec of photons in different angles regarding the sample's surface. The diffraction peak positions, by the lattice planes, are unique for each crystal solid and so they occur at different angles that can be identified by comparison with the peak positions of diffraction databases. So, knowing the Miller indices of each peak and the interplanar spacings, the lattice constants of the solid can be calculated.

3.3.1.1 Bragg-Brentano geometry XRD

The most spread geometry of X-ray diffraction is the Bragg-Brentano geometry. There are two equal types of geometries corresponding to the Bragg-Brentano geometry, the θ - 2θ and the θ - θ modes. The X-rays are elastically scattered by the electrons of the solid forcing them to oscillate as Hertz dipole (Thomson scattering). The emitted radiation can diffract having as a result a XRD pattern. If K_0 and K are the wave vectors of the incident and the reflected beams, respectively, the difference $K_0 - K$ can be defined as the scattering vector

$$Q = K_0 - K = \frac{4\pi}{\lambda} \sin \theta$$

in inverse length units, figure 3.15.

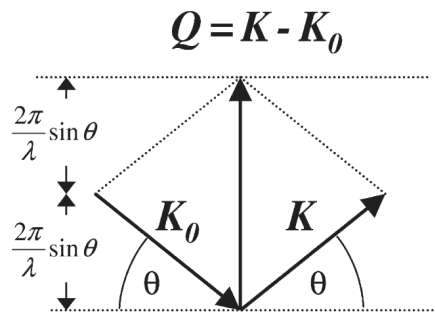


Figure 3.15: Scattering vector of XRD measurements

The scattering vector, also known as vector of momentum transfer, strongly depends on the crystal plane orientations and electron composition of the solid and thus is capable for the determination of the crystal structure. Scanning with the probe beam and the detector to be at the same locked angles to the surface, there is only one scattering vector perpendicular to the surface, figure 3.16. By this measurement geometry, only the diffraction planes that are parallel to the surface will be detected.

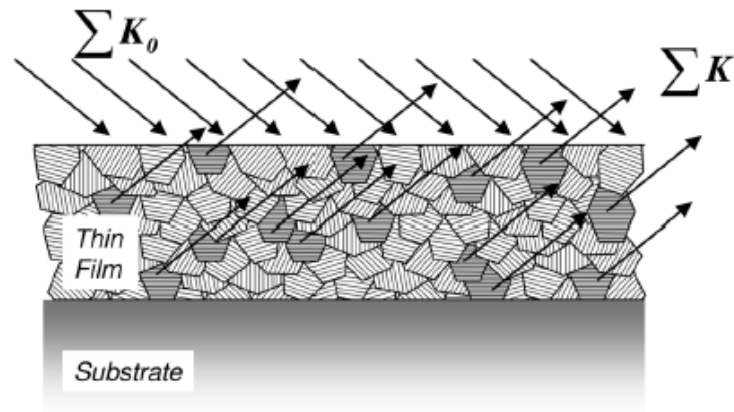


Figure 3.16: Selection principle for X-ray diffraction of face-parallel lattice planes

In figure 3.17 is shown the experimental setup of Bragg-Brentano XRD geometry.

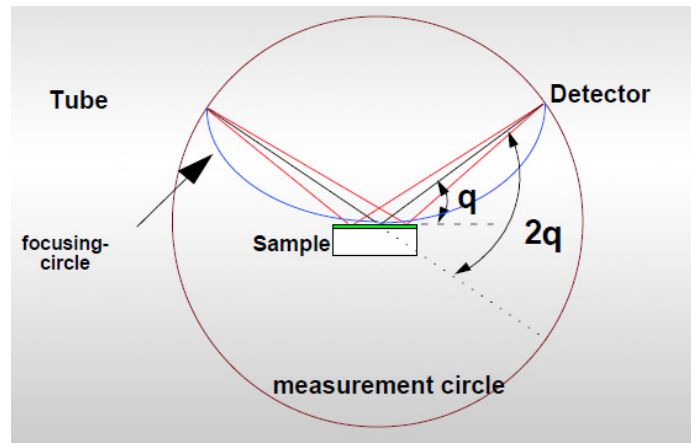


Figure 3.17: Bragg-Brentano XRD geometry setup

3.3.1.2 Grazing incidence XRD (GID)

Characterizing films by XRD has the disadvantage of low diffracted intensities due to their small diffraction volume. In polycrystalline films of no textured growth, the crystal grains are randomly distributed to the film's volume, so the Bragg's condition for diffraction is satisfied by different grains as the detector angle changes. In Grazing Incidence XRD (GID) geometry the incidence beam is fixed in angles at lower than 5 degrees to the film's surface, figure 3.18.

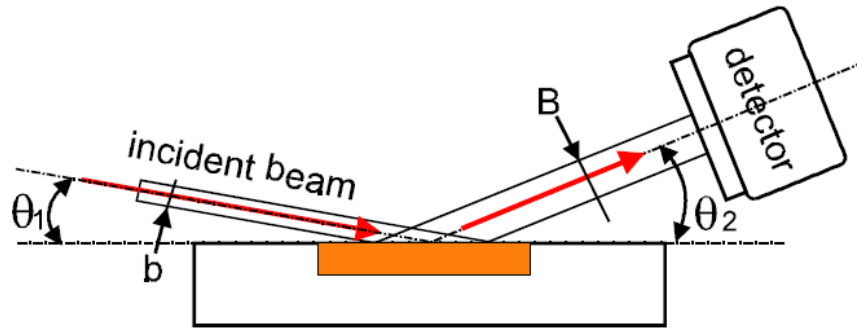


Figure 3.18: Grazing incidence geometry setup

At low incident angles the footprint of the X-rays is wide enough so that the diffraction volume increases significantly. The detector scans in the desirable angles with the intensity of the diffracted peaks to be much stronger compared with the one of the Bragg-Brentano geometry, figure 3.19.

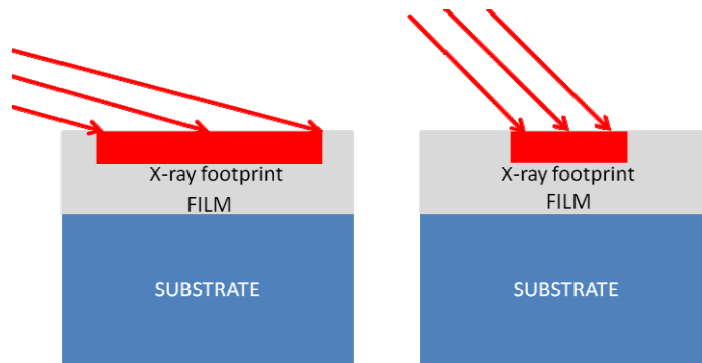


Figure 3.19: X-ray footprint on the sample for two different angles of incidence

The main disadvantage of the GID geometry is the diffraction peaks broadening due to the not well defined diffraction planes, as it is illustrated to the figure 3.20. Also GID does not apply in monocrystalline and textured structures.

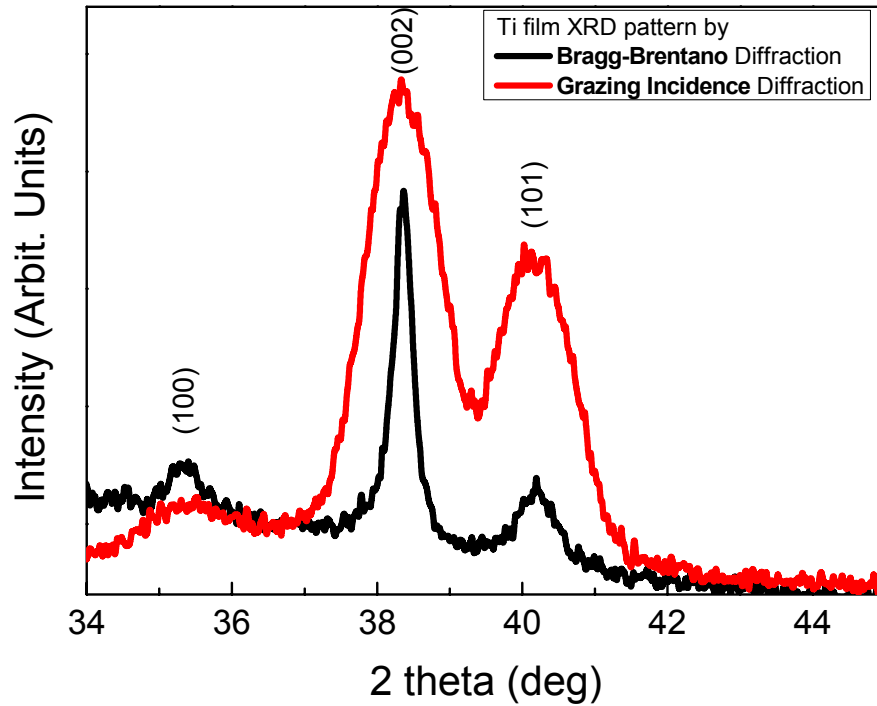


Figure 3.20: XRD diffractograms comparison of Ti in Bragg-Brentano and grazing incidence geometries

3.3.2 Grain analysis- Grain size

X-ray diffraction patterns of polycrystalline films are formed by broader peaks with respect to the bulk solids. There are two reasons for the broadening. The first reason is the grain size of each nanostructured film. In VIS optics the diffraction pattern formed by single slit, is composed by a broad main peak. As the number of slits increases (diffraction grating) the number of diffraction peaks increases, resulting in the narrowing of the main peak. In X-ray diffraction the diffraction slits are the lattice planes of the solid. A bulk solid can be considered as a grating of infinite slits and so the main diffraction peaks are sharp and well defined. As the diffraction volume decreases, the diffraction is fulfilled by less number of lattice planes and so the broadening of the diffraction peak increases.

The diffraction volume depends not only on the macroscopic dimensions of the solid, but also on its microstructure. Polycrystalline films can consist of different grain sizes determined by the element, the structure and the deposition method and parameters. In

figure 3.21 it is illustrated a qualitative graphical representation of diffraction peaks formed by infinite and finite polycrystalline film.

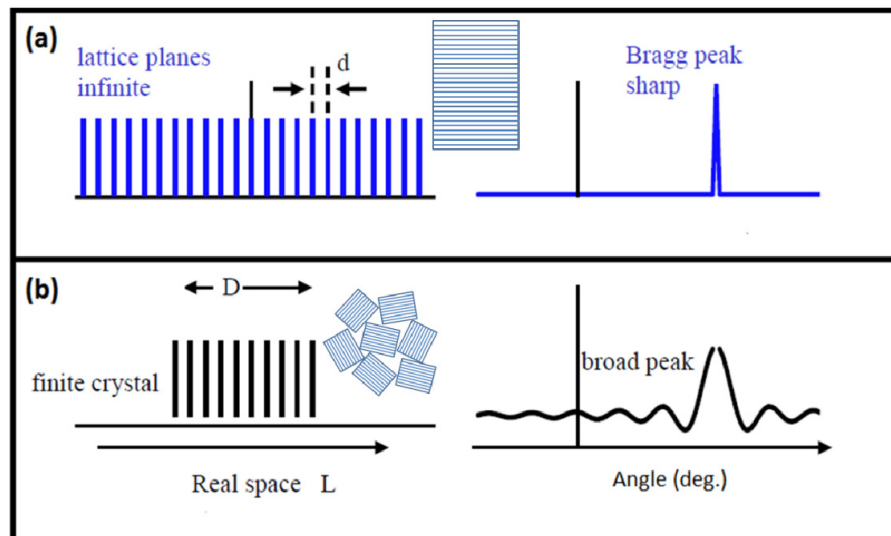


Figure 3.21: XRD peak broadening as result of the crystal size

The second reason of XRD peak broadening is because of internal stresses. Micro strains of crystallites cause a slightly change of the lattice plane distances and so a small peak shift to the XRD peak positions occurs. If the lattice distances are to be increased or decreased as determined by the direction of applied forces to the film, this can be detected by the XRD peak shift in the direction of tensile and compressive stresses, respectively, figure 3.22.

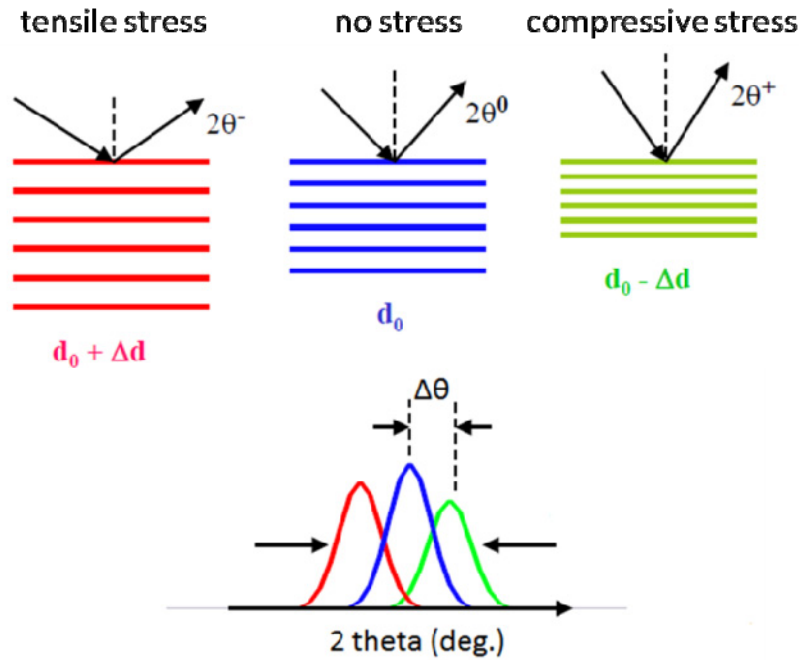


Figure 3.22: XRD peak shift provoked by microstrain effects

Grain size and internal stresses of the film are the two main reasons having as a result XRD peak broadening. Broadening is also entered by the instrumental resolution but this contribution is known for each XRD diffractometer. The strain, ϵ , and the grain sizes of a film can be calculated by the Williamson-Hall analysis according to the equation

$$\beta \cos \theta = \frac{k\lambda}{D} + 4\epsilon \sin \theta$$

where β the FWHM and θ the detection angle of diffraction peak, k is the shape factor of crystallites (Scherrer constant) with values almost always to vary from 0.89 to 0.94, λ the X-ray wavelength, D the grain size and ϵ the internal stress [3].

3.4 Morphological characterization techniques

3.4.1 Scanning electron microscopy (SEM)

Surface morphology of a solid can be carried out by scanning electron microscopy (SEM) at magnifications up to 100,000x. The SEM technique is based on a high energy electron incidence beam scanning the surface and a CCD camera that generates the

surface image by the scattered or emitted electrons from the surface and projected using a cathodic arc tube. More specific, in a high vacuum chamber, a filament is used for the generation of thermal emitted electrons. The electrons are accelerated in a high voltage field (1KeV to 20KeV) creating a high electron beam that is fine focused to the surface by a lens system scanning the surface, figure 3.23.

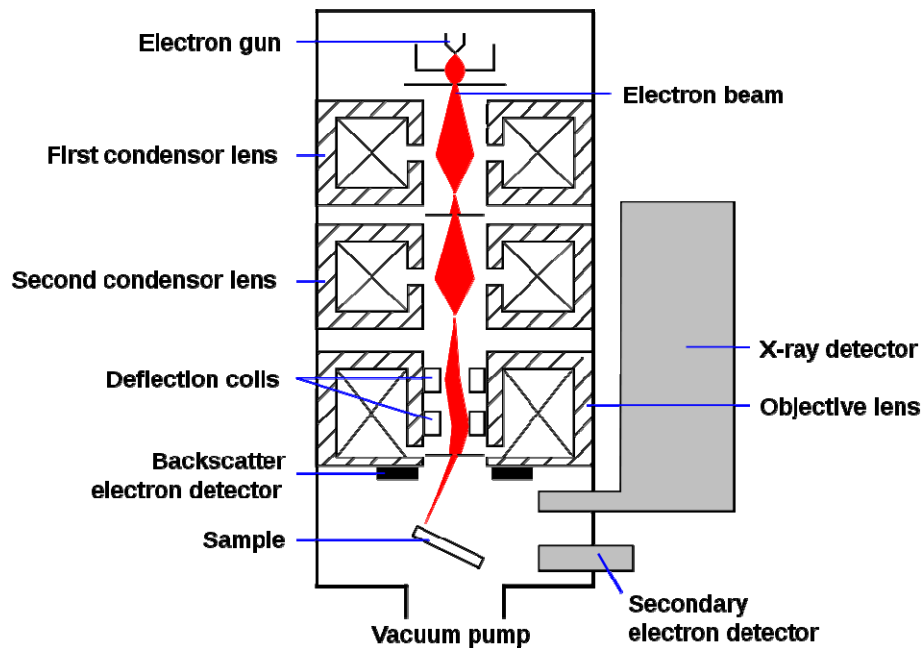


Figure 3.23: Cross section of a SEM chamber

A positive charged detector at 300V is used for the collection of the secondary and backscattered surface emitted electrons where the signal is amplified. As the electron beam scans vertically the surface any morphology irregularity result in different signal strength to the detector and so the image is created, figure 3.24.

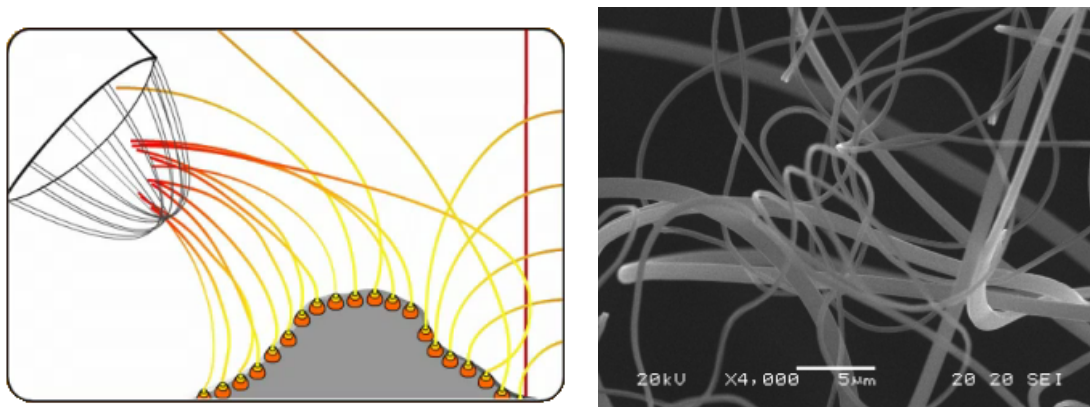


Figure 3.24: Basic principle of operation of an SEM detector (left) and a real SEM image of CNTs

Since the backscattered electrons are scattered by elastic collisions with the solid, a backscatter image of high contrast is obtained, especially if the solid is composed by different elements of high atomic number. By backscattered images information such as element distributions of different atomic number Z , mixed phases, grain sizes, etc. can be collected.

3.4.2 Atomic force microscopy (AFM)

Atomic force microscopy (AFM) is a high resolution surface sensitive characterization technique. The sample is tapping by a sharp tip with edge width of some nanometers or even attached nanotubes on the tip are used. The tip is attached on a cantilever on which a laser beam is incident. The cantilever with the tip oscillates near its resonance frequency and as the scanning is performed the tip interact through strong but low length order forces (Van der Waals) with the sample surface, figure 3.25.

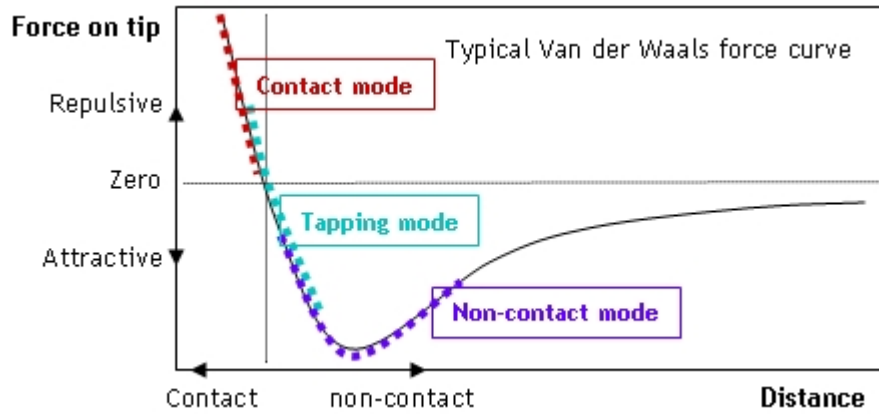


Figure 3.25: Applied force directions of the basic AFM operation modes

As it is seen in figure 3.26 there are three domestic modes in AFM use depending on the distance between the tip and the sample surface. The main difference between the modes is the force interaction type that is used each type for AFM imaging.

These interactions disturb the near resonance oscillation by altering its frequency and/or its amplitude changing the cantilever oscillation. Any perturbation of the cantilever oscillation results in deviation of the reflected by the cantilever laser beam from its initial position. A position sensitive detector is used for collecting the reflected beam deviation and after software analysis surface image is created, figures 3.27.

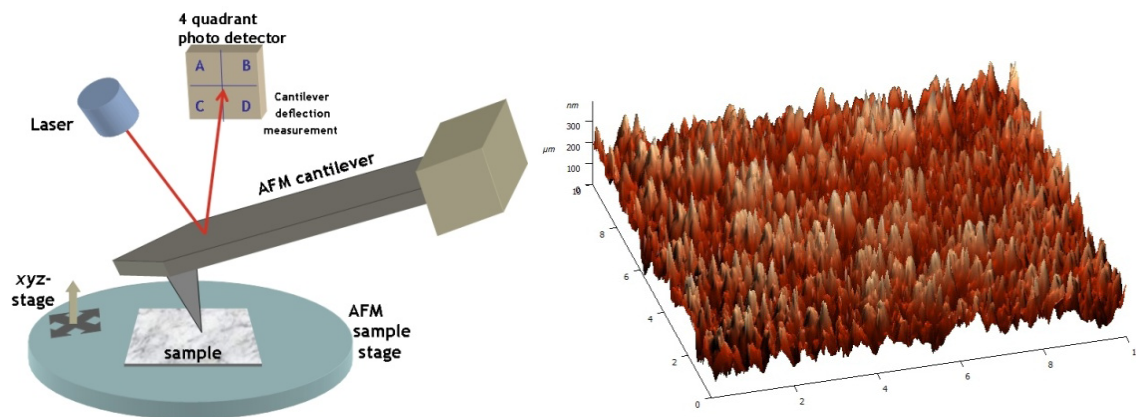


Figure 3.26: Basic parts of AFM setup (left) and real image of nanopillar structured surface (right)

3.4.3 X-ray reflectivity (XRR)

In thin film technology, critical properties like the film thickness, density and surface roughness can be determined by the X-ray reflectivity technique (XRR). The complex refractive index of a solid can be written as

$$\tilde{n} = 1 - \frac{N_A}{2\pi} r_0 \lambda^2 \frac{Z}{A} \rho = 1 - \delta - i\beta$$

where N_A is the Avogadro number; r_0 , is the classical electron radius; λ , is the X-ray wavelength; Z , is the atomic number; A , is the atomic mass number and ρ is the mass density. δ and β are, respectively, the dispersion and absorptance coefficients that can be written by the atomic scattering factors as

$$\delta = \frac{N_A}{2\pi} r_0 \lambda^2 \sum_j \frac{\rho_j}{A_j} (Z_j + f'_j)$$

$$\beta = \frac{N_A}{2\pi} r_0 \lambda^2 \sum_j \frac{\rho_j}{A_j} f''_j = \mu \frac{\lambda}{4\pi}$$

f' and f'' are the real and imaginary parts of the atomic scattering factor and μ the linear absorption coefficient of the solid.

In figure 3.27 the real part of the complex dielectric function of a solid (a-C in this case) is illustrated versus the photon energy of several characterization techniques. As it is shown, the refractive index of a solid for X-rays is slightly less than unity.

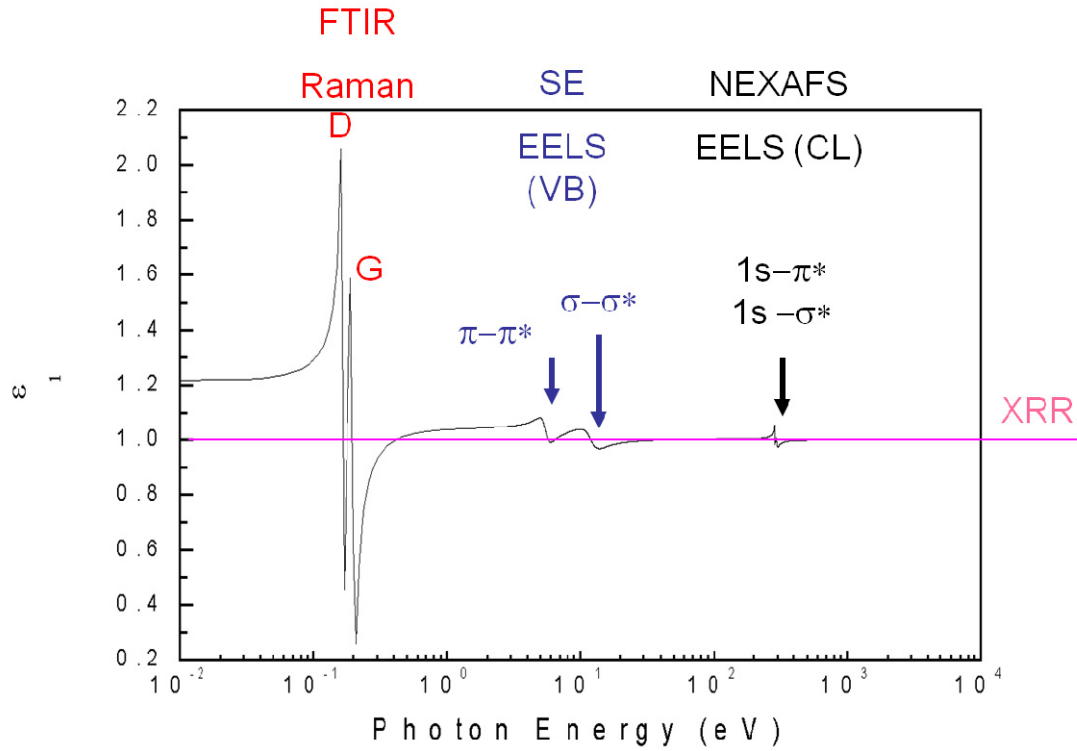


Figure 3.27: Electromagnetic dispersion of a-C film

So according to Snell's law there is a critical angle of incident, θ_c , below which total reflection of X-rays is occurred. For angles greater than θ_c the X-rays penetrate to the film's volume and second reflection is occurred by the substrate. The reflected beams are interfered and by the reflectivity pattern the thickness, the density and the surface roughness can be calculated by a fitting procedure, figure 3.28.

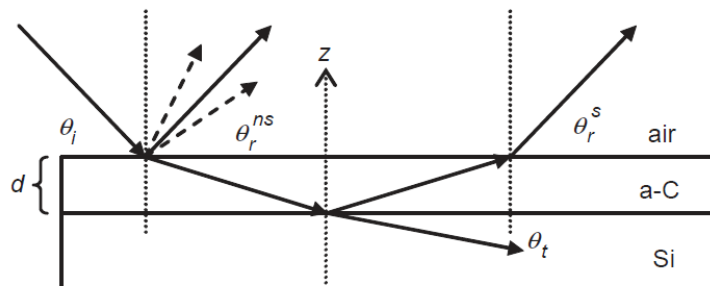


Figure 3.28: Geometry of XRR measurements [4]

In figure 3.29 is illustrated the experimental setup of XRR measurements.

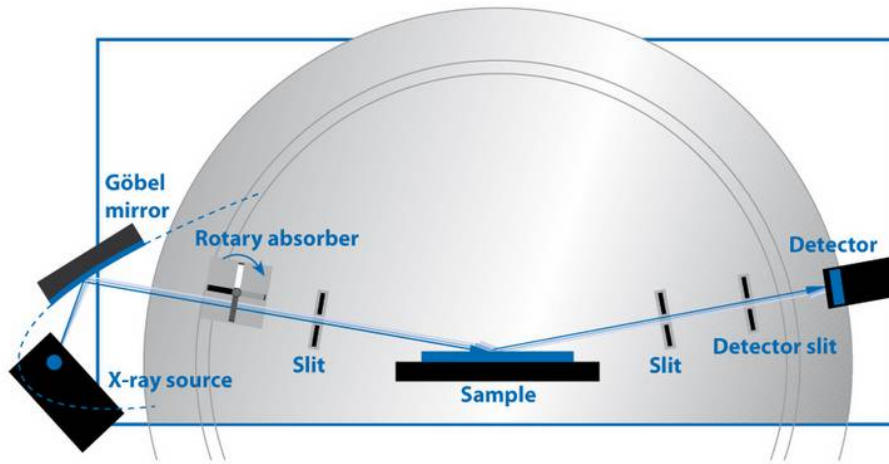


Figure 3.29: Experimental setup of XRR measurements

3.4.3.1 Film thickness

From the period of the interference fringes (Kiessig fringes) the film thickness can be estimated. The range of thicknesses that can be measured varies from 5 to 200nm, since for thicker films the interference fringes are so close to each other that cannot be evaluated. For the thickness calculation the following equation is applied, that emerges from the combination of the Snell' and Bragg's law

$$\theta^2 - \theta_{cr}^2 = m^2 \left(\frac{\lambda}{2d} \right)^2 \text{ or } d \approx \frac{\lambda}{2\Delta\theta}$$

The accuracy in the film's thickness calculation is much less than 1 nm, depending on the range of measurement and the fitting procedure.

Contribution of multiply reflections between the film's and substrate's surface can be neglected due to the fast damping amplitude reflection coefficient $[R(1/\theta)]$.

3.4.3.2 Film density

For X-rays the refractive index of the solid is a function of its atomic number as it is deduced by the δ and β parameters. Also the correlation function of the number of electron per cubic centimeter and the mass density of a solid is

$$n_e = N_A \frac{Z}{A} \rho_m$$

So by applying the Snell's law, with small angle approximations, neglecting the absorption term and using Taylor expansion for the cosine, we can determine the solid's density as

$$1 - \delta = \cos \theta_{cr} \approx 1 - \frac{\theta_{cr}^2}{2} \Rightarrow \theta_{cr} \approx \sqrt{2\delta} \Rightarrow$$
$$\theta_{cr} = \sqrt{\frac{r_0 \lambda^2}{\pi} N_A \frac{(Z + f')}{A} \rho_m}$$

There is also one more empirical way to determine the critical angle of the solid in a XRR measurement. It is widely acceptable to determine the critical angle as the angle at which the reflectivity intensity is the half of the maximum.

3.4.3.3 Film roughness

Rough film and/or substrate surface diffuse X-rays so the reflection Bragg condition is influenced resulting in a intensity decay profile in the XRR measurements. The microscopic surface roughness can be treated as thickness variation with Gaussian distribution (N'evot and Croce), figure 3.30.

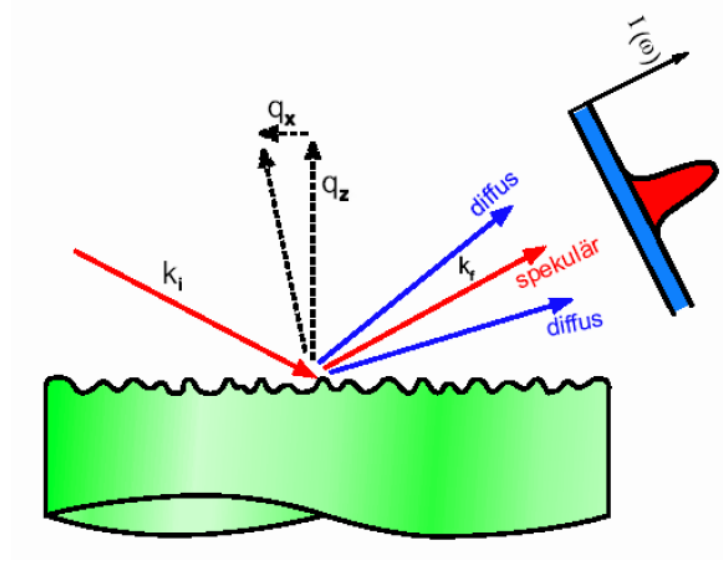


Figure 3.30: Scattering reflection of X-rays by rough surfaces

Taking into account the roughness, σ , can be calculated by the equation

$$r_{i,i+1}^{rough} = r_{i,i+1}^{ideal} e^{(-2k_{z,j}k_{z,j+1}\sigma_j^2)}$$

that is the corrected Fresnel equation of reflection by rough surfaces, with the limitation that roughness is much smaller than the layer thickness

In figure 3.31 depicts a fitted XRR measurement of a-C film. The previously analyzed quantities of thickness, roughness and density can be calculated by a fitting procedure. Additionally, the parts of the spectrum that affect these quantities are illustrated.

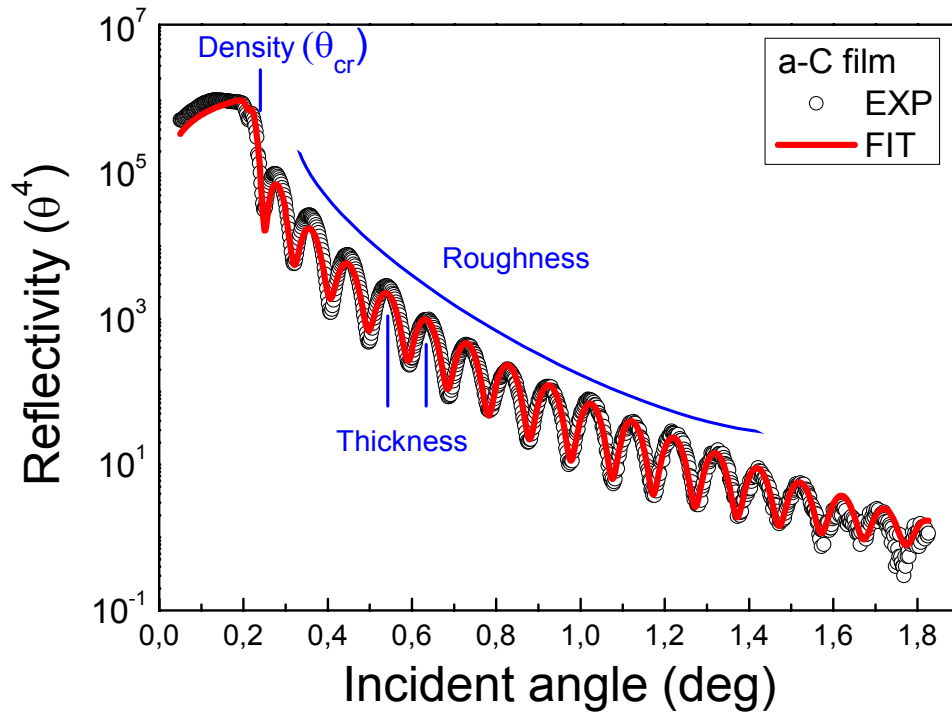


Figure 3.31: XRR measurement and the fit curve of a-C film

3.4.4 Off specular X-ray reflectivity

If the surface is sufficiently rough and thus an accurate alignment is not able, off specular reflectivity can be performed for the determination of the critical angle which is related to the solid's density and for the surface roughness. In transverse diffuse scan a rocking curve around a selected small angle, but larger than θ_{cr} , with locked the angle of the tube and the detector at θ - 2θ geometry, figure 3.32.

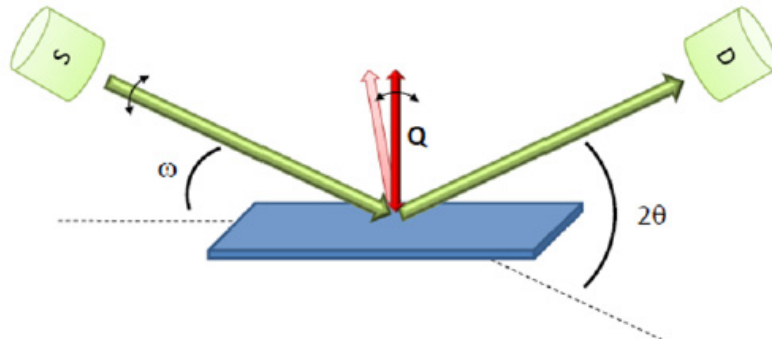


Figure 3.32: Off specular detection process of X-ray reflection measurements

In small angles rocking, curve measurements the main peak corresponds to the reflected by the surface beam when the relation $\omega = \theta - 2\theta$ is satisfied, figure 3.33. Two more peaks are formed on either side to the specular peak, known as Yoneda wings. Both are correlated with critical angle of the solid, with the small angle Yoneda wing peak to be exactly at the critical angle position, no matter the choice of the specular angle around in which the rocking curve measurement is performed.

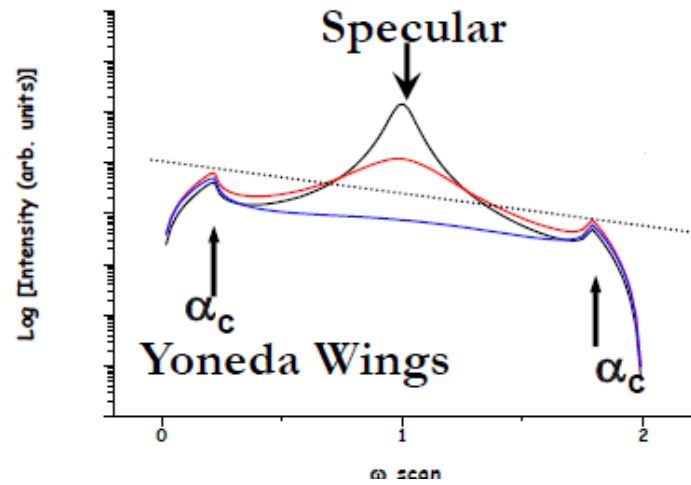


Figure 3.33: Off specular XRR measurements

Due to the diffuse scattering of different lateral roughness, surface roughness can be calculated by the specular peak profile. Introducing as ξ and h the distance and the hurst of the scattering distances, respectively, the surface fluctuation is described as

$$g(R) = 2\sigma^2 - 2C(R)$$

$$C(R) = \sigma^2 e^{-(R/\xi)^{2h}}$$

3.5 Optical properties and electronic structure characterization techniques

3.5.1 Optical Reflectivity Spectroscopy (ORS)

The transmitted and reflected component beams of a irradiated by an electromagnetic field thin solid film, figure 3.34, can be analyzed by the Fresnel equations

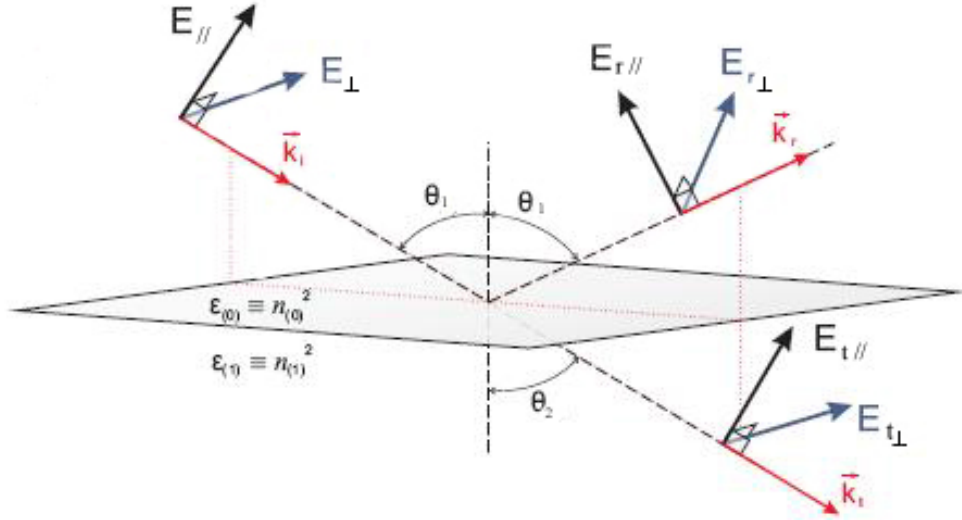


Figure 3.34 Refraction and reflection of a electromagnetic field incidence by angle in a surface

$$r_{//} = \frac{n_2 \cos \theta_1 - n_1 \cos \theta_2}{n_2 \cos \theta_1 + n_1 \cos \theta_2} = \frac{\tan(\theta_1 - \theta_2)}{\tan(\theta_1 + \theta_2)}$$

$$t_{//} = \frac{n_2 \cos \theta_1 - n_1 \cos \theta_2}{n_2 \cos \theta_1 + n_1 \cos \theta_2} = \frac{\tan(\theta_1 - \theta_2)}{\tan(\theta_1 + \theta_2)}$$

and

$$r_{\perp} = \frac{n_1 \cos \theta_1 - n_2 \cos \theta_2}{n_1 \cos \theta_1 + n_2 \cos \theta_2} = -\frac{\sin(\theta_1 - \theta_2)}{\sin(\theta_1 + \theta_2)}$$

$$t_{\perp} = \frac{2n_1 \cos \theta_1}{n_1 \cos \theta_1 + n_2 \cos \theta_2} = \frac{2 \sin \theta_2 \cos \theta_1}{\sin(\theta_1 + \theta_2)}$$

The reflectivity can be defined as the sum of the square components r_{\perp} και $r_{//}$ of the Fresnel equations. In the case of the vertical incidence of the beam, to the surface, and the first medium of the beam is the air in the above equations it is $\theta=0$ and $n_1=1$.

Replacing also the refractive index of the solid by its complex one, so the absorbance can be described, as $n_2 = n - ik$ the reflectance is

$$R(\omega) = \frac{[n(\omega) - 1]^2 + k^2(\omega)}{[n(\omega) + 1]^2 + k^2(\omega)} \quad 3.1$$

where k is the absorbance coefficient of the solid.

The experimental setup of the optical reflectivity is illustrated in figure 3.35. As light sources were used Deuterium and Halogen lamps were in combination the energy wide of the emitted photons are between 1.50 to 5.25eV. By the optical reflectivity of a thin film on a substrate is able to determine its thickness and optical properties via fitting of the function-model to the experimental data.

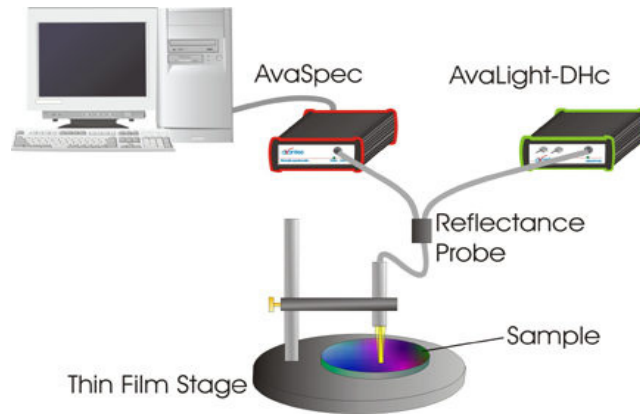


Figure 3.35: Experimental setup of optical reflectivity

The light source emission spectra were measured using a Ag mirror of 100% reflectivity, figure 3.36.

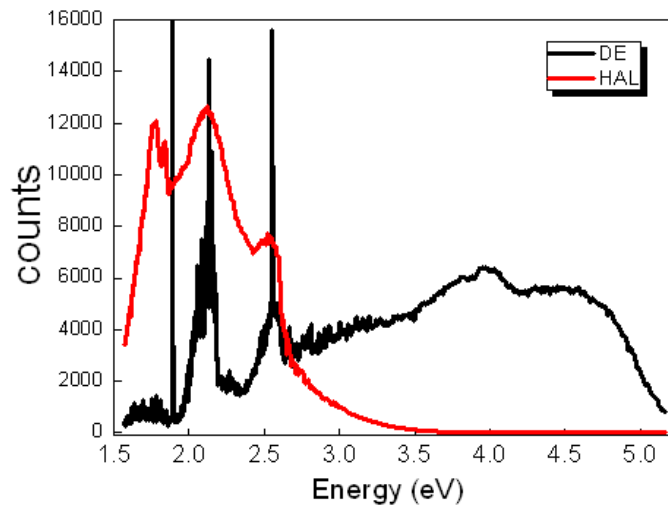


Figure 3.36: Emission spectrums of the Deuterium (black line) and Halogen (red line) lamps used as light sources

In the case of dielectric films, such as a-C and a-C:H films, that are transparent in most of the measured area because of their band gap and their small thickness, exhibit interference fringes in the reflectivity spectra. The interference fringes are developed by the interference of the reflected electromagnetic waves by the film's and the substrate's surface.

The absolute reflectivity of the monocrystalline n-type Silicon wafer that it was used as the substrate in all grown films is illustrated in figure 3.37.

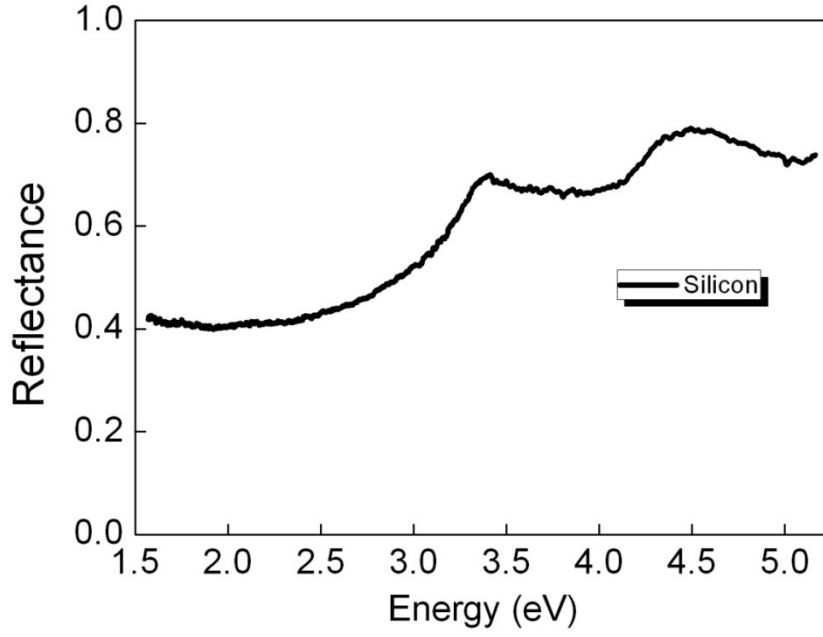


Figure 3.37: Absolute reflectance of monocrystalline Si used as substrate for the films growth

The reflectance that is measured is a function of the film's thickness and its optical properties, the refractive index and the absorbance coefficient. The reflectance and the film's thickness are strongly correlated because the wave's phase changes according to the optical distance that it travels.

Following the route of an incidence beam on a thin film, we can describe the reflected and the transmitted beams that are created till they interfere and are collected by the spectrometer. The reflectance by the surface of the film and the transmitted beam are described by the Fresnel coefficients r_1 and t_1 respectively, while the reflected beam by the substrate surface is described by the product of $t_1 r_2$. So the beam that returns to the first optical medium and it is going to interfere with r_1 is $t_1 t_1' r_2$.

If the thickness of the film is d , then the phase difference, of the electromagnetic field, that emerge during its path through the film and after its reflection by the substrate is

$$\delta_1 = \frac{2\pi}{\lambda} n_1 d \cos \varphi \xRightarrow{\varphi=0} \delta_1 = \frac{2\pi}{\lambda} n_1 d$$

The wave amplitude developed by the interference is

$$R = r_1 + t_1 t_1' r_2 e^{-2i\delta_1} = r_1 + \frac{t_1 t_1' r_2 e^{-2i\delta_1}}{1 + r_1 r_2 e^{-2i\delta_1}}$$

Replacing the Fresnel coefficients we have finally the total reflection equation as

$$R = \frac{(n_0^2 + n_1^2)(n_1^2 + n_2^2) - 4n_0 n_1^2 n_2^2 + (n_0^2 - n_1^2)(n_1^2 - n_2^2) \cos 2\delta_1}{(n_0^2 + n_1^2)(n_1^2 + n_2^2) + 4n_0 n_1^2 n_2^2 + (n_0^2 - n_1^2)(n_1^2 - n_2^2) \cos 2\delta_1} \quad 3.2$$

where n_0 , n_1 and n_2 are refractive indices of the air, the film's and the substrate's respectively.

The fitting procedure is executed combining the equations 5.1, 5.2, 5.3, 5.4 till the determination of the film's thickness and optical properties.

More specific about the fitting procedure, firstly the geometrical model that describes the incidence beam path must be developed. In our case that model is the air-film-substrate. The air and the substrate have known optical properties, while those of the film have to be determined.

Since dielectric materials are studied, the optical response of the film can be described via its complex dielectric function as it is deduced by the Lorentz model. During the fitting procedure, combination of all the free parameters in the complex dielectric function and different values of thickness are combined till the experimental data can be described with the minimum error by physical acceptable values, Fig. 6.12. This procedure is described in figure 3.38.

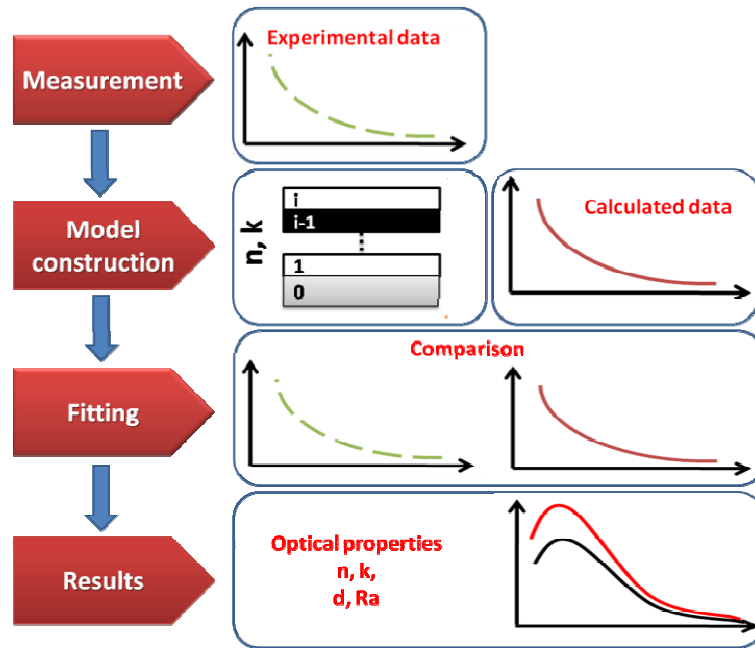


Figure 3.38: Logic diagram of ORS fitting procedure

In figure 3.39 we illustrate the experimental data and the result of the fit as it is deduced by the above fitting procedure. This is an a-C:H film of 330 nm thickness, dielectric constant 3 and the deduced dielectric functions ϵ_1 and ϵ_2 .

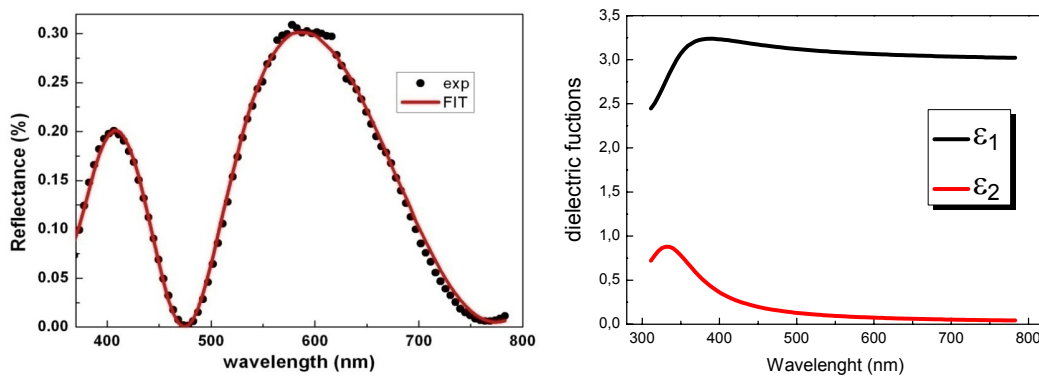


Figure 3.39: Experimental reflectivity data (black dots) and the best calculated function as deduced by the fitting procedure (red line).

3.5.1 Variable angle optical reflectivity

The reflectivity of a solid is strongly depended on the angle of incidence light. Variable angle optical reflectivity measurements were performed using as light source a laser beam of 657 nm wavelength. The polarization of the beam was determined using a polarizer. For the angle measurements of the incidence and reflection beam an X-ray goniometer was used, figure 3.40. For The measurement angles were transformed to the perpendicular axis to the surface.

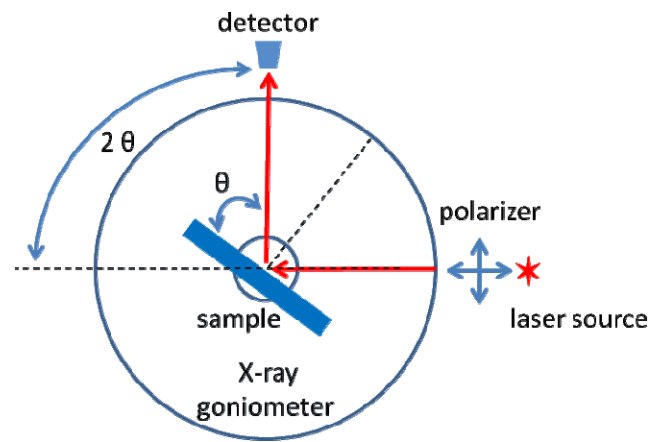


Figure 3.40: Variable angle optical reflectivity setup

Reflectivity versus angle of incidence can be performed using either s, p or mixed s and p polarization. For simplicity during the analysis s polarization is preferred. If p polarization is used there is a specific angle at which minimization of the reflectivity occurs. Since in VIS optics the angle is determined by the normal to the surface axis, the necessary angle transformations were performed.

Knowing that angle it possible to calculate the refractive index of solid by

$$n_1 \sin \theta_B = n_2 \cos \theta_B$$

where n_1 is the refractive index of air ($n_1=1$) and n_2 the refractive index of the material.

In figure 3.41 depicts the variable angle measurements of bare Si using s and p polarized laser beam.

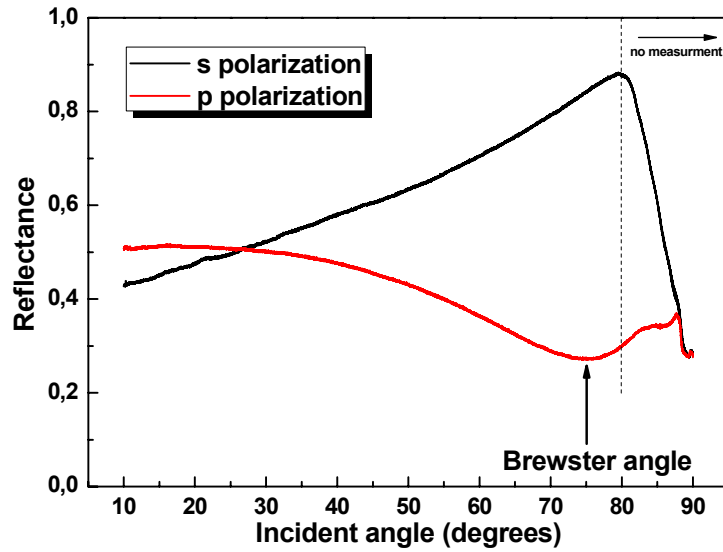


Figure 3.41: variable angle reflectivity of Si in s (black line) and p (red line) polarization

3.5.2 Off specular optical reflectivity

In optics the study of the response of a material in non specular reflectivity is significant. The interest of studying the diffuse response of an optic material is not only limited by their surface roughness scattering but also in their refractive index and diffuse scattering of nanocomposite structures. In our case an X-ray goniometer was used for variable angle measurements, figure 3.42.

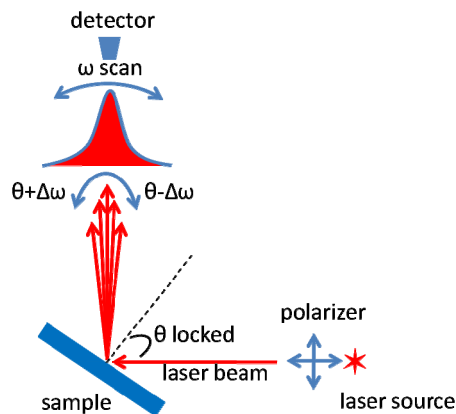


Figure 3.42: Off specular optical reflectivity experimental setup

As light source we used a laser beam of 657nm wavelength with s polarization. The incidence angle of the laser beam to the sample was fixed by locking the sample angle.

With locked incidence angle, scans were performed at $\theta + \Delta\omega$ angles either sides of the specular reflected beam. By these measurements, the angle diffuse scattering of the optic material can be studied.

In 3.43 shows for comparison the off specular reflectivity of evaporated cold film and CNTs.

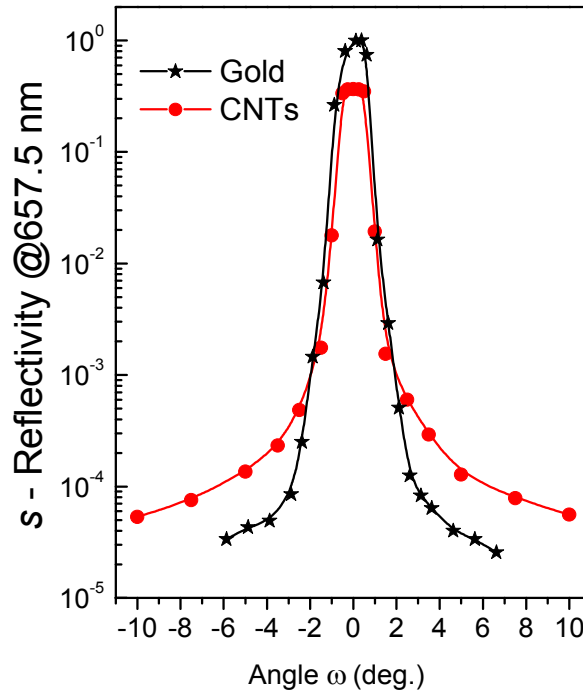


Figure 3.43: Off specular optical reflectivity of Gold (black dots) and CNTs (red dots)

3.5.3 Electron energy loss spectroscopy (EELS)

When high energy electron beam collide to a surface almost 90% of them are elastically scattered [M18]. The rest 10% of the electrons interact inelastically with the solid and are measured with lower than the initial kinetic energy. The energy loss of those electrons is rendered for the plasmon (surface and volume) creation and to interband electronic transitions. Thus the energy loss is characteristic of the electronic structure of the element. Figure 3.44 shows a typical EELS spectrum of a-C:H film and its electronic structure.

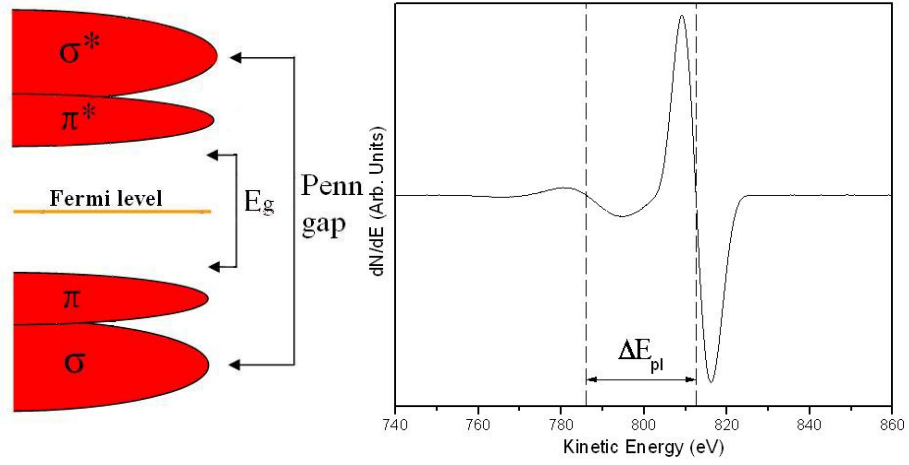


Figure 3.44: Electronic and differential EELS spectrum of a-C:H film

For dielectric or semiconductor DLC solids the measured plasmon energy, E_p , equals to

$$E_p^2 = E_{p0}^2 + E_G^2$$

where E_G , corresponds to the energy of the band gap of σ and σ^* electronic states (Penn gap) and E_{p0} is the free-electron plasmon energy [3].

3.6 References

- [1] M.P. Seah, W.A. Dench, Surf. Interface Anal., 1 (1979) 2
- [2] N. T. Panagiotopoulos, J. Kovac, M. Mozetic, P. Patsalas, G. A. Evangelakis, J. Vac. Sci. Technol. A **29**, 051303 (2011)
- [3] V. Deram, C. Minichiello, R.-N. Vannier, A. Le Maguer, L. Pawlowski, D. Murano, Surf. Coat. Tech. **166**, 153 (2003)
- [4] P. Patsalas, T.S. Logothetidis, P.C. Kelires, Diam. Relat. Mater. **14**, 1241 (2005)
- [5] A.C. Ferrari, A. Libassi, B. K. Tanner, V. Stolojan, J. Yuan, L. M. Brown, S.E. Rodil, B. Kleinsorge and J. Robertson, Phys. Rev. B **62**, 16 (2002)

4 SINGLE ELEMENT

AMORPHOUS SOLIDS;

CARBON

4.1 Introduction

This chapter focuses on the optical properties and the possible applications of a-C:H films and can be divided into two parts.

The first part of this chapter refers to the study of DLC coatings as antireflective coatings. The antireflective coatings are widely used to increase the efficiency of solar cells since they can trap the solar irradiation by the greenhouse effect. Also there are used as optical components as transparent coatings [1], optical lenses [2] and sensors [3]. The DLC coatings have the advantage of the combination of exceptional mechanical and optical properties. As far as the mechanical properties of the DLC are concerned, they have high hardness, low friction coefficient [4], they are anticorrosive [5] and hydrophobic [6]. The main advantage of the optical properties of the DLC is their growth of adjustable refractive index that is very important for optical applications such as the antireflective coatings [7]. Additionally, DLC coatings can be grown by industrial scale methods, i.e. PECVD, with very low cost carbon sources. Hydrogenated DLC films that are mainly grown by PECVD, give the additional deposition parameter of the hydrogen content of the DLC, which can extend the adjustability of the refractive index.

The second part of the chapter refers to the study of a post growth modification procedure of the optical properties of the as grown a-C:H films. Also the selectively planar area modification was interesting, so the laser patterning procedure was chosen. For the needs of this study we investigated the photosensitivity of hydrogenated amorphous Carbon films (a-C:H) and the changes in their structural features and optical properties, when they are exposed to picosecond laser beams of various wavelengths (Nd:YAG, 1st harmonic, $\lambda=1064$ nm and 4th harmonic, $\lambda=266$ nm). The different light–matter interactions, which take place for the various laser wavelengths, are considered and discussed. The main findings include the formation of SiC at the a-C:H film/Si interface and the film graphitization, when the 1064 nm and 266 nm beams, respectively, are used. Finally, we managed to vary locally the refractive index in the range of 1.60–1.95 (20% variations) by laser processing, a fact that is very important for various applications in photonics.

Amorphous Carbon films, either pure (a-C) or hydrogenated (a C:H), have been long established as important engineering materials, which can be used as protective overcoats due to their exceptional mechanical properties [8]. In addition, they exhibit a vast range of optical constant values such as the refractive index and the fundamental gap [9-24]. As a result, the correlations linking the optical properties with the structural features (especially the sp^3 and H fractions) have been subjects of intense study [9–24]. The combination of the excellent mechanical properties with the range of refractive index 1.4–2.7 [9] and of the fundamental gap of 0.5–3.5 eV and the dielectric or conducting character of sp^3 - or sp^2 -bonded carbon, respectively, offers the potential of using laser-patterned a-C:H films as durable, scratch-resistant parts for optical devices [25], as well as metallo-dielectric photonic crystals [26,27]. For the devices' architecture in such applications the photosensitivity is a major asset. Therefore, a study of the photosensitivity of a-C:H films and other forms of carbon is still required, in order to optimize a wide variety of carbon-based optical devices, and relevant studies have been reported [28-40]. In particular, Cirino et al. [28] and Pavelyec et al. [38] engraved diffraction gratings into a-C:H and diamond thin films by optical lithography and plasma etching [28]; Shimizu et al. [29] and Kononenko et al. [33,37] induced structural transitions, mainly diamond to sp^2 a-C, into the bulk of diamond using laser beams; Okuchi et al. [34] managed to produce micromachining patterns in diamond surface patterning of amorphous carbon films by high fluence UV laser annealing, while fs IR laser radiation has been reported by Cappelli et al. [36] and Dumitru et al. [39]; Olivero et al. [31] and Preclíková et al. [32] managed to vary the refractive index of diamond by proton and laser radiation, while Vouagner et al. [40] varied the work function and the photoelectric yield of diamond like carbon films by laser radiation. Although the most frequently reported structural transition in laser radiated carbon is from diamond to sp^2 -carbon, the inverse transition from graphite to sp^3 -carbon has been also reported by Kanasaki et al. [35].

We investigated the photosensitivity of a-C:H films grown on c-Si (001) by Plasma Enhanced Chemical Vapor Deposition (PECVD) by exposing them to the radiation produced in a Q-switched picosecond pulsed laser. Two laser beams have been used, one

with energy 1.165 eV ($\lambda = 1064$ nm), i.e. below the fundamental gap of a-C:H films but above the fundamental gap of Si ($E_{\text{gsi}} = 1.11$ eV), and one with energy 4.661 eV ($\lambda = 266$ nm), i.e. above the fundamental gap of both a-C:H films and Si. Significant variations of the refractive index of a-C:H films have been observed after exposure to the laser beams, even for relatively low laser fluence (below the ablation threshold). In particular, laser radiation with 1064 nm results into a decrease of the refractive index, while radiation with 266 nm results into an increase of the refractive index. Total variations of the refractive index of more than 20% have been achieved by laser processing. These variations of the optical constants have been associated with variations of the fractions of the $\text{sp}^2 \text{C—C}$, $\text{sp}^3 \text{C—C}$ and $\text{sp}^3 \text{C—H}$ bonds, as well as the formation of SiC at the a-C:H film/Si interface. The latter have been identified by the optical modeling and by independent Auger Electron Spectroscopy (AES) and Electron Energy Loss Spectroscopy (EELS) measurements and analyses.

4.2 Parameterization of the PECVD reactor

For the growth of the hydrogenated amorphous carbon films (a-C:H) the described at section 2.5 PECVD reactor was installed. The studied parameters, that influence the physical properties of the grown a-C:H films, were the working pressure, the applied power and the precursors percentage flow. As carbon source was used acetylene (C_2H_2) because of the high deposition rate and the low ratio of Hydrogen to Carbon to the molecule of the acetylene, figure 4.1. Benzene was not preferred due to its hazardous to human nature.

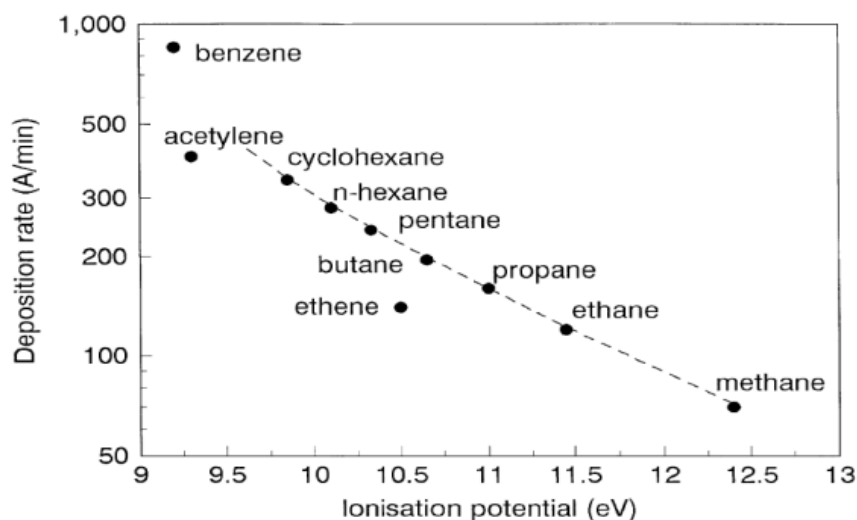


Figure 4.1 Deposition rate of various hydrocarbon precursors used in PECVD reactors [8]

The optical properties and the thicknesses of the grown a-C:H films were determined by optical reflectivity spectroscopy (ORS). Concerning the electronic structure of the a-C:H characterization was carried out by Auger electron (AES) and electron energy loss spectroscopy (EELS). Also the density was deduced by EELS measurements since the density of the DLC films is proportional to the square of the energy positions of the $\pi+\sigma$ plasmons [41].

4.2.1 Influence of the working pressure

Deposition of a-C:H films in various working pressures, from 50 to 900 $\times 10^{-3}$ mbar, were performed under constant applied RF power of 40 Watt, deposition time of 15 min and 50-50% sccm flow of Ar-C₂H₂ precursors. In figure 4.2 the optical properties of the a-C:H films as deduced by ORS are summarized.

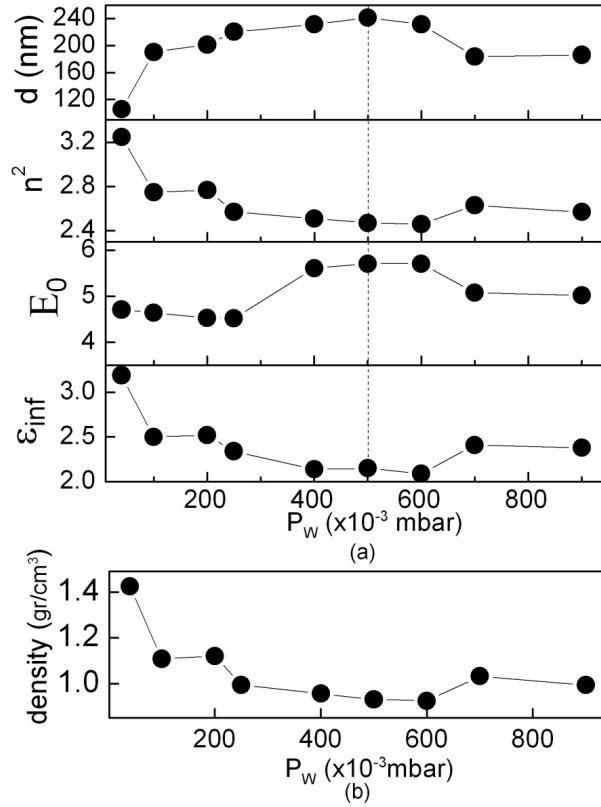


Figure 4.2: Optical properties of a-C:H films deposited in various working pressures

In figure 4.2 two regions of different properties a-C:H films are distinguished. For working pressures from 40 to 500 10^{-3} mbar decrease of the refractive constant, n^2 , and the term, ϵ_{inf} , of the non experimental measured transitions ($\sigma-\sigma^*$, $\sigma-\pi^*$, $\pi-\sigma^*$) is noticed. Combining these results with the energy position of the Lorentz oscillator at around 4 and 5 eV we suggest a sp^2 rich of C-C bonding a-C:H films (M27).

For working pressures from 500 to 900 10^{-3} mbar thinner and denser a-C:H films were grown. Also the term ϵ_{inf} and the energy position of the Lorentz oscillator increases leading us to the assumption of preferred C-C bonding sp^3 rich a-C:H films.

So by deposition in various working pressures selective either sp^3 C-C or sp^2 C-C can be grown with the dielectric constant varying from 3.2 to 2.4.

4.2.2 Influence of the applied RF power

Deposition of a-C:H films in various applied powers, from 20 to 120 Watt, were performed in working pressure of 40×10^{-3} mbar, deposition time of 5 min and 50-50% sccm flow of Ar-C₂H₂ precursors. Two regions with different properties of a-C:H films can be discrete for deposition with different applied RF powers, figure 4.3.

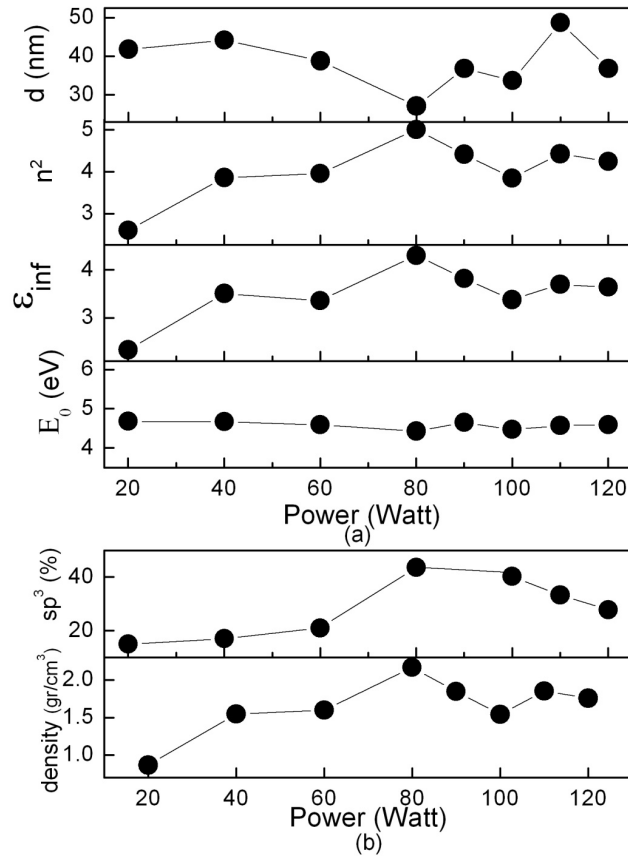


Figure 4.3: optical and electronic properties of a-C:H films deposited in various applied powers

For low applied powers, from 20 to 80 Watt, increasing the power an increase of the sp^3 , ϵ_{inf} and the dielectric constant is observed, with the energy position of the Lorentz oscillator to be almost constant, followed by the decrease of the a-C:H films. By these results we assume that C-C bonding sp^3 rich a-C:H films are grown.

In the second region, 80-120 Watt, the density of the a-C:H films remains almost constant but by the decrease of sp^3 content and the E_0 values we conclude that a more graphite films of C-C bonding sp^2 rich growth is preferred.

The region from 60 to 120 Watt is the sp^3 window of the specific PECVD reactor [Robertson]. Polymer-like of C-H bonding sp^3 rich a-C:H films are grown for 100 Watt applied power in agreement with the proposed subplantation model proposed by Robertson [42]. In that energy region the ions have sufficient kinetic energy to be implanted to the growing film and to form the metastable phase of a sp^3 bonding film. Ions of higher kinetic energy are also implanted to the film but with the temperature to be increased locally leading to graphitization of the a-C:H films [42].

Deposited a-C:H films at applied power higher than 120 Watt were not reproducible because of the unstable plasma character by the sparks.

Summarizing, by deposition in various applied powers the selective growth of C-C bonding sp^3 rich and C-C bonding sp^2 rich a-C:H films with sp^3 content from 20 to 40% was established. The dielectric constants of the a-C:H films was varied from 2.5 to 5.

4.2.3 Influence of the reactants' percentage flow

The influence of the percentage flow of the reactants, Ar and C_2H_2 , was studied by deposition at constant RF applied power of 80 Watt, working pressure at 40×10^{-3} mbar and deposition time of 10 min, Figure 4.4.

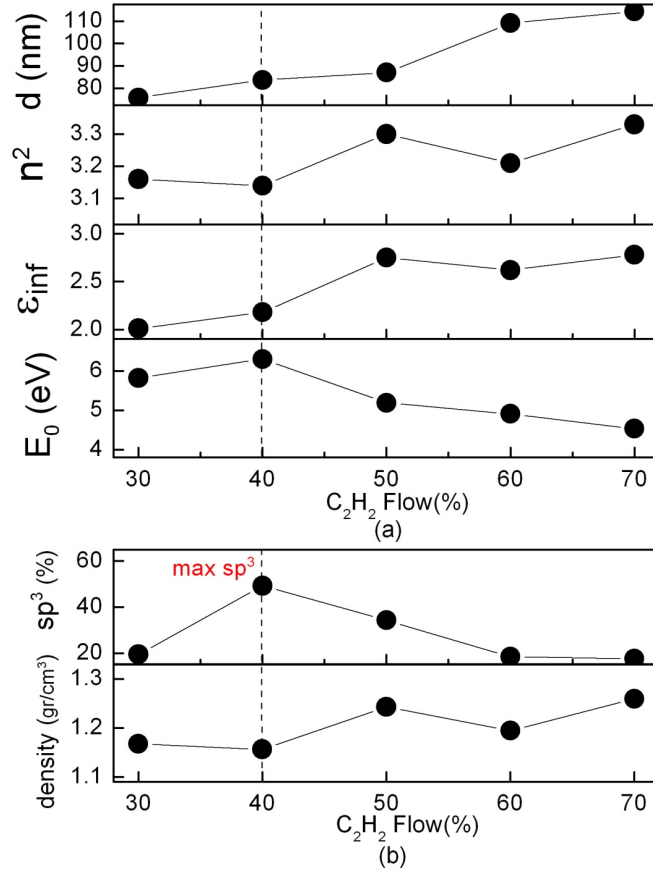


Figure 4.4: Optical and electronic properties of a-C:H films deposited in various rate of reactants' percentage flow

At low concentrations of C₂H₂ sp³ bonding a-C:H films growth is preferred because of the high kinetic energies of the ions. Increasing the percentage of the C₂H₂ the deposition rate increases but C-C bonding sp² rich films are grown with steady increase of the density because of the dramatic decrease of the H content in the films.

4.3 General properties of the as grown a-C:H films by RF PECVD

The Penn gap of carbon based amorphous films is the energy gap of the σ - σ^* electronic states. When an electron absorbs sufficient energy by an external field to transit to the σ^* electron state, it is able to resonant under the frequency of the external field creating a plasmon resonance. The energy loss of the elastically scattered electrons, measured by EELS, is the absorbed energy used for the electron transitions and the electron-plasmon interaction. So the Penn gap equals to

$$E_G^2 = E_P^2 - E_{P0}^2$$

where E_P is the measured plasmon energy by EELS and E_{P0} is the free electron plasmon energy that can be calculated by the formula

$$E_{P0} = \left\{1 - \frac{1}{[n(0)]^2}\right\}^{1/2} E_P$$

where $n(0)$ is the refractive index of the a-C:H film as it is deduced by the ORS [43].

The Penn gap of diamond and the graphite is 9 and 16 eV, respectively. Graphite has higher Penn gap because as the π states are formed the energy distance of σ - σ^* states increases. In fig. P we illustrate the dielectric constant as deduced by ORS and the sp^3 content as deduced by AES versus the calculated Penn gap of the grown a-C:H films, figure 4.5.

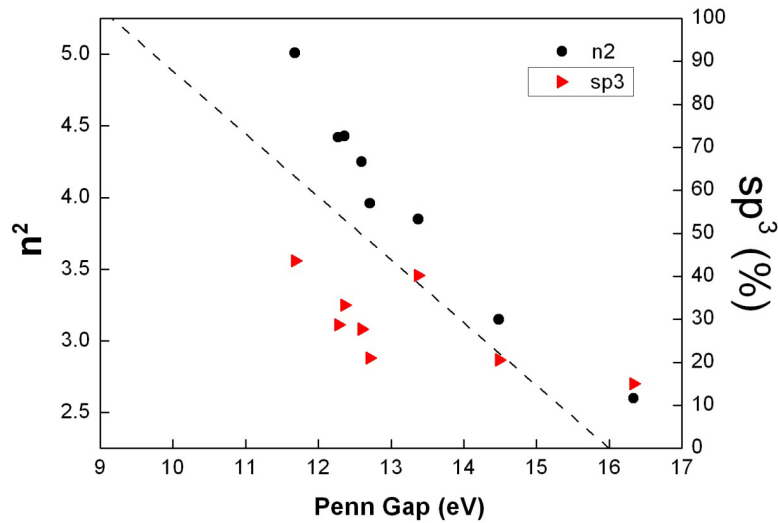


Figure 4.5: Dependence of the sp^3 content (red triangles) and the dielectric constant (black dots) by the Penn gap. The dashed line follows the trend of the sp^3 content versus the Penn gap of graphite and ta-C:H

The results are in good agreement with the theory. The small deviation of the sp^3 contents from the theoretical values (dashed line) is justified by the 20% underestimation of the sp^3 contents caused by three reasons. The first reason is that the AES measurements were performed ex-situ so contamination was not able to be avoided. The

second reason is that AES is surface sensitive technique and DLC films have less percentage of sp^3 in the surface than in their volume. The third reason is that for the specific AES measurements a high energy electron beam was used that cause a slight graphitization of the films. It is worth noting that our EELS data indicate that the increase of sp^3 content is associated with an increase of the n^2 (i.e. of the film's density), which is a strong indication for the development of C-C sp^3 bonds.

Besides the optical and the structural properties of the a-C:H films, it is important for a reactor to be calibrated so that to be able for a selective growth of specific bonding type films. The presence of H in the a-C:H influences significantly the physical properties of the films. For that reason it is important to estimate when C-C and C-H bonds are preferred depending by the deposition parameters, figure 4.6.

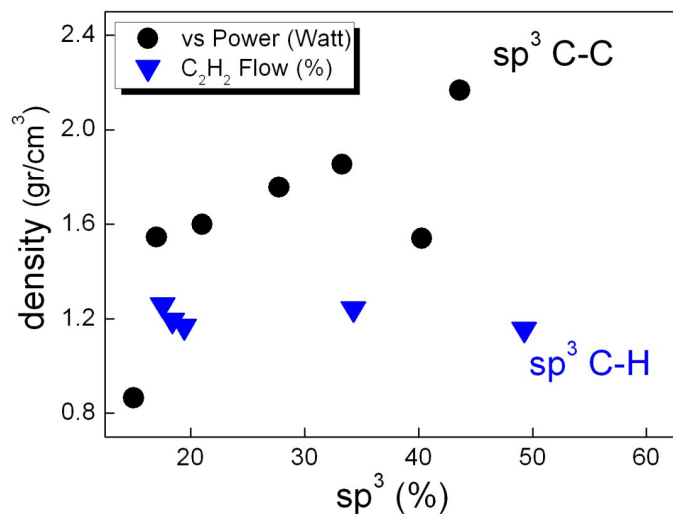


Figure 4.6: Dependence of density versus the sp^3 content of C-C bonding sp^3 rich (black dots) and C-H bonding sp^3 rich a-C:H films (blue triangles)

In figure 4.6 are shown the densities versus the sp^3 contents of deposited a-C:H films in various applied powers (black dots) and C_2H_2 percentage flow (blue triangles). For constant ratio of Ar/ C_2H_2 , the deposition in various applied powers influences mainly the percentage of the sp^3 C-C bonds since as the sp^3 increases the density also increases. The sample of less sp^3 content and density is a graphite-like carbon film deposited with the

lower applied power. The sample of 40% sp^3 content is a single combination of the applied power and the C_2H_2 percentage flow that a polymer-like carbon film growth is preferred.

For samples deposited with constant applied power but with the Ar/ C_2H_2 to be altered the sp^3 increases but the density is constant. By this result we can make the consumption that by altering the Ar/ C_2H_2 ratio the percentage of the H in the a-C:H can be controlled.

4.4 Hydrogenated amorphous carbon films as antireflection coatings

The parameterization of the PECVD reactor made possible the growth of a-C:H films with plethora of optical properties. The design of a a-C:H film intended for the use as a applicable optical sensor or optical part to optical devices, based to its response to light. The physical properties that mainly define the light-thin film interaction are the refractive index and the thickness of the thin film. The refractive index of a solid is determined by the electron density and configuration, while the thickness determines the optical path of the incident light.

4.4.1 Experimental setup

The DLC films were deposited on commercial, Czochralski- grown, n-type Si (001) wafers by PECVD in a RF parallel plate high-vacuum ($P_b < 2 \times 10^{-6}$ mbar) reactor at room temperature. The substrates were cleaned by standard ultrasonic baths of tetrachloroethylene, acetone, and methanol, rinsed by deionized water, and dried by pure (electronic grade) N_2 gas shower prior to introduction to the reactor, in order to remove the organic contaminants on the surface. In the reactor the wafers were plasma-etched with Ar^+ (rf Power 60 W, Ar flow 50 sccm, working pressure 0.16 mbar) for 15 min.

The DLC growth was performed using gas precursor mixtures of Ar/ C_2H_2 (99.999%/99.6% purity respectively) at flow 5/5 sccm respectively, keeping the operating pressure at 4.5×10^{-2} mbar. The RF (13.56 MHz) power is connected to the reactor

electrode through an autotuned matching network. The RF power used for the particular DLC presented in Figure 1 was 60 W.

The optical properties of the DLC films were investigated using optical reflectance spectroscopy (ORS) in the 370-780 nm (1.59-3.35 eV) spectral range. The density of the films has been determined by reflection electron energy loss spectroscopy [43] using an electron gun and a concentric cylindrical mirror analyzer. The specific DLC/Si films used for the antireflection DLC coating at 633nm wavelength have $n_{\text{DLC}}=1.94\text{-}1.98$ and density $\rho= 1.6 \text{ g/cm}^3$, values that are consistent with previous works [9].

4.4.2 Determination of optical properties of a-C:H films for specific visible light wavelength antireflection

In this section we demonstrate the basic operating principles of an antireflection coating. The studied antireflection system was the aforementioned a-C:H films deposited on Silicon substrate.

The goal of an antireflective coating is the determination of the optical properties, as defined by the ϵ_1 function and its thickness so destructive interference of the reflected light occurs. The reflectance of a thin film/substrate caused by normal incidence light irradiation and its minimization needs to be succeed is given by

$$R = \left| \frac{n_{\text{film}}(n_{\text{sub}} - 1)\cos kt - i(n_{\text{film}}^2 - n_{\text{sub}})\sin kt}{n_{\text{film}}(n_{\text{sub}} + 1)\cos kt - i(n_{\text{film}}^2 + n_{\text{sub}})\sin kt} \right|^2 \quad (1)$$

where n_{film} and n_{sub} are the (generally complex) refractive indices of an antireflection coating and of the substrate respectively, t is the film thickness, $k=2\pi n_{\text{film}}/\lambda$, and λ the wavelength in vacuum.

For transparent film and substrate this is achieved when the conditions

$$n_{\text{film}} = \sqrt{n_{\text{sub}}} ,$$

$$t_{film} = \lambda / 4n_{film} , \quad (2)$$

are fulfilled.

As example, is shown the reflectivity of an antireflection coating, figure 4.7. For the specific film's refractive index and thickness to be 1.98 and 80.2 nm, respectively, the antireflection conditions are fulfilled at light with 633 nm wavelength, resulting to an infinitesimally small reflectance (10^{-4}); the 633 nm wavelength has been selected as it corresponds to the most common laser source, i.e. the He-Ne laser. For wavelengths beyond the 633 nm the antireflection condition is gradually not fulfilled and the reflection increases.

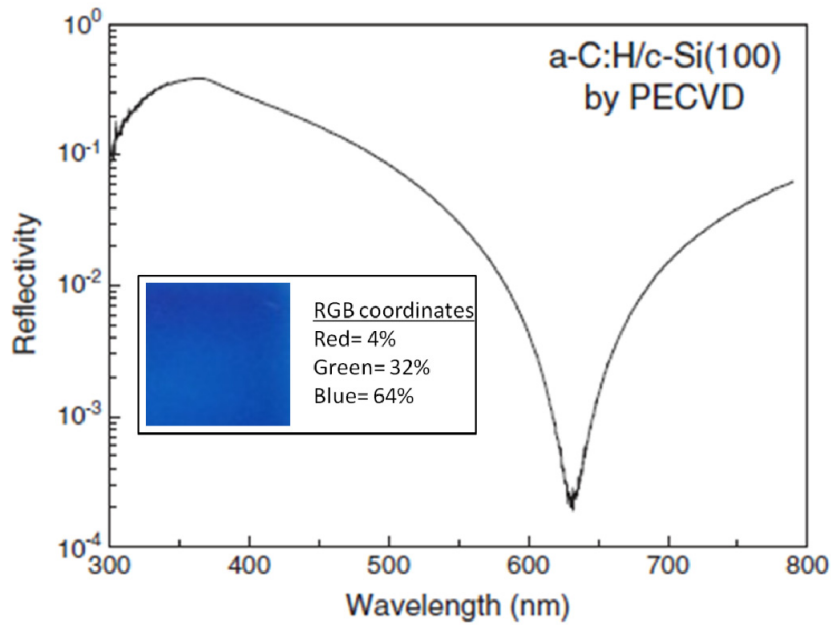


Figure 4.7 Optical reflectivity of a-C:H antireflection coating. The inset shows the RGB coordinates deduced by the photograph of the AR coating under white illumination

As it is illustrated in the inset of figure 4.7, the colour of the film under white illumination is blue. That is because light wavelengths that correspond to red colour (633nm) are absorbed while the reflectance is around 30-40% for the corresponding to blue light wavelengths.

The DLC refractive indices span the range between 1.6 and 2.6 [9]; therefore, variety of DLC films with specific refractive index can easily grown by plasma-enhanced Chemical Vapor Deposition (PECVD) as shown in figure 4.8.

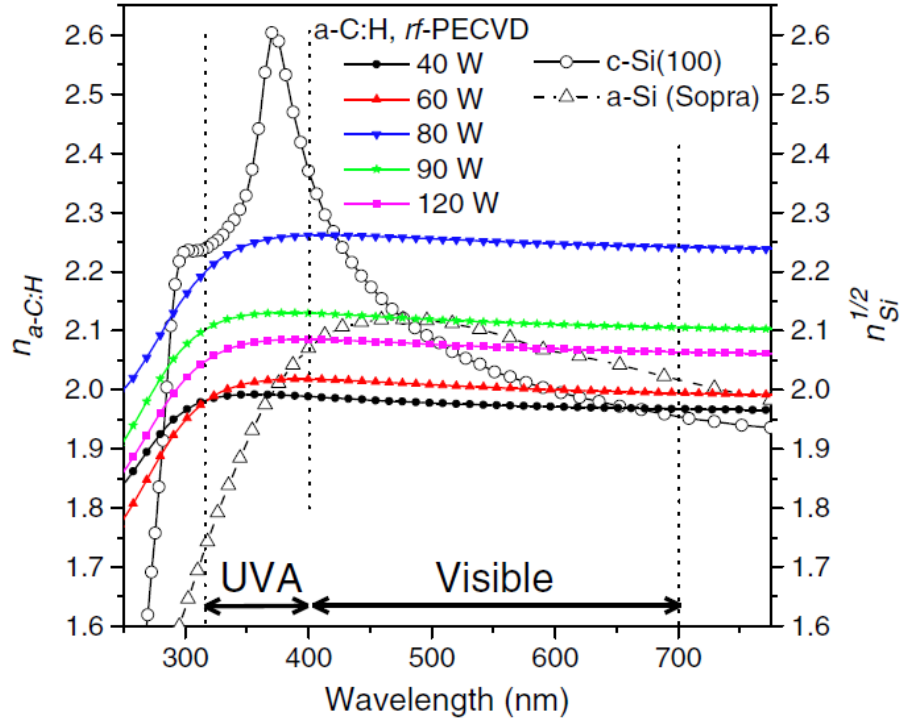


Figure 4.8: Refractive index of a-C:H films and the c-Si and a-Si substrates as determined by ORS [44]

In this figure, the spectral variation of the refractive index of several DLC films grown by PECVD are compared to the square root of the refractive index of the standard Si substrate (both measured using optical reflectance spectroscopy, ORS). Note that the range of the $n_{\text{DLC}} = n_{\text{Si}}^{1/2}$ condition that can be satisfied for the DLC films.

4.4.3 Results and discussion

The first step of our study is the accurate determination of the optical response of the DLC/Si system as an antireflection coating. The optical properties were tested using spectral reflectance measurements, which has been modeled based on the corresponding calculated dielectric function of DLC. The dielectric function of DLC was analyzed using the Lorentz model to describe the π - π^* interband transition [9,45]

$$\tilde{\varepsilon}(\omega) = \varepsilon_{\infty} + \frac{f \cdot \omega_0^2}{\omega_0^2 - \omega^2 - i\gamma\omega}, \quad (3)$$

where ε_{∞} is a background constant, larger than unity predominantly due to the σ - σ^* interband transition (beyond the experimental spectral range) [9]. The Lorentz oscillator is located at an energy position $E_0 = p\omega_0$, with strength f and damping (broadening) factor γ . The ORS spectra were fitted combining equation 3 with the reflectance of a thin-film/substrate system of equation 1, where $\tilde{\varepsilon}_{1/2} = \tilde{n}_{\text{DLC}} = n_{\text{DLC}} + i k_{\text{DLC}}$. The fit is performed using all the reflectance data, with unknowns the ε_{∞} , f , ω_0 , γ , and DLC thickness t . The use of spectral reflectance measurements (i.e., a set of experimental points at 176 different wavelengths) enables the statistically reliable determination of the five (5) fit parameters (ε_{∞} , f , ω_0 , γ , and DLC thickness t). The points are the reflectance experimental data in the range between 370 and 780 nm, whereas the solid line stands for the best fit with equation 3. At $\lambda = 635$ nm, the reflectance is infinitesimally small, as shown in the inset of Figure FIT, demonstrating reflectance values well smaller than 1×10^{-4} (the experimental points cannot be less than 1×10^{-5} due to the limitation of the electronic noise of the used spectrometer); an extrapolation of the experimental points at $\lambda = 635$ nm yields reflectance values.

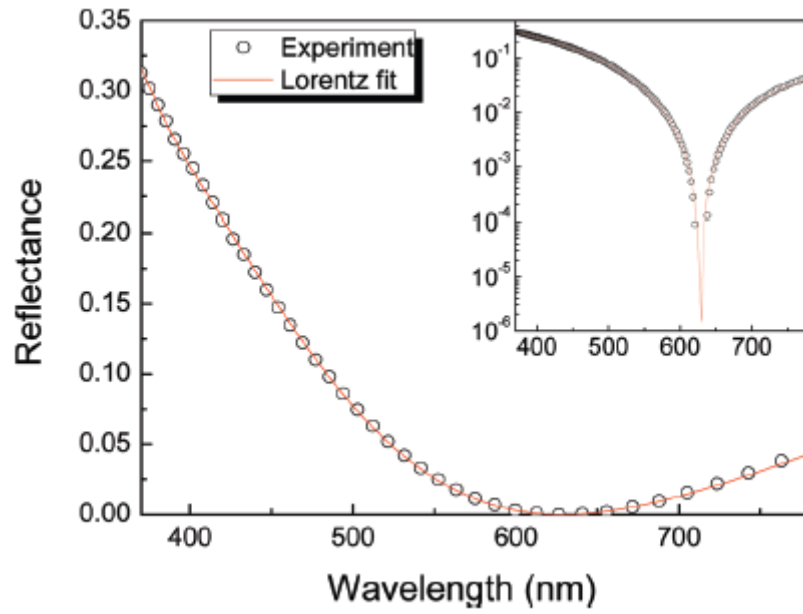


Figure 4.9: Experimental points of optical reflectance (points) and the Lorentz fit (line). The inset shows the optical reflectance in logscale around the antireflection point of $\lambda = 635$ nm [7]

Extrapolating the optical properties of the grown a-C:H films by the fitting procedure variety of antireflection coatings at specific wavelengths was established. In figure 4.10 are shown the antireflection coatings thicknesses of specific refractive indices versus the antireflection wavelength of each antireflection DLC/Si system.

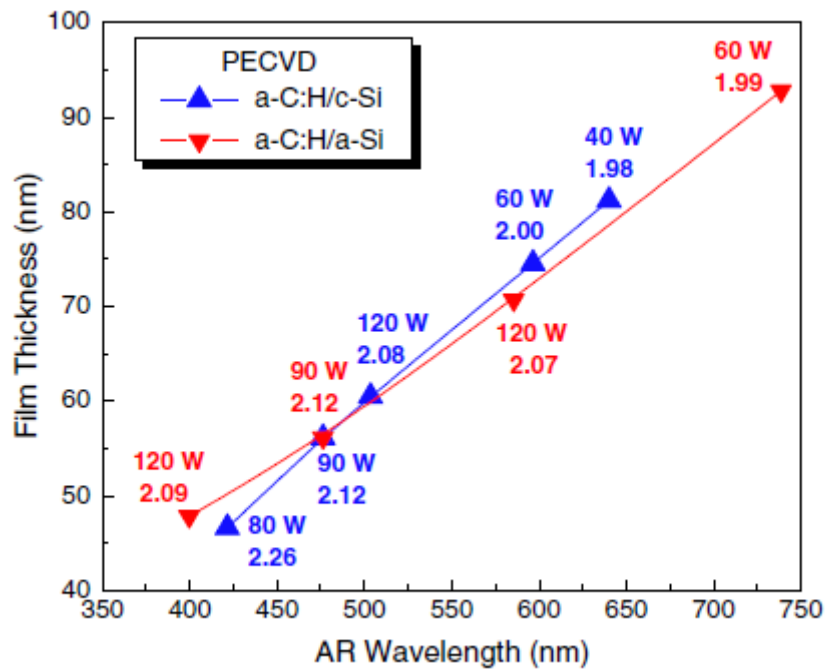


Figure 4.10: The variations of the optical reflectance dip starting from the healthy state of an a-C:H/Si AR device when exposed to (i) plasma and the device acting as radiation indicator (disks), and (ii) oleic acid vapors and the device acting as contamination sensor (triangles) [44]

The deviation the two lines, corresponding to different types of substrates of the same element, but slightly with different refractive index, demonstrates the sensitivity of the antireflection conditions.

All measured reflectivity dips were lower than 5×10^{-2} . Note the possibility of manufacturing a very wide range of antireflection coatings covering the whole visible light spectrum. This is very important because antireflection coatings found implementation in many applications. One research and industrial field that antireflection coatings are widely used is the photovoltaic cells to reduce the amount of the sunlight lost that is reflected by the semiconductor that is usually polished Silicon. Antireflection coatings are also used as optical elements or filters to many optical components in a very wide application fields that is needed the diminishing several and unneeded reflections; laser optical components, microscope optical parts, mirrors and monochromators. Also antireflection coatings usually used to increase the transmittance of a transparent medium by means that they can be used as filters of selected wavelengths. Another use

of antireflection coatings emerges by the high sensitivity of the antireflection conditions. A small deviation of the relative indices or the coating thickness of the antireflection composite, results antireflection conditions for different wavelengths. So, exploiting the sensitivity of the antireflection conditions is able the construction of optical interferometric sensors [7], ophthalmic lenses [46] and antireflection coatings for solar cells [47].

4.5 Photosensitivity and optical performance of hydrogenated amorphous carbon films by picosecond laser

The optical and the structural properties of a-C:H films can be modified by post growth laser radiation. The main advantage in laser radiation processing is the radiation by high energy photons/fluence restricted in a small spot.

In this section we study the photosensitivity and the optical performance a-C:H films by picosecond (ps) laser radiation.

During radiation of a solid by laser beam mainly two phenomena may occur. Firstly, during the pulse duration the ions of the solid are ionized. The free electrons then accelerate depending on the intensity of the electric field of the laser beam. Assuming that the ions are stable in their positions the solid is in non equilibrium state with strong Coulomb forces to be applied to the solid and therefore ablation might occur. After the pulse duration the solid comes to a steady state by the high kinetic energy of the free electrons that transfer their energy to the ions. Typical relaxation times are 5 to 10 ps [39].

Depending on the irradiation conditions/parameters of a-C:H films three possible phenomena can occur; 1) graphitization, 2) layering and terrace construction (spallation) and 3) crater by ablation, figure 4.11. Spallation and ablation result in the reduction of the film volume, while graphitization increases the volume because of the density reduction of the film.

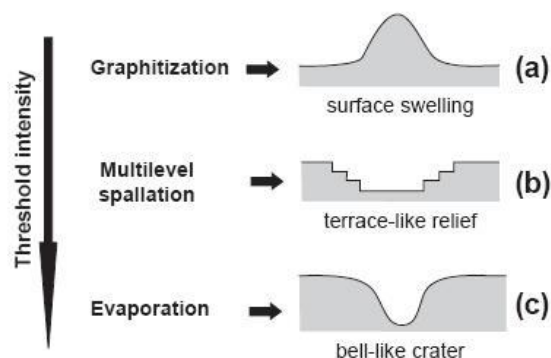


Figure 4.11: Possible surface morphology modifications of irradiated a-C:H films[48]

For the study of the physical mechanisms of the system a-C:H/substrate that take place by laser radiation two laser wavelengths were used; 1064 nm and 266 nm. Laser of 1064 nm (1.17eV) and 266 nm (4.66 eV) laser beams are constituted by photons with energy well below and above the band gap of a-C:H films, respectively.

For irradiation a solid state laser with Nd:YAG (Neodymium:Yttrium Aluminium Garnet) crystal laser was used, which produces the first harmonic laser beam at 1064 nm and the fourth harmonic at 266 nm wavelength, i.e. with photon energy below and above the band gap, E_g , of DLC, respectively.

4.5.1 Characteristics of the as-grown a-C:H films

Prior to the evaluation of the photosensitivity of a-C:H films, it is essential to know accurately the structural features and the optical properties of the as-grown films. The as-grown a-C:H films were purely amorphous and did not exhibit any crystal features in x-ray and electron diffraction experiments. The sp^3 content of the films was determined by AES from the spectral broadening of the C_{KVV} peak in the AES derivative spectrum (see arrows in figure 4.12). The emergence of the π valence states, which are associated with the sp^2 -bonded carbon, in the proximity of the Fermi level, shifts the σ states far below the Fermi level [10,49,50] resulting in a broader valence band in the sp^2 -bonded carbon compared to sp^3 -bonded carbon. Taking into account that the broadening of the observed C_{KVV} AES peak comes exclusively from the spectral width of the valence band (assuming that the 1s states of the K shell are atomic-like and their spectral width is negligible), the value of the

broadening are a good measure of the sp^2/sp^3 content in the studied films as expressed in the formula [50,51,52,53]:

$$sp^2 = 100\% \cdot \left(1 - \frac{\Delta E_G - \Delta E_{a-C:H}}{\Delta E_G - \Delta E_D} \right),$$

$$sp^3 = 100\% - sp^2$$

where ΔE_G , ΔE_D and $\Delta E_{a-C:H}$ are the broadenings of the C_{KVV} AES line of Graphite, Diamond and a-C:H films, respectively. The derivative of the AES spectra around the C_{KVV} peak of the four studied a-C:H film samples (S1–S4) are presented in figure 4.12a, and the determined sp^3 content values are shown in Table 4.1. The AES results regarding the sp^3 -content in the films can be well correlated with the EELS findings regarding the films' density. Valence EELS spectra of the loss function $\text{Im}(-1/\varepsilon)$ of the studied films are presented in figure 4.12b.

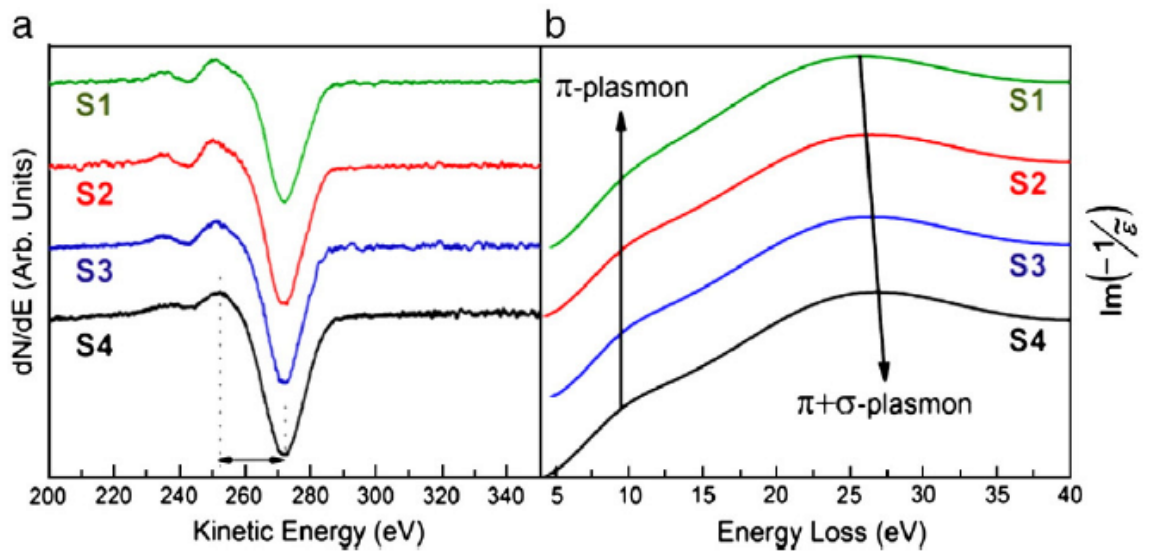


Figure 4.12 (a) Derivative AES spectra around the C_{KVV} peak; the broadening indicated by the arrow is used to determine the sp^3 content. (b) Valence EELS spectra of the as-grown a-C:H films; the spectral position of the $\pi+\sigma$ plasmon is used to determine the films' density

The spectra are characterized by two peaks assigned to a plasmon due to the delocalized π electrons of sp^2 -bonded carbon [17,41] at around 8 eV and the collective $\pi+\sigma$ plasmon at 25–27 eV due to both the delocalized π electrons and the localized σ

electrons. The square of the $\pi+\sigma$ plasmon energy $E_{\pi+\sigma}$ is proportional to the a-C:H films density [17,41,43]. The density values of the as grown a-C:H films of this study have been determined from the spectral position of the $E_{\pi+\sigma}$, following the procedures of Ref. [41], and are summarized in Table 4.1.

Table 4.1: Main characteristics of the studied as grown a-C:H films

Sample	Deposition time (min)	Thickness (nm)	sp ³ (at.%)	$E_{\pi+\sigma}$ (eV)	Density (g/cm ³)
S1	30	85	20	25.9	1.68
S2	60	170	23	26.1	1.72
S3	90	273	33	26.5	1.77
S4	120	333	44	26.9	1.82

The value of the effective mass of valence electrons m^* is required for the determination of the mass density of a-C:H films [43]. The EELS data of this study have been validated by XRR [44] and m^* has been determined to be $0.7 m_e$, where m_e is the free electron mass. This m^* value is consistent with the analysis in Ref. [43].

The microscopic density of hydrogenated amorphous carbons (which does not take into account macroscopic morphological features such as pinholes and voids) can vary due to transformation of sp^2 C—C bonds to sp^3 C—C bonds, as well as because of the variation of the sp^3 C—C and C—H bonds. The sp^2 C—C and sp^3 C—H bonds reduce the density of the films [8,43]. The variation of the $\pi+\sigma$ plasmon energy and the microscopic mass density with the sp^3 content of the as-grown a-C:H films of this study are presented in figure 4.13.

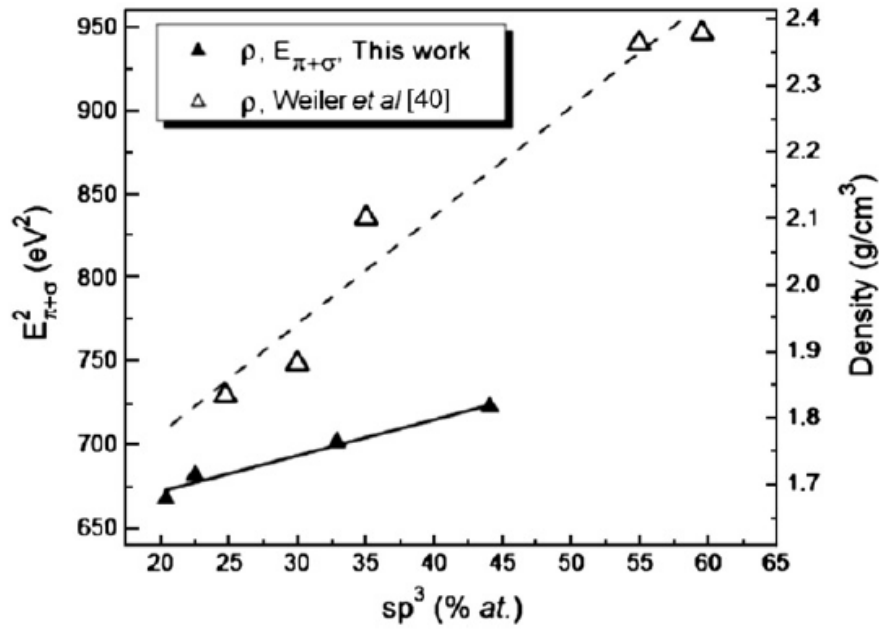


Figure 4.13: The variation of the films' density and of the spectral position of the $\pi+\sigma$ plasmon with the sp^3 content for the as grown films. The axes are scaled in order the solid symbols to correspond to both, while open symbols correspond only to density values (right axis)

There is an almost linear relation of increasing density with sp^3 content, indicating that a significant part of the sp^3 bonds are C—C. However, the slope of the line is less steep compared to the data of Weiler et al. [54] indicating that a significant fraction of sp^3 C—H bonds is also present and their contribution is increasing for higher sp^3 contents. This is in agreement with the work of Angus and Jansen [55], who proposed a correlation of sp^3 bonds with the H-content for topological reasons. Following the analysis proposed by Angus et al., we determine that the hydrogen content of the a-C:H films of this study ranges within 32–42 at.% (2.7–3.5 wt.%). This has been confirmed by Raman spectra, which has shown the typical D and G bands [11], the G band was located at 1510 cm^{-1} and the intensity ratio of the D and G bands (I_D/I_G) was 0.3. These values are consistent with a-C:H films of 35 at.% H [11]. After having characterized the as grown a-C:H films in terms of their density and sp^3 and H contents, we considered their optical properties, which are the main concern of this work. The optical properties of a-C:H films were tested using ORS. The analysis of the optical properties of amorphous carbon is simple and straightforward due to its simple band structure, which comprises the π and σ valence states and the π^* , σ^* unoccupied, anti-bonding states [8,9,10].

Thus, the complex dielectric function of the as grown a-C:H films has been analyzed using the Lorentz model to describe the π - π^* interband transition [9,45]:

$$R = \left| \frac{\tilde{n}_{a-C:H}(\tilde{n}_{Si} - 1)\cos k_o t - i(\tilde{n}_{a-C:H}^2 - \tilde{n}_{Si})\sin k_o t}{\tilde{n}_{a-C:H}(\tilde{n}_{Si} + 1)\cos k_o t - i(\tilde{n}_{a-C:H}^2 + \tilde{n}_{Si})\sin k_o t} \right|^2, \quad (3)$$

For the fitting a multi-algorithm minimization process, based on MERLIN 3.1.1 software [56], has been used. In this work, we use the Lorentz model instead of the Tauc-Lorentz model (TL) [57], although it is less accurate, because the expressions for ε_1 and reflectivity for TL are strongly non-linear and complicated making the divergence of the fit highly unstable (note: for ellipsometry measurements, where the ε_1 and ε_2 are directly measured, the TL model would be more appropriate and accurate).

Figure 4.14 shows a typical ORS spectrum of an a-C:H/Si sample. The points are the reflectance experimental data in the range between 1.5 and 5.25 eV, while the solid line stands for the best fit with Eqs. (2) and (3).

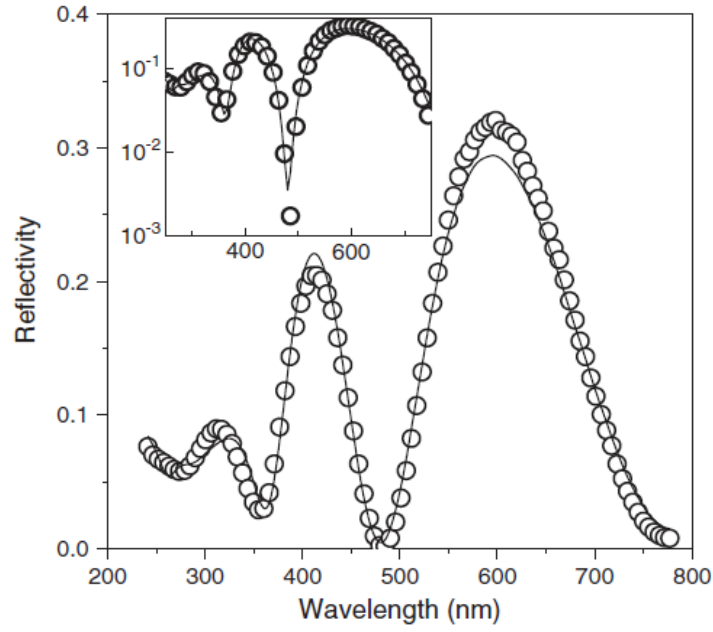


Figure 4.14: Experimental points of optical reflectivity and the fit line using Eqs. (2) and (3) for a representative a-C:H film. The reflectivity in log scale is also shown in the inset

The very good description of the experimental data using only one Lorentz oscillators, instead of two as in reference 58 is due to the excellent transparency of the used a-C:H films, as well as the narrower spectral range used in this study compared to the experimental data of reference 58. The σ - σ^* transitions has a significant contribution beyond 5.5 eVs ($\lambda < 225$ nm) [10]. The spectral position of the Lorentz oscillator, which corresponds to the π - π^* interband transition, for the four as grown samples has been found to be in the range 3.8-4.1 eV; these values are consistent with the sp^3 content of the films measured by AES, according to the relative relation presented in reference 2. This agreement is used for validating the optical analysis using equation (2). It shows that although the Lorentz model is less accurate than the Tauc-Lorentz model close to the absorption edge and underestimates the E_{04} gap (E_{04} is the photon energy value for which $\alpha = 10^4 \text{ cm}^{-1}$, where $\alpha = 4\pi k/\lambda$ is the absorption coefficient), it is capable for determining accurately the spectral position of the maximum optical absorption due to π - π^* electronic transition.

Figure 4.15 shows the calculated complex dielectric function ($\tilde{\epsilon}_{a-C:H}(\omega) = \epsilon_1 + i\epsilon_2$) and complex refractive index ($\tilde{n}_{a-C:H} = n + ik$) spectra, as well as reflectivity spectra of a

hypothetical, semi-infinite a-C:H material with the same optical properties of the corresponding thin film, i.e. excluding the contribution of the substrate, based on best-fit parameters for a representative a-C:H film.

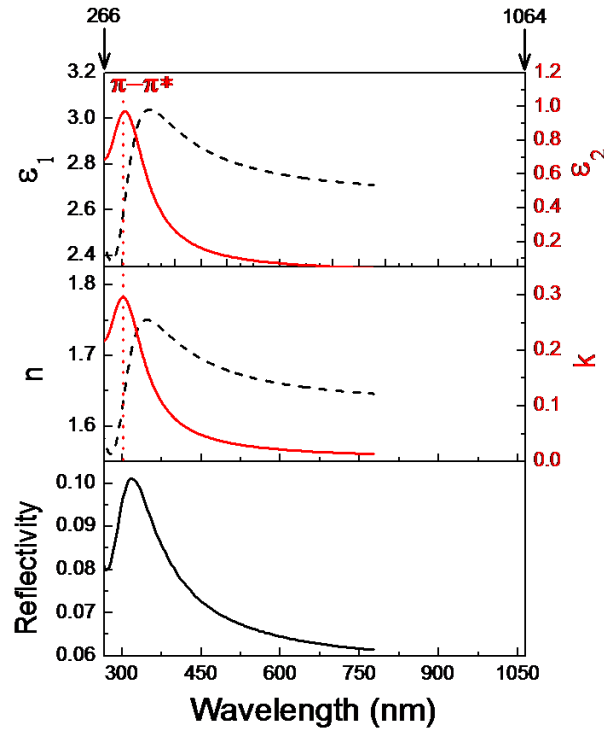


Figure 4.15: The complex dielectric function [$\tilde{\epsilon}_{a-C:H}(\omega) = \epsilon_1 + i\epsilon_2$], the complex refractive index ($\tilde{n}_{a-C:H} = n + ik$) and the reflectivity of a representative a-C:H film after exclusion of the Si substrate contribution. The arrows indicate the laser wavelengths used for the post-growth processing (black and red lines correspond to left and right axes, respectively)

Apparently the optical absorption is significant for photon wavelengths below 550 nm due to the π - π^* electronic transitions. This is more clearly demonstrated if we take into account the value of the E_{04} gap, which was found to be 2.25eV (corresponding to $\lambda=552$ nm); this value is in fair agreement with the H content and the Raman parameters according to the relationships established in reference 59.

4.5.2 Photosensitivity of a-C:H films

Since a Nd:YAG laser is available for our photosensitivity study, we selected to investigate the effect of exposure to the fundamental wavelength of the laser (1064 nm,

1.17 eV) and the fourth harmonic (266 nm, 4.66 eV), which are indicated by arrows in figure 4.15. Samples of 25mm² area were irradiated with the same spot size of laser beam in order to have the possibility of macroscopic ORS measurements, figure 4.16.

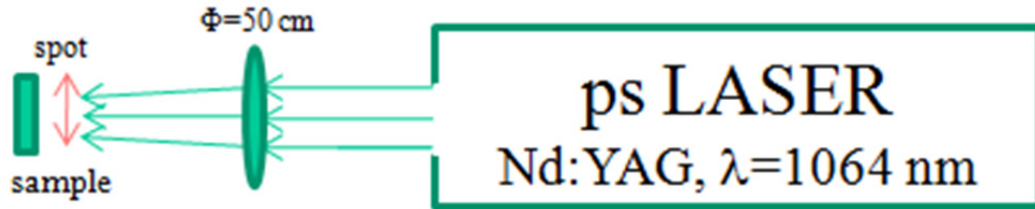


Figure 4.16: Experimental setup used for laser irradiation processing

The energy corresponding to the fundamental wavelength is well below the E_{04} gap and that of the fourth harmonic is above the E_{04} gap and the π - π^* transition. Therefore, completely different light-matter interactions are expected in these two cases.

Figure 4.17 shows the evolution of the optical reflectivity spectra of three a-C:H films (S1, S2, S4) after exposure to several pulses of the 1064 nm fundamental line of the Nd:YAG laser.

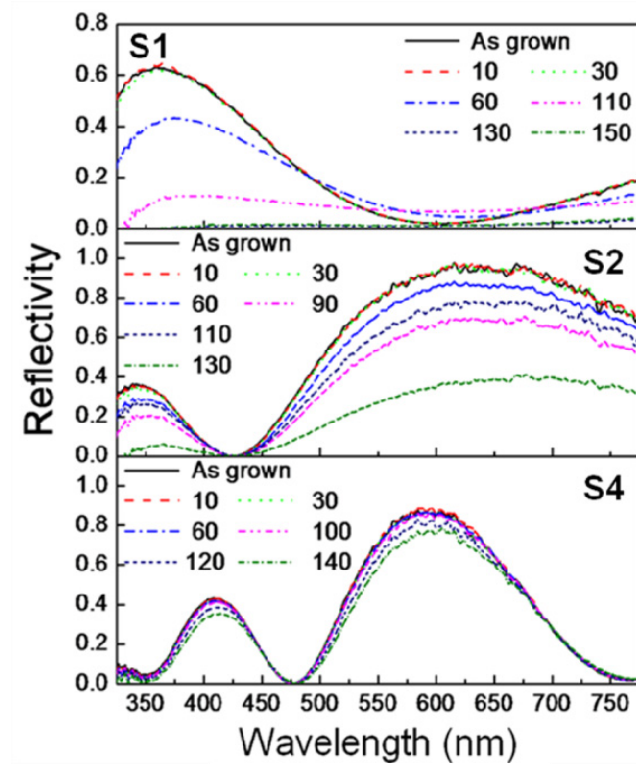


Figure 4.17: ORS spectra of the a-C:H films (S1, S2, S4) exposed to the laser beam of $\lambda=1064$ nm; the number of laser pulses used for each case are indicated

The Arabic numerals in the corresponding legends indicate the number of successive laser pulses. It is apparent that the thinner a-C:H films (S1, S2) exhibit more significant changes in their optical reflectivity spectra. This implies a possible structural change at the film's surface or the film/substrate interface. The possible origin of an interfacial layer is the formation of SiC, as we will show in more detail below, which has been observed in sputtered amorphous films [60] and predicted by Monte-Carlo atomistic simulations of carbon growth on Si [61]. In order to get insights about these changes we employed several different optical models, which are summarized in figure 4.18.

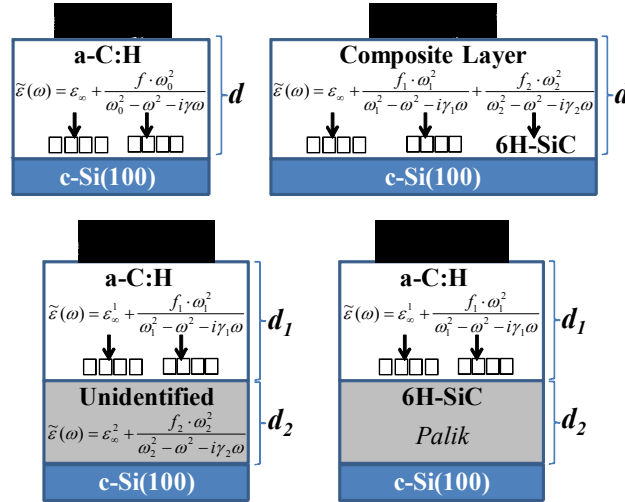


Figure 4.18: Schematic representations of the four optical models, which have been used for the analysis of the ORS spectra and the investigation of the possible structural changes due to laser radiation of a-C:H

In particular the used optical models are:

I. The single Lorentz oscillator [equation (2)], in which the value of ε_∞ describes the σ - σ^* and the oscillator itself the π - π^* transition, in combination with a three-phase (single layer) representation [equation (3)], i.e. the same model used for the as-grown a-C:H samples.

II. The double Lorentz oscillator model:

$$\tilde{\varepsilon}_{a-C:H}(\omega) = \varepsilon_\infty + \frac{f_1 \cdot \omega_{01}^2}{\omega_{01}^2 - \omega^2 - i\gamma_1\omega} + \frac{f_2 \cdot \omega_{02}^2}{\omega_{02}^2 - \omega^2 - i\gamma_2\omega}, \quad (4)$$

in which the last term may describe optical contributions other than the π - π^* transitions of a-C:H, in combination with a three-phase (single layer) representation [equation (3)]. For all spectra acquired from the laser-radiated samples (S1, S2, S4) the second Lorentz oscillator converges to the spectral position 6.8 eVs, which is characteristic of the 6H-SiC [23]. This later finding confirms that SiC may be indeed formed at the a-C:H/Si interface. This is well explained, if we take into account that the fundamental gap of Si E_g^{Si} (1.11 eV) is less than the energy of the used laser photons (1.165 eV, $\lambda=1064$ nm). Therefore, the laser photons can pass through a-C:H and then be

strongly absorbed by Si inducing local annealing [62,63], which is capable for inducing interdiffusion through the a-C:H/Si interface.

III. As there is strong evidence that exposure of a-C:H to laser radiation results in an inhomogeneous material due to possible selective changes close to either the surface or the interface, a model of two successive layers of different optical properties on top of Si has been also considered. Again, in this case the Lorentz oscillator used for the bottom layer (close to the interface) converged to the spectral position of 6.8 eVs, indicating the formation of SiC.

IV. Given that there is strong evidence from the fit results of models II and III that SiC is formed, we considered for the fourth model two successive layers; the bottom layer has been fixed as 6H-SiC, using the reference dielectric functions of SiC from Palik [64], but with varying thickness, while the top layer was the Lorentz oscillator used for a-C:H in the model I.

Figure 4.19 shows the measured reflectivity spectrum (open circles) of a representative a-C:H/Si sample after radiation with the 1064 nm laser wavelength and the results of the fits using the four mentioned optical models.

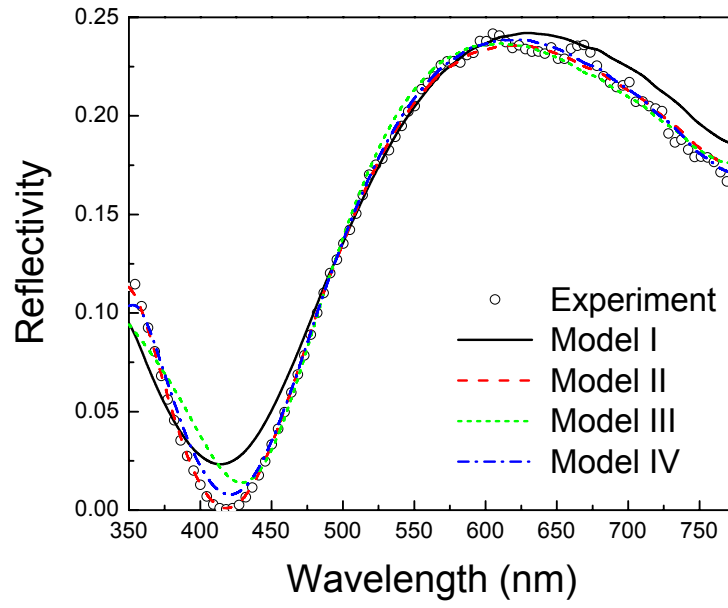


Figure 4.19: ORS data (open circles) from a representative a-C:H/Si sample radiated by the 1064 nm beam of the Nd:YAG laser. The lines represent the results of the fits using the four optical models employed in this work

The parameters and results of the used four optical models, regarding the laser radiated samples, are summarized in table 4.2. Table 4.2 also includes the values of the corresponding mean square error $\Sigma \Delta x^2$ of the various fits, which are used to evaluate the fit quality.

Table 4.2: Summary of the four optical models, which were used for the fitting of the experimental ORS data; $\Sigma\Delta x^2$ is the residual of least square fitting

	Top Layer	Interface Layer	Number of Parameters	$\Sigma\Delta x^2$
Model I	1 Lorentzian $\pi-\pi^*$	-	5	0.0110
Model II	2 Lorentzians 1. $\pi-\pi^*$ 2. 6H-SiC	-	8	0.0011
Model III	1 Lorentzian $\pi-\pi^*$	1 Lorentzian (Free: converging to 6H-SiC)	9	0.0082
Model IV	1 Lorentzian $\pi-\pi^*$	6H-SiC (Palik, Ref. 49)	6	0.0031

It is apparent that models II and IV give the best fit quality; model IV has the additional asset of providing very good results with the use of minimum number of parameters and providing more meaningful physical interpretations. Therefore, for the rest of our work we will present results from model IV fittings.

The evolution of the basic structural and optical features of two representative a-C:H samples of different thickness (S2, S4) after exposure to 1064 nm laser pulses are shown in figure 4.20 (disks and triangles).

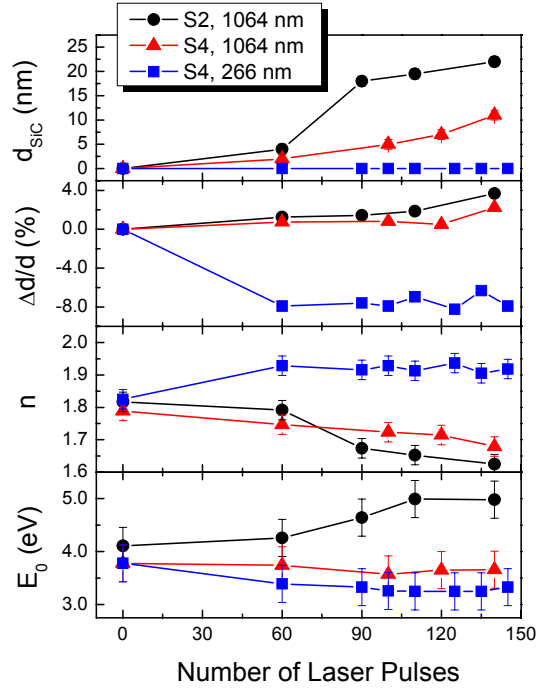


Figure 4.20: The evolution of the main structural (d_{SiC} and $\Delta d/d$) and optical parameters (n , $E_0 = \hbar \omega_0$) of the samples after exposure to 1064 nm and 266 nm laser beams

After 60 pulses the thickness of the SiC layer (d_{SiC}) is steadily increasing with the number of laser pulses. Especially in the case of the thinner sample S2 the SiC formation is more pronounced, most likely because of the lower absorption of the 1064 nm photons from the film (assuming the same E_{04} gap for both films, the thinner film will absorb much less the 1064 nm photons according to Beer-Lambert's law). The increase of the SiC layer might be associated with the effective temperature at the interface, which should increase with increasing the number of laser pulses, due to the absorption of the laser beam by the Si substrate.

Another very interesting feature is that the film thickness does not change significantly, as it is shown by the parameter:

$$\frac{\Delta d}{d} (\%) = \frac{|d_1 - d_{\text{laser}}|}{d_1} \cdot 100\%, \quad (5)$$

where d_1 is the thickness of the as-grown a-C:H film and d_{laser} is the thickness of the same layer (excluding the SiC) after exposure to laser pulses. $\Delta d/d$ is not reducing at all.

Interestingly the refractive index of the a-C:H layer is reducing with the number of laser pulses, while the spectral position E_0 of $\pi-\pi^*$ transition exhibits a strong blueshift for the thinner S2 sample and does not change significantly for the thicker film S4. The refractive index and the E_0 of a-C:H are associated with the film density and the volume fraction of sp^2 C-C bonds, respectively [9]. The observed variations of these parameters indicate that the exposure to laser induced a reduction in both density and volume fraction of sp^2 C-C bonds. Therefore, the remaining of a-C:H after exposure to 1064 nm laser is enriched with sp^3 C-H bonds according to the density- sp^3 -H relations (figure 4.19 and Ref. 35). In order to get insights on the modifications induced by the 1064 nm laser beam we have investigated the sample surfaces by optical microscopy and AFM. Figure 4.21 shows an optical microscopy image at the laser spot of the sample S2 after exposure to 140 pulses of the 1064 nm laser beam.

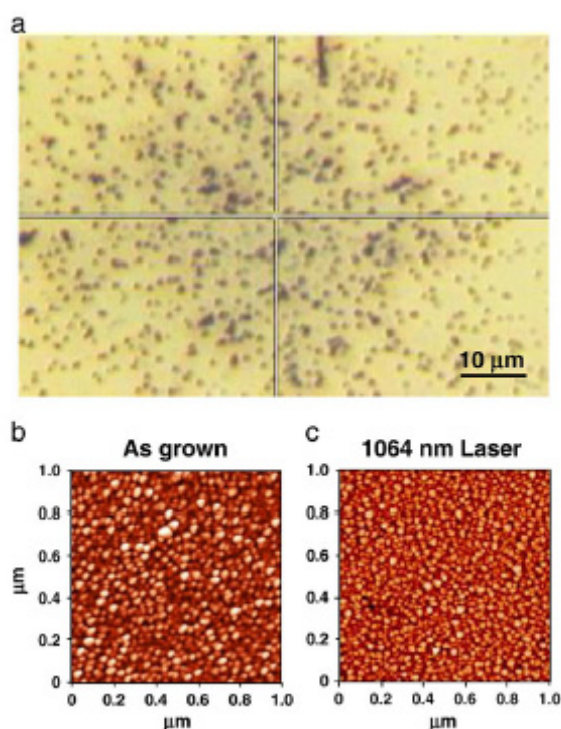


Figure 4.21: (a) An optical microscopy image at the laser spot of the sample S2 after exposure to 140 pulses of the 1064 nm laser beam. AFM phase images of the sample S2 (b) as grown, and (c) after exposure to 140 pulses of the 1064 nm laser beam

The exposure to the laser beam resulted to the formation of pinholes (1-3 μm wide), which explains the decrease of density. Possibly the pinholes are formed in sp^2 -rich

domains, which are more optically absorbing, explaining also the observed reduction of sp^2 C-C bonds. AFM phase images of the as grown sample S2 and after exposure to 140 pulses of the 1064 nm laser beam (in the clear space between the pinholes) are also shown in figures 4.21b and 4.21c, respectively. The root mean square surface roughness for both cases is 1.0 nm (determined over an area of $1 \times 1 \mu m^2$). Therefore, no significant nanoscopic changes on the surface morphology or patterning have taken place away from the pinholes.

A completely different picture has been observed when the thick sample S4 has been exposed to the 266 nm laser beam. Figure 4.22 shows the evolution of the optical reflectivity spectra for the a-C:H/Si sample S4 after exposure to several pulses of the 266 nm 4^{th} harmonic of the Nd:YAG laser.

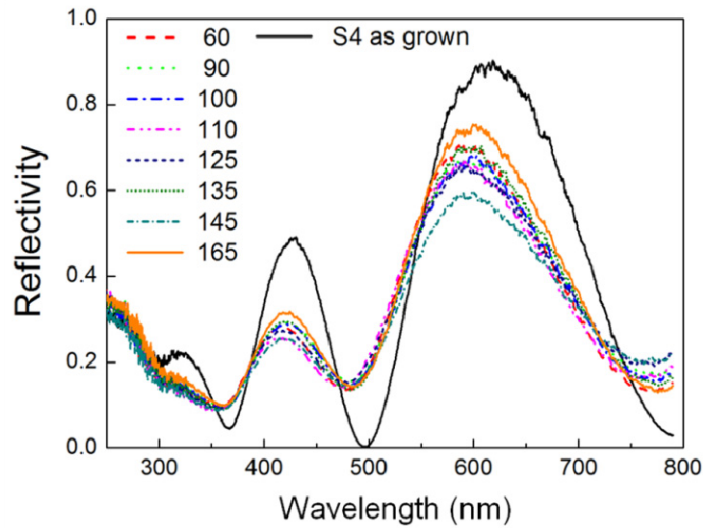


Figure 4.22: ORS spectra of the thick a-C:H sample S4 exposed to the laser beam of $\lambda=266$ nm; the number of laser pulses used for each case are indicated

The Arabic numerals in the corresponding legend indicate the number of successive laser pulses. In this case the ORS spectra could be fitted with model I and converge to very small $\Sigma \Delta x^2$ values. Therefore, the possible structural changes occur in the volume of the film and they are rather homogeneous. This is because the laser beam is absorbed by the film itself, not reaching the Si substrate, thus the laser annealing occurs in the a-C:H layer itself. Fittings with model IV converged to SiC thickness values close to zero,

confirming the different nature of structural transitions in a-C:H when the 266 nm beam was used.

The evolution of the basic structural and optical features of this a-C:H sample after exposure to 266 nm laser pulses are shown in figure 4.20 (squares). We observe that limited ablation occurs ($\Delta d/d \sim -8\%$, i.e. 8% thickness reduction). Concurrently, the refractive index of a-C:H layer is increasing with the number of laser pulses, while the spectral position E_0 of $\pi-\pi^*$ transition exhibits a strong redshift. According to the density- sp^3 -H relations (figure 4.13 and reference 65) these variations indicate that the exposure to 266 nm laser induced a significant increase of the sp^2 C-C bonds at expense of the sp^3 C-H (H reduction). Such a structural transformation has been observed in a-C:H films after thermal annealing above 600 °C [23,66], indicating that the effective macroscopic temperature in our a-C:H films, during exposure to the 266 nm laser, exceeds this threshold.

AFM images revealed that the exposure to the 266 nm laser did not induce formation of pinholes; instead some roughening and surface mounds (of the order of 15 nm high) have been observed, as shown in figure 4.23.

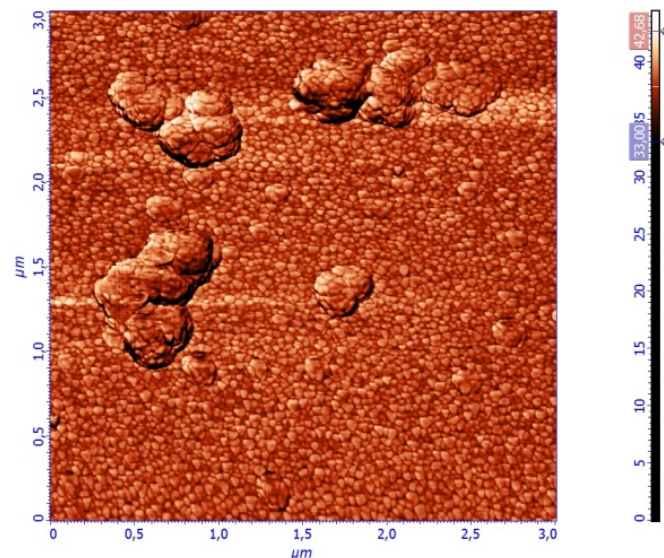


Figure 4.23: AFM phase image of the sample S4 after exposure to 60 pulses of the 266 nm laser beam

Comparing the values of the refractive indices of a-C:H after exposure to either 1064 nm or 266 nm laser beams, a range of $\sim 20\%$ ($n=1.60-1.95$) was established for various optical applications. This is very important if we consider that these local laser-induced variations can be applied with spatial resolution below one μm .

The presented processes, which take place after exposure to laser light, either 1064 nm or 266 nm, have been suggested mainly by the ORS data analyses. In order to validate these indirect results we performed AES and EELS measurements to the samples after their exposure to laser light. AES and EELS provide straightforward information about the sp^3 content and the density of the a-C:H films close to surface. Indeed, the structural changes revealed by ORS analyses are confirmed by the combined AES-EELS results, figure 4.24.

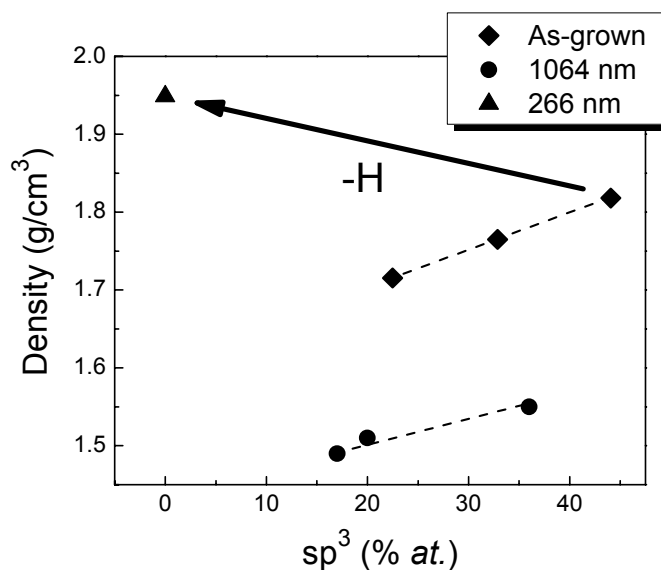


Figure 4.24: The density (determined by EELS) and the sp^3 content (determined by AES) for the as-grown samples (solid diamonds) and laser-radiated samples with the 1064 nm line (solid disks) and 266 nm line (solid triangle). The arrows indicate the variations due to laser radiation, which are attributed to variations of the H-content, as well

For the case of the 266 nm laser exposure, AES and EELS do confirm the increase of sp^2 content and a-C:H film's density. According to the AES-EELS data the sample S4 after exposure to 266 nm laser beam was graphitized and the hydrogen has been desorbed. This is confirmed by the Raman data, since the I_D/I_G increases from 0.3 (as-grown sample) to 0.61, which is an indication of H desorption (from about 35% H to about 20% H) [11]. On the other hand, the density value is consistent with purely hydrogen-free, exclusively sp^2 bonded a-C [43,67]. This difference would be explained, if we took into account that both AES and EELS are measuring only the surface, while Raman is probing the whole film. Therefore, it seems that the dehydrogenation is more pronounced on the surface.

AES-EELS confirm the increase of sp^3 bonds (especially for the thin sample S2) as well as the reduction of density of a-C:H after exposure to the 1064 nm laser beam. This enrichment of the a-C:H film with sp^3 and H (also indicated by Raman, which shows further reduction of $I_D/I_G=0.22$ for the sample S2 after exposure to 140 pulses of 1064 nm) and the reduction of density are possibly due to the selective ablation of sp^2 -rich domains and the formation of pinholes.

4.6 Conclusions

In this chapter the research was based on the study of the properties of single element composed amorphous films for featured and distinct applications. Hydrogenated amorphous carbon films (a-C:H) was chosen to be studied due to its properties that can be developed originated by the capability of carbon element to exist in phases diamond, graphite and diamond-like structures. Growth was performed by PECVD as an industrial scale deposition method.

For the needs of this study a PECVD reactor was installed and parameterization of the grown a-C:H was performed. The grown a-C:H films were utilized in two ways; the exploitation of a-C:H with specific optical properties and the post growth treatment and change of their optical and structural properties by laser irradiation.

So in the first part of the chapter we presented an antireflection coating of a DLC/Si system. Variety of antireflective coatings were grown covering the whole visible light spectrum with negligible reflectivity. Additionally, antireflection coating systems of DLC/Si takes the advantage of the mechanical and anticorrosion properties of the DLC film. Thus DLC can be used as a hard, antiscratch, anticorrosion, biocompatible and environment friendly antireflection coating.

In the second part of this chapter that is focused on the light-matter interaction of the irradiated a-C:H films we show that picosecond laser pulses interact strongly with a-C:H/Si samples changing their structural features and optical properties. The possible local variation of the refractive index in the range 1.60-1.95 (20% variation) by laser processing opens new perspectives for applications in photonics. It came out that the exact processes that occur in a-C:H/Si after exposure to laser light are strongly dependent on the laser wavelength.

In the case of the 1064 nm laser beam, the photon energy of the laser beam is well below the E_{04} gap of a-C:H film but above the fundamental gap of Si E_g^{Si} (1.11 eV). Therefore, the laser photons can pass through a-C:H and then it can be strongly absorbed by Si inducing local annealing, which induces the formation of SiC at the a-C:H/Si interface

and formation of pinholes, as well. In addition, after exposure to the laser beam the a-C:H film is found to be enriched with sp^3 C-H bonds.

In the case of the 266 nm laser beam, the photon energy is above the E_{04} gap of a-C:H as well as above the spectral energy of the $\pi-\pi^*$ interband transition. This results to a massive optical absorption in the volume of the a-C:H and laser annealing of the a-C:H itself. Thus, after exposure to 266 nm laser beam a-C:H is graphitized and the hydrogen is partly outdiffused.

4.7 References

- [1] H.U. Kim, S.H. Jeong, H.J. Kim, J.H. Kim, Key Eng. Mater. **345-346 II**, 1577 (2007)
- [2] W. Hezhao, L. Dongmiao, L. Lei, Vacuum **42**, 1083 (1991)
- [3] C.H.P. Poa, S.R.P. Silva, R.G. Lacerda, G.A.J. Amaratunga, W.I. Milne, F.C. Marques, Appl. Phys. Let. **86** 232102(2005)
- [4] A. Erdemir, C. Donnet, J. Phys. D **39**, R01 (2006)
- [5] H.-G. Kim, S.-H. Ahn, J.-G. Kim, S.J. Park, K.-R. Lee, Diam. Relat. Mater. **14**, 35 (2005)
- [6] F.R. Marciano, L.F. Bonetti, N.S. Da-Silva, E.J. Corat, V.J. Trava-Airoldi, Appl. Surf. Sci. **255**, 8377 (2009)
- [7] N.T. Panagiotopoulos, P. Patsalas, C. Prouskas, G.P. Dimitrakopoulos, P. Komninou, T. Karakostas, A.P. Tighe, E. Lidorikis, ACS Appl. Mater. Inter. **2**, 3052 (2010)
- [8] J. Robertson, Mater. Sci. Eng. R **37**, 129 (2002)
- [9] S. Kassavetis, P. Patsalas, S. Logothetidis, J. Robertson, S. Kennou, Diam. Relat. Mater. **16**, 1813 (2007)
- [10] C. Mathioudakis, G. Kopidakis, P. Patsalas, P.C. Kelires, Diam. Relat. Mater. **16**, 1788 (2007)
- [11] C. Casiraghi, A.C. Ferrari, J. Robertson, Phys. Rev. B72, 085401 (2005)
- [12] T. Katsuno, C. Godet, J.C. Orlianges, A.S. Loir, F. Garrelie, A. Catherinot, Appl. Phys. **A81**, 471 (2005)
- [13] D. Franta, V. Buršíková, D. Nečasa, L. Zajíčková, Diam. Relat. Mater. **17**, 705 (2008)
- [14] S. Logothetidis, Diam. Relat. Mater. **12**, 141 (2003)
- [15] M.L. Theye, V. Paret, A. Sadki, Diam. Relat. Mater. **10**, 182 (2001)
- [16] A. Cannilas, M.C. Pollo, J.L. Andújar, J. Sancho, S. Bosch, J. Robertson, W.I. Milne, Diam. Relat. Mater. **10**, 1132 (2001)
- [17] S. Waidmann, M. Knupfer, J. Fink, B. Kleinsorge, J. Robertson, J. Appl. Phys. **89**, 3783 (2001)
- [18] G. Fanchini, A. Tagliaferro, D.P. Dowling, K. Donnely, M.I. McConnell, R. Flood, G. Lang, Phys. Rev. **B61**, 5002 (2000)
- [19] G.E. Jellison, V.I. Merkulov, A.A. Puretzky, D.B. Geoneghan, G. Eres, D.H. Lowndes, J.B. Caughman, Thin Solid Films **68**, 377 (2000)

- [20] T. Heitz, C. Godet, J.E. Bouree, B. Drevillon, J.P. Conde, Phys. Rev. B **60**, 6045 (1999)
- [21] T. Schwarz-Sellinger, A. von Keudell, W. Jacob, J. Appl. Phys. **86**, 3968 (1999)
- [22] J. Lee, R.W. Collins, V.S. Veerasamy, J. Robertson, Diam. Relat. Mater. **7**, 999 (1998)
- [23] S. Logothetidis, J. Petalas, S. Ves, J. Appl. Phys. **79**, 1040 (1996)
- [24] F. Demichelis, C.F. Pirri, A. Tagliaferro, Phys. Rev. B **45**, 14364 (1992)
- [25] G.A. Cirino, R.D. Mansano, P. Verdonck, R.G. Jasinevicius, L.G. Neto, Surf. Coat. Technol., *in press* (2010)
- [26] M. Shimizu, Y. Shimotsuma, M. Sakakura, T. Yuasa, H. Homma, Y. Minowa, K. Tanaka, K. Miura, K. Hirao, Optics Express **17**, 46 (2009)
- [27] Y. Lin, A. Harb, D. Rodriguez, K. Lozano, D. Xu, K.P. Chen, J. Appl. Phys. **104**, 113111 (2008)
- [28] O.S. Heavens, Optical Properties of Solid Thin Films, Dover, New York, p.55 (1955)
- [29] J.D. Carey, S.J. Henley, Diam. Relat. Mater. **16**, 1782 (2007)
- [30] Y. Lin, A. Harb, D. Rodriguez, K. Lozano, D. Xu, K.P. Chen, J. Appl. Phys. **104**, 113111 (2008)
- [31] P. Olivero, S. Calusi, L. Giuntini, S. Lagomarsino, A. Lo Giudice, M. Massi, S. Sciortino, M. Vannoni, E. Vittone, Diam. Relat. Mater. **19**, 428 (2010)
- [32] J. Preclíková, A. Kromka, B. Rezek, P. Malý, Optics Letters **35**, 577 (2010)
- [33] M. Neff, T.V. Kononenko, S.M. Pimenov, V. Romano, W. Lüthy, V.I. Konov, Appl. Phys. A**97**, 543 (2009)
- [34] T. Okuchi, H. Ohfuji, S. Odake, H. Kagi, S. Nagatomo, M. Sugata, H. Sumiya, Appl. Phys. A**96**, 833 (2009)
- [35] J. Kanasaki, E. Inami, K. Tanimura, H. Ohnishi, K. Nasu, Phys. Rev. Lett. **102**, 087402 (2009)
- [36] E. Cappelli, C. Scilletta, S. Orlando, V. Valentini, M. Servidori, Appl. Surf. Sci. **255**, 5620 (2009)
- [37] T.V. Kononenko, M. Meier, M.S. Komlenok, S.M. Pimenov, V. Romano, V.P. Pashinin, V.I. Konov, Appl. Phys. A **90**, 645 (2008)
- [38] V.S. Pavelyev, S.A. Borodin, N.L. Kazanskiy, G.F. Kostyuk, A.V. Volkov, Optics Laser Technol. **39**, 1234 (2007)

- [39] G. Dumitru, V. Romano, H.P. Weber, S. Pimenov, T. Kononenko, M. Sentis, J. Hermann, S. Bruneau, *Appl. Surf. Sci.* **222**, 226 (2004)
- [40] D. Vouagner, Cs. Beleznai, J.P. Girardeau-Montaut, C. Templier, H. Gonnord, *Appl. Surf. Sci.* **201**, 154 (2000)
- [41] Y. Lifshitz, S.R. Kasi, J.W. Rabalais, *Phys. Rev. Lett.* **62**, 1290 (1989)
- [42] J. Robertson, *Diam. Relat. Mater.* **2**, 984 (1993)
- [43] A.C. Ferrari, A. Libassi, B. K. Tanner, V. Stolojan, J. Yuan, L. M. Brown, S.E. Rodil, B. Kleinsorge and J. Robertson, *Phys. Rev.B* **62**,16 (2000)
- [44] P. Patsalas, *Thin Solid Films* **519**, 3990 (2011)
- [45] Wooten, F. *Optical Properties of Solids*; Academic Press: New York, 1972
- [46] M. Gioti, S. Logothetidis, C. Charitidis, Y. Panayiotatos, I. Varsano, *Sensors and Actuators A* **99**, 35 (2002)
- [47] W.S. Choi, K. Kim, J. Yi, B. Hong, *Mater. Let.* **62**, 577 (2008)
- [48] T.V. Kononenko, V.V. Kononenko, S.M. Pimenov, E.V. Zavedeev, V.I. Konov, V. Romano, G. Dumitru, *Diam. Relat. Mater.* **14**, 1368 (2005)
- [49] C.W. Chen, J. Robertson, *J. Non-Cryst. Solids* **602**, 227 (1998)
- [50] A. Fuchs, J. Scherer, K. Jung, H. Ehrhardt, *Thin Solid Films* **232**, 51 (1993)
- [51] L. Calliari, *Diam. Relat. Mater.* **14**, 1232 (2005)
- [52] P. Patsalas, M. Handrea, S. Logothetidis, M. Gioti, S. Kennou, W. Kautek, *Diam. Relat. Mater.* **10**, 960 (2001)
- [53] C. Laschovich, S. Scaglione, *Appl. Surf. Sci.* **78**, 17 (1994)
- [54] M. Weiler, S. Sattel, T. Giessen, K. Jung, H. Ehrhardt, V.S. Veerasamy, J. Robertson, *Phys. Rev. B* **53**, 1594 (1996)
- [55] J.C. Angus, F. Jansen. *J. Vac. Sci. Technol. A* **3**, 6 (1988)
- [56] D.G. Papageorgiou, I.N. Demetropoulos, I.E. Lagaris, *Comp. Phys. Commun.* **159**, 70 (2004)
- [57] G.E. Jellison, F.A. Modine, *Appl. Phys. Lett.* **69**, 371 (1996)
- [58] C. Morgan, *Nature* **324**, 293 (1986)
- [59] S.I. Bozhevolnyi, V.S. Volkov, E. Devaux, J.-Y. Laluet, T.W. Ebbesen, *Nature* **440**, 508 (2006)

- [60] N.A. Hastas, C.A. Dimitriadis, P. Patsalas, Y. Panayiotatos, D.H. Tassis, S. Logothetidis, J. Appl. Phys. **89**, 5 (2001)
- [61] P. Patsalas, S. Logothetidis, P.C. Kelires, Diam. Relat. Mater. **14**, 1241 (2005)
- [62] H. Watanabe, H. Miki, S. Sugai, K. Kawasaki, T. Kioka, Jpn. J. Appl. Phys. **33**, 4491 (1994)
- [63] S.-D. Kim, C.-M. Park, J.C.S. Woo, IEEE Transact. Elec. Dev. **49**, 1748 (2002)
- [64] E.D. Palik, *Handbook of Optical Constants of Solids*, Academic Press, London (1985)
- [65] V.T. Semikina, A.N. Shmyryeva, Diamond Relat. Mater. **11**, 1329 (2002)
- [66] A.C. Ferrari, B. Kleinsorge, N.A. Morrison, A. Hart, V. Stolojan, J. Robertson, J. Appl. Phys. **85**, 7191 (1999)
- [67] S. Logothetidis, C. Charitidis, P. Patsalas, Diam. Relat. Mater. **11**, 1095 (2002)

5 Multi elemental metallic glassy films for selective crystalline oxide films growth

5.1 Introduction

Although single or multi metallic solids are in general crystalline, some metallic alloys can be grown in a glassy metastable phase. This can be achieved by out of equilibrium deposition conditions. Not all the metallic elements are able to form metallic glassy (MG) films. Last decades research is made on the so called glass form ability (GFA), qualitatively describing the ability for formation of a solid in glassy structure. In this part of the thesis we chose the growth of Zr-Cu-based metallic glassy, as it is one of the most studied metallic glassy systems. The oxidation of the Zr-Cu-based metallic glassy films was studied by post growth treatment by oxygen plasma for the production of specific and selective crystalline oxides.

Transition Metal Oxides such as ZrO_2 , TiO_2 and Yttria-stabilized Zirconia (YSZ) are well known as very effective materials for biocompatible coatings [1-4] and photo-, electro- and physico-chemical catalysis [5-13]. Zirconium oxide (ZrO_2) possesses many interesting physical properties and it is thus widely used in protective and biocompatible coatings [14-17], catalysis [18-21] and optical components [22-26]. This plethora of applications creates the need of an industrial scale processing of controlled and selective growth of pure tetragonal and/or monoclinic structure of ZrO_2 . It has been found that while the monoclinic structure is very attractive for applications such as catalysis [27,28] and bioactive coatings on bone and dental implants [29,30], the tetragonal phase of ZrO_2 is promising for fuel cells and oxygen sensors [31].

In particular, much effort has been devoted towards methanol synthesis and water splitting using Zirconia-based catalysts [10-12]. The bioactivity and the catalytic efficiency may be different depending on the crystallographic structure and the effective surface of the catalyst [32]; therefore, controlling the surface structure and morphology of zirconia is of paramount importance. In addition, zirconia is manifested in various crystal structures and the selective growth of a specific allotrope is a highly demanding task [16,33,34].

Metal oxides are grown by traditional physical and chemical methods (such as sputtering, evaporation, electro-deposition, sol-gel, etc). However, control of the effective

surface of the grown material using these deposition and preparation methods is not always easily achieved at the nanoscale, in particular when a combination of enhanced catalytic activity and selectivity performance is desired, both being related to composition, surface area and structure of the catalyst.

Recently the stabilization of tetragonal ZrO_2 (SZ) at room temperature has attracted the attention of research [35], while the stabilizing role of minor additions such as Yttrium, Copper and Niobium was also thoroughly investigated [36-41]. The main outcome of these studies is that stabilization can be achieved by means of high temperature or pressure treatment [30,31]. These methodologies are time intensive and costly with the additional drawback of producing an oxide mainly in powder form [42,43]. Nowadays new methodologies concentrate their effort in the production of SZ in the form of supported thin films that have greater potential for many realistic applications [3,34,44].

Research of stabilizing the crystal structures of ZrO_2 in film form is focused both in the direct growth of ZrO_2 [45-50], but also by post growth oxidation at high temperature and pressure treatments [51] surface modifications [52] and chemical processes [53].

In the present part of the thesis we adopted an alternative approach that is based on the selective oxidation of ternary and quaternary glassy metallic films, aiming in the exploration of their possibility for use as templates for the selective growth of ZrO_2 . It is essentially a two-step method: firstly, a suitable Metallic Glass (MG) thin film containing an abundance of the metal whose oxide has to be developed is grown on a substrate and, subsequently, the film is subjected to oxygen plasma treatment for selective oxidation and formation of the desired oxides. Metallic glasses can be grown by various methods such as pulsed laser deposition (PLD) and magnetron sputtering [54].

As basis we used the binary Zr-Cu system in glassy film form, which is a simple and well studied system. As ternary we chose the Zr-Cu-Me (Me= Al₅, Ti₉, Si₆) cases. Al was selected because it is already reported as promoter of the formation of the tetragonal ZrO_2 in bulk metallic glasses but not in film form [54], Ti was chosen because of its high

oxidation rate, while Si for its oxidation resistance [55]. Finally the quaternary $\text{Zr}_{62}\text{Cu}_{23}\text{Ti}_9\text{Si}_6$ system was studied because of its high glass forming ability.

Additional extended study was performed to the ternary glassy $\text{Zr}_{74.7}\text{Cu}_{19.7}\text{Nb}_{5.6}$ system, since Nb is widely used as stabilization element of the tetragonal ZrO_2 . The study focuses on the oxygen plasma treatment of $\text{Zr}_{74.7}\text{Cu}_{19.7}\text{Nb}_{5.6}$ glassy thin films and the evaluation of their changes in composition, surface morphology and structure focusing on the selective production of ZrO_2 oxides that are stable in monoclinic and/or tetragonal structures at room temperature.

However, the role of the third element remains unclear, while there are limited studies referring to alternative elemental additions concerning the selective formation of ZrO_2 [56-62]. Similar treatment of pure Zr or binary Zr-Cu systems does not lead to similar oxides, thus manifesting the important role of the minor Nb addition [63].

5.2 Experimental setup

The binary $\text{Zr}_{78}\text{Cu}_{22}$, Zr-based ternary Zr-Cu-Me, (Me= Al₅, Ti₉, Si₆,) and the quaternary $\text{Zr}_{62}\text{Cu}_{23}\text{Ti}_9\text{Si}_6$ metallic glassy films were deposited on commercial, Czochralski-grown, *n*-type Si(001) by dual-cathode, confocal magnetron sputtering using two unbalanced magnetron sources at 45° with respect to the substrate normal in a high vacuum chamber (base pressure $P_b = 2 \times 10^{-5}$ mbar) at room temperature. The working pressure ($P_w = 3.3 \times 10^{-2}$ mbar) was achieved by leaking high purity argon (99.999%) that was used as a sputtering gas. The applied power was 60 W for both guns, adjusted towards high purity Cu and Zr metal targets (99.99% and 99.8% respectively).

For the ternary and quaternary growth of films, high purity foils (99.8%) of the third or the forth elements was fitted partially on the sputtering ring of Zr target. The composition of the as-grown samples has been determined by Energy Dispersive X-Ray Spectroscopy (EDS) in a JEOL Scanning Electron Microscope (SEM). Especially, the choice of Nb was based on the fact that when it is used as a minor addition in an eutectic point of the Cu-Zr system [64] it is known to increase the glass forming ability (GFA) of the as-

grown film [65] and, also, because theoretical and experimental studies suggest that Nb can be used a stabilizer for ZrO₂ instead of using Y [66-68].

The amorphous structures of the as grown metallic glassy films were examined by grazing incidence X-ray diffraction (GID) measurements. It came out that all samples are Zr-based Zr-Cu metallic glasses, while the additional metals (Al, Ti, Si) were found by energy dispersive X-ray (EDX) and Auger electron spectroscopy (AES) depth profiling measurements to be lower than 10%.

The samples after growth were treated with oxygen plasma created by an electrodeless radiofrequency discharge in H mode. Such plasma is characterized by a moderately large density of charged particles (often of the order of 10^{19} m^{-3}) and the molecules are almost 100% dissociated from parent atoms. The treatment was performed in a borosilicate glass tube evacuated by a rotary pump creating a base pressure of 5×10^{-2} mbar. High purity oxygen (99.999%) was leaked into the vacuum system achieving a working pressure of 5×10^{-1} mbar and, by applying RF power of 500W, the H mode of oxygen plasma was created [64]. The treatment was also performed by plasma in the E mode at a much lower power of about 70W. The treatment times in the E mode was up to 80s, but no influence on the composition of the films was observed. This effect is attributed to a much lower density of charged plasma in the E mode where typical values are of the order of 10^{16} m^{-3} .

The chemical composition of deposited and plasma-treated films was analyzed by Auger electron spectroscopy (AES) in a PHI SAM 545 spectrometer. For electron excitation a primary electron beam of 3keV and 1 μ A, with a diameter of 40 μ m, was used. During AES depth profiling the samples were sputtered by two symmetrically inclined Ar ion beams of 3keV. The sputtering rate was estimated to be around 6nm/min when measured on Ni/Cr layers of known thickness. Relative sensitivity factors provided by the instrument manufacturer were used to calculate the concentration values [69]. X-ray photoelectron spectroscopy (XPS) analyses were carried out on a PHI-TFA XPS spectrometer and ion sputtering was performed with a 3keV Ar⁺ beam scanned over a 4 x 4 mm² area. With these parameters a sputtering rate of about 1.7nm/min was measured

on a Ni/Cr structure. The analyzed area was 0.4mm in diameter. XPS spectra were created using X-ray radiation from an Al-monochromatic source and, again, relative sensitivity factors provided by the instrument manufacturer were used to calculate surface concentrations [70]. AFM images were taken in non-contact mode using a Solver PRO microscope (NT-MDT). Surface morphology analysis was carried out in a scanning electron microscope (JEOL JSM-7600F) employing a field emission gun (FEG-SEM) and a JEOL 5600. The crystal structure of the as-deposited and plasma-treated films was examined by X-ray diffraction (XRD) in Bragg-Brentano geometry and grazing incident X-ray diffraction (GID) using a Bruker D4-Endeavour instrument and D8 Advanced, respectively.

5.3 Oxidation of Zr-based ternary Zr-Cu-Me, (Me= Al₅, Ti₉, Si₆) and the quaternary Zr₆₂Cu₂₃Ti₉Si₆ metallic glassy films

The surfaces of all the as grown samples were measured by atomic force microscopy (AFM) and found to be smooth exhibiting roughness of 2-3nm. In the case of Zr₇₃Cu₂₁Si₆ and Zr₆₂Cu₂₃Ti₉Si₆ samples, because of the presence of the Si substrate, EDX measurements were performed on samples that were deposited on Al substrate. XRD measurements, figure 5.1, showed that they were also amorphous, suggesting that the substrate does not play important role in the growth of these specific amorphous structures. As it can be seen in Fig.1a-b-d Zr₇₈Cu₂₂, Zr₇₄Cu₂₁Al₅ and Zr₇₃Cu₂₁Si₆ systems exhibit similar characteristics.

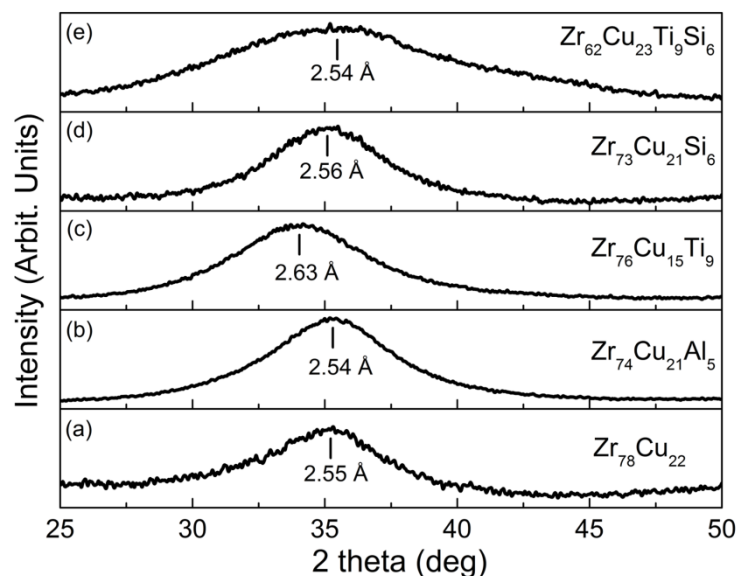


Figure 5.1: GID diffractograms of as grown (a) $Zr_{78}Cu_{22}$, (b) $Zr_{74}Cu_{21}Al_5$, (c) $Zr_{76}Cu_{15}Ti_9$, (d) $Zr_{73}Cu_{21}Si_6$, and (e) $Zr_{62}Cu_{23}Ti_9Si_6$ metallic glassy films

Strong peak shift can be observed in the case of the $Zr_{76}Cu_{15}Ti_9$ system, figure 5.1c, with the mean nearest neighboring atoms being at larger distances (peak at lower angles in GID measurements). This characteristic of the $Zr_{76}Cu_{15}Ti_9$ system seems to be maintained also in the $Zr_{62}Cu_{23}Ti_9Si_6$ case that exhibits a more glassy structure (broader peak), figure 5.1e.

The AES depth profiling of the as grown samples yielded the distribution and the element compositions of the films, figure 5.2. It came out that in all as grown samples oxygen, of about 20 percent was present. However, HRXPS depth profiling measurements indicated no bonding with the metals, in line with the GID measurements, in which no characteristic oxide peaks were found, figure 5.1, and with previous work referring to Nb additions [35]. It worth's to be noted that for all metallic glassy systems the AES depth profiling revealed a small increase of the Cu content on the film's surfaces, figure 5.2. This indicates that Cu is mobile and segregates at the surface of these metastable structures.

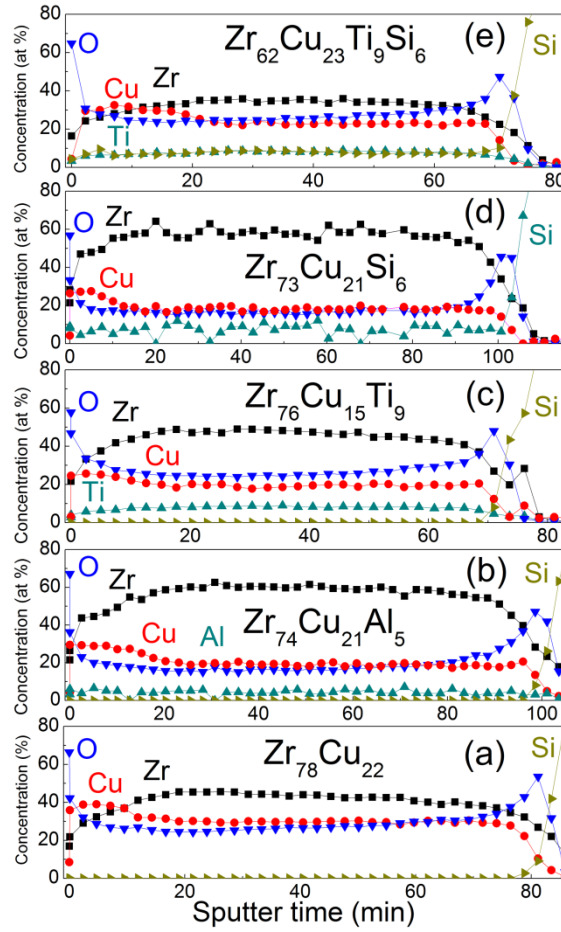


Figure 5.2: AES depth profiles of as grown (a) $Zr_{78}Cu_{22}$, (b) $Zr_{74}Cu_{21}Al_5$, (c) $Zr_{76}Cu_{15}Ti_9$, (d) $Zr_{73}Cu_{21}Si_6$, and (e) $Zr_{62}Cu_{23}Ti_9Si_6$ metallic glassy films

The samples after growth and characterization were treated by oxygen plasma under controlled conditions such as working pressure, applied power, plasma mode and time of treatment. The outcome of this parameterization yielded that the exposure time is a decisive parameter for the structure of the oxide films.

ZrO_2 was found to be the dominant oxide in all systems studied, a result that is dictated from the rich in Zr stoichiometries of the as glassy films. Interestingly, the Cu segregation in the surface, which was found in the as grown samples, is enhanced significantly in the Ti containing samples, resulting in the presence of CuO [35], figure 5.3, the other systems being unaffected. We have to note also that in the case of $Zr_{62}Cu_{23}Ti_9Si_6$ Cu is present in the film/substrate interface too, figure 5.3e.

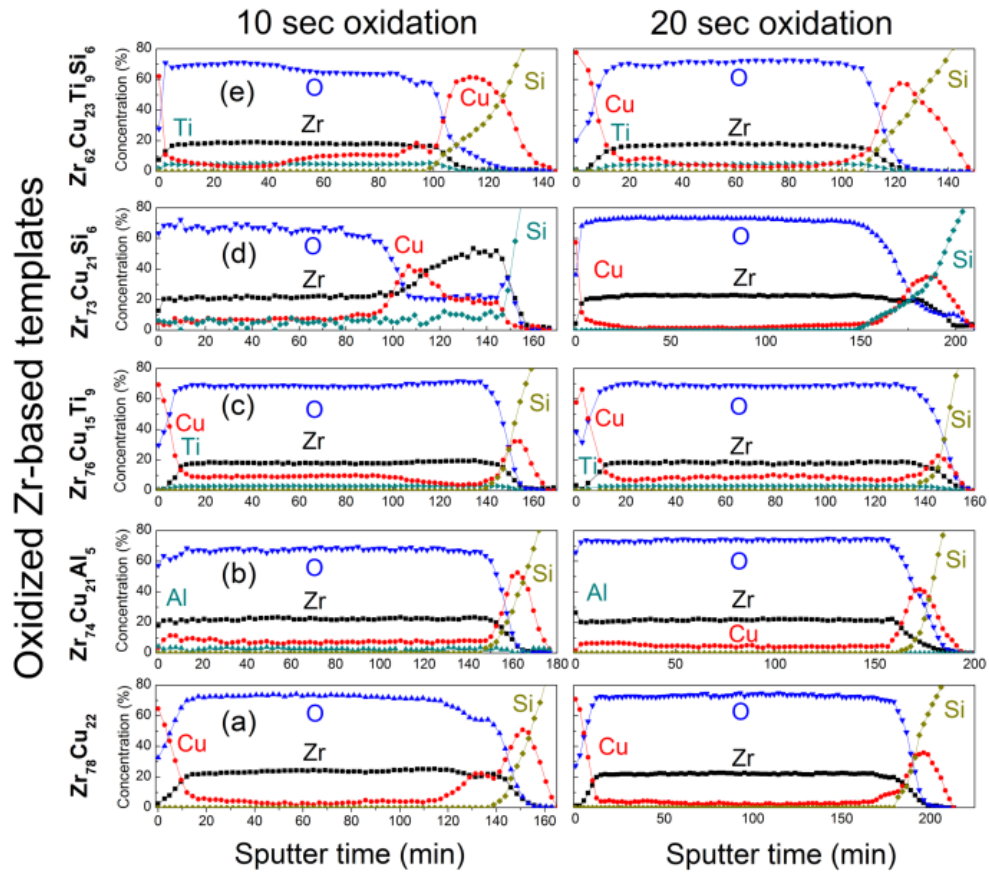


Figure 5.3: AES depth profiles of oxidized (a) $\text{Zr}_{78}\text{Cu}_{22}$, (b) $\text{Zr}_{74}\text{Cu}_{21}\text{Al}_5$, (c) $\text{Zr}_{76}\text{Cu}_{15}\text{Ti}_9$, (d) $\text{Zr}_{73}\text{Cu}_{21}\text{Si}_6$, and (e) $\text{Zr}_{62}\text{Cu}_{23}\text{Ti}_9\text{Si}_6$ metallic glassy films

Another interesting remark refers to the total reduction of Al and Si in the treated for 20 seconds, $\text{Zr}_{74}\text{Cu}_{21}\text{Al}_5$ and $\text{Zr}_{73}\text{Cu}_{21}\text{Si}_6$ systems, respectively, suggesting that small additions of a third element can alter significantly the oxidation behavior of the glassy films leading to different surface composition.

Turning on the structural properties of the ZrO_2 films, it is important to mention that during the plasma treatment and due to the metallic nature of the templates, the electrons of the metallic glassy films interact with the RF field inductively, resulting in an annealing process up to several hundreds of Celsius. Heating in presence of atomic oxygen results in the crystallization (in tetragonal and/or monoclinic ZrO_2 structure) of the oxide films. Figure 5.4 depicts the crystal structure evolution of each one of the systems, the most interesting result being the stabilization of the tetragonal ZrO_2 structure.

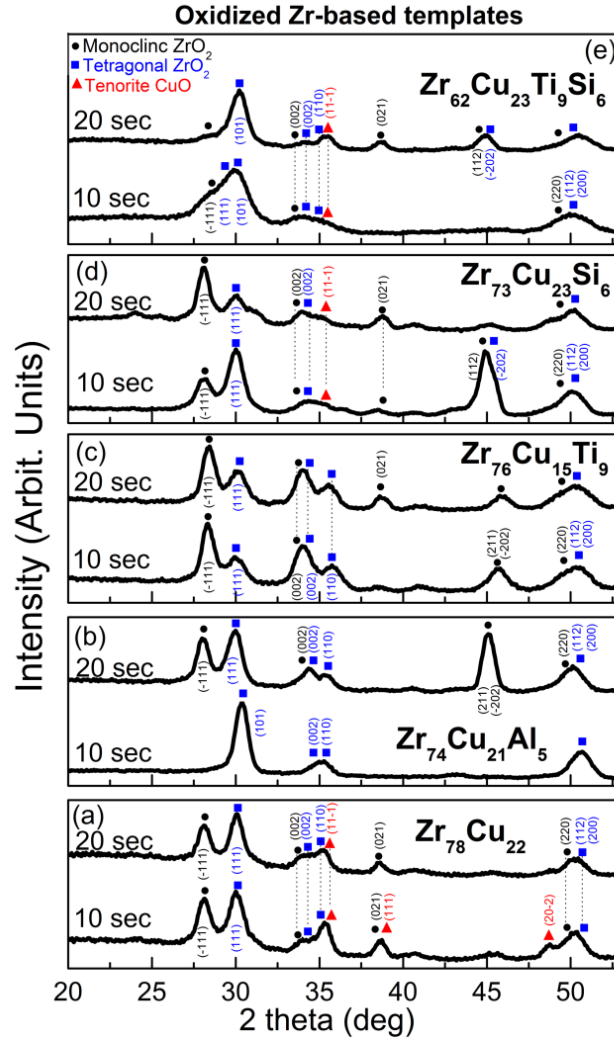


Figure 5.4: GID diffractograms of ZrO_2 formed by 10 and 20 sec of oxygen plasma treatment of Zr-based metallic glassy films; (a) $\text{Zr}_{78}\text{Cu}_{22}$, (b) $\text{Zr}_{74}\text{Cu}_{21}\text{Al}_5$, (c) $\text{Zr}_{76}\text{Cu}_{15}\text{Ti}_9$, (d) $\text{Zr}_{73}\text{Cu}_{21}\text{Si}_6$, and (e) $\text{Zr}_{62}\text{Cu}_{23}\text{Ti}_9\text{Si}_6$

More specifically, in the case of the $\text{Zr}_{78}\text{Cu}_{22}$ system, the oxidation resulted in the formation of both tetragonal and monoclinic ZrO_2 with the tetragonal phase being slightly dominated, figure 5.4a. In the $\text{Zr}_{74}\text{Cu}_{21}\text{Al}_5$ system the high temperature pure tetragonal ZrO_2 is formed after 10 seconds of treatment, while for longer exposure times monoclinic ZrO_2 is also developed and co-exists in the film, figure 5.4b, in line with previous works [43]. In the case of the $\text{Zr}_{76}\text{Cu}_{15}\text{Ti}_9$ system we found that the treatment time has no influence in the oxides growth, as in the case of $\text{Zr}_{78}\text{Cu}_{22}$; on the contrary, the monoclinic structure of the ZrO_2 dominates the oxidation result of this system, figure 5.4c. The structural evolution of the oxides in the case of the $\text{Zr}_{73}\text{Cu}_{21}\text{Si}_6$ system consists of the

formation of tetragonal ZrO_2 after 10 seconds of treatment, while as the treatment time increases monoclinic ZrO_2 is developed and appears to be more stable and preferred, figure 5.4d. Finally, in the case of the quaternary $\text{Zr}_{62}\text{Cu}_{23}\text{Ti}_9\text{Si}_6$ amorphous system, we note that although the film is fully oxidized after 10 seconds of treatment, the crystallinity is low with overlap of the characteristic peaks of tetragonal and monoclinic ZrO_2 . This result suggests that this system requires longer treatment time for obtaining pure and unambiguous crystalline [55], pure tetragonal ZrO_2 , figure 5.4e.

Besides the strong influence in the crystal structure of the ZrO_2 , the additional elements in the Zr-based glassy films affect also decisively the surface morphologies of the obtained oxides, figure 5.5.

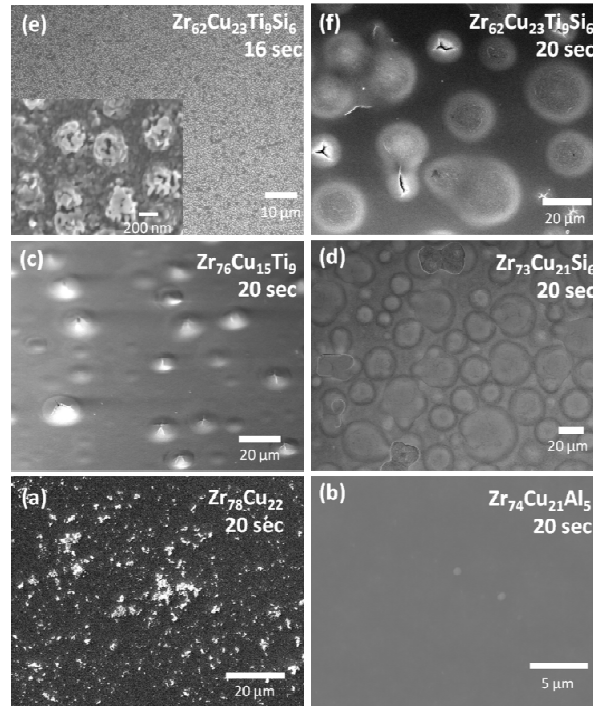


Figure 5.5: Surface morphologies of ZrO_2 formed using as templates the metallic glassy films; (a) $\text{Zr}_{78}\text{Cu}_{22}$, (b) $\text{Zr}_{74}\text{Cu}_{21}\text{Al}_5$, (c) $\text{Zr}_{76}\text{Cu}_{15}\text{Ti}_9$, (d) $\text{Zr}_{73}\text{Cu}_{21}\text{Si}_6$ for 20 seconds, (e) $\text{Zr}_{62}\text{Cu}_{23}\text{Ti}_9\text{Si}_6$ for 16 seconds and (f) $\text{Zr}_{62}\text{Cu}_{23}\text{Ti}_9\text{Si}_6$ for 20 seconds oxygen plasma treatment

In particular, the oxidation of the $\text{Zr}_{78}\text{Cu}_{22}$ template results in rough with attached powder-like ZrO_2 , figure 5.5a, while smooth oxide surface was obtained when the $\text{Zr}_{74}\text{Cu}_{21}\text{Al}_5$ template was used, figure 5.5b. Oxidation of the $\text{Zr}_{76}\text{Cu}_{15}\text{Ti}_9$ resulted in the formation of ZrO_2 cones, figure 5.5c, while dense bubbles were obtained after the

oxidation of the $\text{Zr}_{73}\text{Cu}_{21}\text{Si}_6$, figure 5.5d, and pillars and bubbles in the case of $\text{Zr}_{62}\text{Cu}_{23}\text{Ti}_9\text{Si}_6$. The sizes of these geometries vary between several nanometers up to some micrometers surfaces, figure 5.5e-d. In addition, the sizes and the integrities of these structures are strongly influenced by the plasma treatment conditions. Especially in the case of the quaternary system of $\text{Zr}_{62}\text{Cu}_{23}\text{Ti}_9\text{Si}_6$, vertically oriented nanosponge-like structures of 300 nm in diameter were created, figure 5.5e. Treatment times below or above 16 seconds yielded the creation of bubbles, figure 5.5d.

Since ZrO_2 is one of the most applicable oxides, controlling, by industrial scale methods, both its crystal structure and its surface morphology is highly desirable. Using as oxidation template the $\text{Zr}_{74}\text{Cu}_{21}\text{Al}_5$ system the formation of a smooth and pure tetragonal or monoclinic ZrO_2 is feasible. These virtues might be very interesting for MEMS, optical component development and catalysis. For example, it is easy to construct insulator-metal junctions with tunable thicknesses by just using different thicknesses of the as grown $\text{Zr}_{74}\text{Cu}_{21}\text{Al}_5$ templates and subsequently treat by oxygen plasma at appropriate times in order to obtain the desired oxide film's thickness. In addition, the control of the thickness of a smooth ZrO_2 surface allows also for a wide range of selection of the light wavelength that is going to be reflected, thus enabling the growth of multi-wavelength mirrors. Moreover, the capability of selecting the ZrO_2 crystal structure and surface morphology is closely related with the catalytic activity and selectivity, rendering this system a promising choice for growing ZrO_2 catalysts in thin film form.

5.4 Oxidation of Zr-based ternary metallic glassy films with addition of element known as Zirconia stabilizer.

A more focused study was performed concerning the effort of the ZrO_2 tetragonal phase stabilization using Zr-based metallic glassy film with minor additions of known stabilizing element. For the needs of this part of the study, Nb was chosen as the most widely used stabilizer of tetragonal ZrO_2 , as it was reported in the introduction. $\text{Zr}_{74.7}\text{Cu}_{19.7}\text{Nb}_{5.6}$ metallic glassy films, grown by magnetron sputtering, were used as oxidation templates under Oxygen plasma treatment with the same procedure as described above.

AFM measurements of the surface morphology of the as grown $\text{Zr}_{74.7}\text{Cu}_{19.7}\text{Nb}_{5.6}$ films showed a rather smooth surface with roughness estimated to be around 2 nm (figure (5.6a)).

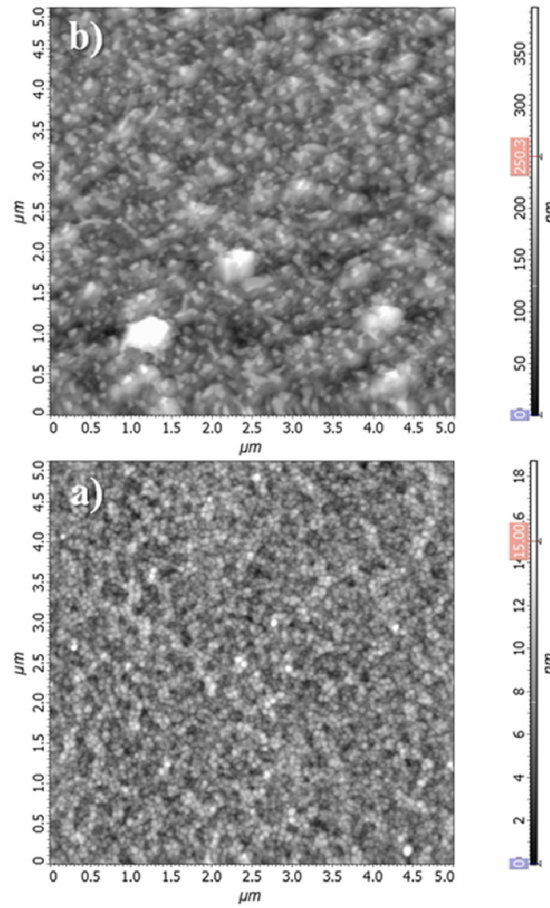


Figure 5.6: AFM images of a) an as-grown sample (z-scale from 0 to 15 nm) and b) a fully oxidized sample treated by oxygen plasma (z-scale from 0 to 250 nm)

After oxygen plasma treatment the roughness was increased by more than an order of magnitude to 27 nm. Figures (5.6b and 5.7) show the AFM and SEM images, respectively, of a treated surface. It can be seen that a uniform distribution of stable nanopillar structures is formed resulting in a large effective surface area.

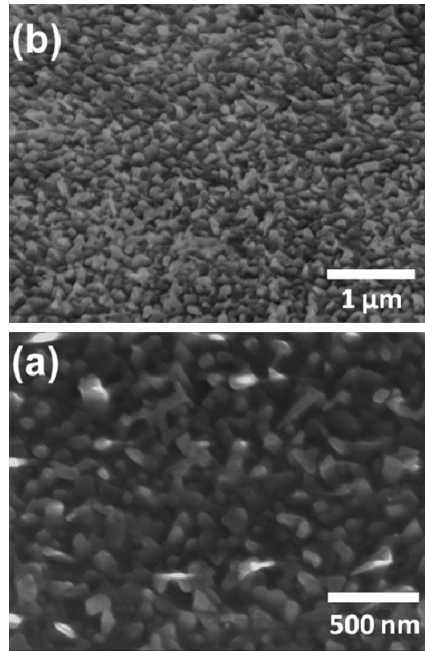


Figure 5.7: SEM images of a fully oxidized sample treated with oxygen plasma

It is worth noting that such nanopillars are formed only after plasma treatment of the $\text{Zr}_{74.7}\text{Cu}_{19.7}\text{Nb}_{5.6}$ and they have not been observed after treatment of pure Zr or ZrCu. Therefore, the specific nanostructure of the ternary compound seems to be essential for their formation.

Figures 5.8 and 5.9 show the AES and XPS depth profiles that exhibit the depth distribution of elements in the as-grown and plasma-treated films.

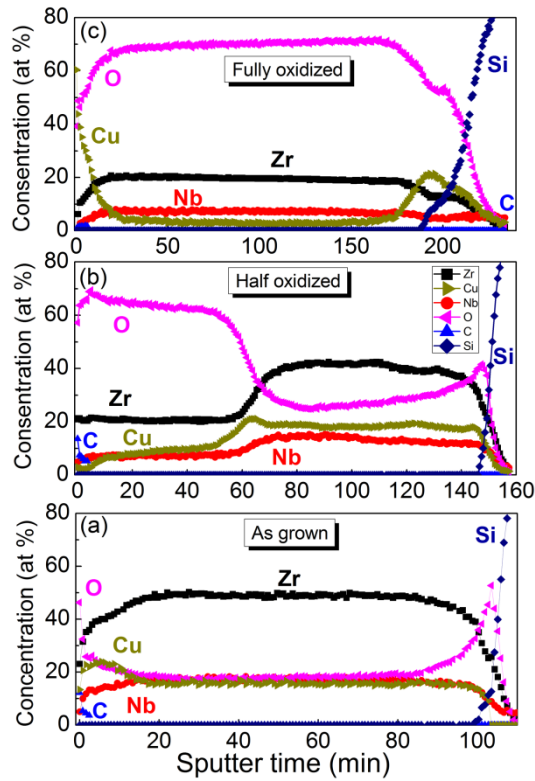


Figure 5.8: AES depth profiles of the (a) as-grown samples and samples treated by oxygen plasma for (b) 10 sec and (c) 80 sec

Measurements by AES and XPS depth profiling of the as-grown samples (figures 5.8a and 5.9a, respectively) revealed oxygen presence at concentration of about 20 at.% in the film; this result is related to α defective thin film growth process which has nonetheless been proven, a posteriori, not to be detrimental for the objective of the present study. In addition, we can detect a small increase of the Cu concentration near the film surface, indicating a tendency for Cu surface segregation (figures 5.8a, 5.9a). Plasma treatment in H mode resulted in the oxidation of the glassy films. For a treatment time of 10s only half of the film was oxidized with the oxidation process proceeding from the surface towards the substrate. The oxidized region contains about 60 at.% of oxygen and depletion of the Cu content is found in the oxidized part with a sharp oxidation front that can be clearly distinguished, as seen in figure 5.8b. Interestingly, Cu enrichment can be seen at the interface between the oxide/non-oxidized films. We point out also that while in the short exposure case (10s) no Cu surface segregation was detected, treatment longer than 10s resulted in completely oxidized films which are marked by migration of Cu to the surface

and the film/substrate interfaces (figure 5.8c). In addition to Cu segregation, the Nb atomic percentage in the film decreased during the oxidation process, remaining almost constant in the oxidized part of the film.

We note here that the sputtering time necessary to reach the Si substrate of the oxidized films during AES depth profiling was almost doubled (increase of about 90%) for treated times of 20, 40 and 80s with respect to the non-treated sample (figures 5.8a and 5.8c). This result can be explained by the transformation of the metallic film to a completely oxidized coating with a greater thickness. We have to note, however, that a lower sputtering yield of the oxide cannot be completely excluded as a possible reason for the longer sputtering times needed for the oxide films. Interestingly, taking also into account that the densities of metallic Zr and of ZrO_2 do not differ significantly ($\text{Zr}=6.52 \text{ g/cm}^3$, $\text{ZrO}_2=5.68 \text{ g/cm}^3$) we can conclude that the number of metallic atoms is the same before and after the plasma treatment, thus revealing that the plasma treatment is neither a sublimation nor a sputtering process but rather a procedure for transforming metallic films into continuous oxide coatings. This is demonstrated by the thickness increase of the initial metallic film after the oxidation process and the formation of the oxide film.

In order to obtain a better assessment of the film's oxidation process we also performed XPS depth profiling on the as-grown sample and on one of the fully oxidized samples that received 40s of treatment (figures 5.9a and 5.9b). The sputtering rate during the XPS profile was much lower than that of the AES depth profile and, since the oxidation is uniform for the fully oxidized films as deduced from AES depth profile measurements, the depth profiling was not performed for the whole film's volume. The depth that was examined was estimated from the Cr/Ni multilayer standard samples to be around 200nm (figure 5.9).

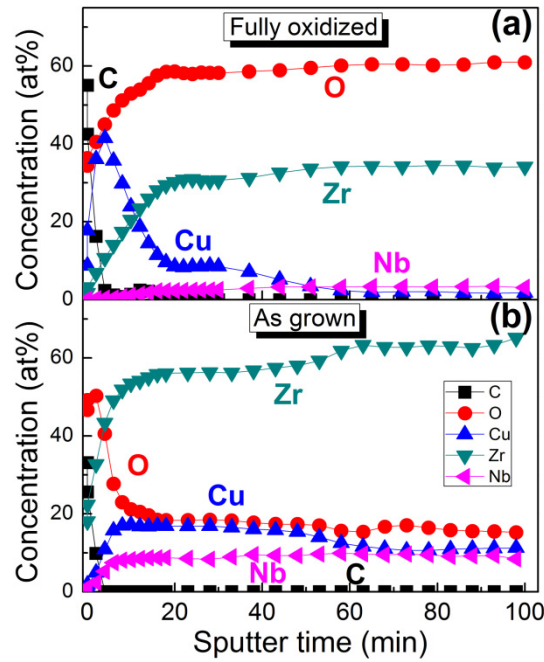


Figure 5.9: XPS depth profiles of an (a) as-grown sample and (b) a fully oxidized sample treated by oxygen plasma

The XPS analysis validates the AES results, showing profiles that are similar to those obtained by AES, with an increase of O in the film's volume and Cu segregation at the film surface for the fully oxidized samples (figure 5.9). High energy resolution surface and subsurface XPS spectra can provide further information on the chemical characteristics of the as grown and oxidized samples [71]. Figure 5.10 shows the Zr $3d$ and Cu $2p$ spectra obtained at the surface and at a depth of about 200nm from the as-grown and oxidized samples.

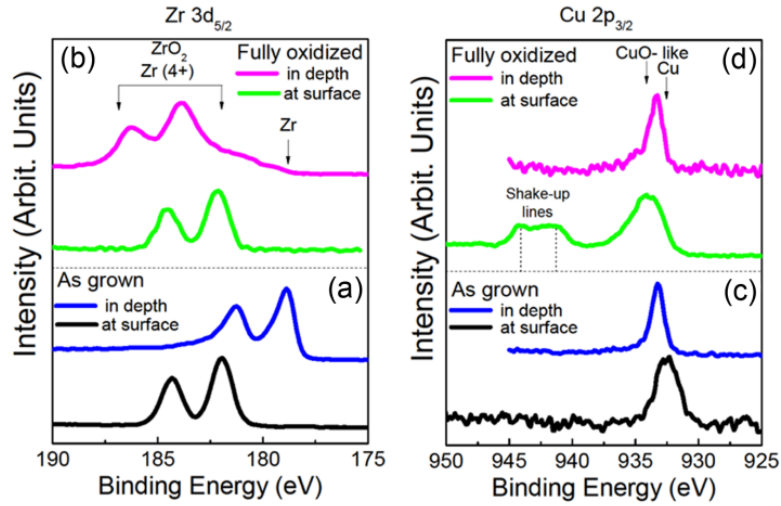


Figure 5.10: High energy resolution XPS spectra of Zr 3d_{5/2}, of the (a1) as-grown sample at the surface (black lines) and in the depth (blue lines), (a2) a fully oxidized sample at the surface (green lines) and in the depth (purple lines) and Cu 2p_{3/2} of the (b1) as-grown sample at the surface (green lines) and in the depth (purple lines)

Except the surface O contamination that was present in all cases, the main outcome of the XPS analysis is evidence of the oxidation of the metallic Zr to Zr⁴⁺ (figure 5.10a1) during plasma treatment. This can be recognized by the energy position of the Zr 3d_{5/2} peak, which is at 179eV for metallic Zr and at 182eV for the ZrO₂ (Ref. PHI-XPS). Our data (figures 5.10a1 and 5.10a2) show a binding energy of 182eV for the surface of the as-grown and oxidized samples as well as for the interior of the oxidized sample. In the interior of the as-grown sample the Zr 3d energy is 179eV, corresponding to metallic bonds of Zr atoms. These data can be explained by a layer of native ZrO₂ oxide on the as-grown sample and with the formation of ZrO₂ oxide through the whole film on the oxidized sample. In addition, for the fully oxidized samples copper segregated at the surface creates Cu 2p_{3/2} shake-up peaks at 941.3 and 944.1eV (figure 5.10b1) suggesting the presence of CuO [72]. These shake-up peaks are absent in the interior of the oxidized film and this can be explained by a transformation of the CuO phase to metallic Cu due to Ar-ion bombardment.

The structures of the samples were examined by means of XRD measurements, figure 5.11.

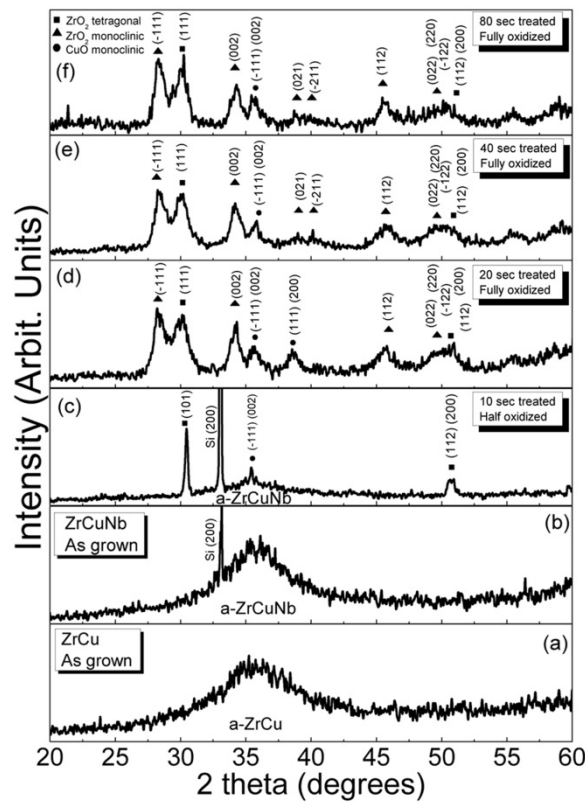


Figure 5.11: XRD patterns of (a) as grown $\text{Zr}_{78.3}\text{Cu}_{21.7}$, (b) as grown $\text{Zr}_{74.7}\text{Cu}_{19.7}\text{Nb}_{5.6}$, (c) 10s, (d) 20s, (e) 40s, (f) 80s treated $\text{Zr}_{74.7}\text{Cu}_{19.7}\text{Nb}_{5.6}$ samples

The diffraction patterns of the as grown $\text{Zr}_{78.3}\text{Cu}_{21.7}$ and $\text{Zr}_{74.7}\text{Cu}_{19.7}\text{Nb}_{5.6}$ samples, which are depicted in figures 5.11a, b, respectively, exhibit clear amorphous character. Very interestingly, the samples treated in O plasma for 10s manifest the characteristic peaks of pure tetragonal ZrO_2 (figure 5.11c). This finding is very important since it provides an explanation for the stability of tetragonal ZrO_2 at room temperature. The small peak shift is attributed to the presence of compressive stresses. For longer treatment times (more than 10s) both monoclinic and tetragonal ZrO_2 structures coexist, while crystalline CuO is also present, manifested by the appearance of the characteristic (111) and (200) peaks (figures 5.11d, e, f, respectively). This finding indicates that t- ZrO_2 is formed early in the treatment followed by the creation of m- ZrO_2 , both oxides finally coexisting upon completion of the oxidation process. No detectable traces of Nb oxides were observed, most probably due to the small amount of this element in the initial composition of the glassy metallic film.

Application of Scherrer's formula to the XRD data provides an estimation of the diameter of the grain size of the metal oxide. It was found that the grain size at the initial stages of treatment (10s, figure 5.11c) is about 40nm, while samples subjected to longer treatment times resulted in significant broadening of the XRD peaks (figures 5.11d,e,f) and in the emergence of additional peaks of the m-ZrO₂.

Given that for these cases there were more than two XRD peaks, we have employed both Scherrer and Williamson-Hall analyses which rendered a significant reduction of the grain size of m-ZrO₂ (estimated to be 12 nm by Scherrer and 16 nm by Williamson-Hall) and a significant level of micro-strain ($8-11 \times 10^{-3}$), possibly due to the competitive growth of t-ZrO₂ and m-ZrO₂.

5.5 Conclusions

In the present chapter of the thesis we demonstrated that oxygen plasma treatment of Zr-based metallic glassy films can be used under appropriate conditions as an industrial scale method for producing ZrO₂ films in predefined structures, roughness and surface morphologies. Pure tetragonal or mixed with monoclinic ZrO₂ films were formed depending on the initial composition of Zr-based metallic glassy films and the oxygen plasma treatment conditions. It came out that minor addition of Al, Ti or Si elements in the Zr-based Zr-Cu glassy films determine the ZrO₂ structure and that they can be also used to selectively tune the morphology of the oxide from completely smooth to nanostructured and/or totally rough.

The extended study that was performed using minor additions of Nb element show that Zr_{74.7}Cu_{19.7}Nb_{5.6} ternary amorphous metallic films, also grown by magnetron sputtering and subsequently treated in oxygen plasma, can successfully be used for developing coatings of selective oxides. It turned out that after 10s of treatment the metallic glassy films turn into a 360nm thick stable tetragonal ZrO₂ coating, while further exposure to oxygen plasma resulted in mixed tetragonal/monoclinic ZrO₂. The oxidation process is accompanied by Cu segregation at the surface and at the oxide/metallic glass interface, indicating that it most probably acts as a stress absorber, thus favoring the development of the ZrO₂ oxide film, which in turn is stabilized by the presence of Nb

minor additions. The fully oxidized films exhibit exceptional stability even under further exposure to O plasma. These results provide an easy and efficient way for developing ZrO₂ coatings in predefined structures suitable for protective and catalytic applications.

By controlling the crystal structure, surface composition and the surface morphology of ZrO₂ we suggest the potential use of Zr-based metallic glassy films as templates for post growth oxygen plasma treatment as a promising method for industrial scale growth of ZrO₂ films that could be used in optics, protective, microelectronic and catalytic industry.

5.6 References

- [1] C.J. Parga, S.K. Varma, Metall. Mater. Trans. **A40**, 2987 (2009)
- [2] L. Zhao, P.K. Chu, Y. Zhang, Z. Wu, J. Biomed. Res. B: Appl. Biomat. **91**, 407 (2009)
- [3] H.G. Kim, Y.H. Jeong, T.H. Kim, J. Nucl. Mater. **326**, 125 (2004)
- [4] A. Yilmazbayhan, A.T. Motta, R.J. Comstock, G.P. Sabol, B. Lai, Z. Cai, J. Nucl. Mater. **324**, 6 (2004)
- [5] D. Matthey, J.G. Wang, S. Wendt, J. Matthiesen, R. Schaub, E. Lægsgaard, B. Hammer, F. Besenbacher, Science **315**, 1692 (2007)
- [6] T.-S. Wu, K.-X. Wang, G.-D. Li, S.-Y. Sun, J. Sun, J.-S. Chen, ACS Appl. Mater. Inter. **2**, 544 (2010)
- [7] M.D. Hernandez-Alonso, F. Fresno, S. Suarez, J.M. Coronado, Energy Environ. Sci. **2**, 1231 (2009)
- [8] I.E. Wachs, Y. Chen, J.M. Jehng, L.E. Briand, T. Tanaka, Catal. Today **78**, 13 (2003)
- [9] V.R. Choudhary, B.S. Uphade, S.G. Pataskar, A. Keshavaraja, Angewandte Chemie **35**, 2393 (1996)
- [10] S. Arrii, F. Morfin, A.J. Renouprez, J.L. Rousset, J. Amer. Chem. Soc. **126**, 1199 (2004)
- [11] C.-M. Wang, K.-N. Fan, Z.-P. Liu, J. Amer. Chem. Soc. **129**, 2642 (2007)
- [12] W. Zhou, E.I. Ross-Medgaarden, W.V. Knowles, M.S. Wong, I.E. Wachs, C.J. Kiely, Nature Chem. **1**, 722 (2009)
- [13] L. Nakka, J.E. Molinari, I.E. Wachs, J. Amer. Chem. Soc. **131**, 15544 (2009)
- [14] M. F. Morks, Mater. Lett. **64**, 1968 (2010)
- [15] Z. Yao, Y. Xu, Y. Liu, D. Wang, Z. Jiang, F. Wang, J. Alloys Compd. **509**, 8469 (2011)
- [16] G. Wang, F. Meng, C. Ding, P. K. Chu, X. Liu, Acta Biomater. **6**, 990 (2010)
- [17] F. Andreatta, L. Paussa, A. Lanzutti, N.C. Rosero Navarro, M. Aparicio, Y. Castro, A. Duran, D. Ondratschek, L. Fedrizzi, Prog. Org. Coat. **77**, 3 (2011)
- [18] J. Becker, P. Hald, M. Bremholm, J.S. Pedersen, J. Chevallier, S.B. Iversen, B.B. Iversen, ACS Nano **2**, 5 (2008)
- A. Sinhamahapatra, N. Sutradhar, M. Ghosh, H.C. Bajaj, A.B. Panda, Appl. Catal. A-Gen. **402**, 87 (2011)

- [19] R. Sasikala, A.R. Shirole, V. Sudarsan, K. G. Girijia, R. Rao, C. Sudakar, S.R. Bharadwaj, J. Mater. Chem. **21**, 16566 (2011)
- [20] K-H Kim, S-K Ihm, J. Hazard Mater. **186**, 16 (2011)
- [21] C.V. Ramana, R.S. Vemuri, I. Fernandez, A.L. Campbell, Appl. Phys. Lett., **95**, 231905 (2009)
- [22] S. Venkataraj, O. Kappertz, H. Weis, R. Drese, R. Jayavel, M. Wuttig, J. Appl. Phys. **92**, 7 (2002)
- [23] S.K. Pandey, O.P. Thakur, R. Raman, A. Goyal, A. Gupta, Appl. Surf. Sci., **257**, 6833 (2011).
- [24] L. Kumari, G.H. Du, W.Z. Li, R. Selva Vennila, S.K. Saxena, D.Z. Wang, Ceram. Inter., **35**, 2401 (2009)
- [25] S. Zhao, F. Ma, K.W. Xu, H.F. Liang, J. Alloys Comp., **453**, 453 (2008)
- [26] K. Sato, H. Abe, S. Ohara, J. Am. Chem. Soc. **132**, 2538 (2010)
- [27] D. He, Y. Ding, H. Luo, C. Li, J. Mol. Catal. **208**, 267 (2004)
- [28] L.W. Hobbs, V.B. Rozen, S.P. Mangin, M. Treska, G. Hunter, Int. J. Appl. Ceram. Technol. **2**, 221 (2005)
- [29] A.-L. Gomes, J. Montero, Med. Oral. Patol. Oral. Cir. Bucal. **1**, 50 (2011)
- [30] K.T. Jung, A.T. Bell, J. Mol. Catal. **A163**, 27 (2000)
- [31] S. Logothetidis, P. Patsalas, C. Charitidis, Mater. Sci. Eng. **C23**, 803 (2003)
- [32] K. Sato, H. Abe, S. Ohara, J. Am. Chem. Soc. **132**, 2538 (2010)
- [33] S. Mráz, J.M. Schneider, J. Appl. Phys. **100**, 023503 (2006)
- [34] G. Áquila, J. Jiménez, S. Guerrero, F. Gracia, B. Chornik, S. Quinteros, P. Araya, Appl. Catal. **A360**, 98 (2009)
- [35] S. Lee, K.-H. Kang, J.-M. Kim, H.S. Hong, Y. Yun, S.-K. Woo, J. Alloys Comp. **448**, 363 (2008)
- [36] X. Guo, Solid State Ionics **99**, 137 (1997)
- [37] B.-Y. Kim, C.-J. Park, H.-S. Kwon, J. Electroanal. Chem. **576**, 269 (2005)
- [38] S.G. Wu, H.Y. Zhang, G.L. Tian, Z.L. Xia, J.D. Shao, Z.X. Fan, Appl. Surf. Sci. **253**, 1561 (2006)
- [39] E.J. Walter, S.P. Lewis, A.M. Rappe, Surf. Sci. **495**, 44 (2001)
- [40] Z.-Y. Ma, C. Yang, W. Wei, W.-H. Li, Y.-H. Sun, J. Mol. Catal. **A231**, 75 (2005)

- [41] F. Maglia, M. Dapiaggi, I. Tredici, B. Maroni, U.A.-Tamburini, J. Am. Ceram. Soc. **97**, 2092 (2010)
- [42] H.B. Zhang, B.-N. Kim, K. Morita, H. Yoshida, J.-H. Lim, K. Hiraga, J. Alloys Comp. **508**, 196 (2010)
- [43] X. Xu, C. Xia, S. Huang, D. Peng, Cer. Int. **31**, 1061 (2005)
- [44] J.H. Shim, C-C. Chao, H. Huang, F.B. Prinz, Chem. Mater. **19**, 3850-3854 (2007)
- [45] S. Heiroth, R. Frison, J.L.M. Rupp, T. Lippert, E.J.B. Meier, E.M. Gubler, M. Dobeli, K. Conder, A. Wokaum, L.J. Gauckler, Solid State Ionics, **191**, 12 (2011)
- [46] D. Pamu, K.Sudheendran, M.G. Krishna, K.C.J. Raju, A.K. Bhatnagar, Thin Solid Films, **517**, 1587 (2009)
- [47] L. Chen, T. Mashimo, E. Omurzak, H. Okudera, C. Iwamoto, A. Yoshiasa, J. Phys. Chem. C, **115**, 9370 (2011)
- [48] J. Li, N. Zhang, K. Sun, W. Sun, W. Li, J. Alloys Comp., **509**, 5388 (2011)
- [49] Z. Chen, N. Prud'homme, B. Wang, V. Ji, Surf. Coat. Tech. **206**, 405 (2011)
- [50] M. Bremholm, J.Becker-Christensen, B.B. Iversen, Adv. Mater. **21**, 3572 (2009)
- [51] M. Skovgaard, K. Almdal, A. van Lelieveld, J. Mater. Sci. **46**, 1824 (2011)
- [52] K. Sato, H. Abe, S. Ohara, JACS **132**, 2538 (2010)
- [53] G.A. Almyras, G.M. Matenoglou, P. Komninou, C. Kosmidis, P. Patsalas, G.A. Evangelakis, J. Appl. Phys. **8**, 107 (2010)
- [54] A. Ishii, A. Iwase, Y. Fukumoto, Y. Yokoyama, T.J. Konno, F. Hori, J. Alloys Comp. **504**, S230 (2010)
- [55] W. Kai, P.C. Kao, P.C. Lin, I.F. Ren, J.S.C. Jang, Intermetallics, **18**, 1994 (2010)
- [56] D. Huang, B. Wang, V. Ji, T. Zhang, Mater. Sci. Forum **675**, 209 (2011)
- [57] C.Y. Tam, C.H. Shek, W.H. Wang, Rev.Adv. Mater. Sci. **18**, 107 (2008)
- [58] C.W. Kim, H.G. Jeong, D.B. Lee, Mater. Letters **62**, 584 (2008)
- [59] L. Liu, Z. Liu, K.C. Chan, H.H. Luo, Q.Z. Cai, S.M. Zhang, Scr. Mater., **58**, 231, (2008)
- [60] H.H. Hsieh, W. Kai, R.T. Huang, M.X. Pan, T.G. Nieh, Intermetallics **12**, 1089 (2004)
- [61] K. Mondal, U.K. Chatterjee, B.S. Murty, J. Alloys Comp., **433**, 162 (2007)
- [62] Triwikantoro, D. Toma, M. Meuris, U. Koster, J. Non-Crystal. Solids, **250**, 719 (1999)
- [63] N.T. Panagiotopoulos, J. Kovač, M. Mozetič, P. Patsalas, G.A. Evangelakis, J. Vac. Sci. Technol. A, **29**, 0513035 (2011)

- [64] M. Mozetic, U. Cvelbar, Plasma Sources Sci. Technol. **18**, 1 (2009)
- [65] L.Q. Xing, P. Ochin, M. Harmelin, F Faudot, J. Bigot, J. Non-Crystalline Solids **205-207**, 579 (1996)
- [66] H. Li, M.G. Glavicic, J.A. Szpunar, Mater. Sci. Eng. A **366**, 164 (2001)
- [67] G. Kuri, M. Gupta, R. Schelldorfer, D. Gavillet, Appl. Surf. Sci. **253**, 1071 (2006)
- [68] T. Niendorf, H.J. Maier, D. Canadinc, G.G. Yapici, I. Karaman, Scripta Mater. **58**, 571 (2007)
- [69] L.E. Davis, N.C. MacDonald, P.W. Palmberg, G.E. Riach, R.E. Weber, Handbook of Auger Electron Spectroscopy, 2nd ed. (Physical Electronics Industries Inc., 1976)
- [70] J.F. Moulder, W.F. Stickle, P.E. Sobol, K.D. Bomben, Handbook of X-Ray Photoelectron Spectroscopy, (Physical Electronics Inc., Eden Prairie, Minnesota, USA, 1995)
- [71] V.N. Zhitomirsky, S.K. Kim, L. Burstein, R.L. Boxman, Appl. Surf. Sci. **256**, 6246 (2010)
- [72] M.A. Dar. S.H. Nam, Y.S. Kim, J. Solid State Electrochem. **14**, 1719 (2010)

6 MULTI ELEMENTAL POLYCRYSTALLINE Ti-BASED FILMS

6.1 Introduction

As it was mentioned in the previous chapter, the preferred structure of metallic elements is the formation of crystals. This chapter is referred to metallic polycrystalline structured films of Titanium based alloys. Titanium alloys are being used in numerous applications fields such as aerospace [1], subsea [2], automobile [3], sport and biomedical industries [4]. The capability of titanium alloys to be involved in this plethora of applications is originated by its unique combination of physical properties. Titanium itself is a light biocompatible element with relatively high hardness and anticorrosion behavior [1,5-7]. Ti and its alloys are also well known biocompatible materials, used nowadays as dental and body medical implants [8,9].

Many studies are focusing on the development of Ti-based implants in the β -Ti phase because of the similar mechanical properties with bones [10]. It is also known that the β phase of these alloys, which is unstable at room temperature, is generally promoted by the presence of Nb and/or Hf [11,12]. In addition, these binary and ternary alloys are in fact solid solutions and the introduction of the substitutional elements (Nb and Hf) distorts the HCP lattice, thus leading to the stabilization of the β phase. In thin film form these alloys could be of valuable use as coatings in other otherwise non biocompatible alloys, which nevertheless could be lighter and more flexible such as Al, Mg, etc. Although the research on the β -Ti phase stabilization is extended, the research directed in growing β -Ti films is limited. This chapter is referred to the study of stabilization of β -Ti alloys films to be used as biocompatible coatings in medical implants.

Magnetron sputtering was intentionally chosen as an industrial scale deposition technique for the growth of Ti-based films. For the study of stabilization of the β -Ti phase, Niobium was chosen as the more studied and widely used element stabilizer. Additionally, ternary Ti-based films with small percentage of additional element of Hf were grown for the study of the influence in structure and hardness. The structure of the films has been evaluated by X-ray diffraction (XRD) and X-ray reflectivity (XRR), while the chemistry and the final compositions have been assessed by means of Energy Dispersive,

X-Ray Photoelectron and X-ray excited Auger spectroscopies. Selected samples were characterized for their mechanical properties by indentation measurements.

6.2 Experimental details

The binaries Ti-Nb and the ternaries Ti-Nb-Hf films were deposited by magnetron sputtering in a high vacuum chamber of base pressure of $P_b = 2 \times 10^{-6}$ mbar. The films were grown at room temperature (RT) on commercial, Czochralski-grown, *n*-type Si(001). The working pressure ($P_w = 4 \times 10^{-2}$ mbar) was achieved by leaking high purity argon (99.999%) that was used as sputtering gas. RF (13.56 MHz) and DC power were applied at the Ti and Nb targets (purities of 99.99%) respectively, to deposit binaries Ti-Nb films in copiousness concentrations. In the case of the binary Ti-Hf and the ternaries Ti-Nb-Hf films, high purity (99.8%) Hf foil was mounted on top of the sputtering ring of Ti target, applied with 80 Watt RF power, at different percentage coverage in each deposition. Optical Emission Spectroscopy (OES) of deposition plasma was used as process control to detect any impurities (carbon, oxygen, nitrogen, water, etc) during growth.

The stoichiometries of the metallic films were determined by Energy Dispersive X-ray Spectroscopy (EDX), the crystal structure by X-Ray Diffraction (XRD) and the densities by X-Ray Reflectivity (XRR). For the surface characterization of the metallic films X-Ray Photoelectron and X-Ray excited Auger Spectroscopies were used. The electronic states and chemical shifts of the films were examined by X-ray fluorescence (XRF).

6.3 Results and Discussion

6.3.1 Deposition details of Ti-based films

Binary Ti-Nb films were grown in stoichiometries ranging between pure Ti and pure Nb by increasing either the RF or DC applied power at Ti and Nb target, respectively, figure 6.1.

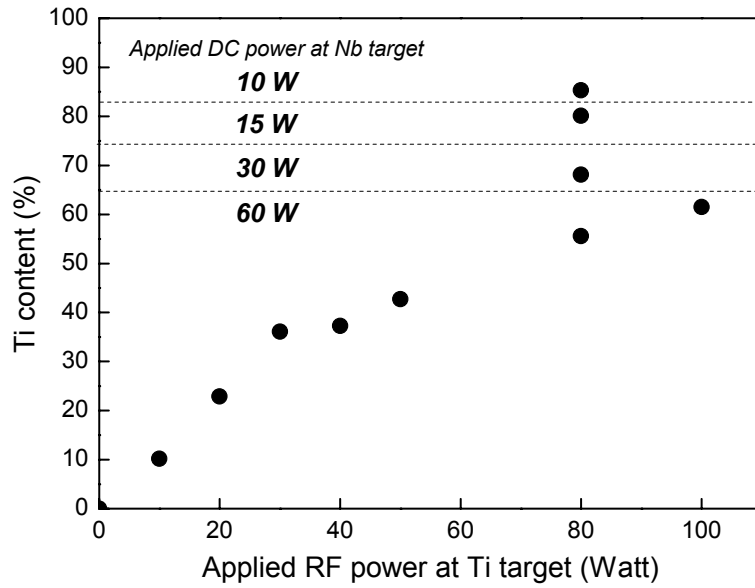


Figure 6.1: Deposition details of Ti-Nb films growth.

For the case of the Ti-Hf the applied RF and DC applied power on the Ti and the Nb targets were fixed to the 80 and 15 Watt respectively while different widths of Hf foils were attached on the Ti target, figure 6.2.

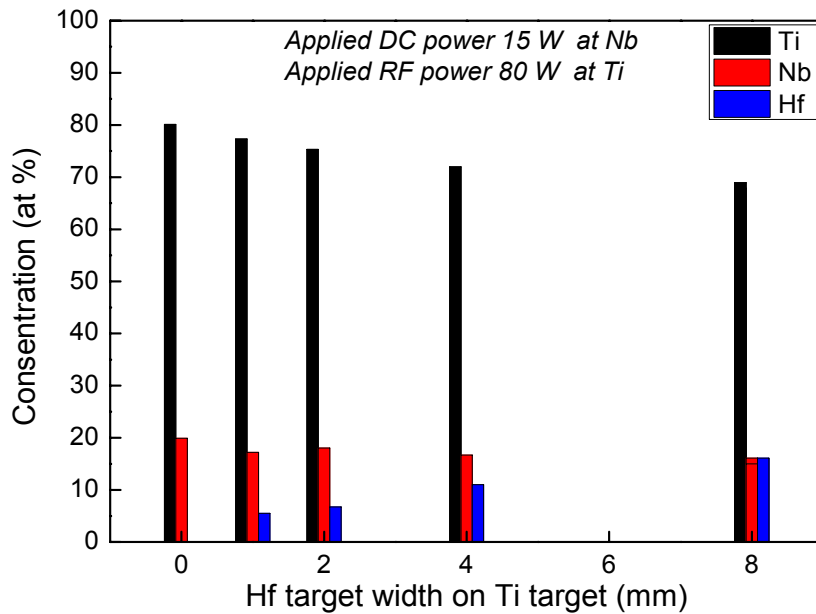


Figure 6.2: Atomic percentage concentrations of the Ti-Nb-Hf films versus Hf foils widths

A characteristic optical emission characterization of the deposition plasma is shown in figure 6.3. Optical emission spectrums of plasma were performed just above both the sputtering targets and just above the substrate.

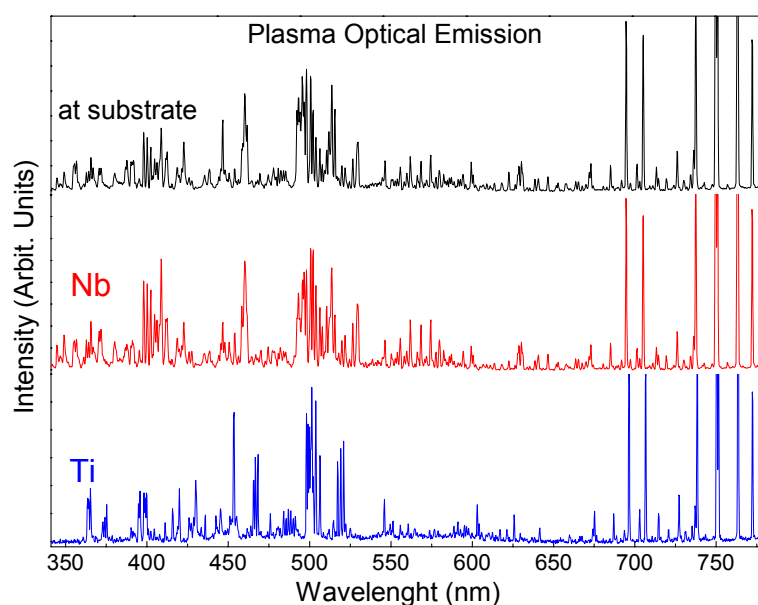


Figure 6.3: Optical emission spectroscopy of deposition plasma above the Ti (blue line) and Nb (red line) targets and close to the substrate (black line)

Each detected atomic emission line was identified and correspond only to the deposition elements.

6.3.2 Structural characteristics of Ti-based films

Ti-based binary Ti-Nb, Ti-Hf films and the ternary Ti-Nb-Hf were grown in various atomic compositions. The compositions of the films were measured by EDX while XRD measurements were performed for the determination of the crystal structures. Grazing incident XRD (GID) geometry was chosen to eliminate any contribution by the substrate and increase the intensity of the diffraction peaks.

The crystal structure of the films was examined by XRD measurements. In figure 6.4 we represent the diffractograms of the pure Ti, pure Nb and the Ti-based Ti-Nb films.

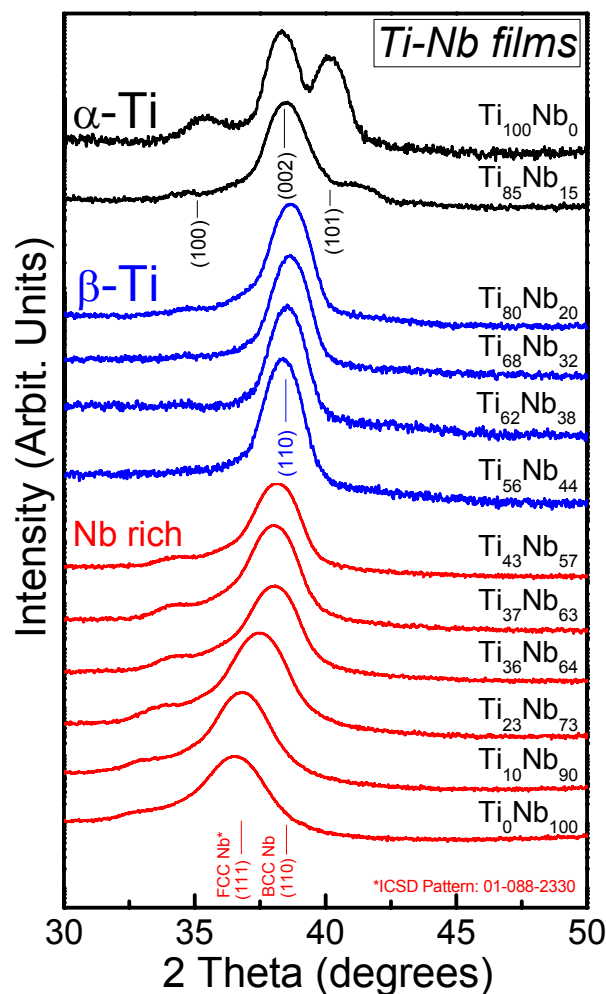


Figure 6.4: GID diffractograms of pure Ti, pure Nb and Ti-Nb films

Since the deposition was at RT, pure Ti has been grown in the stable HCP structure (α -Ti). Growing Ti-Nb films of 15% Nb, the hexagonal structure started to deform by altering the (100) and (101) lattice distances, but maintaining the (002) lattice constant at the same distance. Increasing the Nb content to 20%, BCC Ti structure was formed (β -Ti).

By these notices we can conclude that when Nb is less or equal than 15% (meaning 1 atom of the 6 of the hexagonal base of the HCP structure), it is preferred to be positioned on the hexagonal base, allowing for the growth of the HCP structure. When a second atom of Nb has to be placed in the primitive cell of the HCP structure the HCP structure becomes unstable and Ti in the BCC structure is grown.

This consumption is also verified by figure 6.5, where the lattice constants of the grown samples are calculated. In the inset it is clear that the lattice constant c of the two HCP structures (pure Ti and $\text{Ti}_{85}\text{Nb}_{15}$) is maintained, while a lattice deviates for the $\text{Ti}_{85}\text{Nb}_{15}$ sample regarding to the ICSD database.

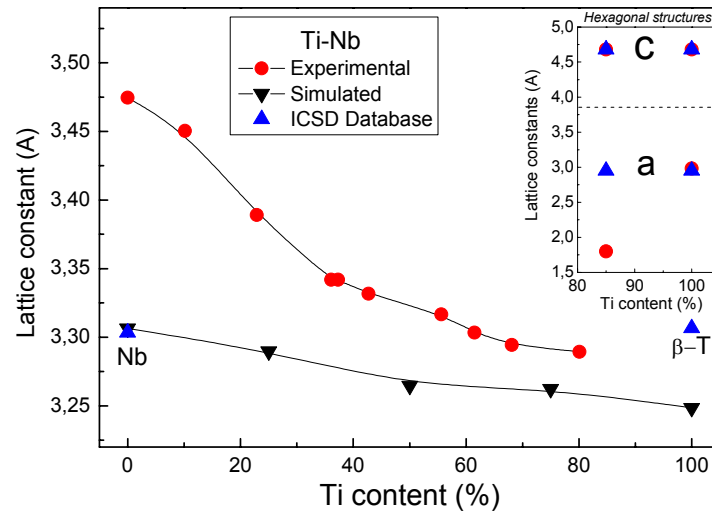


Figure 6.5: Lattice constants of Ti-Nb films versus Ti content

Continuing to increase the Nb content, in below 50 percentage, had no other effect in the crystal structure preserving the Ti BCC as the preferred structure, since the growth of the $\text{Ti}_{56}\text{Nb}_{44}$, were also BCC Ti-Nb.

Addition of Hf in the Ti leads to a different structural evolution as the Hf content increases, figure 6.6.

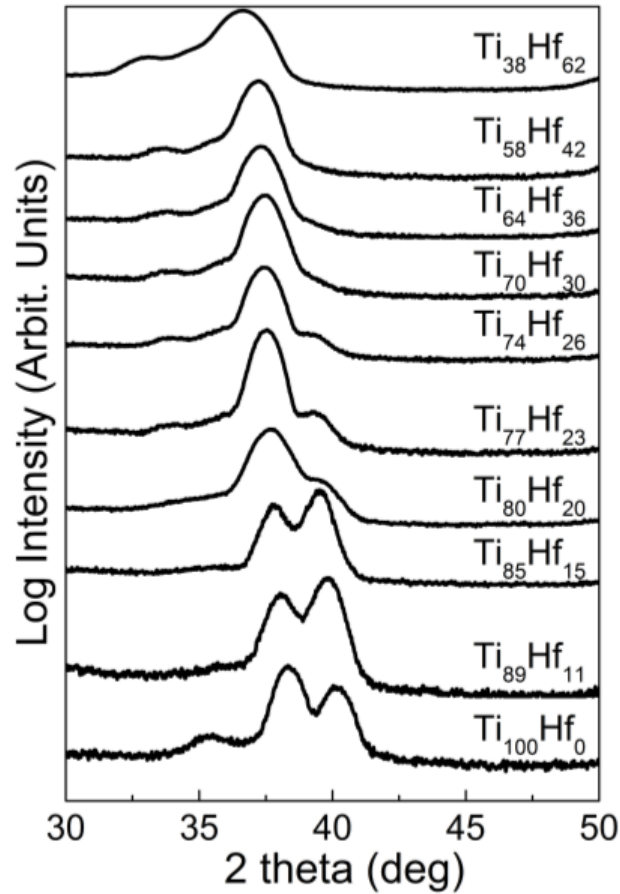


Figure 6.6: GID diffractograms of Ti-Hf films.

The diffractograms of the Ti-Hf films shows that by the atomic percentage increase of Hf the HCP Ti structure starts to collapse. As in the case of Ti-Nb films, almost full deformation of the HCP is achieved for Hf atomic concentration above 20%. For larger atomic concentrations of Hf element, the Ti-Hf films are formed to the martensitic crystal structure, known as α' -Ti or ω -Ti.

For the ternary Ti-Nb-Hf films we selected the stoichiometry of the Ti-Nb to be less than 20%, allowing HCP Ti-Nb films to be grown. In that way it could be studied the influence of a third element, with hexagonal preferred structure, in the Ti-Nb system. Growth of ternary Ti-Nb-Hf films with Hf to be from 5% to 11% resulted a-Ti structured films, figure 6.7.

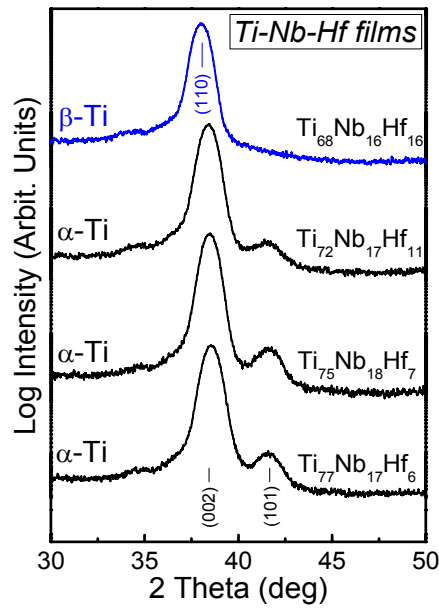


Figure 6.7 GID diffractograms of ternary Ti-Nb-Hf films

Adding and increasing the Hf atomic percentage content in this case has the opposite effect from the Ti-Nb system. Shifts of the (002) lattice distances were observed, but the (101) lattice distances kept constant. By these we conclude that Hf replaces centered Ti atoms in the HCP structure. Increasing the Hf content up to the stoichiometry of $\text{Ti}_{68}\text{Nb}_{16}\text{Hf}_{16}$ β -Ti film growth was established. In that case, it can be said that Hf did not replaces anymore centered atoms of the Ti HCP structure but atoms in the hexagonal base, resulting in the collapse of the HCP structure and promoting the growth of β -Ti films.

6.3.3 Macroscopic density of Ti-Hf films

The macroscopic density of the Ti-based films was calculated by X-ray reflectivity (XRR) measurements. In figure 6.8 we show the deviation of the critical angle of pure Ti, pure Nb and some of the Ti-Nb films XRR spectra, illustrating the density variation of the Ti-based films. Critical angle measurements show the shift of the critical angle to higher values as the Nb content increases.

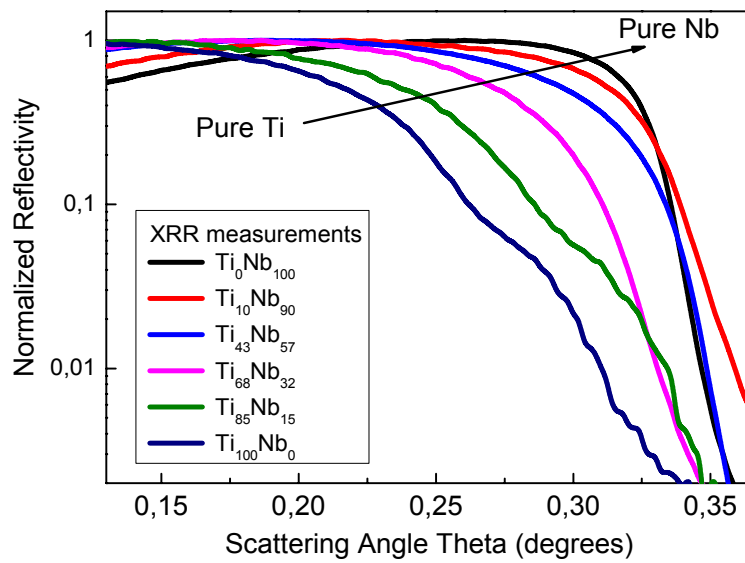


Figure 6.8: Critical angles measurements of Ti-based films by XRR

The densities of the Ti-Nb films are strongly related by the atomic concentration. As the Ti content increases the films are becoming less dense, figure 6.9 (black dots). The deviations from the database values are due to voids in the films volume because of the zero potential on the substrate during deposition.

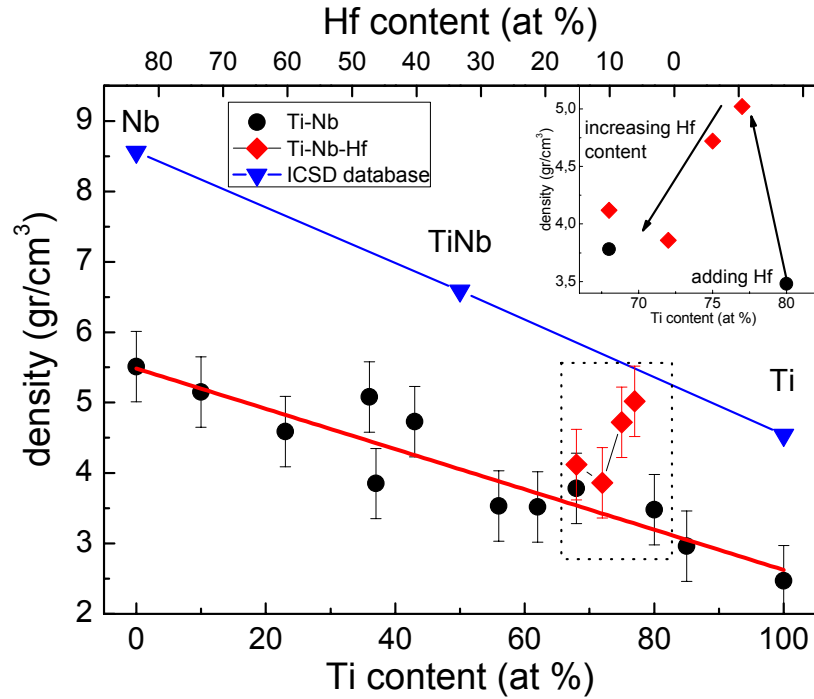


Figure 6.9: Density calculation of Ti-Nb (black dots) and Ti-Nb-Hf (red rhombs) films by critical angle measurements by means of XRR

For the Ti-Nb-Hf system a strong increase of the density is observed especially for the Hf poor samples, inset of figure 6.9 (red rhombs). This increase is due to HCP structure of the films. When BCC structure is grown then the density decreases back to the lower values of the BCC structures.

Same behavior of density decrease, as the Ti atomic percentage increases, was found for the Ti-Hf samples, figure 6.10.

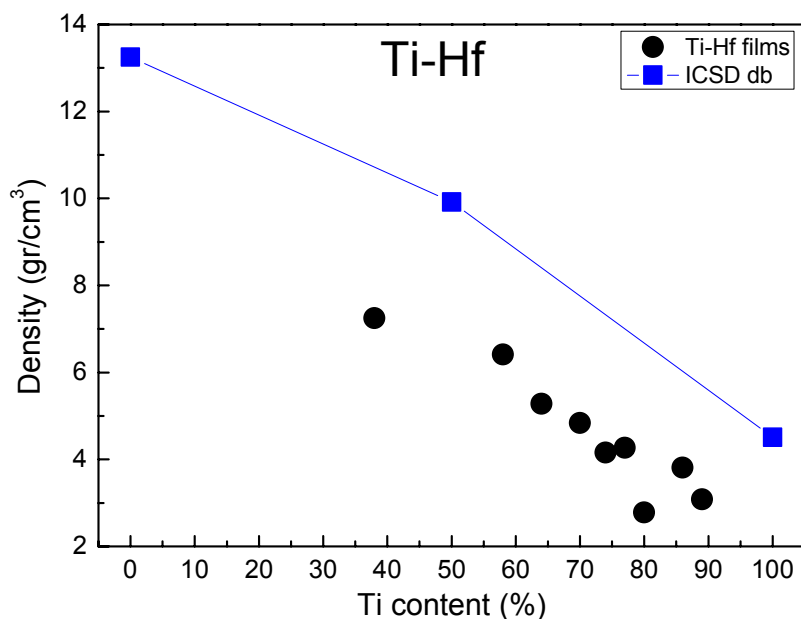


Figure 6.10: Density calculation of Ti-Hf (black dots) films by critical angle measurements by means of XRR.

Lower density values of the Ti-Hf films than the corresponding bulk solids were also calculated as it was expected.

6.3.4 Surface electronic characterization of Ti-based films

This study is based on the research of the potential use as biocompatible coatings of the Ti-based films. Therefore, critical is the surface electronic characterization of the films. Plasma emission lines just above the substrate shows a deposition plasma consisted only by the deposited elements. So by these measurements we conclude that any other measured, by ex-situ EDX, XPS and XAES, elements such as carbon and oxygen are result of surface contamination after deposition. All films were surface characterized by XPS showing contamination of the surfaces by carbon and oxygen. The formed oxides are TiO_2 , Nb_2O_5 and HfO_2 that are biocompatible. In figure 6.11 we show representative high resolution XPS measurements of the Ti, Nb and Hf elements.

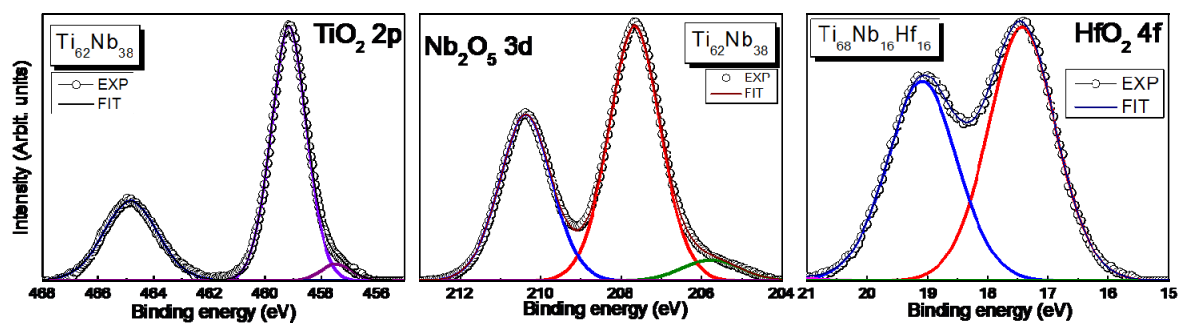


Figure 6.11: High resolution XPS of Ti, Nb and Hf elements

XAES measurements show a steady position of the Ti LMM. In the case of Nb a shift to higher kinetic energies was observed of the Nb LMV peaks as the Ti content was increasing, figure 6.12.

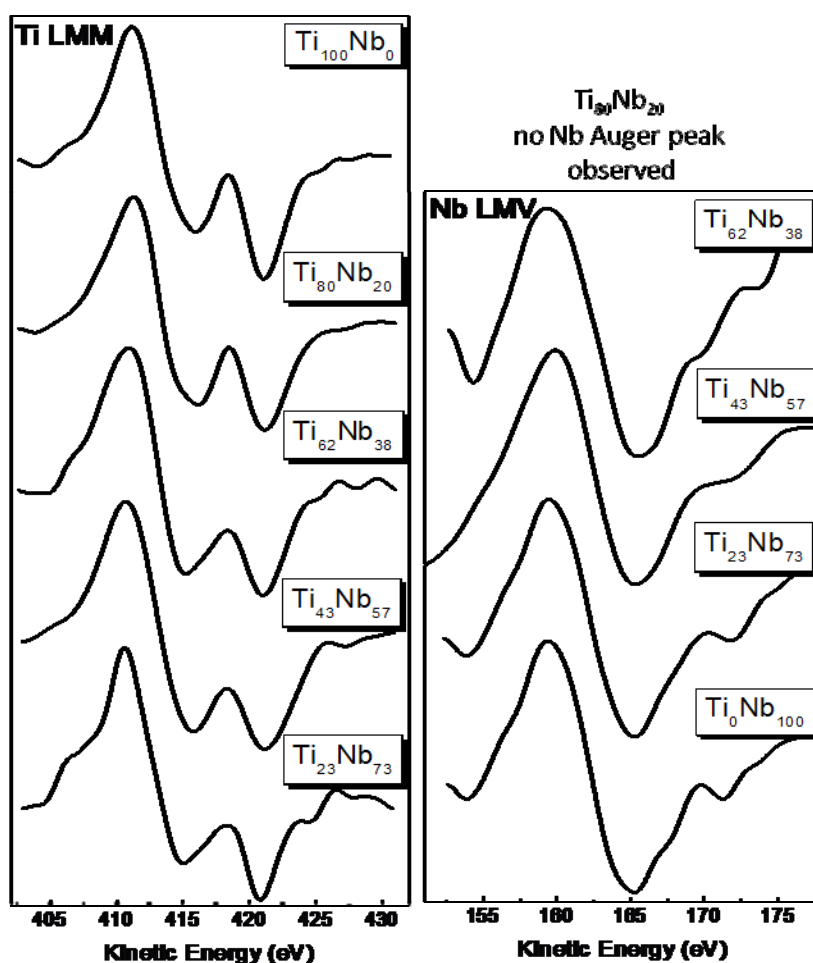


Figure 6.12: XAES of Ti-Nb films

This shift might emerge by a charge transfer of the outer electrons of Nb caused by the bonding with Ti. This consumption is based on the admission that bonding of the elements is made via their outer electrons. Since the Nb Auger electrons emission mechanism, described by LMV transitions, involves valence states, the peak shift might be explained by a charge transfer of the valence electrons of Nb. The Ti Auger electrons emission mechanism, LMM transitions, involves more core level states so no peak shift that could be explained by charge transfer is observed.

6.3.5 Bulk electronic characterization of Ti-based films

Because of the surface sensitive character of the XPS and XAES characterization techniques a thorough study of the chemical states of the Ti-based films could not be established because of the contamination by native oxides formations. X-ray fluorescence (XRF) was chosen as a high resolution bulk characterization technique of electron state transfers [paper-anag]. The measurements were performed on the Ti L_a transitions from $M_{4,5}$ to L_3 states of selective Ti and Nb-based films, figure 6.13.

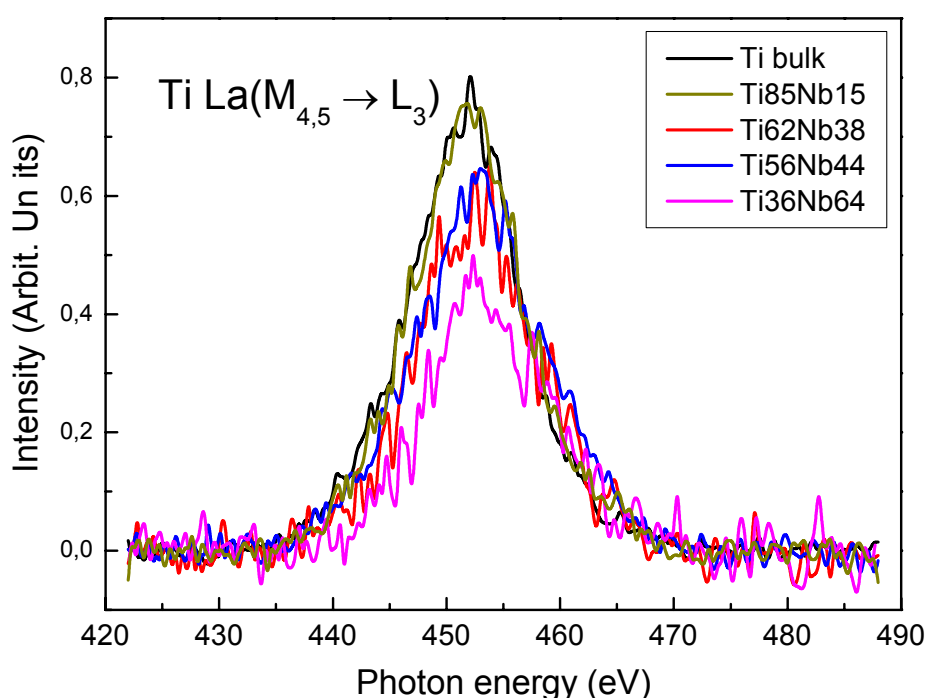


Figure 6.13: Ti L_a transitions from $M_{4,5}$ to L_3 states of Ti-Nb films by XRF

As expected, the intensity of the peaks of the Ti L_a transitions decreases as the Ti content of the films decreases. A small peak shift is observed to higher energies as the Ti content decreases. By peak fitting, using a Gauss-Lorentz pseudo voigt function, we show the photon energy of the Ti L_a transitions versus the atomic concentration of Nb additions, figure 6.14.

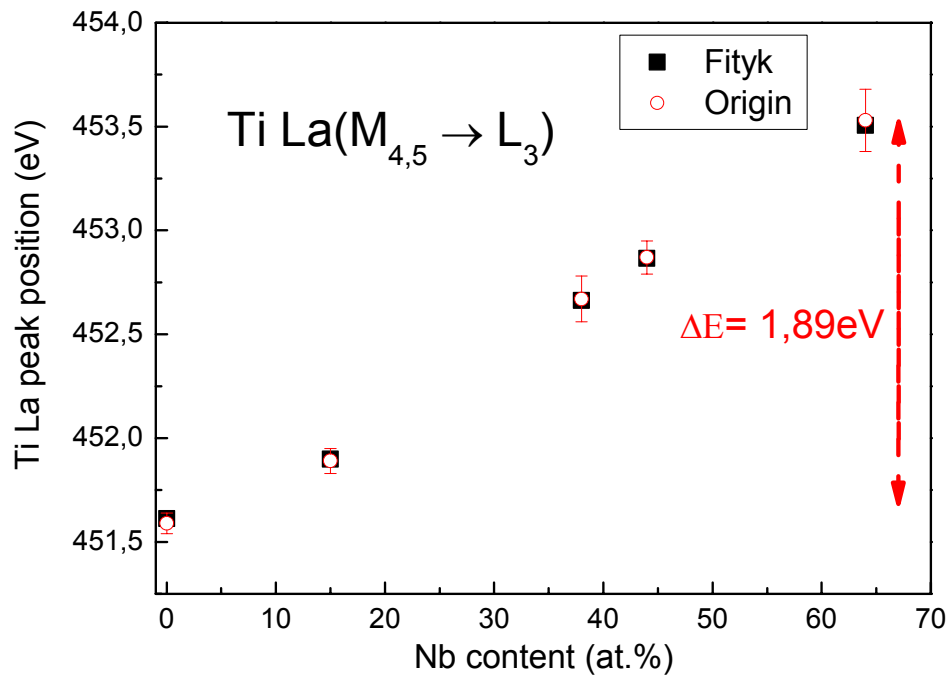


Figure 6.14: Ti La transition peak energy position versus the Nb content

The fitting procedures were executed by two different analysis programs, Fityk and Origin, for comparison and cross check of the results. Figure 6.14 clearly shows the peak position increase, originated by the X-ray photons emissions of the Ti La transitions, up to 1.9 eV as the Nb content increases. By these findings we assume that the bonding of the Ti and Nb elements involve the 3d Ti electrons by charge transfer close to the Fermi level of Ti.

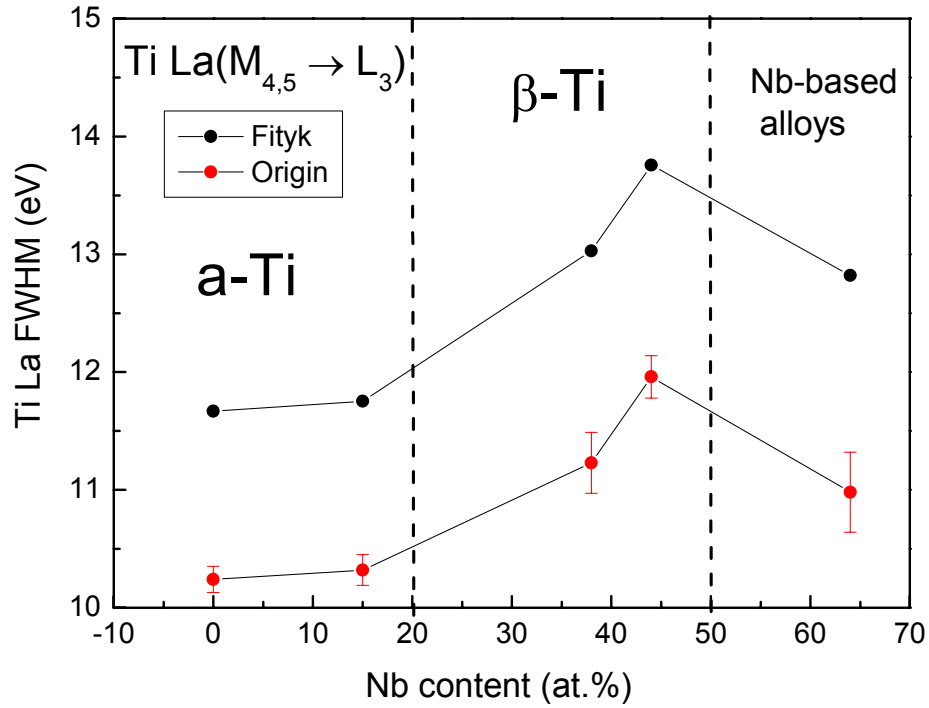


Figure 6.15: Ti La transition peaks FWHM versus Nb atomic concentration

Figure 6.14 shows the FWHM of the Ti La peaks versus the Nb content. The FWHM of the pure Ti and Ti-Nb films with Nb contents lower than 20 % are comparable. We remind here that these Ti-Nb films had HCP or else a-Ti structure. As the Nb content gets concentrations over 20 %, the Ti-Nb films are transformed to BCC or else β -Ti and from figure 6.15 we see an increase of the FWHM of the Ti La peaks. By this we conclude that for the metastable phase of the β -Ti, the electron states that are involved in the bonding of the Ti-Nb films are stressed or expanded. For Nb contents higher than 50 % the FWHM starts to decrease because Nb-based films are starting to form.

6.4 Conclusions

This part of the thesis was focused on the study of the influence of additions of Nb and/or Hf on the structure of Ti-based films. The results showed the capability of growing metastable phases of Ti-based films such as the β -Ti phase or the martensitic ω -Ti phase by the choice of the additional element and the atomic percentage of it. In summary, it came out that Nb at higher than 20 atomic percentages stabilizes the β -Ti as deduced by XRD measurements and the calculated lattice constancies. Additions of Hf element did

not lead to the the β -Ti phase stabilization but in the ω -Ti phase. As in the Ti-Nb systems, the phase structure from the α -Ti phase was established for Hf additions higher than 20 atomic percentages. For the ternary Ti-Nb-Hf alloy the results show the strong influence of the Nb in the stabilization of the Ti-based films in the β -Ti phase since stabilization occurred for the same concentrations as in the Ti-Nb system. The calculated densities of the films were calculated to be 30-40 percentage lower than the bulk ones, as it was expected because of the voids in the films' volumes that produced by the magnetron sputtering deposition technique.

An electronic study of selected Ti-Nb films was made by XRF showing an electron state displacement between α -Ti and β -Ti. Surface electronic characterization of the chemical states of the Ti-based films was carried out by XPS measurements showing the surface formation of the non toxic and biocompatible TiO_2 , Nb_2O_5 and HfO_2 oxides.

6.5 References

- [1] R.R. Boyer, R.D. Briggs, J. Mater. Eng. Perfor. **14**, 681 (2005)
- [2] R.W. Schutz, JOM **46**, 24 (1994)
- [3] M.J. Donachie Jr., Titanium a Technical Guide, (ASM international, USA, 2000)
- [4] M. Niinomi, Mater. Sci. Eng. A **243**, 231 (1998)
- [5] M. Long, H.J. Rack, Biomaterials **19**, 1621 (1998)
- [6] A. Biesiekierski, J. Wang, M. Abdel-Hady Gepreel, C. Wen, Acta Biomaterialia **8**, 1661 (2012)
- [7] R.A. Antunes, M.C.L. De Oliveira, Acta Biomaterialia **8**, 937 (2012)
- [8] J. Breme, V. Biehl, W. Schulte, B. d'Hoedf, K. Donath, Biomaterials **14**, 887 (1993)
- [9] S. Tamilselvi, H. Balaji, P. Srinivasan, N. Rajendran, J. Biom. Mater. Research A **90**, 2 (2008)
- [10] C. Zhao, X. Zhang, P. Cao, **509**, 8235 (2011)
- [11] Q. Guo, Y. zhan, H. Mo, G. Zhang, Mater. Design **31**, 4842 (2010)
- [12] M. Gonzalez, J. Pena, J.M. Manero, M. Arciniegas, F.J. Gil, J. Mater. Eng. Perf. **18**, 490 (2009)

7 METAL-CARBON NANOSTRUCTURED SOLIDS

7.1 Introduction

In this chapter, two systems of metal nanocomposite amorphous diamond-like carbon (DLC) thin films were studied. Nickel (Ni) and Silver (Ag) were selected due to their immiscibility with carbon. So, by sequential pulsed laser deposition (PLD) the growth of a DLC matrix with embedded metal nanoparticles was achieved.

In the first part of the chapter we are going to elaborate the capability of a-C:Ni films as catalytic templates for carbon nanotubes (CNTs) growth. Since their discovery Carbon nanotubes (CNT) have evolved into one of the most dynamic paradigms of modern materials science. Today their production and applications are among the more mature engineering fields; in particular, the emerging applications of CNTs include super-black light absorbers [1], solar harvesting [2,3], photonic devices [4,5] and thermal management systems [6,7]. One of the most effective production processes for CNT is Chemical Vapor Deposition (CVD) [8-19]; the structural quality and morphology of CVD-produced CNT are affected by the carbon precursor (methane, ethylene, acetylene, xylene or ethanol) [8], the gas mixture flow [9] and the level of impurities [10]. However, the most essential issue for the CVD growth of CNT is the required catalyst [11-19] with Ni [11,14,15], Fe [11,14-16,17], Co [11,14,15] and their bimetallic alloys [11-13,16] being the most widely used cases, due to their low miscibility with C and their activity in forming graphitic rings [11]. In addition to the physico-chemical properties of these catalysts, their morphology has been proven to be very important as well; therefore, great research efforts have been carried out to design and optimize nano-catalysts for specific CNT architectures and applications [15,16,17-19]. In particular, nanoparticles (NP) or thin films of Ni have been considered as effective catalysts for CNT growth [12,14,15] and recently the mechanism of graphitization of carbon nearby nanostructured Ni surfaces has been explained [20]. Therefore, the morphological control of Ni at the nanoscale can be an effective way of controlling the morphology and the functional properties of CNT arrays.

Pulsed laser deposition (PLD) has been previously used for the growth of nanocomposite films consisting of metal nanospheres embedded into a dielectric matrix such as diamond-like carbon (DLC) [21] or AlN [22]; the main concept behind this

approach is that during the successive carbon-metal deposition the DLC inhibits the growth of the metal resulting in the formation of small (~10 nm) metal nanospheres instead of metal layers or extended grains [21]. Such an approach might be also promising for producing nanostructured, Ni-containing surfaces for catalytic thermal CVD (T-CVD) growth of CNT.

In this part we demonstrate that a simple, two-step process, based on Ni containing DLC (DLC:Ni) nanocomposite catalyst layers can grow CNTs of varying morphologies (from aligned to inter-linked 'spaghetti-like') and exceptional functional properties (superhydrophobic surfaces with contact angle greater than 165° and extreme optical absorbance: reflectivity lower than 10⁻⁴) without further purification or post-growth processing; we also demonstrate that the combination of the functional properties make these CNT systems promising candidates for solar thermal harvesting.

In the second part of the chapter the study was based on the comparison of a-C:Ag and the a-C:H films regarding their properties as biocompatible coatings. Amorphous carbon either in pure form or in hydrogenated form is widely studied for biomedical coating applications and this is attributed to its chemical inertness, corrosion and wear resistance, low friction coefficient, low roughness and surface energy and also to its compatibility with living cells [23-26]. Such applications include heart devices [27], DLC-coated dialysis membranes [28], orthopedic applications [29-30], medical and surgical instruments [31], as well as films in biosensorics [32] and templates for immobilization of biomolecules [33, 34]. Particularly in the cardiovascular field, carbon demonstrated low thrombogenicity [35-39] and that its surface properties can control the mechanisms of protein adsorption [40, 41] and has also been considered for use in coronary artery stents [42, 43], heart valves [44, 45], left ventricular assist devices [46], and heart prostheses [47].

There are various deposition techniques developed to produce the carbon thin films with variable film densities, surface and interface morphologies. Other types of carbon based thin films are the carbon-metal thin films incorporated with different modifying elements such as gold, copper, silver, silicon, titanium, oxygen, nitrogen, nickel, tin and

tantalum [48, 49]. The main reasons for the incorporation of modifying elements are to improve the limitations of the carbon itself in terms of the large compressive stress, and weak adhesion level resulting in delamination [50, 51]]. Furthermore modifying elements could be incorporated in order to adjust the wettability of the surface of the carbon thin film [52, 53]. In addition, metal particles incorporated into carbon films may also provide biological functionality [54,55].

Cytotoxicity, cell adhesion and spreading are the initial stages of the biocompatibility evaluation of biomaterials [56]. When a material comes into contact with cells at a physiological environment the initial reaction is the protein adsorption on the surface of the material by proteins from the environment and the cells themselves, and then cell adhesion will follow depending on the material's surface. The materials properties such as composition, surface topography, surface energy and chemistry, in relation with the other physical and mechanical properties, play a significant role on the cell-material interactions.

To investigate the cytotoxicity behaviour and cytocompatibility of various carbon based thin films were grown by two different deposition techniques, the pulse laser deposition and the plasma enhanced chemical vapour deposition. Two human cell lines were used; an immortalized cell line HeLa cells regularly used for cytotoxicity studies; and the human umbilical vein endothelial cells in an attempt to focus on the cardiovascular applications for these thin films. A comparison of the different grown thin films in terms of cell adhesion, cell spreading and proliferation by quantitative (cell proliferation assay) and qualitative analysis (imaging by optical microscope and scanning electron microscope) were performed. The wettability of these thin films was estimated by the contact angle measurements of the thin films. The ultimate target is to optimize a series of cell assessment protocols under *in vitro* conditions that would be complemented by characterization techniques and techniques at nanoscale and all together will comprise the initial stages of the characterization of carbon-based nanomaterials for medical applications.

7.2 Experimental setup

All samples were deposited on commercial Czochralski-grown, *n*-type Si (001) wafers. The PLD growth of nanocomposite films is based upon the concept of rotating sector targets [57]. The PLD growth of DLC:Ni and DLC:Ag thin films has been realized in a high-vacuum chamber ($P_b < 5 \times 10^{-8}$ mbar) and working pressure of $P_w = 10^{-5}$ mbar. The chamber was equipped by rotating target and sample holder as shown in Fig. S1 (lower right part). The rotating target consisted of pure, hot-pressed graphite and sterling Ni or Ag plates having the form of two or more opposing sectors (Fig. S1, lower right part). The distance between the target and the substrate was 30 mm. The thickness of the DLC:Ni and DLC:Ag films ranged between 23 to 35 nm and 30 to 35 nm, respectively. The hard-focused laser beam was the 3rd harmonic ($\lambda = 355$ nm) of a Nd:YAG laser (Lambda-Physik, pulse duration 6 ns, repetition rate 10 Hz and pulse energy of 35 mJ, respectively).

For the study of DLC:Ni films, pure Ni films were deposited by PLD (using a pure Ni target) as well as by magnetron sputtering for comparison purposes.

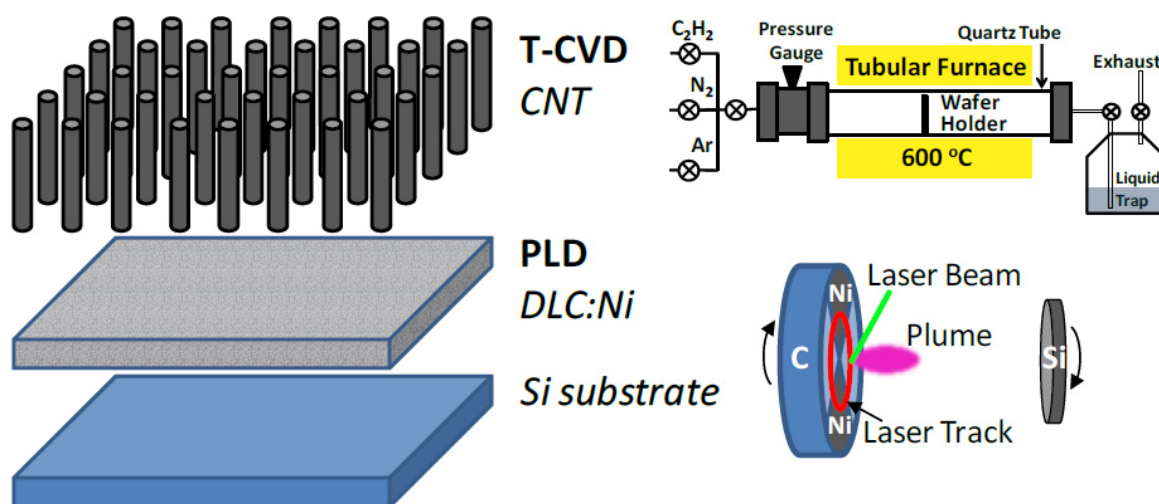


Figure 7.1: The samples of this study were grown on Si in two steps: i) PLD of the DLC:Ni nanocomposite catalyst layers, and ii) thermal CVD of CNTs

For the synthesis of CNTs the DLC:Ni/Si samples were placed in an alumina crucible within a quartz tube, located in a horizontal tubular furnace (Carbolite), following the standard hot-wall reactor design for CNT growth (figure 7.1, upper right part). The samples were heated up to the desired temperature (700 °C) under argon atmosphere. The carbon precursor [acetylene (99.6% purity)] and the carrier gas (Ar, 99.999% pure) were introduced into the reactor at flow rates of 10 sccm and 90 sccm, respectively, when the temperature has been stabilized to 700 °C. The reaction took place for 15 or 30 min; after the completion of the reaction, the ceramic boat was cooled down to room temperature under argon atmosphere.

Amorphous hydrogenated carbon thin films (denoted as a-C:H) were grown by Plasma-Enhanced Chemical Vapor Deposition (PECVD) using a C₂H₂/Ar gas mixture in a high vacuum ($P_b \sim 5 \times 10^{-6}$ mbar) parallel plate reactor on commercial Si{001} crystal wafers. The plasma power was either rf (samples a-C:H_1, a-C:H_2, a-C:H_3,) or dc (a-C:H_4) as described in chapter 4.

The *ex-situ* X-ray Photoelectron Spectra (XPS) and X-ray excited Auger Electron Spectra (XAES) were acquired in an ultra-high vacuum ($P_b < 2 \times 10^{-10}$ mbar) system by SPECS GmbH, equipped with a twin Al-Mg anode X-Ray source and a multi-channel Hemispherical Sector electron Analyzer (HSA-Phoibos 100). The pass energy was 20 eV providing a FWHM of 1.18 eV for the Ag-3d line. The *in-situ* electron excited Auger Electron Spectra (AES) were acquired in an ultra-high vacuum chamber ($P_b < 5 \times 10^{-10}$ mbar) connected to the PLD system through a high-vacuum ($P_b < 5 \times 10^{-8}$ mbar) transfer line using a 1 keV (for sp³ determination) and 3 keV (for the determination of [Ni]/[C]) primary electron beam from a thermionic W electron gun, which is located concentrically into a Cylindrical Mirror Analyzer (CMA) by Physical Electronics. The chemical features of all films have been studied by Auger Electron Spectroscopy (AES), which was employed either *in-situ* or *ex-situ* for the PLD- and PECVD-grown films, respectively. AES is capable of determining the sp³ and Ni or Ag fractions in the films following the procedures described in reference 57; however, note that the PECVD-grown samples were exposed to lab atmosphere and thus the determined sp³ content by AES is significantly underestimated (about 20%) due to the contribution of the organic surface

contaminations to the C_{KLL} AES peak, which is extremely surface sensitive. Additionally, the density values of the a-C:H films have been determined by Electron Energy Loss Spectroscopy (EELS) using 1KeV excitation electron beam.

X-ray Reflectivity (XRR) and diffuse scattering (XDS) data were acquired in a Bruker D8-Advance θ – θ diffractometer equipped with a Göbel mirror, parallel beam optics, a reflectivity sample stage with a knife edge and a linear stripe detector (Lynxeye), using the CuK_{α} line.

Scanning electron microscopy (SEM) images were recorded in a JEOL scanning electron microscope using a W-filament. Chemical microanalysis has been carried out in the SEM by Energy-Dispersive X-Ray Spectroscopy (EDS).

Raman spectra were recorded with micro-Raman system (RM1000 RENISHAW) using a laser excitation line at 532 nm (Nd:YAG) in the range of $100\text{--}3500\text{ cm}^{-1}$. A 0.5-1 mW power was used with $1\text{ }\mu\text{m}$ focus spot in order to avoid photodecomposition of the samples. Optical reflectivity spectra were acquired in the 250-780 nm range at normal incidence using a white light deuterium-halogen source, a co-axial fiber-optic assembly, a high line-density grating and a CCD detector (Avantes); the reflectivity spectra were normalized using two reference mirrors of silver and gold. Variable-angle optical reflectivity (specular and non-specular) measurements were carried out in an *in-house* built instrument consisting of a solid state laser source (657.5 nm), an analog photometer and a high accuracy goniometer capable of independent movement of the θ and 2θ circles; the values were normalized using a gold mirror.

The solar absorption from CNT has been recorded by an infrared camera (CEDIP MWIR) with a cooled InSb detector (waveband 3-5 μm), a frame rate of 150 Hz and resolution of 20 mK and using an integration time of 345 μs .

Contact angle (CA) measurements were used to investigate the wettability of the surfaces of the thin films. The CA technique followed was with an optical contact angle and surface tension meter CAM200 from KSV Instruments Ltd. Deionised water has been

used for the CA measurements. The water droplet was delivered at the centre of each sample, and the volume of each droplet was 5 μl .

7.3 Nickel contained nanocomposite amorphous diamond-like carbon catalysts (a-C:Ni)

All DLC:Ni catalyst templates and CNT bundles have been studied and characterized without further processing or purification.

Optical Microscopy observations of the produced CNTs have been acquired in an Olympus metallographic microscope using a white fluorescent lamp illumination.

Scanning electron microscopy (SEM) images were recorded in a JEOL-JSM5260 scanning electron microscope using a W-filament. Chemical microanalysis has been carried out in the SEM by Energy Dispersive X-Ray Spectroscopy (EDS) using an Oxford Instruments X-Ray analyzer.

For the study of the DLC:Ni surfaces, Atomic Force Microscopy images were obtained in tapping mode with a Bruker Multimode Nanoscope 3D using RTESP n-doped silicon cantilevers.

The *in-situ* electron excited Auger Electron Spectra (AES) of the catalysts layers were acquired in an ultra-high vacuum chamber ($P_b < 5 \times 10^{-10}$ mbar) connected to the PLD system through a high-vacuum ($P_b < 5 \times 10^{-8}$ mbar) transfer line using a 1 keV (for sp^3 determination) and 3 keV (for the determination of $[\text{Ni}]/[\text{C}]$) primary electron beam from a thermionic W electron gun, which is located concentrically into a Cylindrical Mirror Analyzer (CMA) by Physical Electronics.

The *in situ* AES differential spectra (figure 7.2) exhibit the C_{KVV} peak at kinetic energy 272 eV and the Ni_{LMM} triplet at 716-783-848 eV, from which the surface elemental analysis has been carried out taking into account the relative sensitivity factors. Note that given the atomic radii of Ni (0.135 nm) and Carbon (0.07 nm) the atomic percentage of Ni should be multiplied by 3.72 in order to roughly estimate the geometric surface coverage (SC) of Ni (this is a crude assumption, based on a hard sphere geometrical pattern and it

does not take into account any 3D islands, segregation of the C and Ni, *etc*; however we use these numbers to show that the Ni geometrical spread on the surface is significant, though the [Ni] atomic concentrations are low).

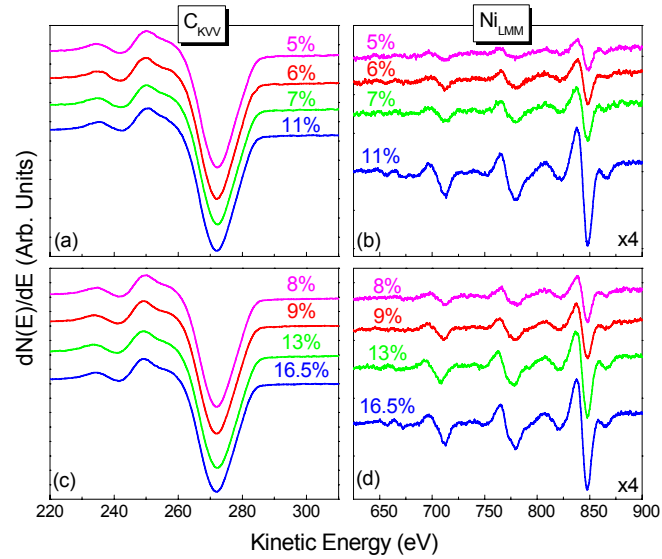


Figure 7.2: AES differential spectra of as grown DLC:Ni films used as templates for CNTs growth

The hybridization of Carbon (sp^3 - sp^2 fractions) has been determined from the broadening of the C_{KVV} peak according to the standard procedure used for carbonaceous materials [21].

The *ex-situ* X-ray Photoelectron Spectra (XPS) and X-ray excited Auger Electron Spectra (XAES) were acquired in an ultra-high vacuum ($P_b < 2 \times 10^{-10}$ mbar) system by SPECS GmbH, equipped with a twin Al-Mg anode X-Ray source and a multi-channel Hemispherical Sector electron Analyzer (HSA-Phoibos 100). The pass energy was 20 eV providing a FWHM of 1.18 eV for the Ag-3d line.

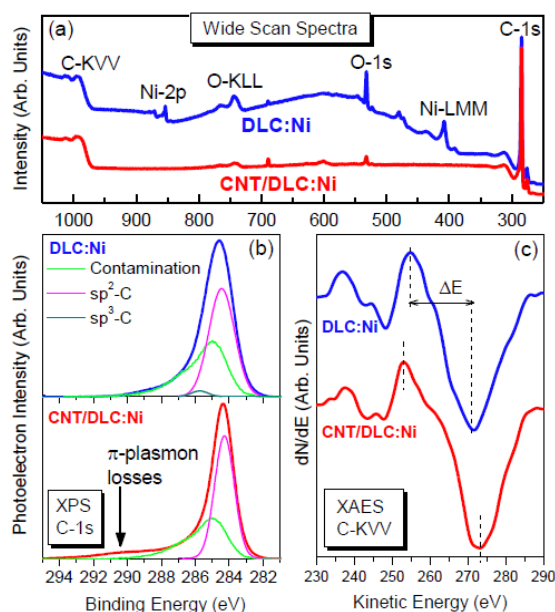


Figure 7.3: Survey, high resolution XPS spectra and XAES of DLC:Ni and CNTs

The sp^3 and sp^2 contents in the DLC:Ni catalysts and in the CNT specimens have been determined by analyzing the C1s envelope to contributions of sp^3 - (285.3 eV, dark cyan lines in Fig. S3b), sp^2 - (284.4 eV magenta lines in figure 7.3b) carbon and organic surface contamination (green lines in figure 7.3b), mainly due to hydrocarbons from the lab ambient; the contribution of the organic surface contamination has been evaluated by measuring the C1s peak for non carbonaceous materials exposed to lab ambient, in particular, a clean Si wafer and a clean sputter-deposited Ag thin film mirror. The XPS wide scan spectrum of the as-grown DLC:Ni sample #A exhibits clearly the Ni-2p photoemission line and the Ni-LMM Auger line (figure 7.3a, blue line), in agreement with the *in-situ* AES spectra; in contrast, no traces of the Ni-2p photoemission line have been observed in the wide scan spectrum after the CVD growth of CNTs (figure 7.3a, red line). In the later case, only the C-1s photoemissions peak and the C-KVV Auger are manifested (with the major exception of a minor oxygen surface contamination) indicating that when the DLC:Ni catalyst templates are used a base-type growth of CNT is occurring. The analysis of the C-1s photoemission spectra and C-KVV XAES lines (figure 7.3b and 7.3c) has shown that the DLC:Ni catalyst exhibit a small fraction of sp^3 bonded C, while the CNTs are completely and exclusively graphitic.

Grazing Incidence X-Ray Diffraction (GIXRD), specular X-ray Reflectivity (XRR) and non-specular diffuse reflectivity/scattering data were acquired in a Bruker D8-Advance θ - θ diffractometer equipped with a Göbel mirror, parallel beam optics, a reflectivity sample stage with a knife edge and a linear stripe detector (Lynxeye), using the $\text{CuK}\alpha$ line. The GIXRD, XRR and non-specular reflectivity measurements have been acquired by detector scans, θ - 2θ locked couple scans and ω - 2θ scans, respectively.

XRR has been implemented for the as grown DLC:Ni sample in order to determine their thickness, density and surface roughness; the corresponding XRR data are shown in figure 7.4. The critical angle (which is associated with the film density) is well correlated with the [Ni] concentration on the surface, showing that Ni is consistently incorporated into the DLC matrix.

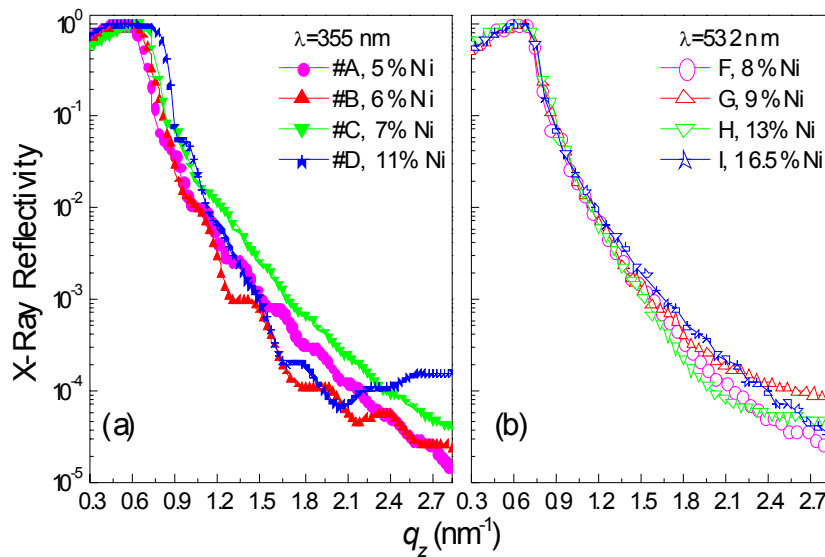


Figure 7.4: XRR spectra of DLC:Ni films with different Ni content grown by PLD with 355nm and 532nm laser wavelength

The XRR data have been fitted using the formulations of Parratt, for the determination of the thickness and critical angle, and Nevot-Croce, for the determination of surface roughness [58].

The x-ray non-specular reflectivity, or diffused scattering, data for the four samples after CVD growth of CNT are shown in figure 7.5.

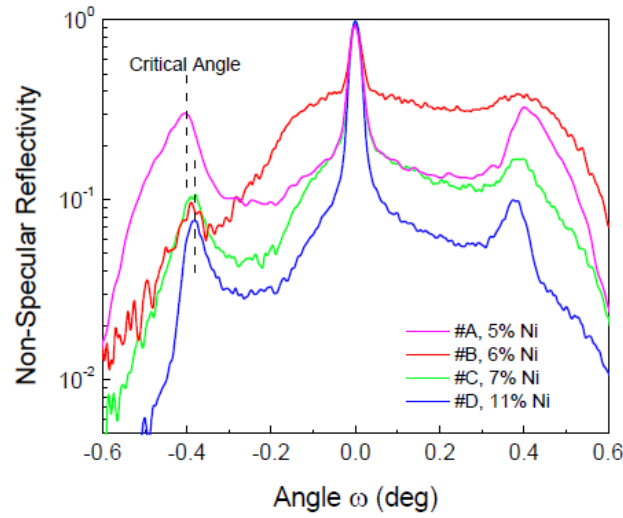


Figure 7.5: Off specular reflectivity of as grown DLC:Ni films with different Ni content

The main feature of the non-specular reflectivity scans is the appearance of the peaks at the angular position where the angle of incidence θ_i is equal to the critical angle θ_c [26], because according to analytic calculations [59] at $\theta_i = \theta_c$ the electric field at the surface is double than the incident field. Therefore, in the non-specular reflectivity the critical angle manifests as a distinct and well defined peak, whose angular position can be determined with great accuracy. Then, the density ρ_c of CNT surface is determined from θ_c according to [58]:

$$\theta_c^2 = \left(\frac{e^2 \lambda^2}{\pi m_e c^2} \right) \cdot \left(N_0 \frac{Z}{A} \right) \cdot \rho$$

where, e and m_e are the free electron charge and mass, respectively, λ is the x-ray wavelength (0.154 nm in our case), c is the speed of light in air, N_0 is Avogadro's number and Z and A are the atomic number and mass of the constituent element (pure C in our case).

Raman spectra were recorded with micro-Raman system (RM1000 RENISHAW) using a laser excitation line at 532 nm (Nd:YAG) in the range of 100–3500 cm^{-1} . A 0.5-1 mW power was used with 1 μm focus spot in order to avoid photodecomposition of the

samples. The Raman spectra raw data are presented in figure 7.6. All spectra display the characteristic D and G bands of multiwall CNT, as well as the second order D' band and traces of the G' band. The D and G bands have been fitted by Lorentzian lines, after a linear background subtraction, from which the G-band broadening (FWHM) and the I_D/I_G ratio have been determined.

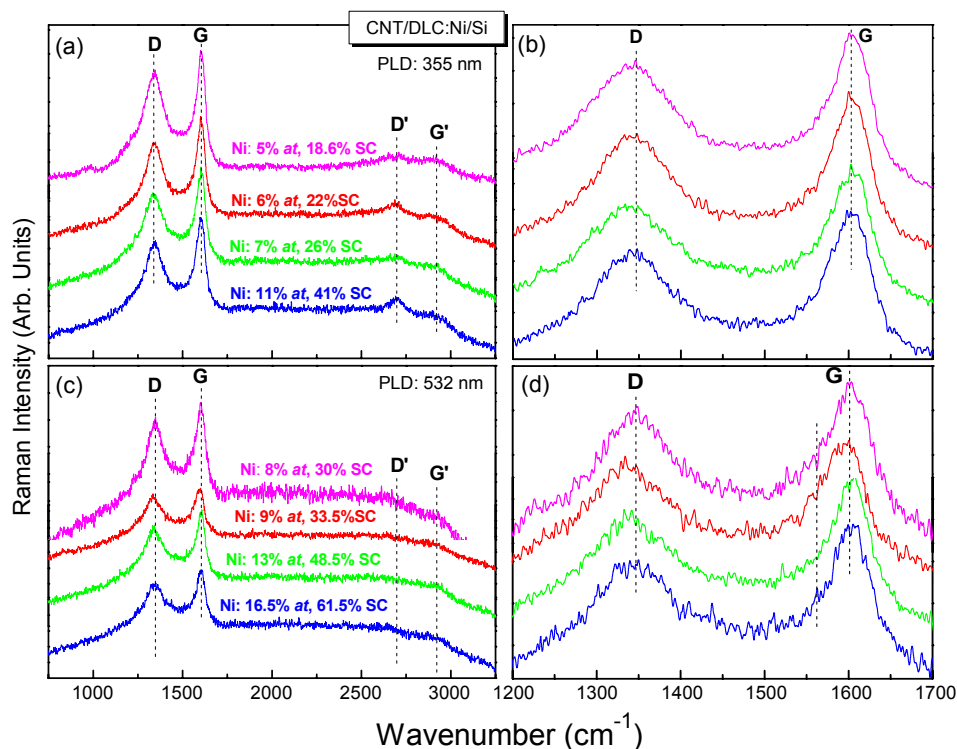


Figure 7.6: Raman spectra of the four CNT samples grown on the corresponding DLC:Si templates

Optical reflectivity spectra were acquired in the 240-790 nm range at normal incidence using a white light deuterium-halogen source, a co-axial fiber-optic assembly, a high line-density grating and a CCD detector (Avantes); the reflectivity spectra were normalized using two reference mirrors of silver and gold.

Variable-angle optical reflectivity (specular and non-specular) measurements were carried out in an *in-house* built instrument consisting of a solid state laser source (657.5 nm), an analog photometer and a high accuracy goniometer capable of independent movement of the θ and 2θ circles; the values were normalized using the specular reflection of gold and silver mirrors.

The DC electrical resistance of the produced CNT have been determined from I-V measurements (figure 7.7) acquired in a four probe station (PM5 by SÜSS MicroTec) using a KEITHLEY 2410 high voltage source meter. The determined electrical resistance values are predominantly affected by the electron scattering areal density of CNT. For samples A,B, and C, which are not completely aligned, the electrical resistance is consistently decreasing with increasing CNT density because of the decreasing empty space between the individual tubes (thus minimizing electron scattering). On the contrary, the sample #D, which is fully dense, exhibits the highest electrical resistance. This is because the current line defined by the four electrodes used for the measurement is perpendicular to the tube direction. Considering that the electron conductivity occurs along the tube, this geometry maximizes the electron scattering at the tube sidewalls.

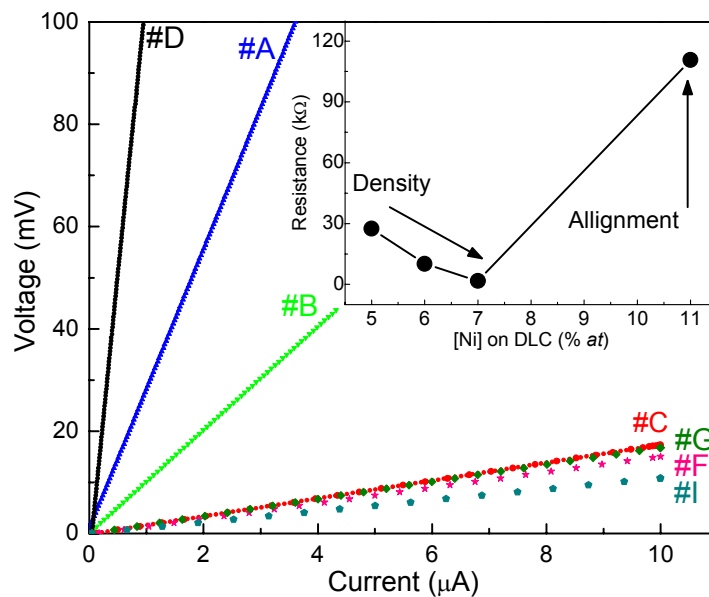


Figure 7.7: I-V measurements from the four CNT samples of this study. In the inset is the surface resistance versus the Ni content

The solar simulator set-up is presented in the inset of figure 7.8 and consisted of A: solar emission lamp (Sciencetech SF150, 150 W solar simulator), B: UV (<400 nm) filter, C: Acrylic Fresnel focusing lens (Edmund optics), D: quartz, plane-convex, near-field, focusing lens, E: sample resulting in a solar power of 20 W/cm² measured by a Melles-Griot broadband power and energy meter system (PEM-2 W) and a photosensitive paper to trace the solar spot size. The spectrum of the incoming light to the CNT surface is

presented in figure 7.8; although the spectrum is not the standardized AM1.5, it can be used for the proof of principle that is attempted in this work.

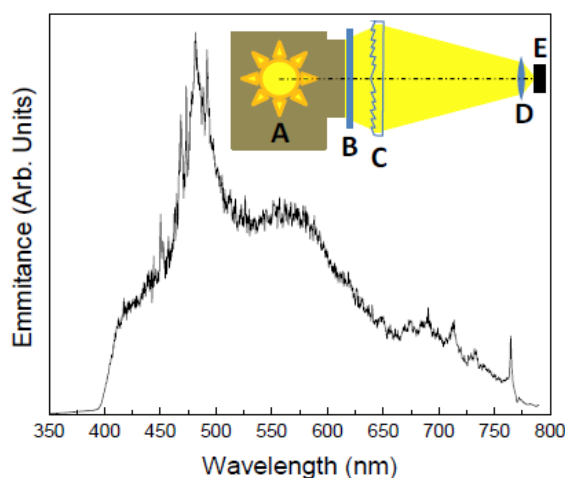


Figure 7.8: The emission spectrum of the used solar simulator; inset: the set up of the solar absorption experiments, A: solar emission lamp, B: UV (<400 nm) filter, C: Fresnel focusing lens, D: plane-convex, near-field focusing lens, E: sample

7.3.1 Growth and Characteristics of DLC:Ni catalysts.

Firstly, a DLC:Ni is grown on Si substrates by Pulsed Laser Deposition (PLD) using a graphite target and Ni sectors of varying area (see online supporting information). This process results in nanostructured films with Ni particle size in the range of approximately 10-30 nm, which appear as bright protrusions in the atomic force microscopy (AFM) image of figure 7.9a for sample #A. Then, the DLC:Ni/Si specimens were used as growth templates for T-CVD of CNTs at 700 °C using acetylene as a carbon source. T-CVD of CNTs has been also implemented on pure Ni catalyst layers grown by PLD and sputtering for comparison. The growth parameters for the DLC:Ni catalysts used in this study are summarized in Table 7.1.

7.1: Growth parameters and structural/chemical features of the DLC:Ni catalysts and CNTs

Sample	Laser wave-length (nm)	Ni on film (% at)	sp ³ -C in DLC:Ni (% at)	DLC:Ni Density (g/cm ³)	CNT Density (g/cm ³)	CNT I _D /I _G	CNT Water CA (deg)
A	355	5.0±0.5	6±7	2.50	1.91	0.77	165
B	355	6.0±0.5	11±7	2.70	2.23	0.72	112
C	355	7.0±0.5	13±7	3.05	2.26	0.71	105
D	355	11.0±0.5	15±7	3.35	2.36	0.70	92
E	355	100	-	-	-	0.73	132
F	532	8.0±0.5	18±7	2.48	2.5	0.79	158
G	532	9.0±0.5	15±7	2.64	2.7	0.79	128
H	532	13.0±0.5	17±7	2.90	2.3	0.77	97
I	532	16.5±0.5	11±7	2.82	2.9	0.71	94

An essential issue is the accurate description of the chemistry of the outer surface of the catalyst layer, which is exactly the part of the catalysts that reacts with the flowing acetylene to form CNTs during T-CVD; Auger Electron Spectroscopy (AES) fulfils the criterion, as being surface-sensitive [21,60] and, thus, it has been employed for the determination of the Ni content and the fraction of the sp³-bonded carbon on the surface of DLC:Ni layers. The sizes of the Ni nanoparticles on the DLC:Ni surface have been determined from AFM images. The Ni content has been determined from the relative strength of the C_{KVV} and Ni_{LMM} peaks manifested in the *in situ* AES differential spectra taking into account the corresponding sensitivity factors, Table 7.1. Note that the small Ni atomic percentage corresponds to higher geometric surface coverage (SC) of Ni, because of the different ionic radii of Ni and C as shown in AFM image of figure 7.9a (sample A). The C hybridization (sp³/sp² ratio) has been determined from the broadening of the C_{KVV} peak [21,60] and has been confirmed by analyzing the C1s envelope of X-Ray Photoelectron Spectra (XPS) [60,61]. The thickness, the density and the nanometric surface roughness of the DLC:Ni layers have been determined by X-Ray Reflectivity (XRR) following the analysis procedures presented on Ref. 25. The main structural and chemical features of the DLC:Ni catalysts are summarized in Table 7.1.

7.3.2 Structural and morphological features of CNTs.

The CNT layers, which have been grown on the DLC:Ni templates, are purely graphitic according to XPS and AES analysis (see on line supporting information), they follow a base growth and exhibit strong morphological variations that are dictated predominantly by the [Ni] concentration on the DLC:Ni surface. This is revealed by the plan-view SEM images presented in figure 7.9b; the capital letters of the SEM images correspond to the relevant samples in Table 7.1.

CNT grown on samples #A and #B exhibit strongly interlinked CNT bundles. The main difference between these two sets of CNTs is the average density; in particular, the sample #A is not fully covered and bundles of interlinked CNT of average diameter about 40 nm co-exist with dark (empty) regions in the corresponding SEM image. The SEM image of sample #B reveals a similar geometry of interlinked CNT, which however, fully cover the DLC:Ni catalyst. On the contrary, for higher Ni content in the catalyst (sample #C) the CNT are becoming thicker (>100 nm); in that case the interlinking of CNT is substantially reduced. Finally, the sample #D, which is the one with the maximum Ni content in the corresponding DLC:Ni catalyst template, is characterized by highly aligned thick (>100 nm) multiwall CNT.

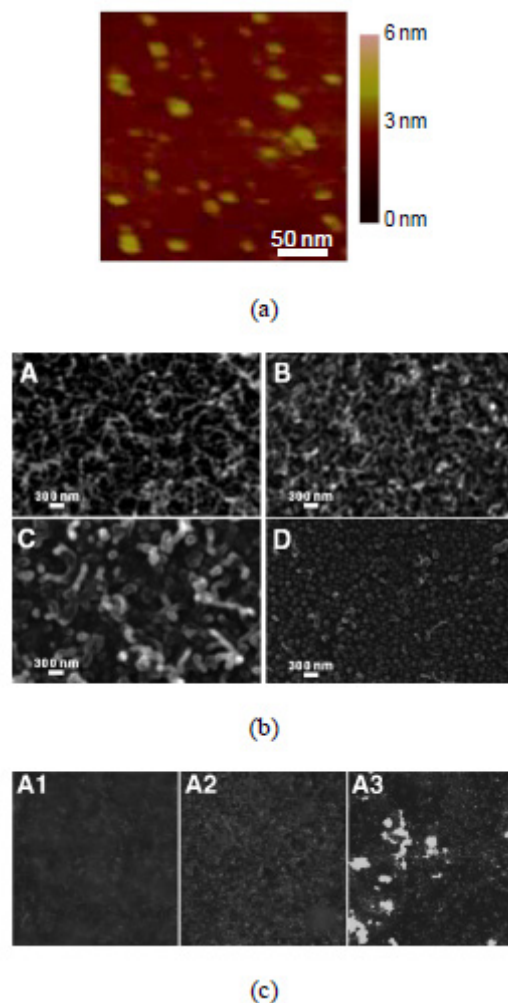


Figure 7.9: (a) AFM image from a DLC:Ni template (sample A) before the growth of CNTs, (b) SEM images of CNTs grown by various conditions on DLC:Ni (the capital letters correspond to the data of table 7.1); (c) Optical microscope images of sample A, A1: as grown (the image is blurred because there CNTs at many different focal depths), A2: after duct tape testing and ultrasonication in water, and A3: after ultrasonication in methanol

The integrity and durability of all the CNT systems grown using the DLC:Ni catalyst templates are exceptional. Unlike the CNT grown on pure Ni, either sputtered or PLD-grown, the CNT samples grown on the DLC:Ni templates endured duct-tape testing, blowing with >3 bar compressed air and ultrasonication in water (for 5 min), as shown for sample #A in the optical microscopy images of figure 7.9c; the integrity of the sample is only challenged by ultrasonication in methanol.

XPS analysis did not detect any traces of Ni on the CNT surface (see on-line supporting information) and proves that a base growth of CNT has occurred on the DLC:Ni templates. The surface morphology of CNT cannot be studied neither by XRR, because their surfaces are too rough, nor by AFM, due to the flexibility of the CNT tips that are swinging when an AFM tip is approaching. Therefore, the qualitative results deduced previously from the SEM observations have been confirmed and quantified by non-specular X-ray reflectivity analysis, which is appropriate for the study of rough surfaces [59,62]. The CNT density has been determined from the critical angle [25], which according to the Distorted-Wave Born Approximation (DWBA) is manifested as the low-angle Yoneda wing in the nonspecular reflectivity scan (see on line supporting information) [26]. The evolution of density of the CNT samples *vs.* the Ni content on the DLC:Ni catalysts is presented in figure 7.10a.

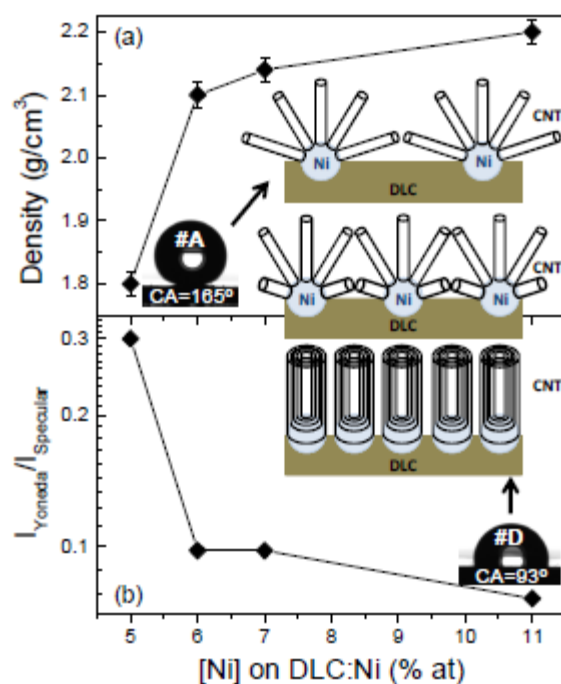


Figure 7.10: The variation of (a) the CNT layer density and (b) the ratio of the intensity of the Yoneda wings over the specular x-ray reflectivity, which is associated with the surface roughness. The insets depict the water contact angles for samples A and D and a sketch displaying the correlation between the Ni nanoparticle density and the CNT's morphology

It is evident that sample D ([Ni]=11% at) is almost as dense as graphite, proving that the aligned CNT are densely packed. As the CNTs become less aligned (samples C, B) the average density is indeed reduced, confirming the SEM observations; finally, sample A, which exhibits the less packed morphology in the SEM images, is substantially underdense. An estimation of the surface roughness can be deduced from the ratio of intensities of the satellite Yoneda wings and the specular peak, $I_{Yoneda}/I_{specular}$ ratio, in the X-ray data [59,62] (see supporting on line information). Sample #A, which is not fully covered by CNTs, are the rougher and the surface roughness (that is associated with the $I_{Yoneda}/I_{specular}$ ratio) is gradually reduced as the sample is fully covered by CNTs (sample #B) and the CNTs become gradually more aligned (samples #C,D). The variation of the surface roughness of the CNTs has a severe effect on their hydrophobicity. Thus, the interlinked and most rough sample #A is superhydrophobic (water contact angle 165° , exceeding the superhydrophobic limit of 150° , due to the two scales of surface features, i.e. ~ 30 nm tube diameter and ~ 1 μ m CNT bundle width), while the most aligned and smooth sample #D

exhibits an intermediate water contact angle (93°). Another confirmation of the morphology of the grown CNT systems over the DLC:Ni catalysts has been also provided by four probe electrical measurements. According to the analysis of the I-V measurements all the CNT systems were conducting with a resistance ranging between 1.7 and 110 k Ω , which are typical of CNTs [63] of the length of our own, due to the morphology variations.

In addition to the study of the morphological features, Raman spectroscopy (RS) was used to evaluate the structural quality of the produced CNT. The Raman spectra of all produced CNT/DLC:Ni samples exhibit the main characteristic graphitic Raman features [13,29,30], at around 1340 and 1600 cm^{-1} corresponding to graphite D (disordered) and G (tangential stretching E_{2g} mode) bands, respectively [64,65] and the corresponding second order D' and G' bands at 2690 and 2900 cm^{-1} , respectively. The relative intensity of D- and G-bands (I_D/I_G), reveals the degree of disorder in the graphitic sheets [13,64]; it was found that that more ordered CNT samples correspond to lower I_D/I_G ratios and sharper G peaks [64]. The Raman results indicate that the structural features of the grown CNT are correlated with the Ni grain size in the catalyst layer, as determined by Scherrer analysis of the Grazing Incidence X-Ray Diffraction (GIXRD) data (figure 7.11a), as well as with the Ni content of the catalyst (Figs. 3b,c).

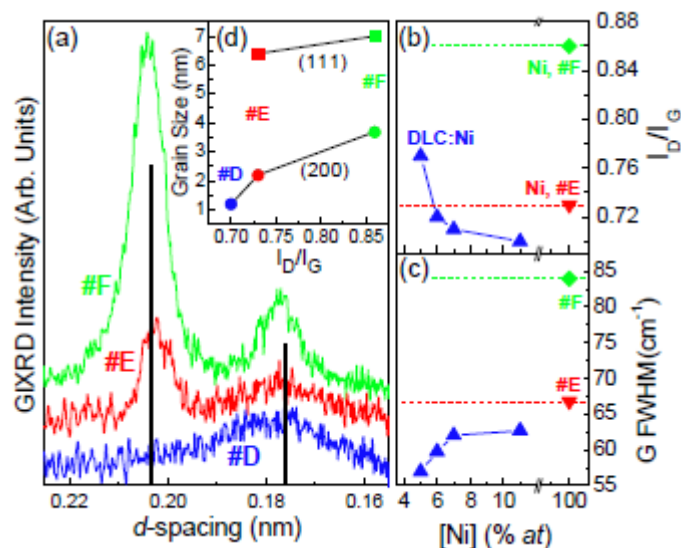


Figure 7.11: (a) GIXRD data of the various catalyst layers; the black bars indicate the reference diffraction lines of Ag powder, (b),(c) the ID/IG ratio and the G FWHM of CNTs vs. the Ni content on the catalyst, respectively, (d) the correlation of the Ni grain size with the ID/IG ratio of the CNTs

In particular, CNT grown using DLC:Ni catalyst, with fine Ni grain size (hardly identifiable by XRD), exhibit substantially lower I_D/I_G ratios compared to the CNT grown using pure Ni catalyst layers deposited by PLD and sputtering (figure 7.11d). Figures 7.11b,c show the variations of the I_D/I_G ratio and of the broadening (Full Width at Half Maximum-FWHM) of the G peak vs the [Ni] content of the corresponding DLC:Ni catalyst. The I_D/I_G ratio was exceptionally low for all CNT systems grown on the DLC:Ni catalysts templates (figure 7.11b) and decreases with [Ni]. The observed I_D/I_G and G-FWHM values are similar or lower than those reported for the best quality multiwall CNTs so far [13-15, 64], indicating that the DLC:Ni catalyst improves substantially the structural quality of the grown CNTs. The G-FWHM increases with increasing [Ni] content in the DLC:Ni catalyst (figure 3c), despite the subsequent decrease of I_D/I_G ratio. This is another indication of the gradual alignment of the CNT with increasing [Ni] content in the catalyst layer, since aligned multiwall CNTs exhibit additional contributions to the G-peak at 1575, 1590 and 1623 cm⁻¹ due to additional vibration modes [65]. This is in accordance with the SEM images of figure 7.9b.

7.3.3 Functional properties of CNT and solar applications.

The thermal emission from the CNT surfaces has been acquired by a CEDIP mid-wavelength infrared camera with a cooled InSb detector (waveband 3-5 μm), a frame rate of 150 Hz and a focal plane array pixel format of 320x240 with focal length 50 mm. The thermal resolution of the camera is 20 mK and the integration time is 345 μs .

CNTs are inherently black (i.e. they absorb all wavelengths of the visible light) [1,66-68] and, in particular, low density bundles of nanotubes have been recently identified as perfect optical absorbers [1] finding applications in stray light control [66] and cryptography [67] and they have been proposed for applications in pyroelectric detectors and solar energy conversion [1]. After the in depth morphological and structural characterization of the produced CNT systems of this work, their optical properties have been thoroughly investigated. The produced CNT exhibit exceptionally low optical reflection (acquired in the 240-790 nm range and in vertical incidence geometry); the reflectivity of the CNT samples for the three primary colors (Red-Green-Blue) are displayed in table 7.2.

Table 7.2: The main properties of the CNT grown using the DLC:Ni templates

Sample	Morphology	Density (gr/cm^3)	Resistance ($\text{k}\Omega$)	I_D/I_G	G FWHM (cm^{-1})	Water Contact Angle ($^\circ$)	Reflectivity		
							Red 635 nm	Green 535 nm	Blue 475 nm
A	Interlinked	1.8	27.438	0.77	57.0	165	5×10^{-4}	2×10^{-4}	$< 5 \times 10^{-5}$
B	Interlinked	2.1	10.099	0.72	59.8	112	4×10^{-3}	2×10^{-3}	1.4×10^{-3}
C	Partly Interlinked	2.14	1.745	0.71	62.1	105	2×10^{-2}	1.8×10^{-2}	1.5×10^{-2}
D	Aligned	2.2	110.736	0.70	62.7	93	1.8×10^{-1}	1.4×10^{-1}	1.2×10^{-1}

The reflectivity values for the fully dense sample #D are similar to those of graphite [1]. On the contrary, the lowest density sample #A exhibits reflectivity lower than 5×10^{-4} for all wavelengths and less than 5×10^{-5} for the shorter wavelengths. In addition to the spectral dependence of optical reflectivity, the angular dependence of specular reflectivity of s- and p-polarized red light (657.5 nm) is also investigated; the relevant data for the marginal cases of samples #A and #D are presented in figure 7.12a.

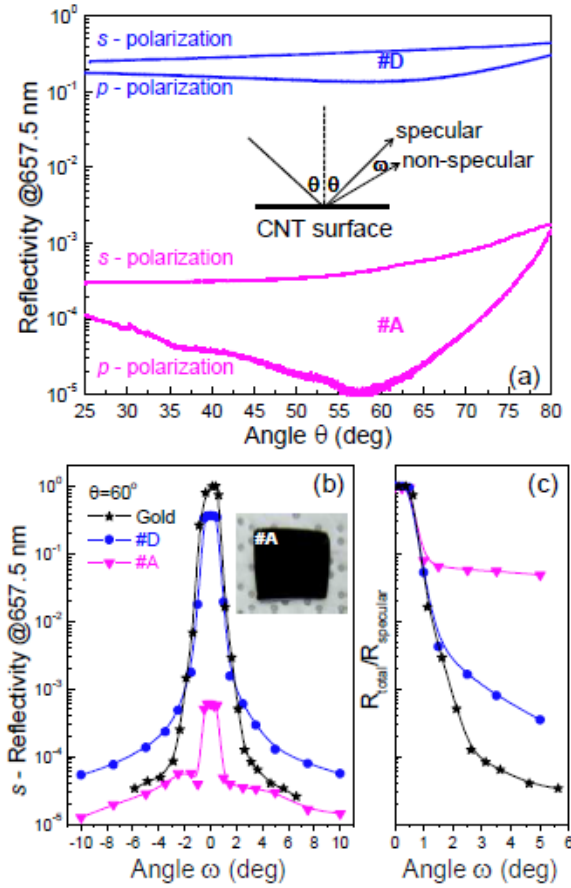


Figure 7.12: (a) the angular dependence of the specular reflectivity of *s*- and *p*-polarized red light from the marginal cases of samples #A (low density, interlinked CNT) and #D (fully dense aligned CNTs), (b) Non-specular optical reflectivity at 657.5 nm of the same CNT samples; the inset shows the actual black appearance of sample #A (photographed on standard clean room paper), (c) the ratio of the total reflectivity (specular and non-specular) over the non-specular component. The angles θ and ω are defined in the inset of (a)

The values for sample #A are exceptionally low, at least two orders of magnitude less than those for sample #D, which imply a very low refractive index as predicted by Garcia-Vidal et al [34] and demonstrated by Yang et al [1] and by Shi et al [67]. It is worth noting that sample #A consists of interlinked CNT proving that the alignment is not a prerequisite for producing super-black CNT-based materials; instead, the low density of the CNT samples seems to be the essential feature for that.

The study of the surface scattering of light to non specular directions is essential, since the produced CNT, especially the low-density interlinked sample #A, have very

complex surfaces, exhibiting features of two length scales, i.e. ~ 30 nm tube diameter and ~ 1 μm CNT bundle width. The non-specular reflectivity has been measured by measuring the intensity of a 657.5 nm, s-polarized laser beam while scanning the off-specular angle ω around the specular angle $\theta=60^\circ$ as presented in the inset of figure 7.12a. The reflectivity values around the specular position $\theta=30^\circ$ ($\omega=0^\circ$) for the marginal cases of CNT samples #A (low-density, interlinked) and #D (fully dense, aligned), as well as for a gold mirror for comparison, are presented in 7.12b. Both CNT samples exhibit a clear specular peak at $\omega=0^\circ$. This is quite different from what has been observed by Yang et al [1] in low-density aligned tubes, most likely due to the higher density of our samples and the complex morphology of our CNT. Nonetheless, even the specular reflection from sample #A is exceptionally low and the diffuse surface light scattering ($\omega \neq 0^\circ$) is two orders of magnitude lower ($<10^{-5}$). The diffuse surface light scattering for both samples #A and #D is substantially higher than that of the gold mirror (this is better illustrated in 7.12c) proving that their overall optical response is greatly affected by their surface roughness.

Summarizing, the CNT produced by this technology, especially the low density interlinked CNT similar to sample #A, combine exceptional assets such as high optical absorption and low reflectivity over the whole visible spectrum, durability to environmental challenges, superhydrophobic and self cleaned surfaces, and high electrical and thermal conductivity [6]. These assets make these materials promising for thermal harvesting of solar energy, such as in trough or parabolic collectors and solar water heaters. In order to investigate this perspective, we have set up the following solar simulation experiment. The divergent light of a solar simulator lamp is collected by a large scale Fresnel lens and concentrated by a secondary lens to achieve a power density of 20 kW/m^2 on the sample surface (see on line supporting information), which is a very moderate concentrated solar power. The sample temperature is monitored by a thermocouple attached on the backside of the sample and by a mid-infrared thermal camera. The CNT sample #A is illuminated by the 20 kW/m^2 concentrated solar light and its temperature vs. time is recorded by the thermocouple and the thermal camera; the thermocouple and camera indications are in excellent agreement (in the range of $\pm 2^\circ\text{C}$) for the CNT samples due to the high thermal conductivity of CNTs. The temperature

increase of the CNT surface vs. time, as recorded by the thermal camera in the middle of the sample, is shown in the bottom side of figure 7.13 (black line); the spatial distribution of temperature on the CNT surface of sample #A at various solar illumination times is demonstrated in the snapshots of the thermal camera in the upper part of figure 7.13, where the CNT sample #A is clearly resolved from the background. In the medium part of figure 7.13 in log-scale in order to reveal the dynamics of temperature increase on the CNT surface at the very initial stages of solar illumination.

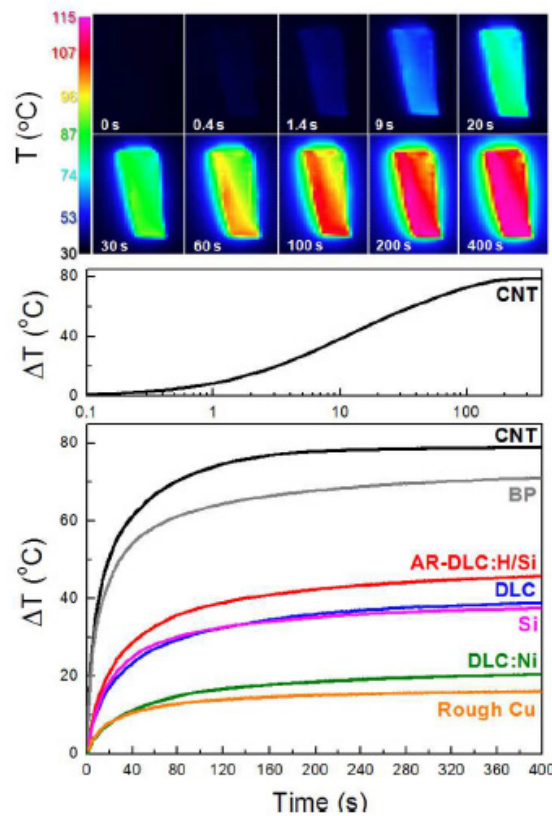


Figure 7.13: Lower part: The temperature increase of the surface of the CNT sample #A due to exposure to the concentrated solar light in comparison to various reference samples such as: (i) a bare Si wafer, (ii) commercial, rough, black paint (BP), (iii) a Si wafer coated by a hydrogenated DLC antireflection layer (AR-DLC:H/Si), (iv) the corresponding DLC:Ni catalyst layer, (v) a pure DLC films of intermediate sp^3 content ($\sim 50\%$), and (vi) a roughened Cu plate. Intermediate: The initial stages of temperature increase due to solar absorption by CNT. Upper part: Snapshots from the thermal camera demonstrating the effective solar absorption by sample #A, which is clearly resolved after 1 s exposure to sunlight

In addition to the CNT sample #A, the corresponding thermal emission curves for a variety of reference samples such as: commercial black acrylic matt paint (BP, grey line), the DLC:Ni catalysts film used for CNT growth (sample #A, green line) a pure Si wafer surface (magenta line), a Si wafer coated by a hydrogenated DLC antireflection coating at 633 nm grown by plasma enhanced chemical vapor deposition (red line) and by intentionally roughened Cu (orange line), which is the standard material of trough collectors, are also shown in the bottom part of figure 7.13. It is evident that the super black CNT can achieve by far the highest temperature increase among all samples, demonstrating their substantial solar potential.

7.4 Silver contained nanocomposite amorphous diamond-like carbon films (a-C:Ag)

Carbon is known for its potential in the biomedical field such as for cardiovascular, orthopaedic and dental applications. Silver is regularly incorporated as a modifying element for the improvement of the adhesion of carbon thin films and to provide antimicrobial properties and protect an implant from infection. In part of the chapter, carbon-based thin films developed by two deposition techniques; Plasma Enhanced Chemical Vapour Deposition (PECVD) and Pulsed Laser Deposition (PLD) were assessed for their cytotoxicity and generally cell behaviour in contact with two human cell lines for various time periods. Human Umbilical Vein Endothelial Cells (HUVEC) and HeLa cells, which is an immortalised carcinogenic cell series with tolerance properties against demanding surfaces were studied by our collaborators in the Aristotle University of Thessaloniki. Cultures were evaluated for cell viability / proliferation at days 3, 4 and 7 (MTT assay) and observed by the optical microscope (methylene blue staining) and by the scanning electron microscope (SEM) in order to assess the cell morphology and cell adhesion during these time periods.

For comparison purposes control samples were prepared. One control related to the cell growth and it was the standard tissue culture plate, while the second control was the silicon wafer, and the substrate were all the thin films were grown.

The samples used in this study are summarized in table 7.3. The basic growth conditions (target material and the laser wavelength used for the ablation) are displayed.

The results of AES and EELS analyses are also summarized in Tables 7.3, 7.4.

Table 7.3: The main growth conditions of the a-C:H samples used in this study

SAMPLE	Power Type	Ar Flow (sccm)	C ₂ H ₂ Flow (sccm)	Rf Power (W)	V _b (V)	P _{working} (mbar x 10 ⁻²)	Deposition Time (min)	sp ³ (% at)	Density (g/cm ³)	Roughness R _q (RMS) (nm)
a-C:H_1	rf	7	3	80	-	4	10	20	1.5	0.5
a-C:H_2	rf	5	5	80	-	4	10	40	1.7	0.2
a-C:H_3	rf	5	5	80	-	5	5	40	1.7	0.2
a-C:H_4	dc	44	32	-	200	48	120	44	1.8	20.1*

* The roughness R_q (RMS) for the a-C:H_4 group of samples was calculated by the 30x30μm² image as there were many aggregates on the surface.

Table 7.4: The main growth conditions of the a-C and a-C with silver inclusion (nominal silver concentration on the PLD target) samples used in this study

Samples	Target material	Laser wavelength (nm)	Pulse energy (J)	Ag area on target (%)	sp ³ (% at)	[Ag] (% at)	Surface Roughness (nm)
a-C	PG	355	35	0.0	28	0	-
a-C:Ag_1	HPG/Ag	355	35	6.25	62	1.1	1
a-C:Ag_2	HPG/Ag	355	35	25	17	5.5	1
a-C:Ag_3	PG/Ag	355	35	25	9	4.3	-
a-C:Ag_4	PG/Ag	355	35	12.5	14	2.3	-
a-C:Ag_5	PG/Ag	355	35	6.25	23	0.7	-

Both PECVD and PLD are techniques that are able to provide thin films with properties such as chemical inertness, lower friction coefficient, high hardness and good biocompatibility and therefore produce thin films ideal for biomedical applications. In this study, the PLD grown thin films showed higher hydrophobic behaviour compared with the PECVD grown thin films and this could be attributed to the different surface topography and chemistry between the thin films. According to another study, the typical threshold for hydrophobicity in biomaterials is of a contact angle of about 65° [69, 70]. Figure 7.14 shows the contact angles for the different thin films. The a-C:H films, which were grown by PECVD, are more hydrophobic than the pure Si but less hydrophobic than the thin films grown by PLD. The as-grown a-C thin films (by PLD) with the different silver inclusions are observed to be very hydrophobic. The PLD grown thin films had a contact angle of about 80° while the PECVD grown thin films were around 65° - 70° .

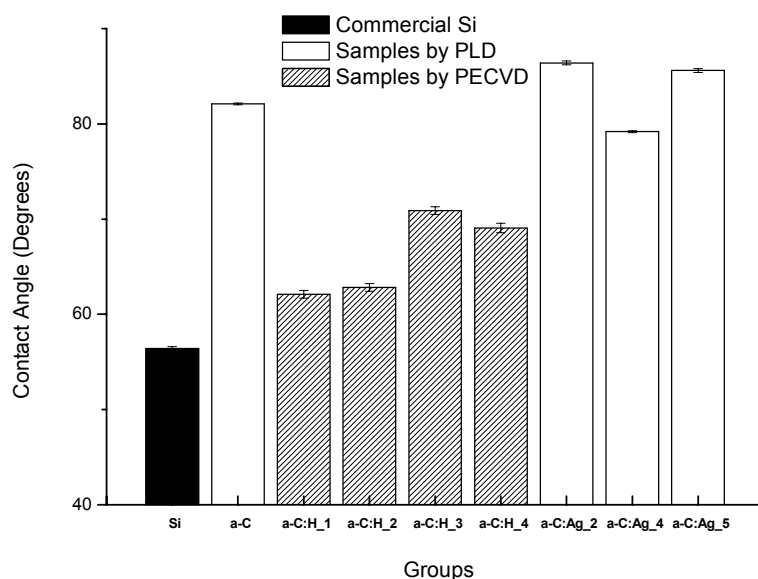


Figure 7.14: Contact Angle measurements of a-C:H grown films by PECVD and of the as-grown a-C with silver inclusions by PLD

It was observed that the PECVD grown thin films of a-C:H were not toxic to the HUVEC at 3, 4 and at 7 days, as shown in figure 7.15. The three different time periods were examined in order to investigate the cell proliferation on the surfaces of the films.

At a closer look between the time periods, it is clear that at 3 days all the thin films and the pure Si sample showed higher cell viability compared to the control (statistically different), while at 7 days the cell viability was similar to the control. Furthermore all the groups followed a similar trend at 3 and 7 days, with the group of a-C:H_3 to have the highest cell viability and the a-C:H_4 always the lowest but similar to the controls and the pure Si. The main difference between these groups is on their surface morphology due to the deposition parameters as shown in table 7.3. The as grown a-C:H_1 and 2 did not appear to have any differences. At the time period of 4 days there was a slight decrease of the cell viability percentage compared to the 3 days curve. The information drawn by this time period were not as valuable so it was chosen not to investigate again the 4 days as a time point for this type of cytotoxicity/cell proliferation assay.

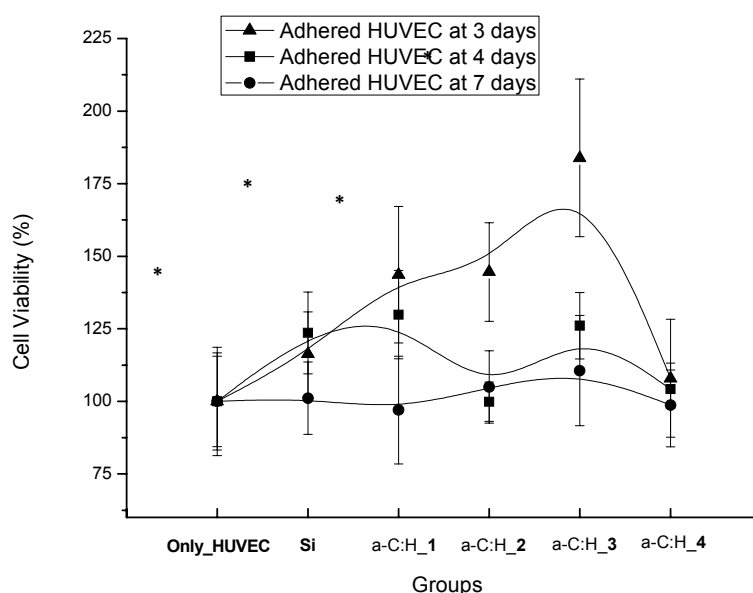


Figure 7.15: Cell viability percentage of a-C:H grown films by PECVD compared to control for three time periods. * Statistically different from control samples (only cells) (t-test; two tailed; $p < 0.05$; $n < 4$) for the 3 and 4 days curves. For the 7 days curve there was not any statistically difference between the groups of thin films and the control

Figure 7.16 shows the cell viability percentage of HUVEC in contact with two different groups of a-C grown films developed by PLD for 3 days. It cannot be considered toxic to HUVEC, however it has to be investigated further. The as-grown a-C:Ag group had a high level of cell viability compared to the control and the a-C group.

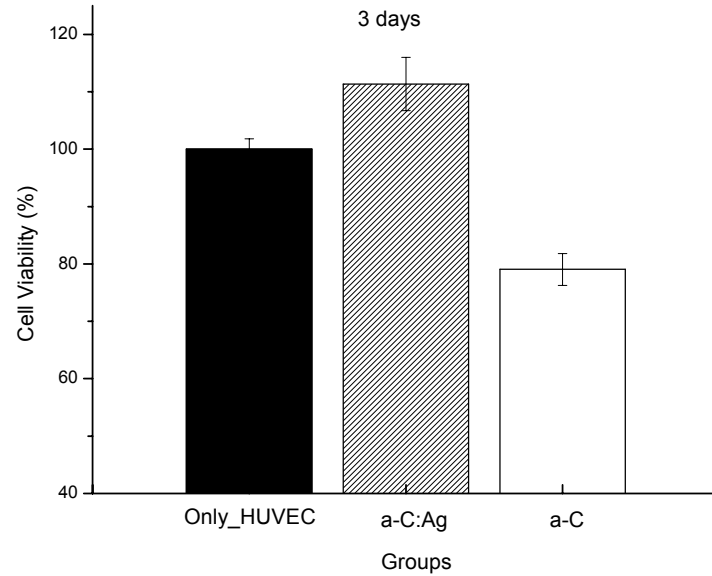


Figure 7.16: Cell viability percentage of the as-grown a-C with silver inclusions by PLD compared to the control for the time period of 3 days. These groups are all statistically different from the control group and from each other; therefore no sign is denoted on the graph

On an attempt to investigate further the cytotoxicity and cell proliferation of thin films grown by PLD, another test was performed. Figure 7.17 demonstrated that the PLD grown thin films of a-C and with silver inclusions were not toxic to the HeLa cells for the 3 days, and they were actually similar to the control. However at 7 days there was an apparent decrease of the cell viability percentage of all the groups compared to the control, which however was not statistically different. Furthermore all groups followed a similar trend at 3 and 7 days, with the group of a-C films, a-C:Ag_1, and a-C:Ag_3 to a-C:Ag_4 to have the highest cell viability and the a-C:Ag_2 and a-C:Ag_5 always the lowest. The variations of these groups were due to the type of target material and on the silver concentration, as shown in table 7.3.

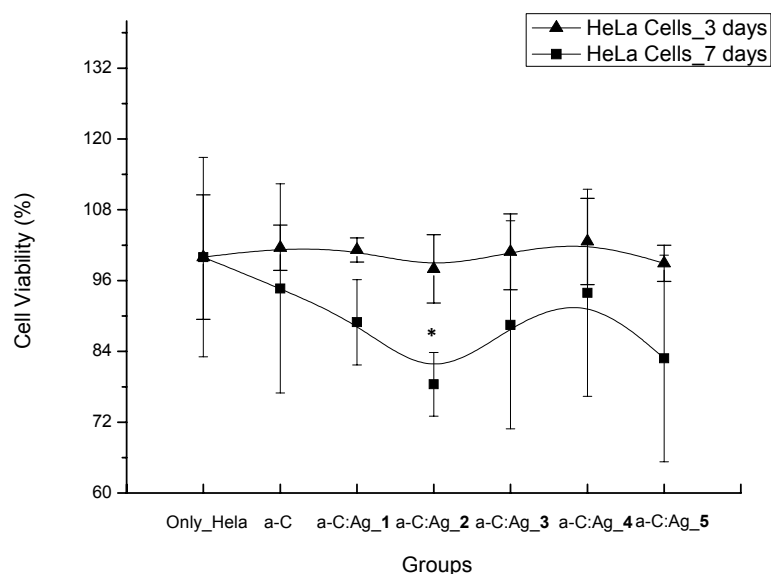


Figure 7.17: Cell viability percentage of the as-grown a-C thin films with silver inclusions by PLD compared to control for two time periods. * Statistically different from control samples (only cells) (t-test; two tailed; $p < 0.05$; $n < 4$) for only the 7 days curve. For the 3 days curve there was not any statistically difference between the groups of thin films and the control

A direct comparison of the thin films grown by the two different deposition techniques is not feasible as there were different cell lines investigated and furthermore there was the presence of silver in some of the groups. Both cell types are human cell lines, commonly used for the cytocompatibility evaluation of biomaterials. In particular HUVEC are used for the study of materials related with the haemocompatibility and endothelialisation of materials [71], while HeLa cells are used for the cytotoxicity investigation of materials. Generally human cell cultures, established from normal tissues, provide a more representative model of the in vivo cell population being very sensitive to external environmental changes, allowing the detection of subtle cell responses.

7.5 Conclusions

DLC:Ni nanocomposite films have been grown by PLD using either a 355 nm or 532 nm laser beams. It turns out that Ni is incorporated into the films produced using the 355 nm laser, while the Ni has the form of both nanoparticles into DLC and microparticles on the DLC surface for the films produced using the 532 nm laser. The DLC:Ni films have

been used as templates for CNT growth with the morphology, the structural quality (in terms of Raman), hydrophobicity and the electrical properties (conductivity) of the grown CNTs bundles vary significantly with the Ni content in the DLC:Ni.

In the case of the DLC:Ni nanocomposite layers that have been produced by PLD with 355nm laser beam wavelength the formed Ni nanoparticles are smaller than 30 nm because DLC inhibits the growth of Ni. The control of the Ni particles at the nanoscale has been proven an efficient pathway for the development of extremely durable and firmly attached CNTs of varying morphologies (from interlinked to aligned), tube thickness (30-100 nm), density and structural quality (indicated by the Raman data). In particular, the low density interlinked CNT grown using the DLC:Ni templates exhibit an extraordinary combination of functional properties, such as super-hydrophobic surfaces, extreme optical absorption in the whole visible range, exceptionally low optical reflection and high thermal conductivity. This combination of assets of the produced CNT offers a great potential for solar thermal applications that has been confirmed by the specially designed solar testing experiments performed.

As far as concerned the a-C:Ag and the a-C:H films the findings showed that the a-C:H and a-C:Ag thin films did not exhibit any cytotoxicity levels. The surface topography of the thin films depended on the deposition parameters. A comparison of the hydrophobicity of the thin films showed higher contact angles for the PLD grown thin films. The cell adhesion and spreading was at a higher level on the PLD grown thin films. The effects of the composition, topography, and wettability of the surface of the thin films are the main factors affecting the cytocompatibility of carbon based thin films for medical applications.

7.6 References

- [1] Z.-P Yang, L. Ci, J.A. Bur, S.-Y. Lin, P.M. Ajayan, *Nano Lett.* **8**, 446 (2008)
- [2] E. Kymakis, G.A.J. Amaratunga, *Appl. Phys. Lett.* **80**, 112 (2002)
- [3] D.M. Guldi, G.M.A. Rahman, F. Zerbetto, M. Prato, *Acc. Chem. Res.* **38**, 871 (2005)
- [4] Avouris, P.; Freitag, M.; Perebeinos, V. *Nature Photon.* **2**, 341 (2008)
- [5] T. Hasan, Z. Sun, F. Wang, F. Bonaccorso, P.H. Tan, A.G. Rozhin, A.C. Ferrari, *Adv. Mater.* **21**, 3874 (2009)
- [6] N. Mingo, D.A. Broido, *Nano Lett.* **5**, 1221 (2005)
- [7] H. Huang, C. Liu, Y. Wu, S. Fan, *Adv. Mater.* **17**, 1652 (2005)
- [8] G. Zhong, S. Hofmann, F. Yan, H. Telg, J.H. Warner, D. Eder, C. Thomsen, W.I. Milne, J. Robertson, *J. Phys. Chem.* **C113**, 17321 (2009)
- [9] J.J. Jackson, A.A. Puretzky, K.L. More, C.M. Rouleau, G. Eres, D.B. Geohegan, *ACS Nano* **4**, 7573 (2010)
- [10] J.B. In, C.P. Grigoropoulos, A.A. Chernov, A. Noy, *Appl. Phys. Lett.* **98**, 153102 (2011)
- [11] M. Yudasaka, Y. Kasuya, F. Kokai, K. Takahashi, M. Takizawa, S. Bandow, S. Iijima, *Appl. Phys.* **A74**, 377 (2002)
- [12] M.H. Römmeli, E. Borowiak-Palen, T. Gemming, T. Pichler, M. Knupfer, M. Kalbáč, L. Dunsch, O. Jost, S.R.P. Silva, W. Pompe, B. Bóchner, *Nano Lett.* **5**, 1209 (2005)
- [13] T. Tsoufis, P. Xidas, L. Jankovic, D. Gournis, A. Saranti, T. Bakas, M.A. Karakassides, *Diam. Relat. Mater.* **16**, 155 (2007)
- [14] B. Zhao, D.N. Futaba, S. Yasuda, M. Akoshima, T. Yamada, K. Hata, *ACS Nano* **3** 108 (2009)
- [15] M. Cantoro, S. Hofmann, C. Mattevi, S. Pisana, A. Parvez, A. Fasoli, C. Ducati, V. Scardaci, A.C. Ferrari, J. Robertson, *J. App. Phys.* **105**, 064304 (2009)
- [16] Y. Li, R. Cui, L. Ding, Y. Liu, W. Zhou, Y. Zhang, Z. Jin, F. Peng, J. Liu, *Adv. Mater.* **22**, 1508 (2010)
- [17] S. Musso, S. Porro, M. Giorcelli, A. Chiodoni, C. Ricciardi, A. Tagliaferro, *Carbon* **45**, 1133 (2007)

- [18] S.A. Steiner, T.F. Baumann, B.C. Bayer, R. Blume, M.A. Worsley, W.J. Moberly-Chan, E.L. Shaw, R. Schlogl, A.J. Hart, S. Hofmann, B.L. Wardle, *J. Am. Chem. Soc.* **131**, 12144 (2009)
- [19] A.W. Orbaek, A.C. Owens, A.R. Barron, *Nano Lett.* **11**, 2871–2874 (2011)
- [20] K.L. Saenger, J.C. Tsang, A.A. Bol, J.O. Chu, A. Grill, C. Lavoie, *Appl. Phys. Lett.* **96**, 153105 (2010)
- [21] G. Matenoglou, G.A. Evangelakis, C. Kosmidis, S. Foulis, D. Papadimitriou, P. Patsalas, *Appl. Surf. Sci.* **253**, 8155 (2007)
- [22] A. Siozios, D.C. Koutsogeorgis, E. Lidorikis, G.P. Dimitrakopoulos, Th. Kehagias, H. Zoubos, Ph. Komninou, W.M. Cranton, C. Kosmidis, P. Patsalas, *Nano Letters* **12**, 259 (2012)
- [23] S.E. Rodil, R. Olivares, H. Arzate, *Bio-Medical Mater. Eng.* **15**, 101 (2005)
- [24] S. Logothetidis, M. Gioti, P. Patsalas, C. Charitidis, *Carbon* **37**, 765 (1999)
- [25] C. Charitidis, S. Logothetidis, M. Gioti, *Surf. Coat. Tech.* **125**, 201 (2000)
- [26] J. Robertson, *Mater. Sci. Eng. R* **37**, 129 (2002)
- [27] M. I. Jones, I. R. McColl, D. M. Grant, K. G. Parker, T. L. Parker, *J. Biomed. Mater. Research* **52**, 413 (2000)
- [28] S. P. J. Higson, P. M. Vadgama, *Analytica Chimica Acta* **300(1-3)**, 77 (1995)
- [29] G. Dearnaley, A.R. McCabe, 4th World Biomaterials Congress, Berlin, (1992)
- [30] M. Allen, F. Law, N. Rushton, *Clinical. Mater.* **17**, 1 (1994)
- [31] D.P. Dowling, P.V. Kola, K. Donnelly, T.C. Kelly, K. Brumitt, L. Lloyd, R.Eloy, M. Therin, N. Weill, *Diam. Relat. Mater.* **6**, 390 (1997)
- [32] J.A. McLaughlin, B.J. Meenan, P. Maguire and N. Jamieson, *Diam. Relat. Mater.* **5**, 486 (1996)
- [33] J.A. Carlisle and O. Auciello, *Electrochem. Soc. Inter.* **12**, 28 (2003)
- [34] J. Wang, M.A. Firestone, O. Auciello, J.A. Carlisle, *Langmuir* **20**, 11450 (2004)
- [35] A. Härtl, E. Schmich, J.A. Garrido, J. Hernando, S.C.R. Catharino, S. Walter, P. Feulner, A. Kromka, D. Steinmüller, M. Stutzmann, *Nature Mater.* **3(10)**, 736 (2004)
- [36] J.Y. Chen, L.P. Wang, K.Y. Fu, N. Huang, Y. Leng, Y.X. Leng, P. Yang, J. Wang, G.J. Wan, H. Sun, X.B. Tian, P.K. Chu, *Surf. Coat. Technol.* **156**, 289 (2002)

- [37] P. Yang, N. Huang, Y.X. Leng, J.Y. Chen, R.K.Y. Fu, S.C.H. Kwok, Y. Leng, P.K. Chu, *Biomaterials* **24**, 2821 (2003)
- [38] S. Zhang, H. Du, S.E. Ong, K.N. Aung, H.C. Too, X. Miao, *Thin Solid Films* **515**, 66 (2006)
- [39] J.R. Monties, I. Dion, P. Havlik, F. Rouais, J. Trinkl, C. Baquey, *Artificial Organs* **21**, 730 (1997)
- [40] V. Karagkiozaki, S. Logothetidis, A. Laskarakis, G. Giannoglou, S. Lousinian, *Mater. Sci. Eng. B* **152**, 16 (2008)
- [41] S. Lousinian, S. Logothetidis, A. Laskarakis, M. Gioti, *Biomolecular Engineering* **24**, 107 (2007)
- [42] S. Lousinian, S. Kassavetis, S. Logothetidis, *Diam. Relat. Mater.* **16**, 1868 (2007)
- [43] I.De Scheerder, M. Szilard, Y.M. Huang, X.B. Ping, E. Verbeken, D. Neerinck, E. Demeyere, W. Coppens, F. van de Werf, *J. Invasive Cardiol.* **12**, 389 (2000)
- [44] K. Gutensohn, C. Beythien, J. Bau, T. Fenner, P. Grewe, R. Koester, K. Padmanaban, P. Kuehn, *Thromb. Res.* **99**, 577 (2000)
- [45] G.F. Yin, J.M. Luo, C.Q. Zheng, H.H. Tong, Y.F. Huo, L.L. Mu, *Thin Solid Films*, **345**, 67 (1999)
- [46] L.J. Yu, X. Wang, X.H. Wang, X.H. Liu, *Surf. Coat. Technol.* **128**, 484 (2000)
- [47] A. Alanazi, C. Nojiri, T. Kido, T. Noguchi, Y. Ohgoe, T. Matsuda, K. Hirakuri, A. Funakubo, K. Sakai, Y. Fukui, *Artif. Organs* **24**, 624 (2000)
- [48] N. Savvides, *J. Appl. Phys.* **59**, 4133 (1986)
- [49] A.K. Sharma, R.J. Narayan, J. Narayan, K. Jagannadham, *Mater. Sci. Eng. B, Solid-State Mater. Adv. Technol.* **77**, 139 (2000)
- [50] R.J. Narayan, *Diam. Relat. Mater.* **14**, 1319 (2005)
- [51] M. Andara, A. Agarwal, D. Scholvin, R. A. Gerhardt, A. Doraiswamy, C. Jin, R. J. Narayan, Chun-Che Shih, Chun-Ming Shih, Shing-Jong Lin, Yea-Yang Su, *Diam. Relat. Mater.* **15**, 1941 (2006)
- [52] F.R. Marciano, L.F. Bonetti, L.V. Santos, N.S. Da-Silva, E.J. Corat, V.J. Trava-Airoldi, *Diam. Relat. Mater.* **8**, 1010 (2009)
- [53] F. Tetard, P. Djemia, B. Angleraud, N. Mubumbia, P.Y. Tessier, *Surf. Coat. Technol.* **151**, 184 (2002)

- [54] P. Zhang, B.K. Tay, G.Q. Yu, S.P. Lau, Y.Q. Fu, *Diam. Relat. Mater.* **13**, 459 (2004)
- [55] J.S. Chen, S.P. Lau, Z. Sun, G.Y. Chen, Y.J. Li, B.K. Tay, J.W. Chai, *Thin Solid Films* **398**, 110 (2001)
- [56] A.P. Marques, R.L. Reis, J.A. Hunt, *Biomaterials* **23**, 1471 (2002)
- [57] G. Matenoglou, G.A. Evangelakis, C. Kosmidis, S. Foulis, D. Papadimitriou, P. Patsalas, *Appl. Surf. Sci.* **253**, 8155 (2007)
- [58] P. Patsalas, S. Logothetidis, P.C. Kelires, *Diam. Relat. Mater.* **140**, 1241 (2005)
- [59] S.K. Sinha, E.B. Sirota, S. Garoff, H.B. Sanley, *Phys. Rev. B* **38**, 2297 (1988)
- [60] S. Kassavetis, P. Patsalas, S. Logothetidis, J. Robertson, S. Kennou, *Diam. Relat. Mater.* **16**, 1813 (2007)
- [61] M. Quintana, K. Spyrou, M. Grzelczak, W.R. Browne, P. Rudolf, M. Prato, *ACS Nano* **4**, 3527 (2010)
- [62] T. Brennan, A.V. Hughes, S.J. Roser, S. Mann, K.J. Edler, *Langmuir* **18**, 9838 (2002)
- [63] M.S. Purewal, B.H. Hong, A. Ravi, B. Chandra, J. Hone, P. Kim, *Phys. Rev. Lett.* **98**, 186808 (2007)
- [64] M. Chhowalla, K.B.K. Teo, C. Ducati, N.L. Rupesinghe, G.A.J. Amaratunga, A.C. Ferrari, D. Roy, J. Robertson, W.I. Milne, *J. Appl. Phys.* **90**, 5308 (2001)
- [65] R. Saito, M. Hofmann, G. Dresselhaus, A. Jorio, M.S. Dresselhaus, *Adv. In Phys.* **60**, 413 (2011)
- [66] J.J. Butler, G.T. Georgiev, J.L. Tveekrem, M. Quijada, S. Getty, J.G. Hagopian, *Proc. of SPIE* **7862**, 78620D (2010)
- [67] H. Shi, J.G. Ok, H.W. Baac, L. Guo, *J. Appl. Phys. Lett.* **99**, 211103 (2011)
- [68] F.J. Garcia-Vidal, J.M. Pitarke, J.B. Pendry, *Phys. Rev. Lett.* **78**, 4289 (1997)
- [69] L. Yang, B.W. Sheldon, T.J. Webster, *Biomaterials* **30**, 3458 (2009)
- [70] A. Bruinink, A. Schroeder, G. Francz, R. Hauert, *Biomaterials* **26**, 3487 (2005)
- [71] M.M. Morshed, B.P. McNamara, D.C. Cameron, M.S.J. Hashmi, *Surf. Coat. Technol.* **163**, 541 (2003)

8 CONCLUSIONS

Summarizing, the successful growth of thin films with specific physical properties by various deposition techniques and post growth treatments was established. The growth of the thin films was carried out by means of plasma enhanced chemical vapor deposition (PECVD), magnetron sputtering and pulsed laser deposition (PLD) techniques. In specific cases, post growth treatment was also performed, by cold oxygen plasma process and by laser irradiation of 1064 nm and 266 nm wavelength with picosecond pulse duration.

The research can be categorized in the following elemental and structural films

- I. Single-element amorphous Carbon films
- II. Multi-element amorphous Zr-based metal films
- III. Metastable polycrystalline Ti-based metal films
- IV. Nanocomposite films consisting of embedded Nickel and Silver nanoparticles in amorphous Carbon matrix

The study, for every aforementioned category of thin films, was focused on the deposition parameters that influence their physical properties, as deduced by various electronic, structural, morphological and optical characterization techniques.

For the study of the single-element amorphous Carbon films a PECVD reactor was setup for the growth of a-C:H films using Ar and C_2H_2 reactants. The physical properties of the a-C:H films grown by PECVD are strongly determined by the kinetic energy of the Carbon ions that is mainly influenced by the deposition parameters, such as applied power, working pressure and reactants percentage ratio. Extended study of each deposition parameter separately was performed making able, the growth of a-C:H films with specific optical properties and thicknesses. These findings led to the capability of growth of a-C:H antireflection coatings covering every desirable wavelength of the visible spectrum.

In addition, the amorphous Carbon films were also studied with respect to their photosensitivity under laser irradiation. We used two laser beams with wavelengths of 1064nm and 266nm that have photon energy well above and below the energy band gap of the a-C:H films and pulse duration of some picoseconds. The findings show that the

alteration of the structural features and the optical properties (local variation of the refractive index in the range 1.60-1.95 or else 20% variation) of the a-C:H films are strongly influenced by the laser wavelength. In the case of the 1064 nm laser beam, the laser photons pass through a-C:H and are absorbed by the Silicon substrate resulting in local annealing followed by the formation of SiC at the a-C:H/Si interface; the phenomenon is accompanied by the formation of pinholes, as well. In addition, after exposure to the laser beam the a-C:H film is found to be enriched in sp^3 C-H bonds. In the case of the 266 nm laser beam irradiation, we found that strong optical absorption by the volume of the a-C:H occurs, followed by laser annealing of the a-C:H. Thus, after exposure to 266 nm laser beam a-C:H is graphitized with the Hydrogen to be partly outdiffused.

In the second part of this thesis, which also refers to amorphous structures, is focused in multi-element amorphous Zr-based metallic films. The amorphous binary Zr-Cu, ternary Zr-Cu-Me (Me= Al, Ti, Nb, Si) and the quaternary $Zr_{62}Cu_{23}Ti_9Si_6$ glassy films were grown, with the third elemental additions to be less than 10%. We found that post growth treatment by cold oxygen plasma results in the formation of Zr-based oxides in both monoclinic and tetragonal ZrO_2 or even pure tetragonal ZrO_2 that is usually stable only at high temperatures. The findings showed that the alteration of the third metallic addition element leads to the option of selecting not only the structure but also the surface details of the ZrO_2 . More specifically, in the case of the $Zr_{74.7}Cu_{19.7}Nb_{5.6}$ and the $Zr_{74}Cu_{21}Al_5$ in low oxidation times (10 seconds), the growth of pure tetragonal ZrO_2 with surface morphologies dominated by nanopillars of less than 100nm diameter or completely smooth surfaces was achieved, respectively. For longer oxidation times coexistence of the monoclinic and the tetragonal structures was observed with the nanopillars length to be increased, in the case of Zr-Cu-Nb, while in the case of the Zr-Cu-Al the surface remained smooth.

In the cases of $Zr_{78}Cu_{22}$, Zr-Cu-Me (Me= Ti₉, Si₆) and the quaternary $Zr_{62}Cu_{23}Ti_9Si_6$ the oxygen plasma treatment resulted in ZrO_2 in both monoclinic and tetragonal structures, but in different amounts, which were also altered with treatment times. The surface morphologies of these systems were strongly influenced, forming a powder-like surface in the case of the $Zr_{78}Cu_{22}$, while in the cases of Zr-Cu-Me (Me= Ti₉, Si₆) and the $Zr_{62}Cu_{23}Ti_9Si_6$

a complete rough surface was formed. We note that especially in the case of the $\text{Zr}_{62}\text{Cu}_{23}\text{Ti}_9\text{Si}_6$ a vertically oriented nanosponge-like structures of 300 nm diameter at specific time treatment.

The third part of the present thesis is focused on the growth of metastable polycrystalline Ti-based metallic films in the β -phase. In particular, Ti-based Ti-Nb, Ti-Hf and Ti-Nb-Hf at various stoichiometries were grown by magnetron sputtering. In the Ti-Nb the stabilization of the β -Ti was established at Nb additions more than 15 atomic percentage. In the case of Ti-Hf the stabilization of the the β -phase was not possible to be achieved, but additions of Hf up to 20 atomic percentage resulted in a distorted HCP structured Ti-based film. At higher Hf contents, the Ti-based films were grown in the martensitic crystal structure, known as α' -Ti or ω -Ti. In the case of the Ti-Nb-Hf films the additional elements of the Nb and the Hf also distorted the HCP lattice of the Ti for contents less than 15 atomic percentages, but at higher concentrations the stabilization of the β -phase of Ti was established. The densities of all grown Ti-based films follow the trend of the density versus the stoichiometry curves, in all the Ti-based systems, in analogy to the bulk counterparts, but lowered by approximately 30-40%, due to voids in the films volume.

The last part of the thesis refers to nanocomposite films consisting of embedded Ni and Ag nanoparticles in amorphous Carbon matrix (DLC:Ni), grown by PLD using either a 355 nm or 532 nm laser beams. It turned out that when using the 355 nm laser, Ni is incorporated mainly into the films, while in the case of the 532 nm beam, the Ni has the form of both nanoparticles into DLC and microparticles (droplets) on the DLC. The DLC:Ni films have been used subsequently as templates for CNT growth. We found that the morphology, the structural quality (in terms of Raman), hydrophobicity and the electrical properties (conductivity) of the grown CNTs bundles vary significantly with the Ni content in the DLC:Ni. In the case of the DLC:Ni nanocomposite layers that have been produced by PLD with 355nm laser beam wavelength, the Ni nanoparticles are smaller than 30 nm because DLC inhibits the growth of Ni. The control of the Ni particles at the nanoscale has been proven an efficient pathway for the development of extremely durable and firmly attached CNTs of varying morphologies (from interlinked to aligned), tube thickness (30-

100 nm), density and structural quality (indicated by the Raman data). In particular, the low density interlinked CNT grown using the DLC:Ni templates exhibit an extraordinary combination of functional properties, such as super-hydrophobic surfaces (contact angle 165°), extreme optical absorption in the whole visible range, exceptionally low optical reflection and high thermal conductivity. This combination of assets of the produced CNT offers a great potential for solar thermal applications that has been confirmed by the specially designed solar testing experiments.

The growth of a-C:Ag films, grown also by PLD, were grown for the study of their biocompatibility. For comparison a-C:H films, grown by PECVD, were also studied. The findings showed that the a-C:H and a-C:Ag thin films did not exhibit any cytotoxicity levels. The surface topography of the thin films depended on the deposition parameters. A comparison of the hydrophobicity of the thin films showed higher contact angles for the PLD grown thin films. The cell adhesion and spreading was at a higher level on the PLD grown thin films. The effects of the composition, topography, and wettability of the surface of the thin films are the main factors affecting the cytocompatibility of carbon based thin films for medical applications.

APPENDIX A

Optical spectroscopy

The response of an irradiated solid by electromagnetic irradiation depends on its electronic band structure. Optical reflectivity spectroscopy (ORS) can be used for the indirect determination of the complex dielectric function of the solid. The complex dielectric function gives information of the electronic structure of the solid and is strongly related to its reflectance, transmittance and absorption. The mathematical formula of the complex dielectric function describing the optical properties of the solid is not influenced by the conducting or insulating character of the solid.

By classical electromagnetic theory, in a solid under the influence of an electric field, E , its electrons are displaced, resulting in the electrical displacement field of the solid, D , which is proportional to the electrical field E . More specifically, the electronic cloud of a neutral atom under an electric field, E , undergoes a displacement by the electric force. If the electric field is below the ionization threshold then the atom is in a polarized state followed by an electric bipolar moment of the same, with the applied electric field E , direction that equals to:

$$\vec{p} = a\vec{E}$$

where a is the characteristic atomic polarizability of the atom.

The created potential field at distance r by the amount of the bipolar momentums of a solid under electric field E can be calculated by the integration of the potential function as

$$V = \frac{1}{4\pi\epsilon_0} \int_{volume} \frac{\vec{P} \cdot \hat{r}}{r^2} d\tau$$

from which two quantities emerge. The first one occurs by the surface density of charge and equals to

$$\sigma = \vec{P} \hat{n},$$

where \hat{n} is the unit vector perpendicular to the surface and the second quantity refers to the volume density of charge that equals to

$$\rho_b = -\vec{\nabla} \vec{P}$$

Generalizing and if ρ_f is the charge density of the free electron of the solid, the total density of charge can be written as the sum of all the charge densities as

$$\rho = \rho_b + \rho_f + \sigma$$

Applying the Gauss law we have

$$\epsilon \vec{\nabla} \vec{E} = \rho = \rho_b + \rho_f + \sigma = -\vec{\nabla} \vec{P} + \rho_f + \sigma \Rightarrow \vec{\nabla} (\epsilon \vec{E} + \vec{P}) = \rho_f + \sigma$$

where ϵ is the complex dielectric function of the solid.

The parenthesized term is called electric displacement that equals to

$$\vec{D} = \epsilon \vec{E} + \vec{P}$$

This evidences the correlation of the solid's complex dielectric function, ϵ , with its polarization.

The Lorentz model

The Lorentz model describes in very accurate approximation the dielectric and semiconducting solids. The basic consumption of the model is to consider the atom's bound electrons of the solid to be connected to nuclei by a spring, figure A1.

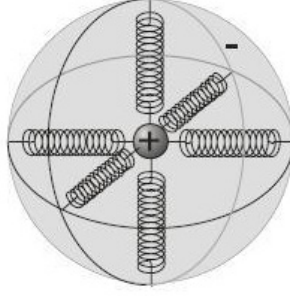


Figure A1: Schematically representation of oscillators in the Lorentz model.

The restoring force by the classical mechanical physics is

$$F_{binding} = -ky = -m\omega_0^2 y$$

As the electron oscillates, it is applied to it also a damping force that is proportional to its velocity and equals to

$$F_{damping} = -m\gamma \frac{dy}{dt}$$

In presence of an electromagnetic field of frequency ω , a driving force is also applied to the electron equals to

$$F_{driving} = qE = qE_0 \cos \omega t$$

So the motion equation of a bounded electron can be described as

$$m \frac{d^2 y}{dt^2} + m\gamma \frac{dy}{dt} + m\omega_0^2 y = qE_0 \cos \omega t$$

and this is the equation of a driven harmonic oscillation of frequency ω .

The bipolar momentum that emerges by this movement is

$$p(t) = qy(t) = \frac{(q^2 / m)}{(\omega_0^2 - \omega^2) - i\gamma\omega} E_0 e^{-i\omega t}$$

and because

$$\vec{P} = \varepsilon_0(\chi_e + 1)\vec{E} \quad \vec{D} = \varepsilon\vec{E}$$

the dielectric function for insulating solids occurs as

$$\varepsilon = \varepsilon_0 \left[1 + \frac{Ne^2}{m\varepsilon_0} \frac{1}{(\omega_j^2 - \omega_0^2) - i\Gamma_j\omega} \right]$$

by the use of one oscillator. In the case that more oscillators are needed for the description of electronic transitions, losses by absorbance or if the solid is composed by more than one element of different optical properties then the dielectric function is

$$\varepsilon = \varepsilon_0 \left[1 + \frac{Ne^2}{m\varepsilon_0} \sum_j \frac{f_j}{(\omega_j^2 - \omega_0^2) - i\Gamma_j\omega} \right] \quad 8.1$$

where ω is the energy position of the oscillator and describes the transition's required energy, f_j is the power of the oscillator and expresses the amount of electrons that oscillate with frequency ω_j . The Γ_j parameter expresses the damping energy losses of the oscillator that originated by electron-electron, electron-nuclear interactions and the radiation damping.

Absorbance and refractive index

When an electromagnetic wave interacts with a non magnetic solid, since it is elastically scattered in a linear medium, its phase and the amplitude are changed while its frequency does not.

The complex refractive index is

$$\tilde{n} = n + ik$$

where n is the refractive index and k is the absorbance coefficient of the solid.

The complex dielectric function is

$$\tilde{\epsilon} = \epsilon_1 + i\epsilon_2$$

Also

$$\tilde{\epsilon} = \epsilon_1 + i\epsilon_2 = (n + ik)^2 = \tilde{n}^2$$

Or

$$\left. \begin{aligned} \epsilon_1 = n^2 - k^2 &= 1 + \frac{4\pi N e^2}{m} \frac{(\omega_0^2 - \omega^2)}{(\omega_0^2 - \omega^2)^2 + \Gamma^2 \omega^2} \\ \epsilon_2 = 2nk &= \frac{4\pi N e^2}{m} \frac{\Gamma \omega}{(\omega_0^2 - \omega^2)^2 + \Gamma^2 \omega^2} \end{aligned} \right\} \quad 8.2$$

or

$$n = \sqrt{\frac{\sqrt{\epsilon_1^2 + \epsilon_2^2} + \epsilon_1}{2}} \quad k = \sqrt{\frac{\sqrt{\epsilon_1^2 + \epsilon_2^2} - \epsilon_1}{2}}$$

The dependence of ϵ_1 and ϵ_2 of the solid by the frequency of the incidence wave is illustrated in figure A3.

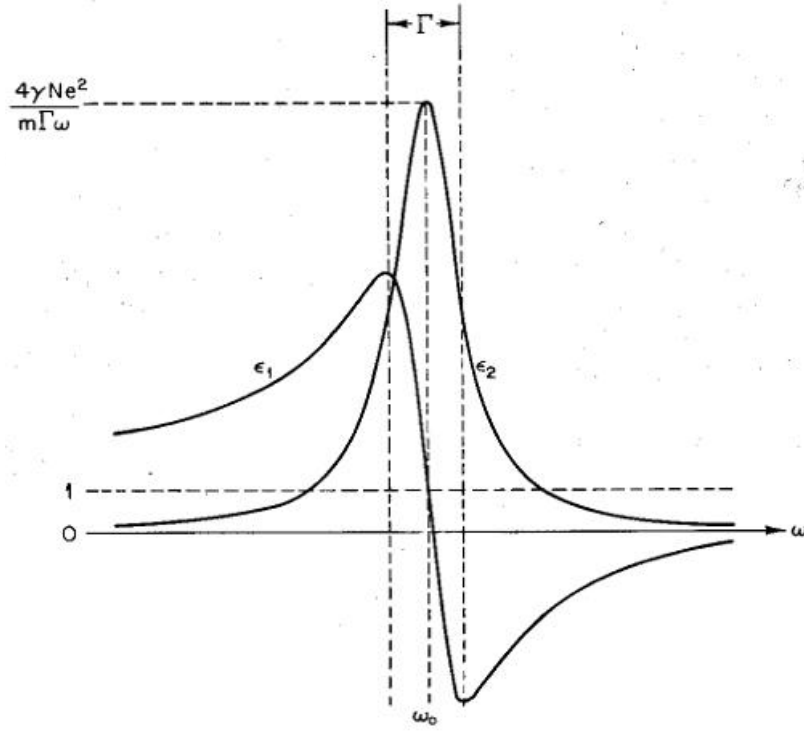


Figure A3: Graphs of ϵ_1 and ϵ_2

We observe that if a narrow area around ω_0 is excited, ϵ_1 increases as ω also increases; in other words as the frequency increases the refractive index of the solid increases too. That frequency area it is called as normal dispersion. Contrariwise, in the area around ω_0 reduction of ϵ_1 is observed as the frequency increases. This area of frequency is called anomalous dispersion. In that area the electrons of the solid are oscillating in resonance frequencies with the applied field followed by the maximization of the absorbance, as it is described by the graph of function ϵ_2 . The full width at half maximum of function ϵ_2 equals to $\Gamma=1/\tau$ in reverse time units (sec^{-1}), where τ is the relaxation time of electrons describing the energy losses of the oscillated in resonance electrons.

